Uncertainty Propagation in Hypersonic Vehicle Aerothermoelastic Analysis

by

Nicolas Etienne Lamorte

A dissertation submitted in partial fulfillment
of the requirements for the degree of
Doctor of Philosophy
(Aerospace Engineering)
in the University of Michigan
2013

Doctoral Committee:

Professor Peretz P. Friedmann, Chair
Professor Carlos E. S. Cesnik
Associate Professor Bogdan I. Epureanu
Assistant Professor Krzysztof J. Fidkowski

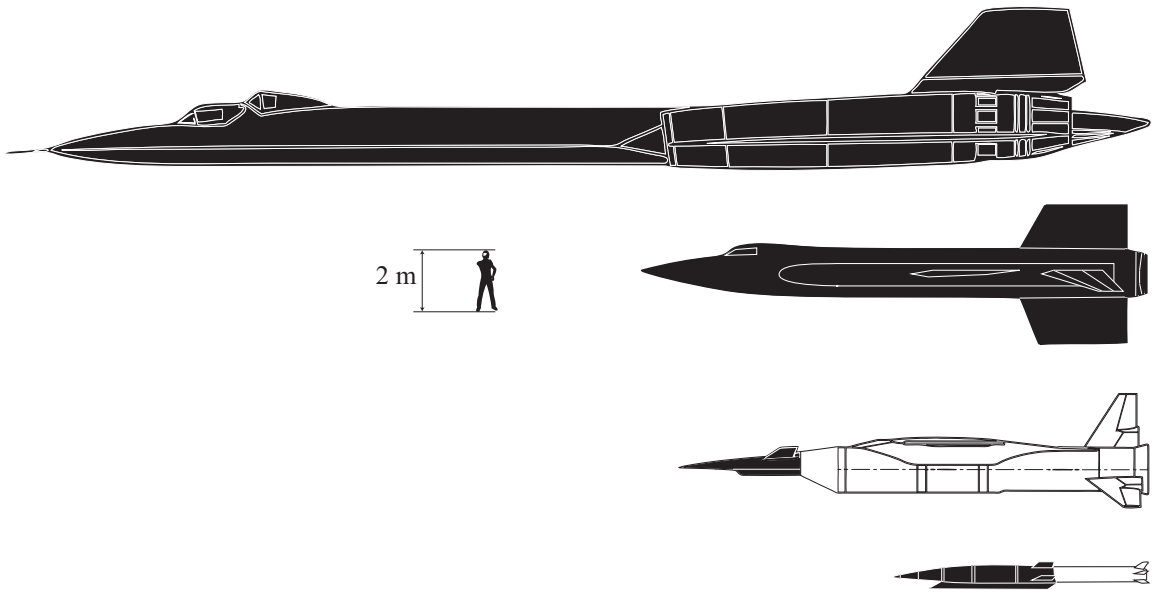
2 m

2013

Dedication

A mon frère, Vincent

Acknowledgments

Many people have made this dissertation possible. My advisor Prof. Friedmann has set high standards from the very beginning. Our interactions made me a stronger researcher dedicated to precise and innovative work. Hopefully this will show in my future career as an individual and aerospace engineer. I am grateful to Prof. Fidkowski, Prof. Cesnik and Prof. Epureanu for agreeing to serve on my thesis defense committee. My interactions with the professors in the aerospace department through research, classes, GSI positions or seminars fostered my interest for innovation and my commitment to the field of aerospace engineering.

I would like to express my gratitude to Metacomp Technologies for providing the CFD++ code; more specifically to Nili, Berinder and Shaun for the constant support in using the different features of this code.

This research was funded under NASA grant NNX08AB32A with Donald Soloway and Jorge Bardina as technical monitors. Partial support was provided by the Michigan/AFRL (Air Force Research Laboratory) Collaborative Center in Aeronautical Sciences, via grant Air Force grant FA8650-06-2-3625 and by the University of Michigan.

This work is built upon the outstanding work of many previous researchers such as Prof McNamara who has always been very helpful and responsive to my requests. Adam Culler and Andrew Crowell at Ohio State University also contributed significantly to this study. Derek Dalle and Sean Torrez gave me the opportunity to explore the field of SCRAM-jet thanks to their hard work put into the code MASIV. In addition Nathan Falkiewicz and Torstens Skujins have been kind enough to listen to my questions about hypersonic aerothermoelasticity. I would like to thank all my colleagues here in my research group with Prof. Friedmann: Li Liu, Bryan Glaz, Abhijit Gogulapati, Ashwani Padthe, and Eric Muir. I would also like to thank all my friends of the aerospace department. Thanks to Denise Phelps, Kelley Bowen, and Anne Rhoades who has been of great help and constant support with the administrative paper work. I would also like to express my appreciation to the Aerospace Engineering technicians and staff.

Prof. Candel from Ecole Centrale Paris was the first to support my enthusiasm for pursuit of the PhD program and helped me to come to Michigan. His work as a teacher

and researcher was a source of inspiration to me. I have to mention my undergraduate math teacher, Mr Mohan at Lycée Janson–de–Sailly, who has the unique talent of making difficult concepts intuitive which skyrocketed me into engineering studies!

My path in Michigan has been shared with many people who kept me going and made this experience exciting and rewarding. Thanks to the members of the European Student Association, the NCRB swimmers, the Master's swimmers, the Ann Arbor Triathlon Club, and Epic Races.

Finally, and most importantly, I would like to thank my family and friends around the world, without whom I would not be who I am now.

TABLE OF CONTENTS

LIST OF FIGURES

LIST OF TABLES

LIST OF APPENDICES

LIST OF ABBREVIATIONS

1D one dimensional

2D two dimensional

3D three dimensional

ANOVA analysis of variance

ARMA auto regressive moving average

BC boundary condition

CDF cumulative density function

CFD computational fluid dynamics

CFL3D NASA Langley CFL3D computational aeroelastic code

CSD computational structural dynamics

CHT conjugate heat transfer

CI confidence interval

DOF degree of freedom

EFF expected feasibility function

EOM equations of motion

FEM finite element model

IG ideal gas

IMCS indirect Monte Carlo simulation

KG kriging surrogate

LHS latin hypercube sampling

LSCF least–squares curve fit method

MASIV Michigan/Air Force scramjet in vehicle code

MCS Monte Carlo simulation

NASP National Space Plane

NS Navier Stokes

PCE polynomial chaos expansion

PDF probability density function

PG perfect gas

PT piston theory

RAND random number generator

RANS Reynolds-averaged Navier-Stokes

RBF radial basis function

RBFN radial basis function networks

RF radial function

RG real gas

ROM reduced order models

SA Spalart Allmaras turbulence model

SI system identification

SC stochastic collocation

SCE extended stochastic collocation

SCF spatial correlation function

TPS thermal protection system

UQ uncertainty quantification

LIST OF SYMBOLS

$[\mathbf{A}]$	Transition matrix in the time domain
$A,\ B$	Coefficients for Beta distribution
A_r	Reaction rate parameter
A_j	Fitting coefficients
$A_n(t)$	Deformed shape coefficients
a	Non–dimensional elastic axis position, positive aft from midchord
a_i	Average regression coefficient
$b = c/2$	Semi–chord
$C_1,\ \ldots,\ C_4$	Deformed shape coefficients
$\mathbf{C_A}, \mathbf{K_A}$	Aerodynamic influence damping and stiffness matrices
$C_P = \frac{P-P_\infty}{q_\infty}$	Pressure Coefficient
c	Chord
c_p	Specific heat of air at constant pressure
c_v	Specific heat of air at constant volume
c_m	Specific heat of material
D	Bending stiffness of the panel
D_f	Variance of f in Sobol's analysis
$D_{j_1,\ldots,j_k}$	Contribution of the variance of f in Sobol's analysis
E	Young's modulus
ER	Equivalence ratio, $\left(\frac{\dot{m}_f}{\dot{m}_{4,O_2}}\right) / \left(\frac{\dot{m}_f}{\dot{m}_{4,O_2}}\right)_{st}$
E_a	Activation energy
e_a	Air internal energy
e_k	Excitation
F_x	Force acting in the $x-$direction
F_Z, F_N	Stability metric
f	Quantity of interest
$\hat{f}$	Approximation of f
$f_0 = \langle f \rangle$	Constant term in the Sobol's expansion of f
$f_{j_1,\ldots,j_k}$	Functions in the Sobol's expansion of f
$\boldsymbol{f_x}$	Vector of basis functions associated with assumed polynomials in kriging
$\boldsymbol{F}_x$	Matrix of basis functions associated with assumed polynomials in kriging
$f(x) = y$	Output of interest
H	Altitude

h	Plunge degree of freedom
h_1	Radiation shield thickness
h_2	Thermal insulation thickness
h_3	Thickness of the structural layer
h_a	Air enthalpy
h_w	Heat flux coefficient
h_p	Panel thickness
$\mathbf{I}$	Identity matrix
I_α	Static moment of inertia of the wing section about elastic axis
K_α	Spring constant in pitch
K_h	Spring constant in plunge
$\mathbf{K}$	Structural stiffness matrix
k_r	Reaction rate coefficient
k	Thermal conductivity
L	Lift
L_2	Mean square error
L_∞	Maximum error
l_p	Panel length
M	Mach number
$\mathbf{M}$	Structural mass matrix
$\mathbf{M_A}$	Apparent mass matrix
M_{ea}	Aerodynamic moment about the elastic axis
M_∞	Free stream Mach number
M_f	Flutter Mach number
M_{fd}	Deterministic flutter Mach number
M_{fm}	Flutter margin expressed in terms of Mach number
M_T	Thermal bending moment
m	Cross sectional mass of the cross section
$\dot{m}_{air}$	Air mass flow rate
$\dot{m}_f$	Fuel mass flow rate
$m_f \equiv \langle f \rangle$	Expected value of f
$\mathcal{N}(.)$	Normal probability density function
$N(.)$	Normal cumulative density function
N_I	Number of points in the numerical integration scheme
N_m	Number of modes
N_s	Number of sampling points
N_v	Number of random variables
N_x	In-plane stress resultant
n	Temperature exponent in rate–coefficient expression
$\boldsymbol{n} = (n_x, n_y, n_z)$	Normal to the surface of the wing
$p_x(x)$	Probability density function (PDF)
$P_x(x)$	Cumulative density function (CDF)
$p_f(\beta)$	Probability of failure
$p_{x(A,B)}(x)$	Beta(A, B) probability density function

$P(x,t)$	Pressure
P_3	Pressure behind the leading edge shock
$p(x)$	Polynomial function in the RBF interpolant
p_n	Polynomial function
p_i	Root of the aeroelastic stability equation
p_k, θ_k	Fitting parameters in kriging corresponding to the k^{th} design variable
(p_n)	Polynomial function basis
Q_i	Generalized aerodynamic load
q_a	Dynamic pressure
q_{aero}	Aerodynamic heat flux
q_i	Generalized degree of freedom
q_{rad}	Radiation heat flux
Re	Reynolds number based on a length of 1 m
R	Perfect gas constant
$\boldsymbol{R}_{krg}$	Spatial correlation matrix used in kriging
$R_{krg}()$	Spatial correlation function in kriging
$r_{krg}(x)$	Spatial correlation vector in kriging
r_α	Non dimensional radius of gyration
$r = \|\boldsymbol{x}\|$	Euclidian distance from the origin
S_α	Static mass moment of the wing section about elastic axis
T	Temperature
T_0	Initial panel temperature
T_E	Kinetic energy
T_f	Flight Time
T_r	Recovery temperature
T_s	Sampling time in ARMA
T_u	Turbulent kinetic energy intensity
T_w	Wall temperature
t	Time
t_h	$= \tau b$, Airfoil thickness
U_E	Elastic energy
U_∞	Freestream velocity
u	Axial displacement at elastic axis
v_n	Velocity in the z direction
$w(x,t)$	Structural deformation in the z direction
w_k	Weight in numerical integration
$\bar{w}_1$	Deformation of the airframe of the vehicle
$\bar{w}_2$	Deformation of the cowl
$\boldsymbol{X} = \{\mathbf{q}; \dot{\mathbf{q}}\}$	State variable
(x', y', z')	Coordinate system for the corrugated panel
x	Coordinate from leading edge, positive aft
$\boldsymbol{x}$	Vector position
x_e	Distance of panel location from leading edge
$x_e a$	Elastic axis offset

x_t	Location of transition point from laminar to turbulent flow from leading edge
x_{ti}	$= x_e - x_t$, Distance between the leading edge of the panel and the transition point
x_α	Normalized center of gravity location, positive aft
y	Spanwise coordinate
y_{lim}	Limit state for the output of interest
z	Coordinate normal to vehicle, from leading edge point, positive up
$Z(x)$	Realization of a stochastic process in kriging
$Z_s(x, y)$	Structural shape
z	Coordinate normal to the wing

Symbols

$\|\boldsymbol{x}\| = \sqrt{\sum_i x_i^2}$	Euclidian norm
$\partial\Omega$	Fluid–structure interface
$\partial\Omega_k$	Cell face at the fluid–structure interface

Greek Symbols

$\{\alpha\}$	RBF coefficients
α	Pitch degree of freedom
α_f	Angle of attack of the trajectory
α_q	Aerodynamic heat flux scaling factor
α_s	Static angle of attack
α_T	Thermal expansion coefficient
β	$\frac{M_f}{M_{fd}}$, Flutter Mach number ratio
β_j	RBF coefficients for the polynomial
β_s	Shock angle
$\boldsymbol{\beta}$	Vector of coefficients used in kriging
$\gamma = \frac{c_p}{c_v}$	Specific heat ratio
δ_{jk}	Kronecker symbol
ΔT_f	$= T_f - T_{fd}$, Variation of flight time
ϵ	Emissivity
ϵ_G	Precision to estimate the limit state in the EFF
ζ_i	Damping coefficient
η	Correction factor in linearized PT
θ	Forebody surface inclination
$\boldsymbol{\Theta}$	Integral of the state transition matrix
μ_G	Prediction of the kriging surrogate
μ_L	Laminar viscosity
μ_T	Turbulent viscosity
ν	Poisson ratio
$\tilde{\nu}$	Dependent variable in SA turbulence model

ξ_1, ξ_2	Uncertain variables in the integrated Scramjet engine analysis
ρ	Density of air
ρ_m	Density of material
ρ_p	Density of the panel
σ_f	Standard deviation of f
σ_G	Standard deviation of the kriging surrogate
σ^2_{var}	Variance of the Gaussian process Z(x)
$\hat{\sigma}^2_{var}$	Generalized least squares estimate of σ^2_{var}
τ	Normalized airfoil thickness
ϕ_j	Interpolation function
Ω_x	Uncertain variables design space
ω_α, ω_h	Natural frequency in pitch and plunge respectively
ω_i	Natural frequency
$\omega_{n,max}$	Maximum natural frequency
$\omega_{di} = \omega_i\sqrt{1-\zeta_i^2}$	Damped frequency
$\mathbf{\Phi}$	State transition matrix
ϕ	Radial basis function
ϕ_i	Basis function
$\psi_i\left(x, y, z\right)$	Mode shape deformation in the $z-$direction in the i^{th} mode

Subscripts

∞	Freestream condition
0	Total condition
4	Condition at the exit of the combustor
i	Initial value
st	Stoichiometric condition
$wall$	At the wall

Superscript

F	Pertaining to the fluid
S	Pertaining to the structure
$\dot{} = \frac{d}{dt}$	Differentiation with time

ABSTRACT

Uncertainty Propagation in Hypersonic Vehicle Aerothermoelastic Analysis

by

Nicolas Etienne Lamorte

Chair: Professor Peretz P. Friedmann

Hypersonic vehicles face a challenging flight environment. The aerothermoelastic analysis of its components requires numerous simplifying approximations. Identifying and quantifying the effect of uncertainties pushes the limits of the existing deterministic models, and is pursued in this work. An uncertainty quantification framework is used to propagate the effects of identified uncertainties on the stability margins and performance of the different systems considered.

First, the aeroelastic stability of a typical section representative of a control surface on a hypersonic vehicle is examined. Variability in the uncoupled natural frequencies of the system is modeled to mimic the effect of aerodynamic heating. Next, the stability of an aerodynamically heated panel representing a component of the skin of a generic hypersonic vehicle is considered. Uncertainty in the location of transition from laminar to turbulent flow and the heat flux prediction is quantified using CFD. In both cases significant reductions of the stability margins are observed.

A loosely coupled airframe–integrated scramjet engine is considered next. The elongated body and cowl of the engine flow path are subject to harsh aerothermodynamic loading which causes it to deform. Uncertainty associated with deformation prediction is propagated to the engine performance analysis. The cowl deformation is the main contributor to the sensitivity of the propulsion system performance.

Finally, a framework for aerothermoelastic stability boundary calculation for hypersonic vehicles using CFD is developed. The usage of CFD enables one to consider different turbulence conditions, laminar or turbulent, and different models of the air mixture, in particular real gas model which accounts for dissociation of molecules at high temperature. The system is found to be sensitive to turbulence modeling as well as the location of the transition from laminar to turbulent flow. Real gas effects play a minor role in the flight conditions considered.

These studies demonstrate the advantages of accounting for uncertainty at an early stage of the analysis. They emphasize the important relation between heat flux modeling, thermal stresses and stability margins of hypersonic vehicles.

CHAPTER 1

INTRODUCTION, BACKGROUND AND OBJECTIVES

1.1 The Hypersonic Environment

Hypersonic flight is an active area of research motivated by interest in unmanned rapid response to threats and reusable launch vehicles for affordable access to space [1–6]. Such vehicles are based on lifting body designs which tightly integrate the airframe and propulsion system. For hypersonic cruise applications, the propulsion system is expected to consist of air–breathing engines that operate for sustained periods in atmospheric flight. [6–8]

The hypersonic environment is depicted in terms of altitude and Mach number in Fig. 1.1. Two iso–dynamic pressure curves corresponding to $q_\infty = 0.5$ atm and $q_\infty = 1.0$ atm, respectively are depicted in Fig. 1.1. The lower dynamic pressure corresponds to a limit under which the Scramjet engine cannot function efficiently. The higher limit of 1 atm is the structural limit. Exceeding this limit results in extreme static pressure and thermal loading that practical configurations cannot withstand. The two curves define the hypersonic corridor and illustrate the fact that air–breathing hypersonic vehicles are tightly constrained in their operating environment [9]. Furthermore, the shaded areas correspond to real gas effects that occur at high speeds corresponding to high static temperatures [7]. The perfect gas model is sufficient for the air flow for Mach numbers less than 3, vibration of the biatomic molecules becomes important above this speed. For higher flight Mach

numbers, oxygen dissociates first, then nitrogen, and gas ionization occurs at reentry conditions.

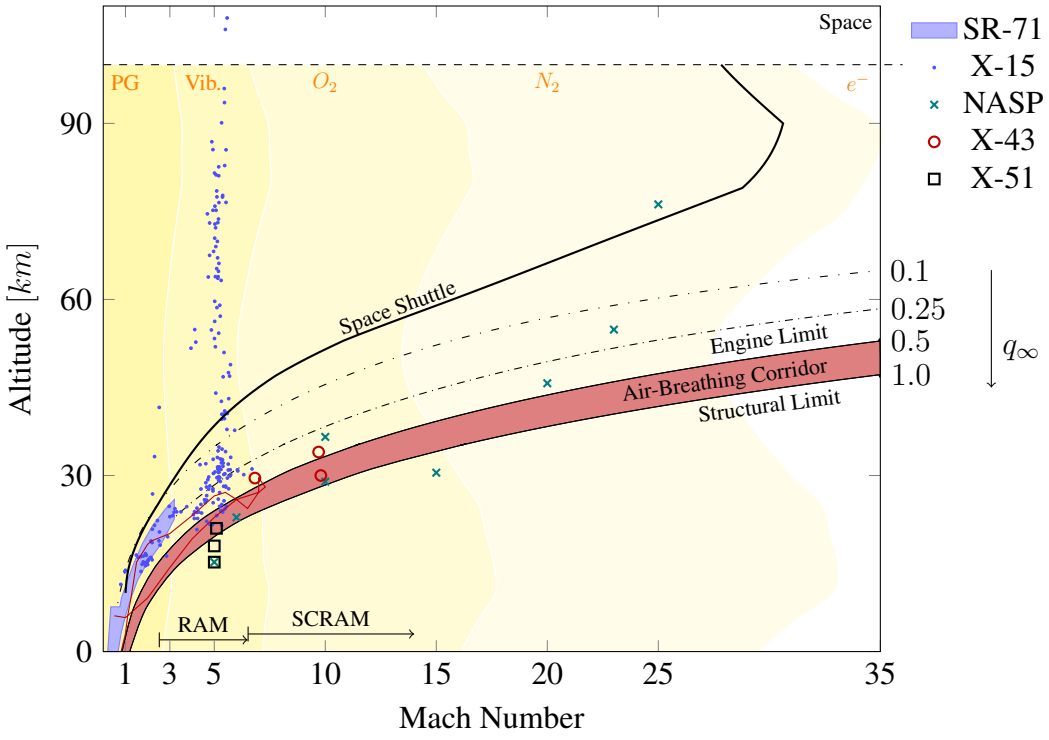

Figure 1.1: Flight envelops of existing and potential hypersonic vehicles, and corresponding flow regimes with respect to vehicle's speed and altitude

Flight envelopes of several previous and prospective hypersonic vehicles are depicted in Fig. 1.1. Only few air–breathing hypersonic vehicles have flown. The X–15 was the first experimental aircraft capable of reaching hypersonic speeds for a limited time owing to its rocket engine [10]. As preliminary steps towards reaching hypersonic speeds, sustained air-breathing supersonic flights were demonstrated with the F–104 and SR–71, Blackbird [11]. The later flew at supersonic speeds for extended periods of time in the atmosphere [11]. For the X–15 and SR–71, the structure had to be made of titanium to withstand the thermal loads. The National Aerospace Plane (NASP) was intended to be an air-breathing hypersonic vehicle capable of long duration flight at hypersonic speeds at the edge of the atmosphere [12, 13]. However, the program was canceled due to numerous unresolved technological challenges connected to structural and material reliability

(a) F–104

(b) X–15

(c) SR–71

(d) X–43

(e) X–51

Figure 1.2: Previous and current supersonic and hypersonic aircrafts

at elevated temperatures. More recent scramjet engine demonstrators are represented by the X–43 and the X–51 vehicles. These experimental vehicles were designed to test and advance the scramjet propulsion technology. Both of them are dropped from the B–52 bomber. A rocket booster accelerates them to approximately Mach 4 to 5. After separation from the booster, the scramjet engine is turned on. The flights were intended to last for a few hundred seconds. In the case of the X–51, 2 out of 4 flights faced early termination due to engine's unstart, thermal management issues and loss of control.

In the case of the SR–71, several challenges were faced during the development of this program. When cruising at Mach 3, aerothermoloads are significant and resulted in the selection of titanium as the structural material, despite its weight penalty. Flight after flight the structure changed and became stronger over time because of both the high aerodynamic heat and pressure loads. Furthermore, the panels on the wing surface were corrugated to handle the heating and cooling cycles from one mission to another. The two Ramjet engines would unstart unexpectedly in flight due to large airflow disturbances or improper inlet control. This phenomena occurred frequently and illustrates the sensitivity of the

propulsion system to small changes in its environment. [14]

> The unstart condition is not a gradual thing; it happens immediately with a bang. When the inlet unstarts and loses its smooth flow, there is a large directional input to the aircraft and also some pitch-up moment. At certain Mach numbers around 2.3 to 2.6, the input to the aircraft is so violent that it can snap the pilots head and helmet against the inside of the canopy.
>
> *Don Mallick, research pilot [14]*

Thus, it is apparent that the flight environment of air–breathing hypersonic vehicles is replate with challenges that prevent sustained flight. An illustration of the interactions between various disciplines relevant to hypersonic flight is represented by an octahedron, shown in Fig. 1.3. At the bottom, propulsion (P) refers to the air–breathing propulsion system consisting of a Ram or scramjet engine, combustion, internal flows, boundary layer–shock interactions. This discipline poses several challenges which are a barrier in the development of air breathing vehicles. At the top, the control (C) discipline poses challenges. Studying the interactions between aerodynamics, propulsion, and control systems is not sufficient for the design of safe flight. Aerothermoelastic interactions are significant and are represented by the shaded surface which highlights the mutual interaction between aerodynamic loads (A), elastic deformations (E), inertia loads (I) and effect of temperature (T).

Hypersonic flows are inherently complex and involve phenomena that are not present in supersonic conditions, such as: dissociations, chemically reacting flow, viscous interactions and higher levels of aerodynamic heat flux [7, 8, 15]. The development of hypersonic systems requires reliable design data that cannot be fully validated in ground test facilities [5]. Primarily because there are no suitable high speed, high enthalpy wind tunnels capable of testing scaled models of hypersonic vehicles. Furthermore, hypersonic aerothermoelastic scaling laws are not available at high Mach numbers [16].

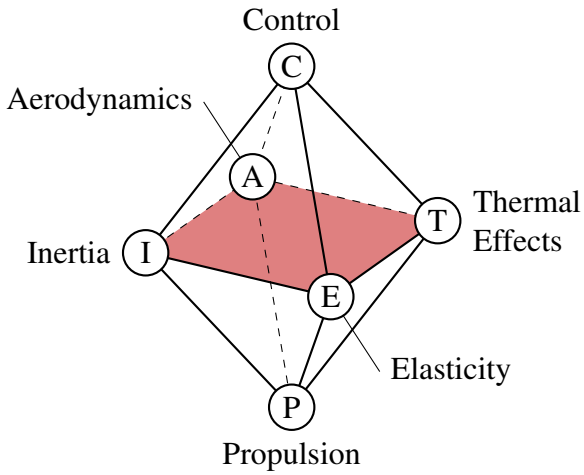

Figure 1.3: The aerothermoelastic propulsion and control interactions

Flight tests are very expensive and require reliable analysis tools. High fidelity numerical simulations of the complex hypersonic flow environment are computationally expensive. The state of the art is at a relatively early stage of development where the precise role of important factors such as real gas effects, chemically reacting flows and complex viscous interactions are not well understood. Current analysis tools employ computationally efficient models based on simplifying assumptions on the physics and/or reduced order models (ROM). Therefore, the development of accurate aerothermoelastic simulation capabilities is critical for the design and analysis of hypersonic vehicles. Compensating for shortcomings in modeling requires the use of uncertainty propagation techniques in hypersonic aerothermoelastic analyses.

This work focuses on hypersonic aeroelastic and aerothermoelastic studies for structures representative of prospective air–breathing hypersonic vehicle components. The objective is to use uncertainty propagation techniques to compensate for modeling approximations.

1.2 Literature Review

Approaches to aerothermoelastic analysis of hypersonic vehicles and applying uncertainty quantification approaches require various tools. A review of previous study is given in this section. First uncertainty quantification approaches are listed. Then accomplishment in aerothermoelastic analysis for hypersonic vehicles are briefly described. Finally airframe–integrated scramjet engine studies are presented.

1.2.1 Uncertainty Quantification

The uncertainty quantification (UQ) analysis encompasses numerous approaches which share the common goal of identifying uncertainty and quantifying its effect on a given prediction. The main motivation is to design under uncertainty and provide a robust analysis tool [17]. Uncertainty can arise from input variables, model parameters, choice of competing models, experimental data, and approximations or usage of surrogate models. Two types of uncertainty have been defined in the literature [18, 19]: epistemic and aleatory uncertainty.

Epistemic uncertainty encompasses uncertainty inherent to the modeling assumptions pertaining to a given analysis. For instance, several models or codes can be considered for a given analysis, where each model is accurate to a certain degree of confidence [20]. Bayesian averaging is the most popular method to combine the probabilities associated with the multiple predictions coming from the various model. [21, 22]. In addition, it can be used iteratively for calibration and to locate areas of high uncertainty and improve a given model [23, 24]. Experimental data and high fidelity simulations can be combined to calibrate model parameters iteratively and decrease their uncertainty for a specific range of application [21]. These considerations go beyond the scope of this study which is focused on identifying and propagating uncertainties in hypersonic vehicle computational analyses.

Aleatory uncertainty refers to variability inherent to input variables, e.g. atmospheric

properties, change in materials properties due to manufacturing and defects. This uncertainty cannot be eliminated and is modeled using probability distributions, often arbitrarily assumed to be Gaussian. Once sources of uncertainty have been identified and quantified by probability distributions, the effect of uncertainty can be studied using two methods: *intrusive*, using polynomial chaos expansion and a Galerkin approach [25–28], and *non–intrusive* [18, 19, 29, 30].

Intrusive methods require the modification of the code to account for the uncertain parameter dependency. Also, they often limit the number of uncertain variables that can be considered simultaneously due to the curse of dimensionality. Hypersonic aerothermoelastic problems require the use of non-intrusive methods due to the complexity of analysis codes which are difficult to modify.

Direct Monte Carlo simulation (MCS) is a non–intrusive approach widely used in relatively simple aeroelasticity studies, such as: aeroelastic failure risk assessment of composite structures with more than 20 uncertain variables [31], panel flutter with uncertainty in the material properties [32, 33] or boundary conditions [34], robust design of a wing under material and geometric uncertainty [35], robust flutter calculation with uncertainty in the aerodynamic influence coefficients [36] or mass properties [37], helicopter performance evaluations with uncertainty in the composite materials properties [30] or aerodynamic coefficients and geometric parameters of the airfoil [38]. In the case of hypersonic vehicles, thermal protection system (TPS) margin estimation [39] and scramjet performance under inflow uncertainty [40, 41] were also studied using MCS. The MCS approach allows consideration of cases with a large number of uncertain variables. It can be enhanced by using gradient information [41]. However, the method requires numerous evaluations of the function of interest (e.g. flutter Mach number), at values of the uncertain inputs dictated by their probability distributions. This approach is computationally prohibitive in the context of complex hypersonic aerothermoelastic analyses. Therefore, response surface based methods have been developed and are employed in this study as a computationally

efficient alternative to direct MCS [42].

An extended list of non–intrusive alternative approaches is implemented in the DAKOTA code [42], a multilevel parallel object-oriented framework for design optimization, parameter estimation, uncertainty quantification, and sensitivity analysis (developed at Sandia National Laboratories). In response surface based methods, the expensive analysis f is replaced by a computationally inexpensive approximation $\hat{f}$. Various approximations can be considered. Two approaches to generating an inexpensive response surface in wide use are: polynomial chaos expansion (PCE) which is developed from the intrusive method approaches [43–45] and stochastic collocation (SC) [18, 46]. Both rely on polynomial expansions. In Ref [47], the aeroelastic stability of a transonic wing is studied introducing variability in the inflow conditions using PCE compared to MCS. Stochastic collocation is shown to be an efficient response surface method in Ref. [18]. This computationally efficient approach is applied for the first time, in this thesis, to study uncertainty quantification (UQ) in hypersonic aeroelastic and aerothermoelastic problems.

The choice of the response surface is problem dependent. Alternatively other interpolation techniques have been considered such as regressions [48], Padé–Legendre approximants [49], radial basis function networks (RBFN) [50], or multi-variable splines [51, 52]. Model reduction is also a computationally efficient approach to UQ: in Ref. [53], a proper orthogonal decomposition reduced order model is used to reduce the cost of an expensive CFD analysis and is subsequently used in a parameter identification study.

In the case of a high number of uncertain variables, adaptive sampling is the only approach to alleviate the curse of dimensionality. Several adaptive sampling approaches exist. Adaptive sparse grid interpolation [54–56] is also based on a polynomial fit of the expensive analysis but uses its error prediction to adaptively refine the response surface. Kriging surrogates [57] are used as a goal–oriented method with adaptive sampling which focuses only on accurately capturing the probability of failure, thus reducing the cost of the UQ analysis [57, 58]. A combination of response surfaces is also an efficient way of exploring

a design space [59]. More recently, in Ref. [60], simplex based interpolation combined with adjoint solutions is used to improve the accuracy of the response surface. Error estimates for the functional are used to adaptively sample the solution in uncertain parameter space leading to an efficient goal–oriented adaptive approach to UQ.

Finally, note that UQ requires that the analysis is valid for the uncertain variable space considered which adds requirements on the development of the analysis tool. This constraint is also one of the benefits of UQ analysis as will be shown in this work. For example, in Ref. [61], a CFD mesh is optimized to be used for a wide range of cases determined by the distribution of the uncertain input variables.

1.2.2 Hypersonic Aeroelasticity and Aerothermoelasticity

The complex aerodynamic environment in which a hypersonic vehicle operates makes the structural design challenging necessitating high performance materials [62]. A detailed survey of aeroelastic and aerothermoelastic studies of hypersonic vehicles was presented in Ref. [1]. Early studies were based on simple models for both fluid and structure and later became more complicated.

1.2.2.1 Thermal Structures

As mentioned in the introduction, designing structures and materials suitable for long endurance hypersonic flight is still challenging, despite numerous developments in structural layout [63, 64] and innovative materials technology [65, 66].

Thermal management is the main issue for hypersonic vehicles. During the National Space Plane (NASP) program, two main strategies were considered: actively cooled structures and hot structures. Several studies have been conducted to investigate the temperatures in the load carrying structure for various structural layouts and missions [67, 68]. Material performances were found to be the main limiting factor [69]. Thermal protection systems are required. In Ref. [64], the structure is designed under thermal and fuel

capacity constraints. A finite element model (FEM) analysis is combined with three analysis codes that predict the pressure distribution, heat distribution and fuel requirements. The TPS protected cold–skin integrated–tank structure performs better than a hot structure. In Refs. [70, 71] a simple one dimensional (1D) FEM analysis is used to investigate the performance of various TPS layouts. Corrugated panels allow for light–weight load carrying structure capable of sustaining thermal expansion without developing high thermal stresses [69, 72–75].

In a recent joint effort initiated by the Air Force and DARPA, Goodrich Aerostructures Group [76], Lockheed Martins [77], and Boeing [78, 79], critical milestones to advance the structural design for sustained hypersonic flight were identified. In Ref. [76], the importance of thermal and acoustic loading on stresses that develop in the panel is presented. In Ref. [77], four hypersonics programs (SR-71/YF-12, DARPA HTV–3X, NASP, NASA X–33) are reviewed to identify the gaps that were faced. Hypersonic vehicles require coupled aerothermal and structural design methodologies for detailed hypersonic vehicle design, eventual reusable flight capability, and service life predictability. In Ref. [78], a generic hypersonic vehicle is investigated. Integration of thermal analysis and structural design as well as CFD based load predictions are identified as one of the limitations to the current analysis. Finally, in Ref. [79], a nonlinear reduced order model methodology is utilized to investigate vibrations of heated panels under acoustic loads.

1.2.2.2 Hypersonic Aeroelasticity

A review of aeroelastic and aerothermoelastic issues during the National Space Plane (NASP) program is given in Ref. [80]. Three areas are emphasized: experimental results, unsteady aerodynamics and integrated analysis methodology. For the development of NASP, extensive aeroelastic and experimental studies were compared in Ref. [81]. The calculations relied on approximate methods such as piston theory and also CFD–based calculation using the CFL3D code.

Piston theory was developed by Lighthill [82], based on the observation of supersonic flow past an airfoil at high Mach number. It became a popular unsteady aerodynamic approximate model for aeroelastic studies at high Mach numbers as the result of the work of Ashley and Zartaria [83]. Third order piston theory (PT) was successfully used in flutter prediction of a typical supersonic control surface in hypersonic flow [84] and it outperformed other approximate approaches when compared with CFD. [2]

The CFL3D Code is a powerful aeroelastic solver developed by NASA Langley which has been recently used in hypersonic aeroelastic studies of a hypersonic vehicle and a low aspect ratio wing [85].

A computational fluid dynamics approach is the only alternative that allows increased complexity of the unsteady aerodynamic loading and heating. Coupling of a CFD code with a computational structural dynamics (CSD) model is considered in this study. A CFD code provides the aerodynamic pressure distribution at the structural interface, while the structural dynamics are represented using the finite element method. Aeroelasticity using CFD can be formulated as the three–fields problem [86]: the structure, the fluid and the dynamic mesh.

Due to the classical Eulerian representation of the CFD approach and the Lagrangian formulation of the CSD, a key component of these simulations is the fluid/structure coupling scheme [87–90]. For the CFD approach, the arbitrary Lagrangian–Eulerian formulation accommodates for the moving boundaries and grid deformation [87, 91]. Monolithic schemes which solve the fluid, structure and dynamic mesh equations simultaneously are not appropriate for hypersonic aeroelasticity and aerothermoelasticity.

The deformation of the fluid domain is induced by the deformation of the structure at the wetted interface. Common mesh deformation methods include automatic remeshing, which is computationally expensive, or spring analogy which was used in Ref. [2] for hypersonic aeroelasticity and aerothermoelasticity studies. The latter is used as a reference to verify the results presented in this thesis. The radial basis function (RBF) interpolation

is an efficient method for mesh deformation and has been successfully used to compute large mesh deformations in several aeroelastic applications; [50, 92–100], however it has not been applied to hypersonic problems.

The stability of an aeroelastic system is determined by looking at its damping as a function of the flight condition. When simple aerodynamic models were used, the p–method was the method of choice [101]. In the case of CFD–based aerodynamics, a least–square fit approach is more natural [102]. More recently, the auto regressive moving average (ARMA) method was shown to be an efficient method to identify frequency and damping in the transient aeroelastic response [103, 104] and successfully used in the context of hypersonic aeroelasticity problems [84]. Other system identifications (SIs) methods focused on looking at the relationship between the generalized loads and generalized degree of freedom (DOF)'s have also been developed [105–107].

1.2.2.3 Aerothermoelasticity

The importance of thermal effects has been recognized at a very early stage of the development of high speed flight using analytical and experimental results [108–110]. Torsional stiffness of the wings under chordwise varying heat flux was investigated [111]. Leading edge buckling was also identified to be critical in hypersonic flight [112]. In early studies, panel buckling was studied experimentally and analytically using beam theory to predict fatigue and failure under thermal loads [113]. Actively cooled honeycomb panels built of Aluminium alloy were initially designed using analytical methods and tests [67, 68].

Panel flutter investigations allowed for tremendous research on aero–thermo–structural coupling. An extensive review is given in Ref. [114]. Early studies relied on analytical methods [115]: von Karman plate theory combined with Galerkin methods for the structure, piston theory or potential flow for the pressure loading. Thermal effects were included later. More complex formulation of the structure using FEM allowed to account for arbitrary temperature distributions, as well as composite materials [116]. In parallel, the ef-

fect of arbitrary flow direction [117], or curvature [118, 119] were also investigated using Galerkin approaches. In Ref. [120], the influence of imperfections in the shape of the panel is considered.

Two common simplifying assumptions used in aerothermoelastic analysis of hypersonic vehicles are piston theory for computing the aerodynamic loading [2,83], and Eckert's reference temperature or enthalpy method for calculating aerodynamic heat flux [7, 121], especially for tightly coupled analyses. In Refs. [122, 123], coupling strategies are investigated using a FEM model. The importance of the coupling between deformation and aerodynamic heat flux for the aerothermoelastic response of a panel is demonstrated. Recent studies on panel flutter include acoustic loading [124] and developing CFD–based ROM of the heat load [125]. The use of ROM's currently under development for hypersonic vehicles are significant steps towards investigating the fine interactions that occurs in tightly integrated aerothermoelastic studies. [125–130].

The use of approximate or reduced order models yield computationally efficient calculations and can benefit from the introduction of uncertainty, since several important effects are neglected. For instance, the influence of transition has not been investigated.

1.2.3 Airframe Integrated Scramjet Engine Analysis

A review of the development of ram and scramjet engine propulsion is given in Ref. [9]. Propulsion/airframe integration, materials, and thermal management as well as CFD code analysis and validation methodologies were identified as part of the 10 enabling technologies for sustained hypersonic flight.

A scramjet engine is a highly integrated propulsion system composed of various components: inlet, combustor, nozzle [131]. The structure of the flow in the inlet can be experimentally studied only for short durations for a given flight condition [132, 133]. Shocks, expansion fans, boundary layers, detachment and reattachment regions and their interactions at the inlet are complex and computationally expensive to predict. Therefore, com-

prehensive analysis codes must employ models based on simplifying assumptions of the physics and/or reduced-order modeling of full order computations. Due to the critical role of simulation codes in hypersonic vehicle analysis, the importance of quantifying the risk/reliability in such computational simulations is particularly important. For instance, the inlet can be sensitive to change in the free stream properties, unstart corresponds to choking of the flow [128]. This choking is normally induced by an increase in the contraction ratio, turning angle, overfueling or mass flow blockage.

Simplified models are computationally efficient and enable comprehensive analysis of a hypersonic vehicle in a control–oriented or optimization–oriented framework. One such code is the Michigan/Air Force scramjet in vehicle code (MASIV) developed at the university of Michigan. It relies on approximate models to provide an efficient tool to investigate design and performance of airframe integrated ramjet/scramjet engine propulsion [134, 135]. Its latest version includes transition from ram to scramjet but is not used in this work [136]. In this study, a UQ approach will be used to quantify the effect of thermal deformations to the propulsion system performance using the code MASIV.

Majority of studies concerning propulsion systems neglect aerothermoelastic deformations. A few studies showed that aeroelastic deformations of the inlet have a significant impact on the performance of the engine [137]. In Ref. [137], the airframe is modeled using a FEM approach. The propulsion model uses a 2D inlet and nozzle inviscid solution with a 1D combustor. The impact of aeroelastic deformations on the propulsion system are given as error bars and emphasizes the importance of small deformations on engine performance. More integrated control–oriented studies have focused on simple beam models to account for flexibility [6, 138]. Simple 1D models are used for the propulsion system analysis. Heat is neglected.

To compensate for unmodeled physics and simplifications, an uncertainty propagation approach can be used. In Ref. [40], each component of the flow path, inlet–engine–nozzle, is investigated with its own method. The analyses are combined to predict the thrust of a

scramjet. The uncertainty associated with the use of each model that compose the propulsion system analysis is calibrated using experiments and propagated to the net thrust as a function of fuel inflow rate for two fixed configurations using MCS. Error associated with the approximate models have a significant impact on the prediction of the thrust. In Ref. [139], a combination of epistemic and aleatory uncertainties is used to highlight the importance of the Reynolds-averaged Navier-Stokes (RANS) turbulence model in scramjet simulations. Similarly, UQ emphasizes the importance of uncertain operating conditions in predicting the unstart probability of a scramjet engine [41].

1.3 Objectives

As evident from this literature review, hypersonic aeroelasticity, aerothermoelasticity and interaction models for integrated airframe propulsion interactions are based on numerous simplifying assumptions. Furthermore model uncertainties in the representation of hypersonic flows and their impact on aerothermoelastic stability have not been considered. In particular, the effect of turbulence modeling and real gas on aeroelastic stability have not been investigated.

Thus, the overall objectives of this dissertation are to (1) identify uncertainties relevant to specific hypersonic aerothermoelastic problems, and (2) propagate uncertainty in this class of problems and determine their effect on stability boundaries and integrated vehicle–propulsion system behavior. The specific objectives of this research are to:

1. Examine the influence of uncertainty propagation on the aeroelastic stability of a representative hypersonic problem consisting of a typical section.

2. Examine the effect of uncertainty propagation on the behavior of a representative aerothermoelastic problem consisting of a panel mounted on the surface of a hypersonic vehicle.

3. Investigate the potential effects of coupling vehicle aerothermoelastic deformation with the propulsion system as represented by a simple scramjet engine model.

4. Assess the influence of real gas effect and turbulence modeling on the aeroelastic and aerothermoelastic behavior of a low aspect ratio wing that represents a control surface on a hypersonic vehicle.

1.4 Key Novel Contributions

Accomplishing the stated objective requires several contributions toward developing aerothermoelastic analyses of hypersonic components and uncertainty propagation analysis. The following contributions are unique to this study:

1. Use of stochastic collocation (SC), a powerful method for uncertainty propagation, for the aeroelastic and aerothermoelastic studies considered in this thesis. The SC method replaces conventional MCS when the number of uncertain variables is limited. Thus it is ideally suited for this class of problems, and has never been used for such problems in the literature of the field.

2. Development of a framework combining conjugate heat transfer (CHT) with the structural model of hypersonic vehicle/engine combination, so as to evaluate the effect of aerothermoelastic deformation on inlet, cowl and nozzle of a scramjet engine on engine performance.

3. Uncertainty propagation in the integrated vehicle/propulsion system so as to assess the variations in performance associated with the predicted aerothermoelastic deformations in a probabilistic manner.

4. Development of a computational framework for CFD/CSD coupling using RBF and its application to aeroelastic and aerothermoelastic studies on a low aspect ratio wing.

It includes a new system identification method verified for a three-dimensional low aspect ratio wing, representative of a control surface of a hypersonic vehicle.

1.5 Outline of the Document

This thesis is divided into 9 chapters. The motivations, including a literature review, and objectives are given in Chapter 1. An extensive description of the uncertainty propagation methods considered in this study is given next in Chapter 2 with illustrative analytical examples. Chapter 3 describes the framework for hypersonic aerothermoelastic studies using CFD and a mesh deformation based on RBF combined with a CSD model.

Next, the uncertainty propagation approach results are presented for increasingly more complex systems. The UQ framework is applied to four different analyses, each of them is described concisely before the UQ results are discussed. The importance of non–deterministic approaches for hypersonic vehicle analysis is characterized by comparing the results with those obtained from deterministic analyses.

In Chapter 4, the aeroelastic analysis of a hypersonic control surface section is considered. Uncertainty is incorporated in the natural frequencies to account for changes due to thermal effects. Next, the aerothermoelastic stability of a panel located on the surface of a hypersonic vehicle is examined in Chapter 5. For this case, uncertainties due to modeling assumptions associated with the aerodynamic heat flux and laminar to turbulent transition predictions are quantified, and their effects on flight time before the onset of flutter are examined. In Chapter 6, aerothermal deformations of a generic hypersonic vehicle are estimated. The code MASIV is used to quantify the sensitivity of the propulsion system to the identified aerothermoelastic deformations.

Aeroelastic results using CFD are given next in Chapter 7. The effect of turbulence and gas models on stability boundaries are investigated. In Chapter 8, the effect of heat is incorporated. The effect of transition from laminar to turbulent and the importance of

thermal stresses are emphasized.

Finally, Chapter 9, provides conclusions and directions for possible future work.

CHAPTER 2

UNCERTAINTY PROPAGATION ANALYSIS

2.1 Introduction

The uncertainty propagation framework developed for this study is schematically illustrated in Fig. 2.1. The effects of uncertain inputs $\boldsymbol{x}$ are propagated through a computational analysis symbolically represented by the function f in order to quantify the effects of uncertainty on the output of interest $y = f(\boldsymbol{x})$. The function f can represent an aeroelastic or an aerothermoelastic stability analysis and $\boldsymbol{x}$ are the uncertain input parameters. Once the outputs of interest have been defined and the relevant uncertain inputs have been identified, probabilistic approaches are applied to quantify the effects of uncertainty. The curve on the left illustrates a given probability density function for the inputs. The vertical line indicates the deterministic value. The blue curve on the right represents the results from the probability propagation framework, ie. the probability distribution of the output. The probability of failure is represented by the shaded area. The probabilistic approach to uncertainty quantification consists of the following steps:

1. Each uncertain input is treated as a random variable characterized by a probability distribution, $p_x(x)$.

2. A response surface method is used to approximate the computationally expensive functional dependence $f(\boldsymbol{x})$ of the output of interest on the uncertain inputs.

3. Conventional Monte Carlo simulation (MCS) is applied to the computationally efficient approximate representation and the effects of the uncertain inputs on the output of interest are quantified in terms of probability distributions $p_y(y)$.

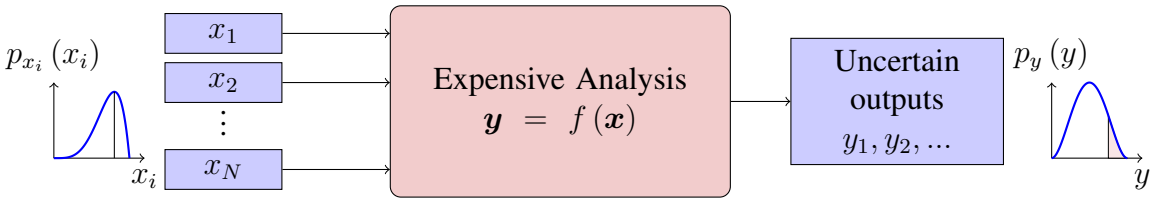

Figure 2.1: Uncertainty propagation approach

Detailed descriptions of the probabilistic characterization of the uncertain inputs and the function approximations are provided in this section. The different metrics of sensitivity used to identify important variables are presented first. Next, various response surfaces are described. Finally analytical examples, used as test cases, are presented before applying the framework to more complicated problems.

2.2 The Probabilistic Framework

The probabilistic framework is used to quantify the uncertainty in the variables: inputs as well as outputs. Randomness associated with an uncertain input, x taking values in Ω_x, is modeled by a *probability density function (PDF)*, $p_x(x)$, which describes the relative likelihood for this random variable to take a given value. The *cumulative density function (CDF)*, $P_x(x)$, describes the probability that a random variable is less than a particular value. The relation between PDF and CDF is given by Eq. (2.1).

$$P_x(x) = \int_{x' < x} p_x(x')dx' \tag{2.1}$$

Several metrics for uncertainties are defined next. The mean or expected value is defined in Eq. (2.2). Equation (2.3) defines the variance and standard deviation which char-

acterize the variability associated with a random variable.

$$\langle x \rangle = \int_{\Omega_x} p_x(x) x dx \tag{2.2}$$

$$\sigma_x^2 = \int_{\Omega_x} p_x(x) \left(x - \langle x \rangle\right)^2 dx \tag{2.3}$$

Subsequently, the same metrics are applied to any quantity y that depends on x. The mean or expected value of $y = f\left(x\right)$ is defined in Eq. (2.4), and its variance by Eq. (2.5)

$$\langle y \rangle = \int_{\Omega_x} p_x(x) f(x) dx \tag{2.4}$$

$$\sigma_y^2 = \int_{\Omega_x} p_x(x) \left(f(x) - \langle y \rangle\right)^2 dx \tag{2.5}$$

As a useful measure of the uncertainty in the output variable is an interval that contains $y = f\left(x\right)$ with a likehood of 95% is defined by Eqs. (2.6) and referred to as the 95% confidence interval (95%CI). It is uniquely characterized by two bounds denoted y_{CImin} and y_{CImax}, which satisfy Eqs. (2.7) and (2.8) respectively. The 95%CI is illustrated in Fig. 2.2.

$$P_y(y \in 95\%CI) = 0.95 \tag{2.6}$$

$$P_y(y < y_{CImin}) = 0.025 \tag{2.7}$$

$$P_y(y_{CImax} < y) = 0.025 \tag{2.8}$$

The probability of failure is the probability that the output cannot exceed a certain value y_{lim} as defined by Eq. (2.9) and illustrated in Fig. 2.3.

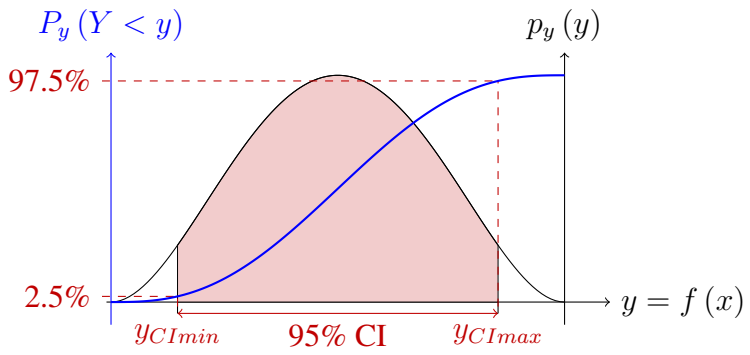

Figure 2.2: Illustration of the 95% CI

$$p_f = P_y(y > y_{lim}) = \int_{y>y_{lim}} p_x\,(x)\,dx \tag{2.9}$$

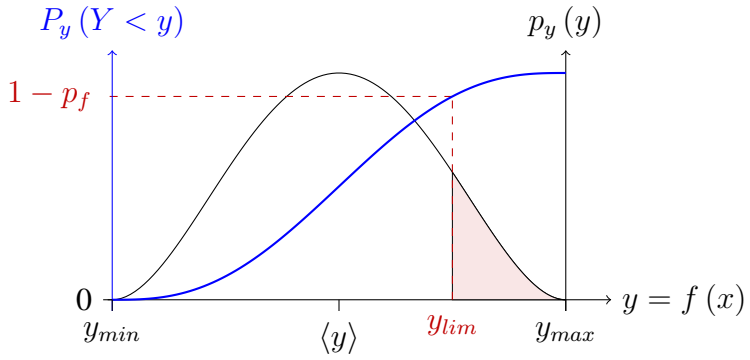

Figure 2.3: Probability of failure

The uncertainty in the inputs are quantified by describing their PDF's. Commonly used PDF's include normal, log-normal, exponential or Cauchy distributions which are defined on unbounded domains given in Table 2.1 and illustrated by Fig. 2.4. Using such PDF's may require evaluating the output of interest at input combinations that have no physical significance and lead to unfeasible computations.

In contrast, the beta distributions, also given in Table 2.1, represent a family of bounded probability distributions in which the range of the random input variables can be controlled by prescribing bounds. Moreover, the choice of both parameters A and B permits one to

Table 2.1: Classical probability density functions

PDF	$p_x(x)$
Gaussian	$\frac{1}{\sigma\sqrt{2\pi}} e^{\left(\frac{-x^2}{2\sigma^2}\right)}$
Exponential	$\frac{1}{\sigma} e^{-\frac{x}{\sigma}}$
Log Normal	$\frac{1}{\zeta_X x\sqrt{2\pi}} e^{-\frac{(\ln x-\lambda_X)^2}{2\zeta_X^2}}$
Beta	$p_{x(A,B)}(x) = \frac{\Gamma(A+B)}{\Gamma(A)\Gamma(B)} \frac{(1+x)^{A-1}(1-x)^{B-1}}{2^{A+B-1}}$

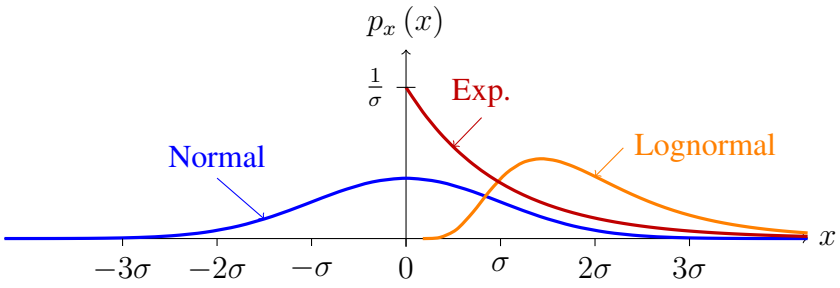

Figure 2.4: Typical probability distribution functions

control the shape of the PDF as illustrated in Fig. 2.5. The parameters A and B control the shape of the tail of the PDF at the bounds $\xi = -1$ and $\xi = 1$, respectively. The values A=1 and B=1 yield a non-zero PDF at the two edges. A value for A, B greater than 1 produces a flat tail as illustrated in Fig. 2.5. Thus high values of A and B produce a PDF that assigns small probabilities to uncertain parameters at the outer edges, while emphasizing the central portion. Thus, uniform, symmetric or non-symmetric PDF's can be accommodated by using beta distributions [17]. A beta distribution corresponding to particular values of A and B will be denoted by $Beta(A, B)$.

These definitions can easily be extended to a multidimensional input vector $\boldsymbol{x}$. Once the probabilistic framework is defined and the uncertainty in the inputs is quantified, uncertainty is propagated through the analysis.

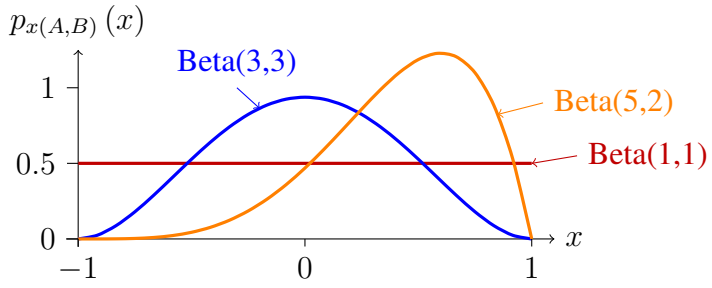

Figure 2.5: Examples of beta PDF for different combinations of A and B

2.3 Sensitivity Analysis

Sensitivity analysis is often required in multidimensional complex analyses to highlight the importance of particular input variables and the effect of their interactions. Several approaches exist. Gradients are a good indication of the local sensitivity of the output with respect to each input. However this sensitivity is only local. In a multidimensional input space, it is common to study the variation of the output of interest with respect to only a small set of variables (1 or 2) at a time and fix the others. This approach allows the assessment of the sensitivity of the output in one or more direction(s) of the input space.

Gradients The gradient of a function f at a given point $\boldsymbol{x}$ gives the local sensitivity. For a given output of interest $f(\boldsymbol{x})$, the derivative of f at a point $(\boldsymbol{x})$ with respect to a given input variable x_i can be estimated using a finite difference scheme. For example, the forward difference scheme is given in Eq. (2.10), where h_i is small compared to x_i. Other approaches for efficient computation of gradients exist such as complex step or the adjoint method but are beyond the scope of the current study. Automatic differentiation is another efficient approach to "differentiate" a given code and calculate gradients analytically [140].

$$\left.\frac{\partial f}{\partial x_i}\right|_{\boldsymbol{x}_0} = \frac{f(\boldsymbol{x}_0 + h_i\{\delta_{ij}\}_j) - f(\boldsymbol{x}_0)}{h_i} \tag{2.10}$$

In order to compare the importance of different input variables, gradients can be nor-

malized with respect to the baseline value of f, $f(\boldsymbol{x}_0)$ and the range of variation of the input variable x_i, in the case of a bounded variable, as given in Eq. (2.11). In the case of unbounded uncertain variables, the standard deviation can be used instead of the range of variation.

$$\overline{\left.\frac{\partial f}{\partial x_i}\right|}_{\boldsymbol{x}_0} = \frac{\Delta x_i}{f(\boldsymbol{x}_0)} \left.\frac{df}{dx_i}\right|_{\boldsymbol{x}_0} \tag{2.11}$$

To study global sensitivities, the effect of varying only one variable at a time while keeping the others fixed in their baseline values can be investigated. Similarly to highlight interactions, one can vary two variables simultaneously, while the remaining variables are fixed to their baseline values. For N_v variables, this analysis can result to up to $\frac{N_v(N_v-1)}{2}$ combinations of two variables and is computationally expensive.

Sobol's Approach This approach defines a global sensitivity metric for a design variable by calculating the contribution of each variable to the total variance of a function. A high Sobol's index is an indication of the importance of one variable or group of variables in the uncertainty of the output of interest. It separates the total variability in the objective function into contributions from main effects, i.e. variability due to each design variable alone, and contributions from interactions between all of the design variables. This is based on analysis of variance (ANOVA) developed by Sobol and described in Ref. [141, 142]. This methodology developed initially for optimization problems can be easily extended to uncertainty quantification (UQ). A brief overview is this approach is given next.

The ANOVA decomposition states that an N-dimensional function f can be decomposed into a sum of functions of different dimensions given in Eq. (2.12) where $f_0 = \langle f \rangle$ is a constant, $f_{j_1,\ldots,j_k}$ are functions of increasing dimensionality which depends on independent groups of variables.

$$f\left(x_1, x_2, \ldots, x_{N_v}\right) = f_0 + \sum_{j_1=1}^{N_v} f_{j_1}\left(x_{j_1}\right) + \sum_{1 \le j_1 < j_2 \le N_v} f_{j_1,j_2}\left(x_{j_1}, x_{j_2}\right) + \sum_{1 \le j_1 < j_2 < j_3 \le N_v} f_{j_1,j_2,j_3}\left(x_{j_1}, x_{j_2}, x_{j_3}\right) + \ldots + f_{1,\ldots,N_v}\left(x_1, \ldots, x_{N_v}\right) \tag{2.12}$$

It was shown in Ref. [141], that by enforcing the condition in Eq. (2.13), the decomposition given by Eq. (2.12) is unique.

$$\int f_{j_1,\ldots,j_k} dx_{j_1} \ldots dx_{j_k} = 0 \quad \text{for} \quad 1 \le j_1 < \ldots < j_k \le N_v \tag{2.13}$$

The total variance of $f(\boldsymbol{x})$, D_f, given in Eq. (2.14), is decomposed in a similar fashion given in Eq. (2.15).

$$D_f = \int_{\Omega_x} \left(f\left(\boldsymbol{x}\right) - f_0\right)^2 d\boldsymbol{x} \tag{2.14}$$

$$D_f = \sum_{j_1=1}^{N_v} D_{j_1} + \sum_{1 \le j_1 < j2 \le N_v} D_{j_1,j_2} + \sum_{1 \le j_1 < j_2 < j_3 \le N_v} D_{j_1,j_2,j_3} + \ldots + D_{1,\ldots,N_v} \tag{2.15}$$

The contribution of x_j alone to the total variance is accounted for with D_j, while $D_{j_1,\ldots,j_k}$ accounts for the variance due to interactions among $x_{j_1}, \ldots, x_{j_k}$. The total variance due to x_j is defined by Eq. (2.16). It accounts for the contribution due to main effects as well as those due to the interactions with the other variables.

$$D_j^{TOTAL} = D_j + \sum_{1 \leq j_2 \leq N_v} D_{j,j_2} + \sum_{j \in j_1 < j_2 < j_3} D_{j_1,j_2,j_3} + \ldots + D_{1,\ldots,N_v} \tag{2.16}$$

For sake of clarity, $\boldsymbol{x_1}$ denotes the set of variables $(x_{j_1}, \ldots, x_{j_k})$ and $\boldsymbol{x_2}$ denotes the remaining variables such that $\boldsymbol{x} = \{\boldsymbol{x_1}, \boldsymbol{x_2}\}$. Correspondingly, $d\boldsymbol{x_1}$ and $d\boldsymbol{x_2}$ denotes $dx_{j_1}, \ldots, dx_{j_k}$ and $\frac{dx_1 \ldots dx_{N_v}}{dx_{j_1} \ldots dx_{j_k}}$,respectively. It is shown that the partial variances in Eq. (2.17) are given by:

$$D_{j_1,\ldots,j_k} = \int_{\boldsymbol{x_1}} \int_{\boldsymbol{x_2}} \int_{\boldsymbol{x_2'}} f(\boldsymbol{x_1}, \boldsymbol{x_2}) f(\boldsymbol{x_1}, \boldsymbol{x_2'}) d\boldsymbol{x_1} d\boldsymbol{x_2} d\boldsymbol{x_2'} - f_0^2 \tag{2.17}$$

The important contribution of Ref. [141] is a computational algorithm that allows a direct estimation of global sensitivity indices using Eq. (2.17). The algorithm relies on a Monte Carlo algorithm. In this dissertation, the implementation of the algorithm is done through numerical integration using the tensor product of the Gauss points. Furthermore, the definition of the Sobol's indices, $D_{j_1,\ldots,j_k}$, is extended to include the probability distribution of the inputs, as given in Eqs. (2.18) and (2.19). Calculation of Sobol's indices can take advantage of the UQ framework described in the following section by utilizing the same numerical scheme to compute the various integrations required for the calculation of $D_{j_1,\ldots,j_k}$'s. The numerical quadrature approach is accurate and does not require any additional evaluation of the analysis f.

$$f_0 = \langle f \rangle = \int_{\boldsymbol{x}} p_x(\boldsymbol{x}) f(\boldsymbol{x}) d\boldsymbol{x} \tag{2.18}$$

$$D_{j_1,\ldots,j_k} = \int_{\boldsymbol{x_1}} \int_{\boldsymbol{x_2}} \int_{\boldsymbol{x_2'}} p_{x_1}(\boldsymbol{x_1}) p_{x_2}(\boldsymbol{x_2}) p_{x_2'}(\boldsymbol{x_2'}) f(\boldsymbol{x_1}, \boldsymbol{x_2}) f(\boldsymbol{x_1}, \boldsymbol{x_2'}) d\boldsymbol{x_1} d\boldsymbol{x_2} d\boldsymbol{x_2'} - f_0^2 \tag{2.19}$$

Finally, variances are normalized to define sensitivity indices. For example, the first

and second order sensitivity indices are given by:

$$S_{j_1,\ldots,j_k} = \frac{D_{j_1,\ldots,j_k}}{D} \quad \text{and} \quad S_j^{TOTAL} = \frac{D_j^{TOTAL}}{D} \tag{2.20}$$

The relative significance of each design variable is obtained by ranking each variable according to its respective total sensitivity index, with the most significant variables corresponding to higher indices. The index also quantifies the contribution of each variable and groups of variables to the uncertainty in the output. It accounts for the range of variation of each variable x, and its probability distribution.

Once the uncertain inputs have been identified, their uncertainty is propagated through the analysis. The uncertainty of the output is quantified. Various approaches considered in this study are described next.

2.4 Direct Monte Carlo Simulations

Direct Monte Carlo simulation (MCS) has been a widely used approach in relatively simple studies. This method is guaranteed to converge to the correct probability distribution for the output of interest as the number of analysis is increased. It can be applied to any output of interest, even discontinuous ones. Mean and standard deviation, probability of failure, as well as probability distribution of the output, are obtained directly from the results of direct MCS as given in Eqs (2.21), (2.22), and (2.23) respectively.

$$m_y = \frac{1}{N}\sum_{i=1}^{N} y_i \tag{2.21}$$

$$\sigma_y^2 = \frac{1}{N-1}\sum_{i=1}^{N} (y_i - m_y)^2 \tag{2.22}$$

$$p_f = \frac{\text{Number of } y_i > y_{max}}{N} \tag{2.23}$$

The selection of the sampling points is important. A random number generator routine is usually employed. Alternatively, the choice of the sampling points can be enhanced using latin hypercube sampling (LHS) [143]. The latin hypercube sampling explores the uncertain variables space more efficiently than a uniform cartesian grid (UNIF) and sampling points do not cluster as much as for random number generator (RAND), as illustrated in Fig. 2.6(a) where each cell of the grid has the same probability. The LHS, which is usually encountered in space filling sampling, can accommodate any common probability distribution as illustrated in Fig. 2.6(b) for $PDF(x) = 6x(1-x)$.

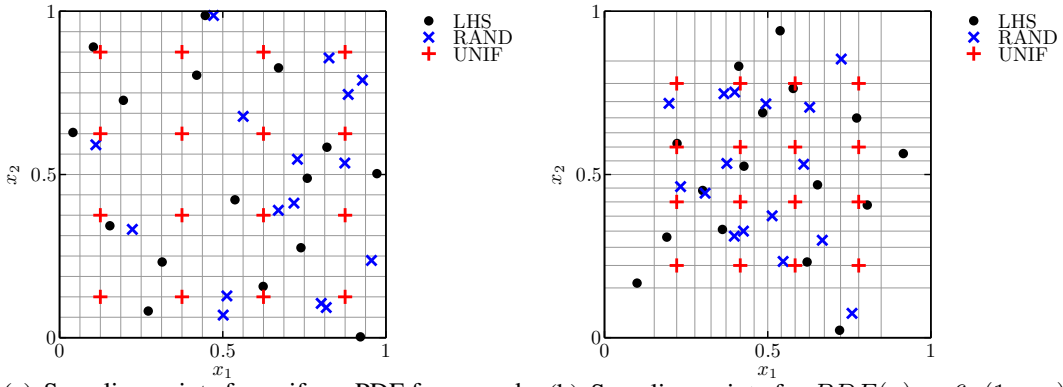

(a) Sampling points for uniform PDF for x_1 and x_2

(b) Sampling points for $PDF(x) = 6x(1-x)$ for x_1 and x_2

Figure 2.6: Illustration of different sampling approach for two random variables x_1 and x_2 in $[0, 1]$

In MCS, depending on the number of input variables and the degree of nonlinearity between $\boldsymbol{x}$ and $f(\boldsymbol{x})$, the computational cost associated with the numerous analysis evaluations for complex problems can be prohibitive. Response surface methods are an efficient alternative for reducing the computational cost of the uncertainty propagation analyses.

2.5 Response Surface Methods

The computational cost associated with numerous analysis evaluations is prohibitive for complex problems such as hypersonic aeroelastic and aerothermoelastic analysis. There-

fore, a response surface based method is employed in this study as a computationally efficient alternative to direct MCS.

In response surface methods, the expensive analysis f is replaced by a computationally inexpensive approximation of f , denoted $\hat{f}$. Various approximation can be considered. A comparison between direct MCS and response surface based method is given Fig. 2.7. The approximation, $\hat{f}$, is constructed based on evaluating the expensive analysis, f, at a limited number of sampling points. Next, MCS is applied to the computationally inexpensive polynomial response surfaces in order to obtain the probability distributions associated with the output of interest. This process will be referred as indirect Monte Carlo simulation (IMCS).

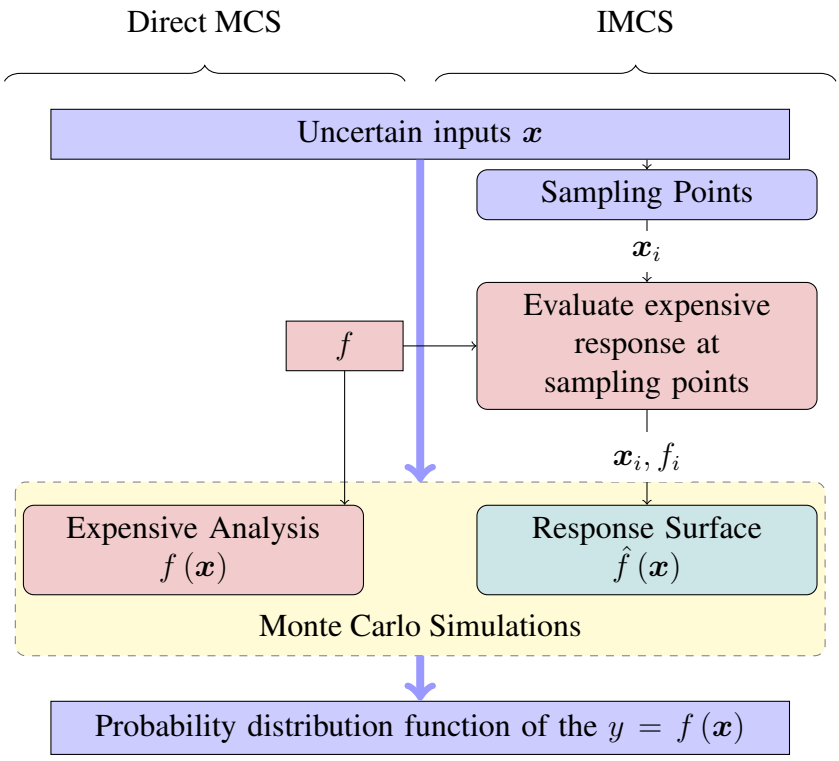

Figure 2.7: Direct Monte Carlo simulations v.s. Response surface based methods

Two approaches for generating an inexpensive response surface are commonly used: polynomial chaos expansion (PCE) and stochastic collocation (SC) [18]. Both rely on polynomials expansion. Alternatively kriging surrogate (KG) or radial basis function net-

works (RBFN) have been also considered. The usage of one response surface compared to another is problem dependent. Therefore it is useful to know the strengths and advantages of various methods. In addition, comparing the predictions of several response surfaces allows to assess the accuracy of the fit without the computational cost of an expensive convergence study.

2.5.1 Stochastic Collocation

In stochastic collocation (SC), computationally efficient polynomial response surfaces are used to approximate the functional relationship between uncertain inputs x, and the output of interest $f(x)$.

$$f(x) \approx \hat{f}(x) = \sum_{j=1}^{N_P} A_j \phi_j(x) \tag{2.24}$$

The response surface $\hat{f}$ given by Eq. (2.24) consists of an expansion in terms of polynomial basis functions $(\phi_j(x))_{1<j<N_P}$, in which A_j's are fitting coefficients, and N_P represents the number of basis functions. Once the approximate representation is constructed, MCS can be applied to the computationally inexpensive polynomial response surface in order to obtain an approximate probability distribution associated with the output of interest.

In SC, the expensive analysis is evaluated at a set of inputs x_i, called collocation points. The collocation points are chosen such that mean m_f, given by Eq. (2.25), and variance ${\sigma_f}^2$, given by Eq. (2.26), are estimated numerically using an integration scheme defined by N_I integration points, $(x_k)_{k=1,N_I}$ and their corresponding weights $(w_k)_{k=1,N_I}$. Thus the collocation points correspond to numerical integration points.

$$m_f \equiv \langle f \rangle = \int_{\Omega_x} p_x(x)\, f(x) dx \simeq \sum_{k=1}^{N_I} w_k f(x_k) \tag{2.25}$$

$$\sigma_f{}^2 \equiv \left\langle (f - \langle f \rangle)^2 \right\rangle = \int_{\Omega_x} p_x(x) \left(f(x) - \langle f \rangle\right)^2 dx \simeq \sum_{k=1}^{N_I} w_k (f(x_k) - \langle f \rangle)^2 \qquad (2.26)$$

For a one dimensional case, the polynomial response surface, given by Eq. (2.24), is generated using Lagrange polynomials $(\phi_j)_{j=1,N_I}$, Eq. (2.27) associated with the collocations points $(x_k)_{k=1,N_I}$, Eq. (2.28). The degree of the polynomial approximation P, in Eqs. (2.27) and 2.28 is equal to $N_I - 1$.

$$\phi_j(x) = \prod_{k=1,k\neq j}^{N_I} \frac{x - x_k}{x_j - x_k} \quad j = 1, N_I \qquad (2.27)$$

$$\phi_j(x_k) = \delta_{jk} \quad j,k = 1, N_I \qquad (2.28)$$

The coefficients of the expansion are the output evaluated at the collocation points, Eq. (2.29).

$$A_j = f(x_j) \quad j,k = 1, N_I \qquad (2.29)$$

For a multidimensional random input space, $\boldsymbol{x} = (x^{i_v})_{i_v=1,N_v}$, in which N_v is the number of uncertain inputs, the multi–variate extension of Eq. (2.27) is given by considering the tensor–product of the one dimensional cases as given in Eqs. (2.30) and (2.31). The coefficients of the expansion are the function evaluations at the numerical integration points.

$$\phi_j(\boldsymbol{x}) = \prod_{i_v=1}^{N_v} \prod_{k=1,k\neq j}^{N_I} \frac{x^{i_v} - x_k^{i_v}}{x_j^{i_v} - x_k^{i_v}} \quad j = 1, N_I \qquad (2.30)$$

$$A_j = f(\boldsymbol{x}_j) \quad j = 1, N_I \qquad (2.31)$$

The corresponding numerical integration scheme is computed using Gaussian quadrature developed by Golub [144]. For a single beta–distributed random variable, the numeri-

cal integration points are the roots of the Legendre polynomial function of degree N_I associated with the beta probability distribution of the input. The numerical integration scheme is exact for polynomial functions of order less than $2N_I - 1$. In the two-dimensional case, the collocation points are depicted in Fig. 2.8 for beta distributions corresponding to various combinations of A and B for $N_I = 7^2$. This method tends to concentrate collocation points in the regions of higher probability. For instance, integration points associated with the $Beta(3, 3)$ PDF have a higher concentration at the center of the domain compared to the grid associated with $Beta(1, 1)$. Additional details about alternative numerical integration schemes are given in Appendix A.

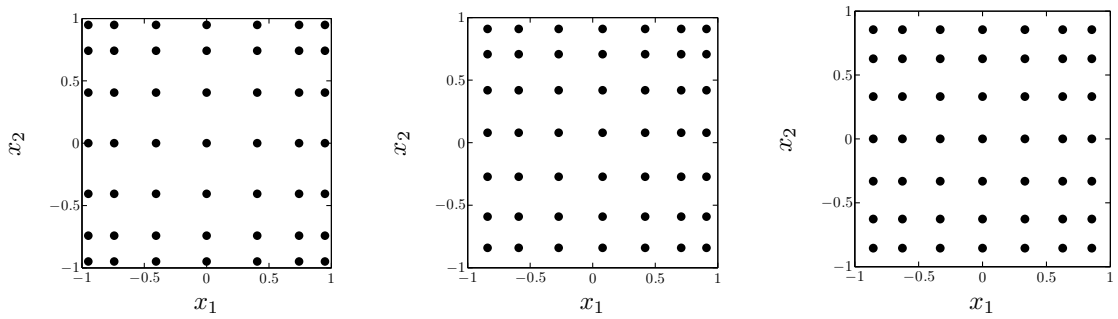

(a) Beta(1,1) (b) Beta(3,2) (c) Beta(3,3)

Figure 2.8: Collocation points for 2 random variable for different beta distributions, $N_I = 7^2$

Since there is strong evidence that the SC approach has outperformed PCE [18], another widely used technique, SC is the method chosen for the main part of this study. It should be noted that this method suffers from the curse of dimensionality which implies that increasing the number of random inputs exponentially increases the number of analysis runs and the computational cost of the method. The number of analyses required for the implementation of the SC approach is $(P + 1)^{N_v}$ due to the tensor–product interpolation. Furthermore the collocation points associated with most integration schemes are located strictly within the domain of the input variable. Therefore, extrapolation is required for response surface evaluations close to the domain boundaries which may adversely affect

accuracy.

To prevent extrapolation, the bounds of the interval can be added to the set of the integration points with weight $w_k = 0$. They do not improve the accuracy of the integration scheme but ensure that the boundary of the uncertain parameter space is discretized and that there is no extrapolation. It will be referred to as extended stochastic collocation (SCE).

2.5.2 Polynomial Chaos Expansion

An alternative method to SC is the so-called polynomial chaos expansion (PCE) method. In this method, a polynomial response surface replaces the actual expensive analysis of interest as given in Eq. (2.24) where $(\phi_i(x))_{0<i<N_P}$ are polynomial basis functions chosen based on the probability distribution of the inputs: the polynomial basis functions are orthogonal with respect to the scalar product defined by the probability distribution of the inputs as expressed in Eq. (2.32).

$$\langle \phi_i, \phi_j \rangle = \int_{\Omega_x} p_x(x)\, \phi_i(x)\, \phi_j(x)\, dx = \|\phi_i\|^2 \delta_{ij} \tag{2.32}$$

Since $\phi_j = 1$, it yields:

$$A_1 = \int_{\Omega_x} p_x(x) f(x) dx = \langle f \rangle \tag{2.33}$$

and

$$\sigma_f = \sum_{j=2}^{N_I} A_j^2 \|\phi_j\|^2 \tag{2.34}$$

For common PDFs, the family of polynomials are given in Table 2.2.

In Eq. (2.24), two methods exist to determine the coefficients, $(A_j)_{1<j<N_P}$: a linear least-square fit, or a spectral projection.

Table 2.2: Orthogonal polynomials basis

PDF	Polynomial ϕ_j
Gaussian	Hermite
Exponential	Laguerre
Uniform	Legendre
Beta	Jacobi

Least Square Fit method The expensive analysis is evaluated at N_s sampling points, $(\boldsymbol{x}_i, f(\boldsymbol{x}_k))_{k=1,N_s}$. These samplings points are chosen to "uniformly" sample the input space, using LHS for instance. Based on this information, the coefficients A_j are calculated to minimize the error between the function of interest and the polynomial expansion as given in Eq. (2.35).

$$\min_{A_j} \left(\sum_{k=1,N_s} \left\| f(\boldsymbol{x}_k) - \sum_{j=1}^{N_P} A_j \phi_j(\boldsymbol{x}_k) \right\|^2 \right) \tag{2.35}$$

This yields a linear system which is inverted in a least square sense [145] as given in Eqs. (2.36) and (2.37).

$$\{\boldsymbol{A}\} = \left([\boldsymbol{\phi}]^T [\boldsymbol{\phi}] \right)^{-1} [\boldsymbol{\phi}]^T \{F\} \quad \text{where} \tag{2.36}$$

$$[\boldsymbol{\phi}] = \begin{bmatrix} \phi_1(\boldsymbol{x}_1) & \dots & \phi_{P+1}(\boldsymbol{x}_1) \\ \vdots & \ddots & \vdots \\ \phi_1(\boldsymbol{x}_{N_s}) & \dots & \phi_{P+1}(\boldsymbol{x}_{N_s}) \end{bmatrix} \quad \{\boldsymbol{A}\} = \begin{Bmatrix} A_1 \\ \vdots \\ A_{P+1} \end{Bmatrix} \quad \{F\} = \begin{Bmatrix} f(\boldsymbol{x}_1) \\ \vdots \\ f(\boldsymbol{x}_{N_s}) \end{Bmatrix} \tag{2.37}$$

There are N_P coefficients. Therefore, a minimum of $N_s = N_P$ *properly distributed* points is required. It has been shown that using $N_s = 2N_P$ or larger improves the fit significantly.

Quadrature Method In this approach, the polynomial basis functions are chosen to be orthogonal with respect to the scalar product defined by the probability distribution of the

inputs as given in Eq. (2.32). For this choice of polynomial basis, the coefficients A_j satisfy Eq. (2.38).

$$A_j \|\phi_j\|^2 = \langle f, \phi_j \rangle = \int_{\Omega_x} p_x(x) f(x) \phi_j(x) dx \tag{2.38}$$

In a computational framework, numerical integration is used to evaluate Eq. (2.38) as given in Eq. (2.39)

$$A_j = \frac{1}{\|\phi_j\|^2} \sum_{i=1}^{N_I} w_i f\left(x_i\right) \phi_j\left(x_i\right) \tag{2.39}$$

In this case, the expensive analysis is evaluated at the numerical integration points. Thus, $N_s = N_I$ evaluations of the function of interest are required. In the one dimensional case, quadrature methods require $N_I = P + 1$ points to approximate f as a polynomial function of degree P.

2.5.3 Kriging surrogate

In kriging, the unknown function $f\left(\boldsymbol{x}\right)$ is assumed to be of the form [57, 146]:

$$f\left(\boldsymbol{x}\right) = \boldsymbol{f}_{\boldsymbol{x}}\left(\boldsymbol{x}\right)^T \boldsymbol{\beta} + Z\left(\boldsymbol{x}\right) \tag{2.40}$$

where $\boldsymbol{f}_{\boldsymbol{x}}(\boldsymbol{x})$ is an assumed family of functions (usually polynomials of order of 0, 1 or 2, e.g. $\{1, x_1, x_2, x_1^2, x_1 x_2, x_2^2, ...\}$), $\boldsymbol{\beta}$ are fitting coefficients, and $Z(\boldsymbol{x})$ is a realization of a stochastic (random) process which is assumed to be a Gaussian process with zero mean and variance σ_{var}^2. The function $\boldsymbol{f}_{\boldsymbol{x}}(\boldsymbol{x})^T \boldsymbol{\beta}$ represents global approximation of $f(\boldsymbol{x})$, while the error, $Z(\boldsymbol{x})$, accounts for local deviations which ensure that the kriging model interpolates the data points exactly. This interpolation method is based on the assumption that errors, $Z(\boldsymbol{x})$, are spatially correlated, which is in contrast to the assumption of independent or uncorrelated errors made in polynomial approximation. This implies that the errors at

two points close to each other will be close. In fact, the assumption that the errors are uncorrelated is only appropriate when the sources of error are random, such as in the case of measurement error or noise. In the case of deterministic computer simulations, there is no source of random error.

The covariance matrix of $Z(\boldsymbol{x})$, which is a measure of how strongly correlated two points are, is given by

$$Cov[Z(\boldsymbol{x}_i), Z(\boldsymbol{x}_j)] = \sigma^2_{var}\boldsymbol{R}_{krg} \tag{2.41}$$

where each element of the N_s x N_s correlation matrix, $\boldsymbol{R}_{krg}$ is given by

$$(\boldsymbol{R_{krg}})_{ij} = R_{krg}(\boldsymbol{x}_i, \boldsymbol{x}_j) \tag{2.42}$$

and $R_{krg}(\boldsymbol{x}_i, \boldsymbol{x}_j)$ is a correlation function which accounts for the effect of each interpolation point on every other interpolation point. This function is called the spatial correlation function (SCF). The most commonly used SCF is the Gaussian correlation function, which is also employed in this study.

$$R_{krg}(\boldsymbol{x}_i, \boldsymbol{x}_j) = \exp\left[-\sum_{k=1}^{N_v} \theta_k \left|x_i^k - x_j^k\right|^{p_k}\right] \tag{2.43}$$

The gaussian SCF is dependent on the distance between two points. As two points move closer to each other, $\left|x_i^k - x_j^k\right| \rightarrow 0$ and Eq. (2.43) approaches its maximum value 1 and goes to 0 as two points are far from each other. In other words, the Gaussian SCF recovers the intuitive property that the closer two points are to each other, the greater the correlation between the points. The fitting parameters θ_k and p_k are unknown correlation parameters which need to be determined and depend on the form of $\boldsymbol{f_x}$. Previous studies have found that modeling with the SCF is so effective, that using a constant for the global behavior results in little loss of fidelity. In order to find θ_k and p_k, the generalized least square estimates of β and σ^2_{var}, denoted $\hat{\beta}$ and $\hat{\sigma}^2_{var}$ respectively, are employed:

$$\hat{\boldsymbol{\beta}} = \left(\boldsymbol{F}^T \boldsymbol{R}_{krg}^{-1} \boldsymbol{F}\right)^{-1} \boldsymbol{F}^T \boldsymbol{R}_{krg}^{-1} \boldsymbol{y} \tag{2.44}$$

$$\hat{\sigma}_{var}^2 = \frac{\left(\boldsymbol{y} - \boldsymbol{F}\hat{\boldsymbol{\beta}}\right)^T \boldsymbol{R}_{krg}^{-1} \left(\boldsymbol{y} - \boldsymbol{F}\hat{\boldsymbol{\beta}}\right)}{N_s} \tag{2.45}$$

where $\boldsymbol{F}$ is a vector populated by $\boldsymbol{f_x}(\boldsymbol{x}_i)$ and $\boldsymbol{y}$ is a vector of observed function outputs at the interpolation points; both vectors are of length N_s. With $\hat{\boldsymbol{\beta}}$ and $\hat{\sigma}_{var}^2$ known, θ_k and p_k are found such that a likelihood function is maximized. The likelihood function, given in Eq. (2.46), is a measure of the probability of the sample data being drawn from a probability density function associated with a Gaussian process. Since the stochastic process associated with kriging has been assumed to be Gaussian, one seeks the set of θ_k and p_k that maximize the probability that the interpolation points have been drawn from such a process. The most common choice for $\boldsymbol{f_x}(\boldsymbol{x})^T \hat{\boldsymbol{\beta}}$ is a constant β.

$$-\frac{N_s \ln\left(\hat{\sigma}_{var}^2\right) + \ln\left(\boldsymbol{R}_{krg}\right)}{2} \tag{2.46}$$

The maximum likelihood estimates (MLEs) of θ_k and p_k represent the 'best guesses' of the fitting parameters. Any values of θ_k and p_k would result in a surrogate which interpolates the sample points exactly, but the 'best' kriging surrogate is found by optimizing the likelihood function. This auxiliary optimization process can result in significant fitting time depending on the size of the system. Due to the optimization process needed to create the kriging surrogate, kriging is only appropriate when the time needed to generate the interpolation points is much larger than the time to interpolate the data which is the case in hypersonic aerothermoelastic problems. With all parameters known, the kriging approximation to a function $f(x)$ can be written as

$$f_{krg}\left(\boldsymbol{x}\right) = \boldsymbol{f_x}\left(\boldsymbol{x}\right)^T \hat{\boldsymbol{\beta}} + r_{krg}(\boldsymbol{x})^T (\boldsymbol{R_{krg}})^{-1} \left(\boldsymbol{y} - \boldsymbol{f_x}\left(\boldsymbol{x}\right)^T \hat{\boldsymbol{\beta}}\right) \tag{2.47}$$

where

$$r_{krg}(\boldsymbol{x})^T = \left[R_{krg}\left(\boldsymbol{x}, \boldsymbol{x}^{(1)}\right), \ldots, R_{krg}\left(\boldsymbol{x}, \boldsymbol{x}^{(N_s)}\right)\right] \tag{2.48}$$

The column vector $r_{krg}(\boldsymbol{x})$ of length N_s is the correlation vector between an arbitrary point $\boldsymbol{x}$ and the interpolation points, $\boldsymbol{x}_1$, ... , $\boldsymbol{x}_{N_s}$.

The main advantage of kriging surrogates is the fact that they provide an approximation of the function of interest and an estimate of the error made in the interpolation. This estimate is used in optimization studies to explore the design space where the fit of the KG response surface is not good. In uncertainty propagation studies, this error can be utilized to add sampling points in regions of interest. Depending on whether one is interested in determining a probability of failure only, or creating an accurate surrogate over the entire design space, different approach can be considered. The first one is an extension of the efficient global optimization approach (EGO) presented in Ref. [147] and refereed to as efficient global reliability analysis (EGRA).

Expected feasibility function The analysis f is approximated using a kriging surrogate. The expected feasibility function (EFF) is defined to provide an indication of how well the true value of the response is expected to satisfy the equality constraint $f(\boldsymbol{x}) = y_{lim}$. This expectation is obtained from Eq. (2.49) by integrating over a region in the immediate vicinity of the threshold value $y_{lim} \pm \epsilon_G$:

$$EFF = \int_{y_{lim}-\epsilon}^{y_{lim}+\epsilon_G} \left[\left|\hat{f}(\boldsymbol{x}) - y_{lim}\right| - \epsilon_G\right] p_f df \tag{2.49}$$

where $\hat{f}$ denotes the kriging approximation of f. Define $y^+ = y_{lim}+\epsilon_G$ and $y^- = y_{lim}-\epsilon_G$. This integral can be expressed analytically as:

$$EFF = (\mu_G - y_{lim}) \left[2\mathcal{N}\left(\frac{y_{lim} - \mu_G}{\sigma_G}\right) - \mathcal{N}\left(\frac{y^+ - \mu_G}{\sigma_G}\right) - \mathcal{N}\left(\frac{y^- - \mu_G}{\sigma_G}\right) \right] -$$
$$\sigma_G \left[2N\left(\frac{y_{lim} - \mu_G}{\sigma_G}\right) - N\left(\frac{y^+ - \mu_G}{\sigma_G}\right) - N\left(\frac{y^- - \mu_G}{\sigma_G}\right) \right] +$$
$$\epsilon_G \left[\mathcal{N}\left(\frac{y^+ - \mu_G}{\sigma_G}\right) - \mathcal{N}\left(\frac{y^- - \mu_G}{\sigma_G}\right) \right] \tag{2.50}$$

$$\tag{2.51}$$

where ϵ_G is proportional to the standard deviation of the kriging predictor, σ_G. In this case, y_{lim}, y^+, y^-, $\mu_G = \hat{f}$, σ_G and ϵ_G are all functions of the location $\boldsymbol{x}$. The functions $\mathcal{N}$ and N represent the normal distribution CDF and PDF respectively, which is consistent with the choice of correlation function used to built the kriging surrogate.

The EFF provides a balance between exploitation of the response surface and exploration of the design space. Points where the response surface has a large uncertainty, in the kriging sense, will have large EFF values. Similarly, points close to y_{lim} will also. Using the points that maximizes the EFF for future function evaluations increases the accuracy of the kriging surrogate in estimating the limit state.

The algorithm that describes the adaptive sampling approach based on the EFF is as follow:

1. Generate a small number of sampling points, using LHS.
2. Build the kriging surrogate and the EFF function with $\epsilon_G = 2\sigma_G$
3. Find the point(s) that maximizes the EFF using the DIRECT global optimization algorithm [148].
4. If the EFF is smaller than 10^{-6}, go to 5. Otherwise, evaluate the expensive analysis at the new point(s) and go to 2.
5. The surrogate is used to calculate the probability of failure using IMCS.

Note that this method is not guaranted to provide a response surface that is accurate over the entire design space. Therefore quantities such as expected value, standard deviation, or 95% confidence interval (CI) may be inaccurate.

This framework can be adapted by using a modified expected feasibility function which represents the error of the response surface weighted by the probability of the input as given in Eq. (2.50). This approach populates regions of high probability distribution and high surrogate error by producing a response surface that estimates mean and variance more accurately. However, the computational costs are greatly increased since more sampling points may be required.

$$\widetilde{EFF} = \sigma_G(\boldsymbol{x})\, p_{\boldsymbol{x}}(\boldsymbol{x}) \tag{2.52}$$

2.5.4 Radial Basis Function Networks

The radial basis function networks (RBFN) are an effective approach for multivariate interpolation of both scattered and gridded data [50]. A radial function (RF), ϕ, is a scalar function whose value depends only on the distance from the origin, $r = \|\boldsymbol{x}\|$. Given a set of N_s sampling points, $\boldsymbol{x}_j$, at which a quantity of interest $f(\boldsymbol{x})$ has been evaluated: $(\boldsymbol{x}_j, f_j)_{j=1,N_s}$, the radial basis function (RBF) interpolant of f, $\hat{f}$, is constructed in the form given in Eq. (2.53). The interpolated value at a new point, $\boldsymbol{x}$, depends only on the Euclidian distance between $\boldsymbol{x}$ and the sample points $(\boldsymbol{x}_j)_{j=1,N_s}$.

$$\hat{f}(\boldsymbol{x}) = \sum_{j=1}^{N_s} \alpha_j \phi\left(\|\boldsymbol{x} - \boldsymbol{x}_j\|\right) + p(\boldsymbol{x}) \tag{2.53}$$

In Eq. (2.53), the polynomial $p(\boldsymbol{x})$ and the fitting coefficients α_j are determined such that the interpolant, $\hat{f}$, is equal to the actual value of f at the sampling points as given in Eq 2.54.

$$f_i = \hat{f}(\boldsymbol{x_i}) = \sum_{j=1}^{N_s} \alpha_j \phi\left(\|\boldsymbol{x}_i - \boldsymbol{x}_j\|\right) + p(\boldsymbol{x}_i) \quad 1 \leq k \leq N_s \tag{2.54}$$

Introducing $(p_n(\boldsymbol{x}))$ a polynomial basis, $p\left(\boldsymbol{x}\right)$ is written as $\sum_{n=0}^{P} \beta_n p_n(\boldsymbol{x})$. The coefficients β_n uniquely determine p. To ensure uniqueness of the form given in Eq. (2.53), i.e. the uniqueness of the coefficients α_j and β_n, an additional condition given in Eq. (2.55) has to be satisfied.

$$\sum_{j=1}^{N_s} \alpha_j p_n\left(\boldsymbol{x}_j\right) = 0 \tag{2.55}$$

Combining Eqs. (2.54) and (2.55), α_j and the coefficients β_n are uniquely defined by solving the linear system written in the form of Eq. (2.56), where $\boldsymbol{M_{bb}}\left(\boldsymbol{x}\right)) = [\phi\left(\|\boldsymbol{x} - \boldsymbol{x}_j\|\right)]$, $\boldsymbol{Q_b}\left(\boldsymbol{x}\right) = \left[p_n(\boldsymbol{x})\right]_{j=1,N_s;\, n=0,P}$.

$$\begin{bmatrix} \boldsymbol{M_{bb}}\left(\boldsymbol{x_d}\right) & \boldsymbol{Q_b}\left(\boldsymbol{x_d}\right) \\ \boldsymbol{Q_b}\left(\boldsymbol{x_d}\right)^T & \boldsymbol{0} \end{bmatrix} \begin{bmatrix} \boldsymbol{\alpha} \\ \boldsymbol{\beta} \end{bmatrix} = \begin{bmatrix} \boldsymbol{f} \\ \boldsymbol{0} \end{bmatrix} \tag{2.56}$$

The choice of the RBF is an important component in the method. Classical RBF, ϕ, used in engineering applications [50] are presented in Table 2.3 and illustrated in Fig. 2.9. In the cases of volume spline, Duchon's thin plate spline, and Hardy's multiquadratics, the amplitude of the radial function increases with the distance from the origin. Consequently the value of the RBF interpolant at a given location is influenced by all the sampling points even those that are far from the interpolated point. For Hardy's inverse multiquadratics and Gaussian cases, the radial function decreases monotonically to zero with increasing distance from the origin. Therefore the contribution of a sampling point in the interpolant diminishes as the interpolated point is located further away from this sampling point. Finally in the cases of Euclid's hat, and Wedland functions, the radial function is non-zero only at the vicinity of the origin. Thus a sampling point influences only a limited region of the space. Similarly the value of the RBF at a given point depends only on the sampling

points located in its vicinity. In addition, the matrix of the linear equations which determine the RBF coefficients, $\boldsymbol{M_{bb}}(\boldsymbol{x_d})$ in Eq. (2.56), is sparse which limits computational cost in the case of larger systems. Finally, note that the radial functions presented here can be scaled to accommodate specific dimensions of the system considered by replacing $\phi(r)$ by $\phi\left(\frac{r}{r_0}\right)$ where r_0 is a reference distance.

Table 2.3: Classical radial basis functions

RBF	Support	$\phi(r)$
Volume spline		r
Duchon's thin plate spline		$r^2 log(r)$
Hardy's multiquadratics		$(1+r^2)^{1/2}$
Hardy's inverse multiquadratics		$(1+r^2)^{-1/2}$
Euclid's Hat function	*compact*	$\begin{cases} \pi\left(\frac{r^3}{12} - r + \frac{4}{3}\right) & \text{if} \quad r < 2 \\ 0 & \text{otherwise} \end{cases}$
Wedland C^0	*compact*	$\begin{cases} (1-r)^2 & \text{if} \quad r < 1 \\ 0 & \text{otherwise} \end{cases}$
Wedland C^2	*compact*	$\begin{cases} (1-r)^4 (4r+1) & \text{if} \quad r < 1 \\ 0 & \text{otherwise} \end{cases}$
Gaussian		$\exp(-r^2)$

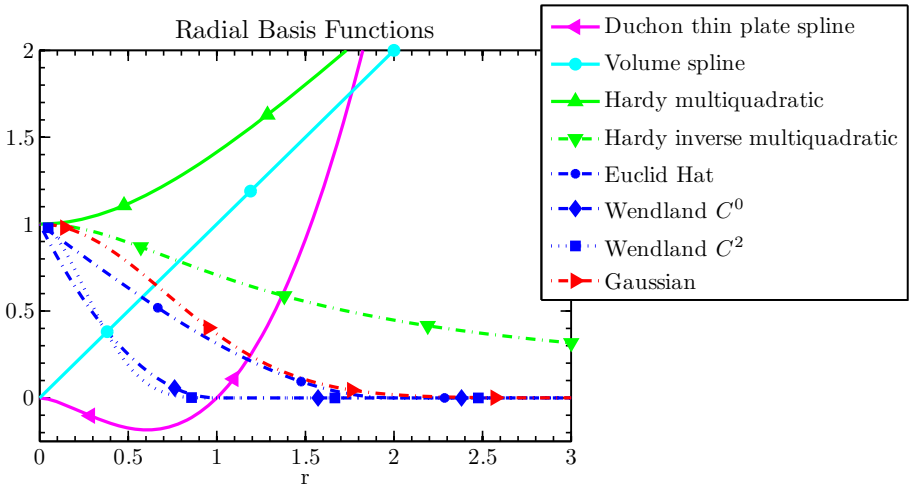

Figure 2.9: Examples of radial basis functions

2.6 Summary

A brief summary of the response surface methods presented in this chapter is given in Table 2.4. The SC and PCE require that the sampling points to be the numerical integration points (Quad) in the form of Gaussian quadrature. Other methods such as kriging or RBFN are more flexible and can use different sampling approach such as a uniform grid (Unif.) or a LHS method. The number of evaluations is given as function of P, the order of the polynomial approximation and N_v the number of uncertain variables. For kriging, an initial LHS hypercube of the order of $10N_v$ points can be a good starting point depending on the nonlinearities present in f.

Table 2.4: Summary of the response surface approaches

Response surface	Sampling	Evaluations	Remarks
MCS	random, LHS	as many as possible	Expensive
SC	Quad.	$(P+1)^{N_v}$	Very accurate mean and variance
PCE	Quad.	$(P+1)^{N_v}$	
	LHS	$2\,(P+1)^{N_v} <$	Spectral projection removes noise
Kriging	Quad., Unif., LHS	$\propto 10N_v$	Robust, Adaptation, $N_v < 20$
RBFN	Quad., Unif., LHS	$\propto 10N_v$	Robust, $N_v < 20$

The SC and PCE methods show good performance when the relationship between the output(s) and the input(s) can be approximated by a polynomial function. They are robust, provide a good estimation of expected value and standard deviation as well as an accurate response surface that can be used for the statistical analysis. In addition they can accommodate multiple outputs using the same sampling points, at no extra computational cost.

Both approaches suffers from the curse of dimensionality. Sparse grids interpolation is a good alternative to reduce the curse of dimensionality. In the case of a high number

of variables, kriging combined with adaptation using the EFF metric, can be an efficient approach. Yet, the sampling points are optimized for a specific quantity related to one output, e.g. a probability of failure.

2.7 Analytical Examples

Four analytical examples are given to verify the implementation of the UQ framework. In addition, the strength and weaknesses of the response surfaces are investigated. It also illustrates the results that are obtained from the acUQ approach.

2.7.1 Description of the examples

Four examples are considered. For the first two the uncertain variables are uniformly distributed. In the last two, Gaussian distribution is considered. For each example, the analytical form of the function, the input variables and their PDF are given in a table along with a contour plot of the function; the limit state, $y_{lim} = 0$ is given by the black thick line.

Example 1 A nonlinear example is presented in Table 2.5 and illustrated by Fig. 2.10. Both uncertain variables are uniformly distributed. The convergence of a global polynomial fit is investigated with this example.

Table 2.5: Summary of Ex.1

$f_1(\boldsymbol{x})$	$\ln(1+x_1^2)\sin(5x_2)$
x_1	Uniform $[1.3072\ 2.6928]$
x_2	Uniform $[1.3072\ 2.6928]$
p_f	$p[f(\boldsymbol{x}) < 0]$

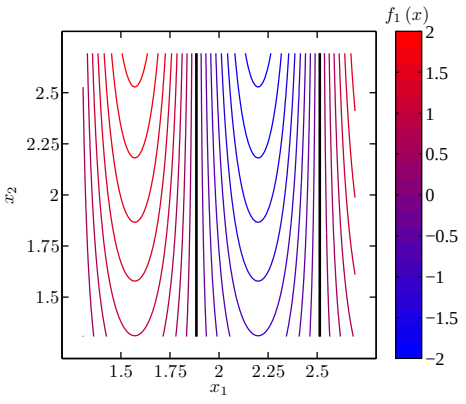

Figure 2.10: Contour plot of $f_1(\boldsymbol{x})$

Example 2 The second example is the Rosenbrock function taken from Ref. [46], presented in Table 2.6 and illustrated by Fig. 2.11. It is a polynomial function often used as a challenging problem for optimization purposes as it presents a "flat" region close to the global minimum. For this reason, it is also a challenging problem for UQ.

Table 2.6: Summary of Ex.2

$f_2(\boldsymbol{x})$	$100\left(x_2 - x_1^2\right)^2 + \left(1 - x_1\right)^2$
x_1	Uniform $[-2\ 2]$
x_2	Uniform $[-1\ 3]$
p_f	$p\left[f\left(\boldsymbol{x}\right) < 0\right]$

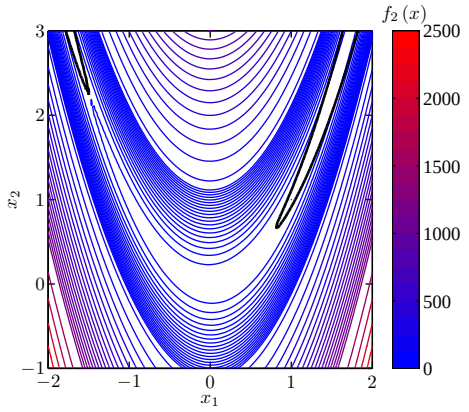

Figure 2.11: Contour plot of $f_2(\boldsymbol{x})$

Example 3 This example is presented in Table 2.7 and illustrated by Fig. 2.12 [58]. It is a highly non–linear problem with a wide range of variation for the output yielding conditioning issues. The distributions of the inputs are normal.

Table 2.7: Summary of Ex.3

$f_3(\boldsymbol{x})$	$\frac{\left(x_1^2+4\right)(x_2-1)}{20} - \sin\left(\frac{5x_1}{2}\right) - 2$
x_1	$\mathcal{N}\left[1.5, 1\right]$
x_2	$\mathcal{N}\left[2.5, 1\right]$
p_f	$p\left[f\left(\boldsymbol{x}\right) < 0\right]$

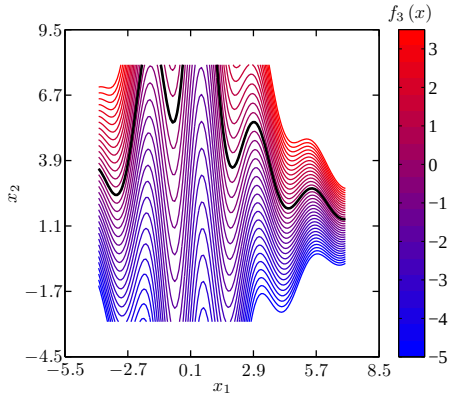

Figure 2.12: Contour plot of $f_3(\boldsymbol{x})$

Example 4 This example is presented in Table 2.8 and illustrated by Fig. 2.13. The inputs are normally distributed, the function is polynomial. Similarly to example 3, the

limit state $y_{lim} = 0$ is also located near a flat region of the uncertain parameters space. It makes this problem difficult for non–polynomial approaches.

Table 2.8: Summary of Ex.4

$f_4(\boldsymbol{x})$	$x_2^3 + x_1^3 - 18$
x_1	$\mathcal{N}[10, 5]$
x_2	$\mathcal{N}[9.9, 5]$
p_f	$P[f(\boldsymbol{x}) < 0]$

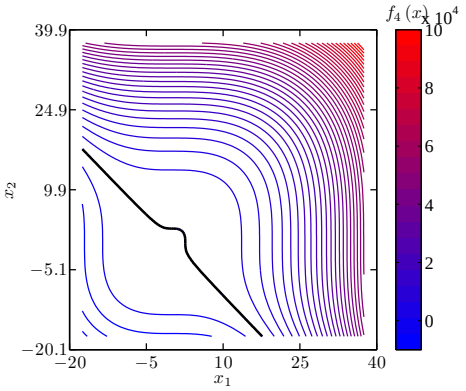

Figure 2.13: Contour plot of $f_4(\boldsymbol{x})$

2.7.2 Results and Discussion

First, the Sobol's sensitivities are given with the convergence study in Figs. 2.14, 2.15, 2.16, and 2.17 for Exs. 1 to 4, respectively. Good convergence is observed as the number of integration points increases for all cases. In Exs. 2 and 4, the estimation of the Sobol's indices is exact as expected for those two polynomials. The Ex. 3 is the harder to converge due to two facts: the nonlinear behavior of the function, and the Gaussian distribution of the input variables which requires to explore a large design space. In Ex.2, the converged sensitivities showed the importance of the interaction between the two variables as $S_{12} = 54\%$.

Next, for each example, the uncertainty propagation studies using SC are given and closely investigated. The contours of the converged response surface generated with SC are given in Figs. 2.18(a), 2.19(a), 2.20(a), and 2.21(a) for Exs. 1 to 4 respectively. The contours of the relative error of the response surface are depicted in Figs. 2.18(b), 2.19(b), 2.20(b), and 2.21(b) for Exs. 1 to 4 respectively. The black dots referred to sampling points.The L_∞ and L_2 errors compare the exact value to the response surface prediction at 121^2 uniformly distributed points. In cases 3 and 4, test points cover the domain given

by $m_x \pm 5\sigma_x$. As expected, for the polynomial cases, the response surfaces are exact and the error is close to machine precision. Example 4 has the highest error, located on the edges of the tested domain. In fact for gaussian distribution, the numerical integration points are spreads away from the mean as the order of the numerical integration scheme is increased. Therefore, the accuracy of the response surface is not significantly increased in those regions of low probability.

The PDFs are depicted in addition to the CDFs in Figs. 2.18(c), 2.19(c), 2.20(c), and 2.21(c) for Exs. 1 to 4, respectively. These figures illustrates the complete results that the UQ analysis gives. In addition to PDF and CDF, a vertical line indicates the deterministic prediction. A dashed line indicates the limit value $y_{lim} = 0$. In all examples, the IMCS are performed using a set of 50000 points generated using LHS. The probability distributions show some discrepancies due to the statistical results associated with the MCS.

The convergence of the stochastic collocation method is given for the 4 different metrics: L_∞, L_2, errors in $\langle f \rangle$, and σ_f in Figs. 2.18(d), 2.19(d), 2.20(d), and 2.21(d) for Exs. 1 to 4, respectively. Mean and standard deviation have the same convergence behavior as the Sobol's indices. This is expected since the same integration scheme is used to compute these quantities. Note that the first quantity to converge is the mean value which is the integration of f. The standard deviation and Sobol's indices require a higher integration scheme as they require the integration of f^2.

In addition, for each example, two additional figures show the convergence of the UQ results for other approaches. In Figs. 2.18(e), 2.19(e), 2.20(e), and 2.21(e) for Exs.1 to 4, respectively, the convergence of the expected value is compared for different approaches: SC, SCE, and PCE with quadrature is compared to PCE using a least square fit for three different numbers of sampling points obtained with LHS: n=1.3, 2, and 4 times the required minimum number of points as detailed in the presentation of PCE. In all examples, the numerical integration scheme associated with SC and PCE shows superior convergence than the PCE with least–square fit.

In Figs. 2.18(f), 2.19(f), 2.20(f), and 2.21(f), the performance of the response surface prediction is verified for Exs. 1 to 4, respectively. Kriging surrogates (KG) as well as RBF are added. The KG label refers to kriging using the integration points as sampling points, KG1 uses LHS points. The RBF is presented using Duchon thin plate spline with either SCE–type or LHS sampling. The methods that use LHS sampling show poor performance especially PCE when the order of the expansion is higher than the order of the exact function in Exs. 2 and 4. The error L_∞ does not converge for the PCE due to the ill–conditioning issue. In Ex.3, the better response surfaces are obtained for KG and RBF. In the other cases, note the strong convergence of the SC and PCE combined with Gaussian quadrature approaches, closely followed by kriging surrogate approximation.

The UQ results are quantitatively given for the converged response surfaces in Tables 2.9, 2.10, 2.11, and 2.12 for Exs. 1 to 4, respectively. The expected values and standard deviations are converged. discrepancies occur first in the estimation of the minimum and maximum values, and also in the CI and probability of failure p_f.

The results using adaptive sampling are illustrated for Exs. 1, 3, and 4 in Figs 2.22(a) to 2.22(f). The sampling points are shown on top of the contours of the response surface. In the three cases, when using the EFF approach, the points are located around the contours of the limit state. When using the $\widetilde{EFF}$ approach, the points are distributed in the region(s) of higher probability as expected. The second approach ensures that mean, variance, 95%CI are accurately predicted by focusing on the higher probability regions of the design space. The first approach focuses on the probability of failure only and uses therefore fewer sampling points. Both methods alleviate the curse of dimensionality by focusing on specific regions of interest, especially in the case of normally distributed variables.

2.7.3 Conclusions

These simple examples highlight the strengths and weaknesses of the UQ methods and justify the primary usage of SC in the next studies. The SC approach shows superior per-

formance in examples 1, 2 and 4. It compares well to PCE and kriging surrogate when using the same collocation points. Therefore SC is the method of choice in the rest of the studies. The PCE and kriging approaches are also considered for comparison and convergence assessment.

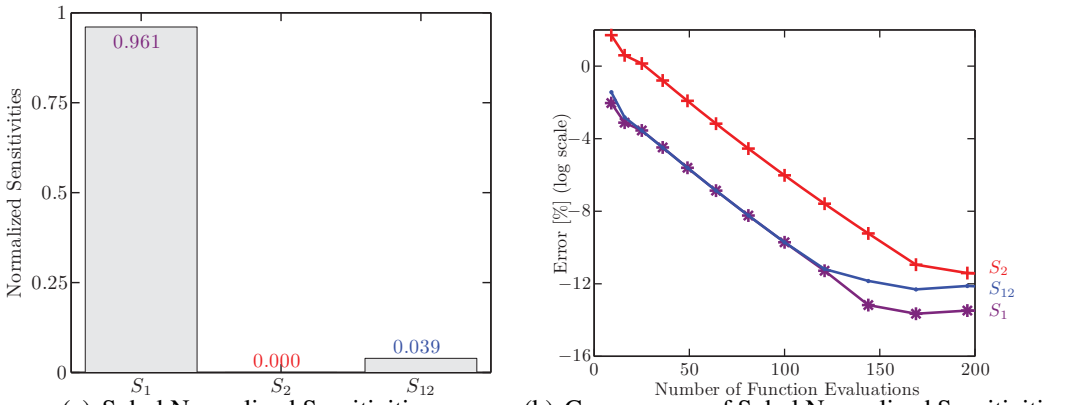

(a) Sobol Normalized Sensitivities (b) Convergence of Sobol Normalized Sensitivities

Figure 2.14: Sobol sensitivities analysis, Ex.1

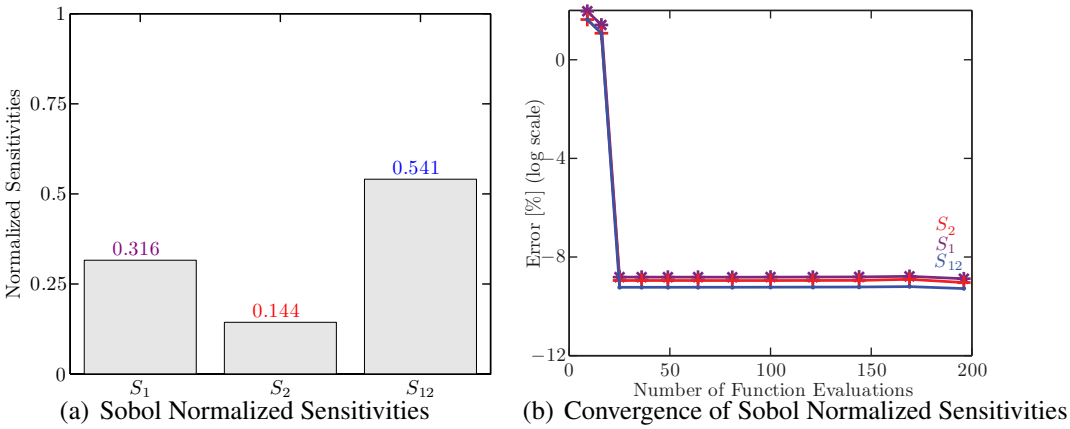

(a) Sobol Normalized Sensitivities (b) Convergence of Sobol Normalized Sensitivities

Figure 2.15: Sobol sensitivities analysis, Ex.2

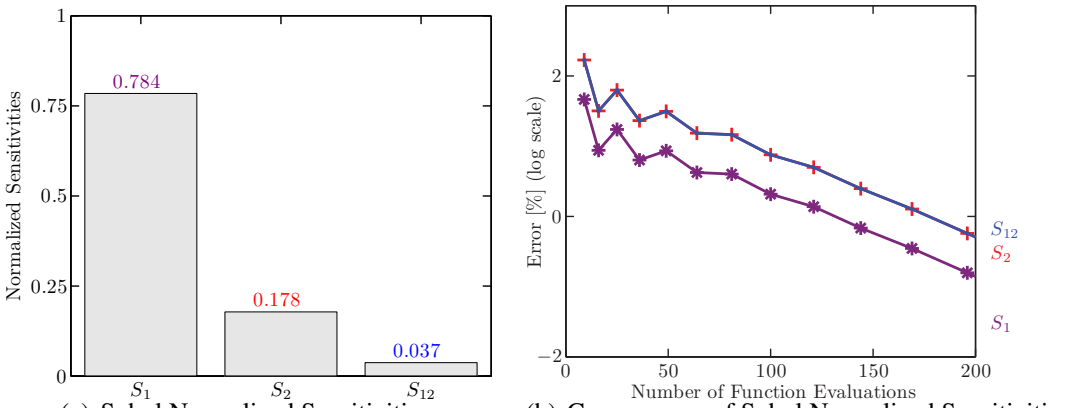

(a) Sobol Normalized Sensitivities (b) Convergence of Sobol Normalized Sensitivities

Figure 2.16: Sobol sensitivities analysis, Ex.3

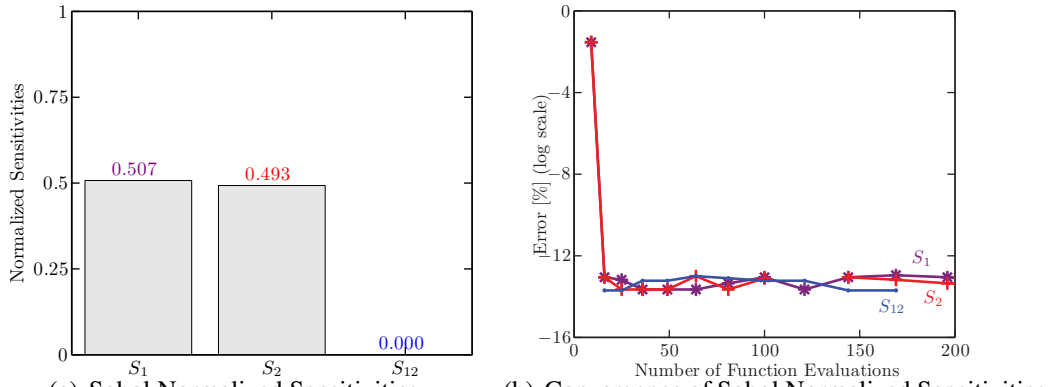

(a) Sobol Normalized Sensitivities (b) Convergence of Sobol Normalized Sensitivities

Figure 2.17: Sobol sensitivities analysis, Ex.4

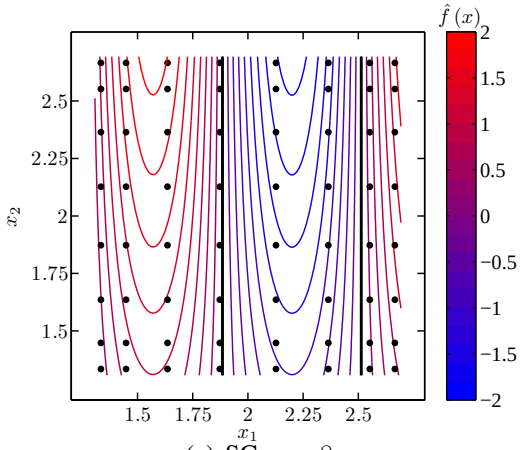

(a) SC, $p = 8$

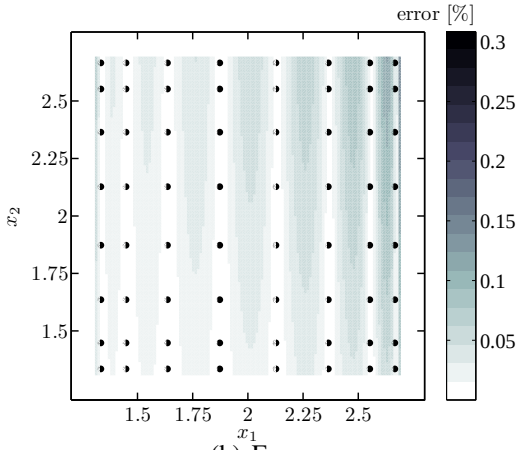

(b) Error

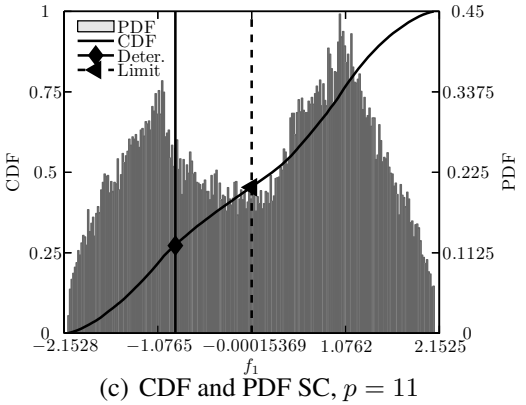

(c) CDF and PDF SC, $p = 11$

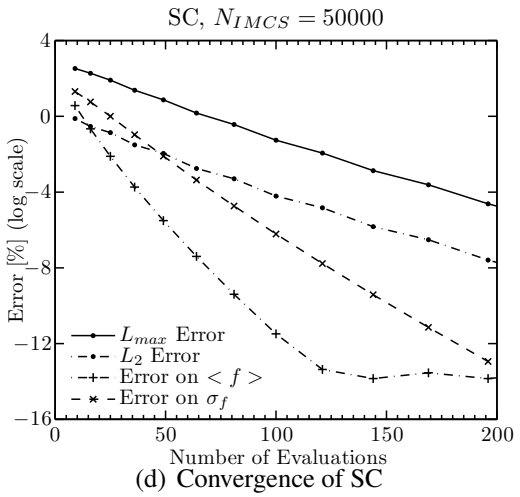

(d) Convergence of SC

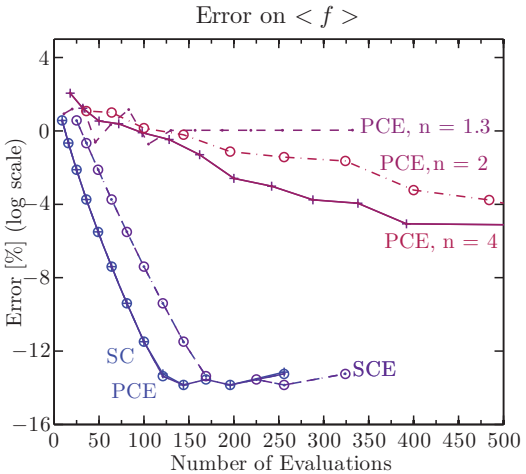

(e) Convergence of $\langle f \rangle$

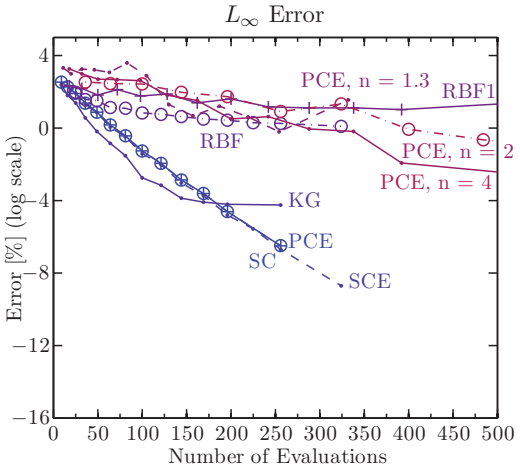

(f) Convergence of L_∞

Figure 2.18: Uncertainty propagation results for Ex.1

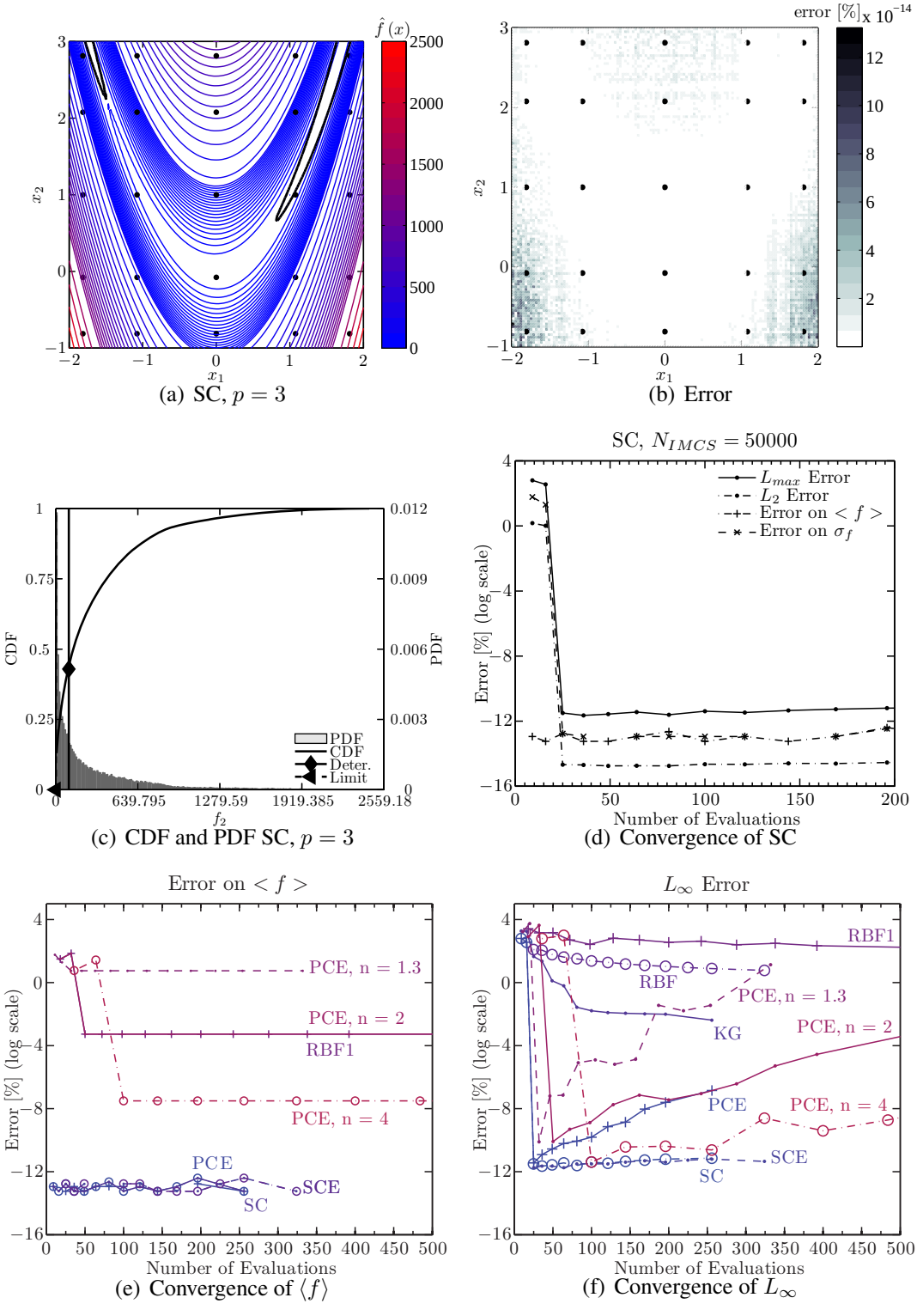

(a) SC, $p = 3$ (b) Error

(c) CDF and PDF SC, $p = 3$ (d) Convergence of SC

(e) Convergence of $\langle f \rangle$ (f) Convergence of L_∞

Figure 2.19: Uncertainty propagation results for Ex.2

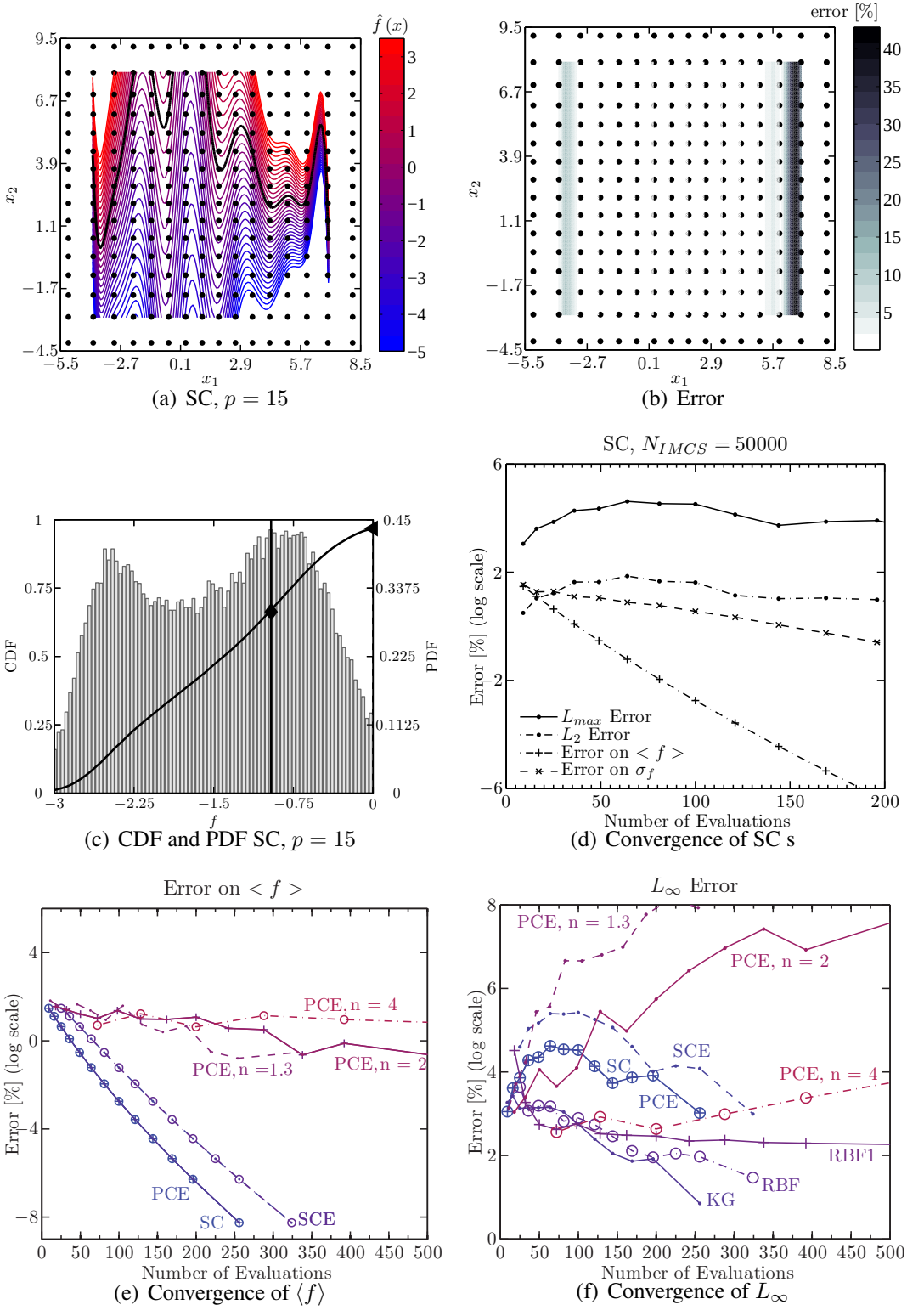

(a) SC, $p = 15$ (b) Error

(c) CDF and PDF SC, $p = 15$ (d) Convergence of SC s

(e) Convergence of $\langle f \rangle$ (f) Convergence of L_∞

Figure 2.20: Uncertainty propagation results for Ex.3

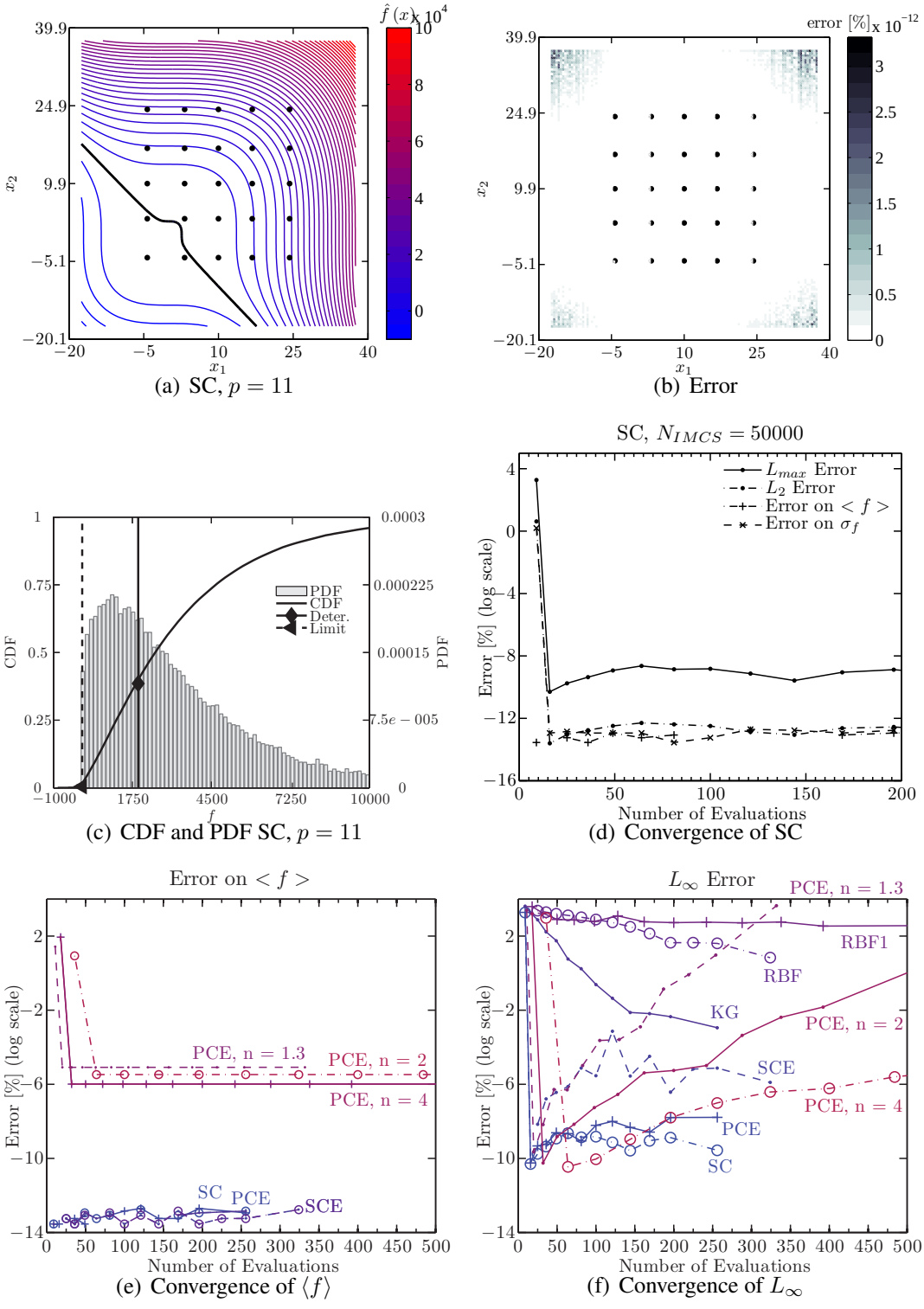

Figure 2.21: Uncertainty propagation results for Ex.4

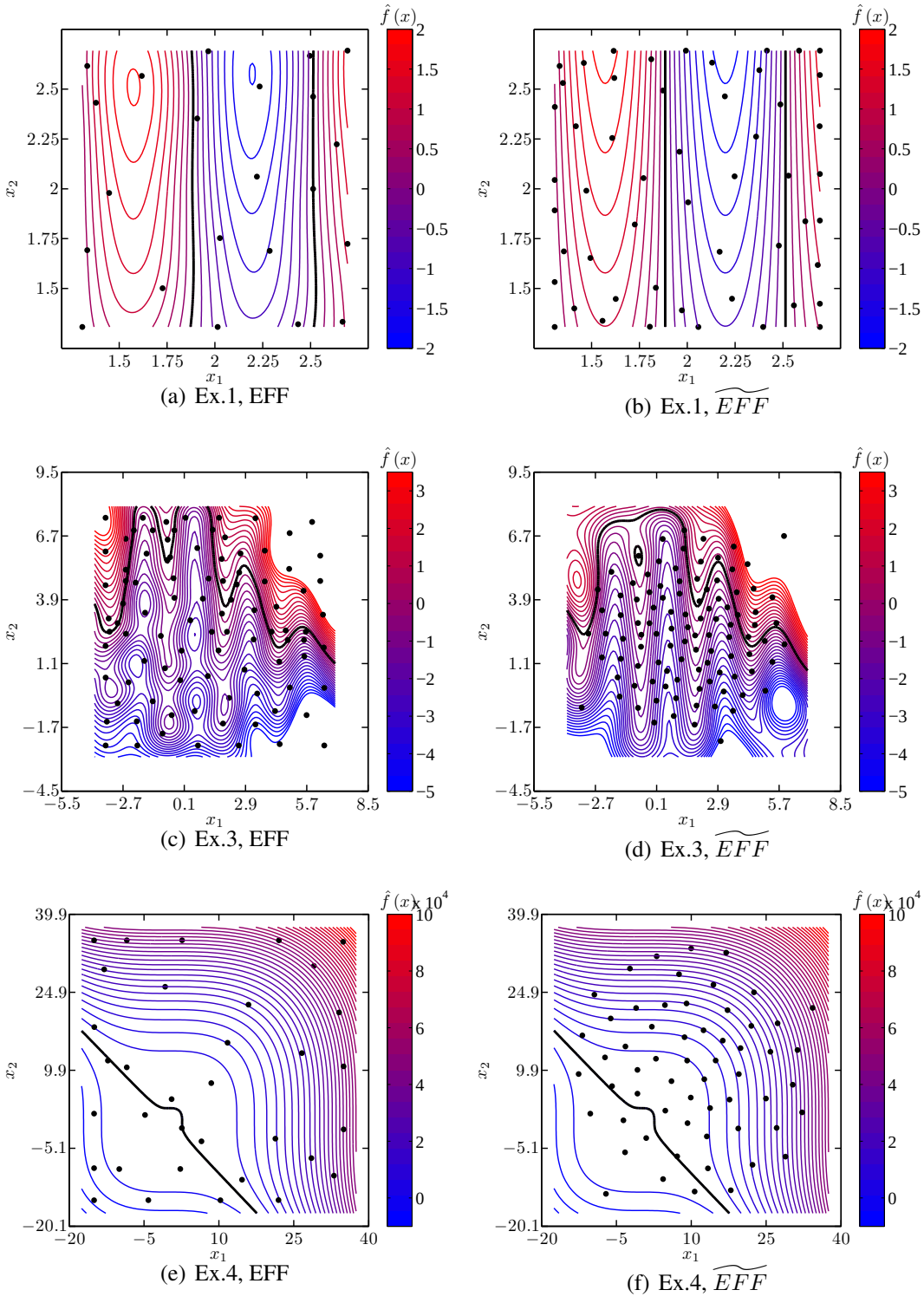

(a) Ex.1, EFF (b) Ex.1, $\widetilde{EFF}$

(c) Ex.3, EFF (d) Ex.3, $\widetilde{EFF}$

(e) Ex.4, EFF (f) Ex.4, $\widetilde{EFF}$

Figure 2.22: Uncertainty propagation results for two adaptive sampling strategies

Table 2.9: Uncertainty propagation results, Ex.1

Method	Sampling	N_s	$\langle y \rangle$	σ_y	$[y_{min}\ y_{max}]$	95% CI	p_f
MCS	LHS	50000	0.0798	1.12	$[-2.11\ 2.11]$	$[-1.87\ 1.87]$	0.453
SC	Qu	64	0.0798	1.12	$[-2.11\ 2.11]$	$[-1.87\ 1.87]$	0.453
PCE	Qu	64	0.0798	1.12	$[-2.11\ 2.11]$	$[-1.87\ 1.87]$	0.453
KG	Qu	64	0.0798	1.12	$[-2.11\ 2.11]$	$[-1.87\ 1.87]$	0.453
SCE	Qu	100	0.0798	1.12	$[-2.11\ 2.11]$	$[-1.87\ 1.87]$	0.453
RBF	Qu	100	0.08	1.12	$[-2.11\ 2.11]$	$[-1.86\ 1.86]$	0.453
RBF	LHS n=2	128	0.0839	1.12	$[-2.11\ 2.11]$	$[-1.85\ 1.86]$	0.454
PCE	LHS n=1.3	83	0.189	1.56	$[-2.11\ 30.1]$	$[-1.87\ 2.01]$	0.453
PCE	LHS n=2	128	0.0828	1.13	$[-2.11\ 2.11]$	$[-1.87\ 1.87]$	0.453
PCE	LHS n=4	256	0.0802	1.12	$[-2.11\ 2.11]$	$[-1.87\ 1.87]$	0.453
KG	EFF	22	0.0771	1.13	$[-2.11\ 2.11]$	$[-1.87\ 1.89]$	0.457
KGN	$\widetilde{EFF}$	52	0.0799	1.12	$[-2.11\ 2.11]$	$[-1.87\ 1.87]$	0.453

Table 2.10: Uncertainty propagation results, Ex.2

Method	Sampling	N_s	$\langle y \rangle$	σ_y	$[y_{min}\ y_{max}]\ 10^3$	95% CI	p_f
MCS	LHS	50000	288	373	$[0\ 2.51]$	$[1.54\ 1420]$	0
SC	Qu	25	288	373	$[0\ 2.51]$	$[1.54\ 1420]$	0
PCE	Qu	25	288	373	$[0\ 2.51]$	$[1.54\ 1420]$	0
KG	Qu	81	288	373	$[0\ 2.51]$	$[1.54\ 1420]$	0
SCE	Qu	36	288	373	$[0\ 2.51]$	$[1.54\ 1420]$	0
RBF	Qu	576	288	373	$[-0.1\ 2.51]$	$[1.49\ 1420]$	0.001
RBF	LHS	576	288	373	$[-0.1\ 2.51]$	$[1.49\ 1420]$	0.001
PCE	LHS n=1.3	32	288	373	$[0\ 2.51]$	$[1.54\ 1420]$	0
PCE	LHS n=2	50	288	373	$[0\ 2.51]$	$[1.54\ 1420]$	0
PCE	LHS n=4	100	288	373	$[0\ 2.51]$	$[1.54\ 1420]$	0
KG	EFF	37	288	373	$[0\ 2.51]$	$[1.57\ 1420]$	0.001
KG	$\widetilde{EFF}$	75	288	373	$[0\ 2.51]$	$[1.54\ 1420]$	0

Table 2.11: Uncertainty propagation results, Ex.3

Method	Sampling	N_s	$\langle y \rangle$	σ_y	$[y_{min}\ y_{max}]$	95% CI	p_f
MCS	LHS	50000	-1.43	0.858	$[-11.6\ 17.5]$	$[-2.86\ 0.0656]$	0.968
SC	Qu	256	-1.43	0.858	$[-11.6\ 17.5]$	$[-2.86\ 0.0693]$	0.968
PCE	Qu	256	-1.43	0.858	$[-11.6\ 17.5]$	$[-2.86\ 0.0693]$	0.968
KG	Qu	256	-1.43	0.858	$[-11.6\ 17.5]$	$[-2.86\ 0.0658]$	0.968
SCE	Qu	324	-1.43	0.858	$[-11.6\ 17.5]$	$[-2.86\ 0.0656]$	0.968
RBF	Qu	324	-1.43	0.833	$[-11.6\ 17.5]$	$[-2.83\ 0.0364]$	0.971
RBF	LHS	512	-1.43	0.838	$[-11.6\ 17.5]$	$[-2.82\ 0.0502]$	0.971
PCE	LHS n=1.3	332	-1.43	0.858	$[-11.6\ 17.5]$	$[-2.87\ 0.0612]$	0.969
PCE	LHS n=2	512	-1.43	0.853	$[-11.6\ 17.5]$	$[-2.86\ 0.0605]$	0.969
PCE	LHS n=4	1024	-1.43	0.855	$[-11.6\ 17.5]$	$[-2.85\ 0.0591]$	0.969
KG	EFF	94	-1.43	0.813	$[-11.6\ 17.5]$	$[-2.71\ 0.0543]$	0.97
KG	$\widetilde{EFF}$	102	-1.43	0.858	$[-11.6\ 17.5]$	$[-2.86\ 0.0648]$	0.968

Table 2.12: Uncertainty propagation results, Ex.4

Method	Sampling	N_s	$\frac{\langle y \rangle}{10^3}$	$\frac{\sigma_y}{10^3}$	$[y_{min}\ y_{max}]\ /10^5$	95% $CI \cdot /10^4$	p_f %
MCS	LHS	50000	3.44	3.06	$[-0.108\ 1.05]$	$[0.0127\ 1.16]$	0.51
SC	Qu	16	3.44	3.06	$[-0.108\ 1.05]$	$[0.0127\ 1.16]$	0.51
PCE	Qu	16	3.44	3.06	$[-0.108\ 1.05]$	$[0.0127\ 1.16]$	0.51
KG	Qu	16	3.44	3.06	$[-0.108\ 1.05]$	$[0.0205\ 1.16]$	0.23
SC	Qu	36	3.44	3.06	$[-0.108\ 1.05]$	$[0.0127\ 1.16]$	0.51
RBF	Qu	36	3.47	3.05	$[-0.108\ 1.05]$	$[0.0149\ 1.16]$	0.178
RBF	LHS	32	3.45	3.08	$[-0.108\ 1.05]$	$[0.0024\ 1.16]$	2.25
PCE	LHS n=1.3	20	3.44	3.06	$[-0.108\ 1.05]$	$[0.0127; 1.16]$	0.51
PCE	LHS n=2	32	3.44	3.06	$[-0.108\ 1.05]$	$[0.0127\ 1.16]$	0.51
PCES	LHS n=4	64	3.44	3.06	$[-0.108\ 1.05]$	$[0.0127\ 1.16]$	0.51
KG	EFF	32	3.45	3.06	$[-0.108\ 1.05]$	$[0.0127\ 1.16]$	0.51
KG	$\widetilde{EFF}$	51	3.44	3.06	$[-0.108\ 1.05]$	$[0.0127\ 1.16]$	0.51

CHAPTER 3

AEROTHERMOELASTIC AND AEROELASTIC FRAMEWORKS

3.1 Overview of the Aerothermoelastic Framework

Computational costs for a tightly coupled analysis of the entire trajectory of a hypersonic vehicle structure subject to aerodynamic heating and pressure loading are excessive. Therefore various approximations are introduced to reduce the computational costs to manageable levels. One of these approximations is a loosely coupled aerothermoelastic analysis. The complete aerothermoelastic analysis is illustrated by the flow chart in Fig. 3.1. It combines a loosely coupled thermo–elastic analysis with an aeroelastic solver. In both analyses, the solution of the Navier–Stokes (NS) equations is obtained using the commercial software CFD++, capable of accounting for dynamic mesh deformation and different gas models. The various components of this framework are described next.

3.2 Thermal Analysis

The heat transfer problem is treated using computational fluid dynamics (CFD) to evaluate the aerodynamic heat flux combined with a finite element model (FEM) solver for determining the temperature distribution. The heat transfer problem is governed by Eq. (3.1) and schematically depicted in Fig. 3.2. Figure 3.2 illustrates that the load carrying struc-

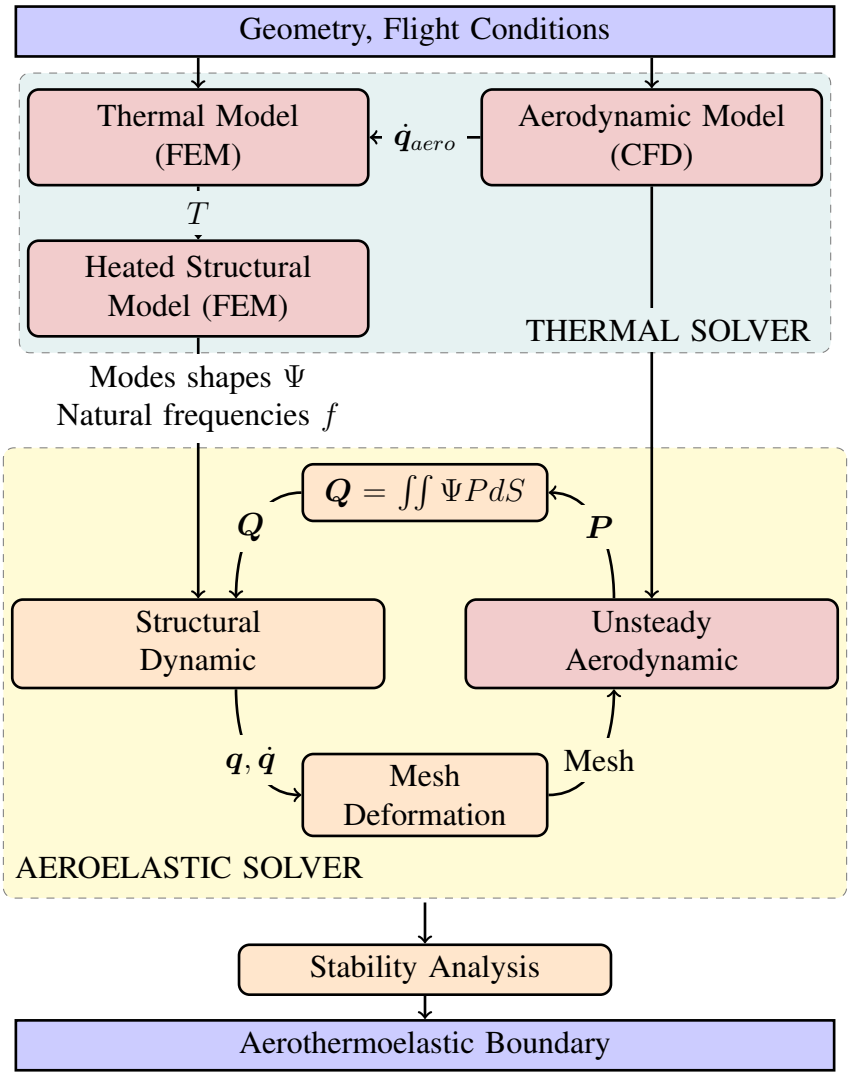

Figure 3.1: Aerothermoelastic Framework

ture is protected by a thermal protection system composed of two layers: the thermal insulation and the radiation shield. At the surface of the thermal protection system (TPS), the aerodynamic heat flux, $\dot{q}_{aero}$, and the radiation heat flux, $\dot{q}_{rad}$, are in equilibrium with the conductive heat flux, $\dot{q}_{cond}$, and the variation of energy stored in the TPS, $\dot{q}_{st}$, as given by Eq. (3.2).

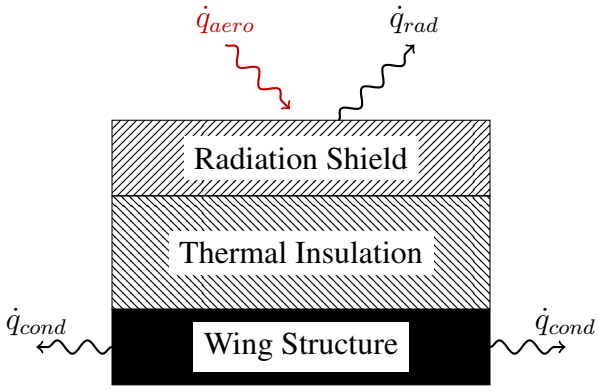

Figure 3.2: Two-dimensional model of the thermal structure

$$\rho_m c_m \frac{\partial T}{\partial t} = k_x \frac{\partial^2 T}{\partial x^2} + k_y \frac{\partial^2 T}{\partial y^2} + k_z \frac{\partial^2 T}{\partial z^2} \tag{3.1}$$

$$\dot{q}_{aero} = \dot{q}_{rad} + \dot{q}_{cond} + \dot{q}_{st} \quad \text{where} \quad \dot{q}_{aero} = h_w \left(T_{AW} - T\right) \tag{3.2}$$

In the steady state, the flux equilibrium yields an algebraic equation, Eq. (3.3), for the radiation equilibrium temperature T_R which gives an indication of maximum surface temperatures.

$$h \left(T_{AW} - T_R\right) = \sigma \epsilon T_R^4 \tag{3.3}$$

Since thermal degradation, thermal stresses and heat transfer are highly dependent on each other, heat flux prediction is a key component of the analysis. The aerodynamic heat flux, $\dot{q}_{aero}$, is obtained using CFD++. The calculation of the heat flux coefficient h_w and the adiabatic wall temperature are obtained by using CFD++ twice for a particular flight condition: once with adiabatic wall boundary condition (BC) to determine T_{AW} and once

with constant wall temperature BC to calculate h_w. Both of these quantities are used to define the boundary conditions of the heat transfer problem in the FEM solver. The heat flux is calculated with a CFD mesh that is finer that the FEM mesh. When applying the aerodynamic heat load at the surface of the FEM mesh, the total heat flux applied to the structure is equal to that given by the fluid solver.

As illustrated in Fig. 3.1, the heated modes are obtained in two steps. First, the temperature distributions in the structure and the TPS layer are calculated with the MSC.NASTRAN (Sol.159) solving the heat transfer problem with appropriate boundary conditions as given in Eqs. (3.1) and (3.2). The temperature distribution of the undeformed structure is calculated as a function of time for the entire trajectory. Next, the heated modes are obtained from the temperature distribution in the wing. The nonlinear solver MSC.NASTRAN (Sol.106) is used to calculate the normal modes of the heated structure. Material properties are functions of temperature and thermal stresses are included. The thermal coupling is a one way coupling that implies that the heat flux is not affected by deformation or by the wall temperature. The heated modes and modal frequencies are used in the aeroelastic solver described next.

3.3 Aeroelastic Analysis

The aeroelastic simulation is represented in the lower portion of Fig. 3.1, and enclosed by a box having dashed lines. The structure is represented by a limited number of mode shapes, Ψ, computed using a FEM obtained with MCS.NATRAN. The equations of motion are integrated using a predictor/corrector explicit scheme which requires the evaluation of the generalized loads only once per time step. At each time step, the deformation of the structure is passed to the mesh deformation routine. The fluid mesh is deformed using RBF and the updated nodal positions and velocities are passed to the fluid solver. The CFD solution is marched in time for the deformed configuration using a point–implicit

scheme. The generalized loads, $\boldsymbol{Q}$, are calculated based on the pressure distribution at the wetted interface. Finally the structural deformation is advanced to the next time step. Eventually the transient aeroelastic response is obtained. The stability of the aeroelastic system is determined using a system identification approach that extracts the damping from the response.

3.3.1 Formulation of the Equations of Motion

The formulation of the equations of motions is presented for the heated structure. Therefore, the mode shapes and modal frequencies are function of the temperature distribution in the structure. For conciseness, this dependency is kept implicit.

Hypersonic vehicle structures undergo small deformations and the structure is represented by a limited number of its natural modes [84]. The in–plane displacements of the wing, u and v, are assumed to be negligible. The out–of–plane displacement, $w(t, \boldsymbol{x})$, at any point of the structure is described by a finite series of modes given by Eq. (3.4).

$$w(t, \boldsymbol{x}) = \sum_{i=1}^{N_m} q_i(t)\, \psi_i(\boldsymbol{x}) \tag{3.4}$$

The equations of motion (EOM) of the aeroelastic system obtained from Lagrange equations are given in Eq. (3.5).

$$\frac{d}{dt}\left(\frac{\partial T_E}{\partial \dot{q}_i}\right) - \frac{\partial T_E}{\partial q_i} + \frac{\partial U_E}{\partial q_i} = Q_i \quad i = 1, \ldots, N_m \tag{3.5}$$

From Eq. (3.5), the final EOM can be written as in Eq. (3.6).

$$\mathbf{M}\ddot{\boldsymbol{q}} + \mathbf{K}\boldsymbol{q} = \boldsymbol{Q}(t, \boldsymbol{q}, \dot{\boldsymbol{q}}, \ddot{\boldsymbol{q}}) \tag{3.6}$$

The coupling algorithm between the CFD solver and the structural solver employed in solving the EOM is described next.

3.3.1.1 Time Integration and Fluid–Structure Coupling

The fluid and the structure are coupled through the generalized loads. The EOM in the state–vector form can be written as Eq. (3.7).

$$\left\{ \begin{array}{c} \dot{\boldsymbol{q}} \\ \ddot{\boldsymbol{q}} \end{array} \right\} = \left[\begin{array}{cc} \mathbf{0} & \mathbf{I} \\ -\mathbf{M}^{-1}\mathbf{K} & \mathbf{0} \end{array} \right] \left\{ \begin{array}{c} \boldsymbol{q} \\ \dot{\boldsymbol{q}} \end{array} \right\} + \left\{ \begin{array}{c} \mathbf{0} \\ \mathbf{M}^{-1}\boldsymbol{Q} \end{array} \right\} \tag{3.7}$$

written as:

$$\{\dot{\boldsymbol{X}}\} = [\mathbf{A}]\{\boldsymbol{X}\} + [\mathbf{B}]\{\boldsymbol{Q}\} \tag{3.8}$$

where

$$\{\boldsymbol{X}\} = \left\{ \begin{array}{c} \boldsymbol{q} \\ \dot{\boldsymbol{q}} \end{array} \right\} \qquad [\mathbf{A}] = \left[\begin{array}{cc} \mathbf{0} & \mathbf{I} \\ -\mathbf{M}^{-1}\mathbf{K} & \mathbf{0} \end{array} \right] \qquad [\mathbf{B}] = \left\{ \begin{array}{c} \mathbf{0} \\ \mathbf{M}^{-1} \end{array} \right\} \tag{3.9}$$

The transition matrix in the time domain, $[\mathbf{A}]$, is constant. The solution of the EOM is obtained by multiplying Eq. (3.8) by $e^{-[\mathbf{A}]t}$; it yields:

$$\frac{d}{dt}\left(e^{-[\mathbf{A}]t}\{\boldsymbol{X}\}\right) = e^{-[\mathbf{A}]t}[\mathbf{B}]\{\boldsymbol{Q}\} \tag{3.10}$$

The exact solution of the EOM is obtained by integrating Eq. (3.10) in time and given by Eq. (3.11). The first term corresponds to the homogeneous solution and the second term is the forced response that accounts for the effect of the aerodynamic loads.

$$\boldsymbol{X}_{n+1} = \underbrace{e^{[\mathbf{A}]\Delta t}\boldsymbol{X}_n}_{\text{homogeneous solution}} + \underbrace{\int_{t_n}^{t_{n+1}} e^{[\mathbf{A}](t_{n+1}-\tau)}[\mathbf{B}]\,\boldsymbol{Q}\left(\tau, \boldsymbol{X}\right) d\tau}_{\text{forced response}} \tag{3.11}$$

The transient response of the aeroelastic system is integrated in time using an explicit method which combines a second order Adams-Bashforth predictor [149] and a trapezoidal corrector as given in Eqs. (3.12) and (3.13), respectively.

$$\tilde{\boldsymbol{X}}_{n+1} = \boldsymbol{\Phi}\boldsymbol{X}_n + \frac{\boldsymbol{\Theta}}{2}\left(3\boldsymbol{Q}\left(\boldsymbol{X}_n, t_n\right) - \boldsymbol{Q}\left(\boldsymbol{X}_{n-1}, t_{n-1}\right)\right) \tag{3.12}$$

$$\boldsymbol{X}_{n+1} = \boldsymbol{\Phi}\boldsymbol{X}_n + \frac{\boldsymbol{\Theta}}{2}\left(\boldsymbol{Q}\left(\tilde{\boldsymbol{X}}_{n+1}, t_{n+1}\right) + \boldsymbol{Q}\left(\boldsymbol{X}_n, t_n\right)\right) \tag{3.13}$$

In Eqs. (3.12) and (3.13), the state–transition matrix, $\boldsymbol{\Phi}$, and the integral of the state–transition matrix, $\boldsymbol{\Theta}$, are given in Eqs. (3.14) and (3.15), respectively.

$$\boldsymbol{\Phi} = e^{[\mathbf{A}]\Delta t} \tag{3.14}$$

$$\boldsymbol{\Theta} = \int_{t_n}^{t_{n+1}} e^{[\mathbf{A}](t_{n+1}-\tau)}\left[\mathbf{B}\right] d\tau = \left[\mathbf{A}\right]^{-1}\left(\boldsymbol{\Phi} - \mathbf{I}\right)\left[\mathbf{B}\right] \tag{3.15}$$

The state transition matrix, $\boldsymbol{\Phi}$, is calculated using the Padé approximation with scaling and squaring [150] implemented in MATLAB's $expm$ function. This method scales the matrix by a power of 2 to reduce its norm to order 1, computes a Padé approximant to the matrix exponential, and then repeatedly squares to undo the effect of the scaling. This process ensures robustness and accuracy of the calculation of the exponential of the matrix. Details of the implementation can be found in Ref. [150].

The time marching is illustrated in Fig. 3.3. At the beginning of each time step, the structural deformation at time t_{n+1} is estimated using the generalized loads at the previous and current time step as given by the predictor step, Eq. (3.12), and represented by the dashed arrows in Fig. 3.3. Next, the fluid mesh is deformed based on the predicted structure deformation, shown by the arrow indicated by $\tilde{\boldsymbol{q}}_{n+1}$. The pressure distribution is updated by multiple sub iterations within a time step of the CFD solver to march the Navier Stokes solution to the next time step, as represented by the dotted arrow. The small circles symbolically represent the subiterations of the CFD solver within the time step. Finally, the generalized loads are transferred to the structural solver and the deformation of the structure at time $t_n + \Delta t$ is updated using the corrector step given by Eq. (3.13) based on the

generalized loads calculated at time t_{n+1}. The corrector step is represented by the arrow $\tilde{\boldsymbol{Q}}_{n+1}$.

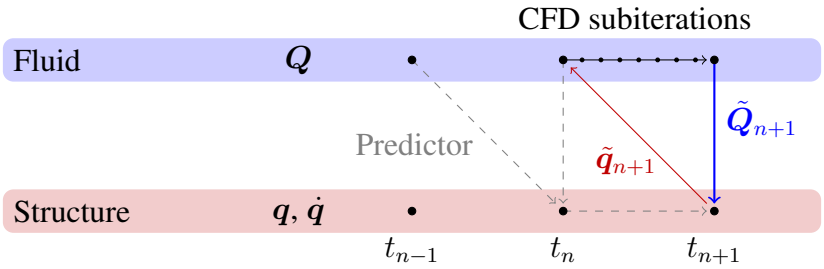

Figure 3.3: Time marching and coupling approach

The coupling between the fluid and the structure depends on both the mesh deformation method and the calculation of the generalized loads.

3.3.1.2 Computation of the Generalized Aerodynamic Loads

The generalized loads are defined by Eq. (3.16). The loads depends on the deformation $(\boldsymbol{q}, \dot{\boldsymbol{q}}, \ddot{\boldsymbol{q}})$ through the pressure distribution on the deformed wing. This dependency is explicitly stated in Eq. (3.16), but is implied in the rest of the document for sake of conciseness.

$$Q_i\left(t, \boldsymbol{q}, \dot{\boldsymbol{q}}, \ddot{\boldsymbol{q}}\right) = \int_{\partial\Omega} -\psi_i\left(\boldsymbol{x}\right) P\left(\boldsymbol{x}, \boldsymbol{q}, \dot{\boldsymbol{q}}, \ddot{\boldsymbol{q}}\right) n_z dS \quad 1 \leq i \leq N_m \tag{3.16}$$

As illustrated in Figs 3.4(a) and 3.4(b), the wing is defined by the faces of the cells of the fluid mesh which are on the boundary. The entire wing is depicted in Fig 3.4(a) where the dots correspond to the face centroid. Figure 3.4(b) is a close-up view of the face of one cell and its centroid.

The CFD++ code cannot calculate the generalized forces. Therefore the integration of the generalized loads is implemented externally to CFD++ and consists of the following: The calculation of the generalized aerodynamic loads is performed using the CFD mesh. The integration over the surface of the wing, $\partial\Omega$, is replaced by the summation of the

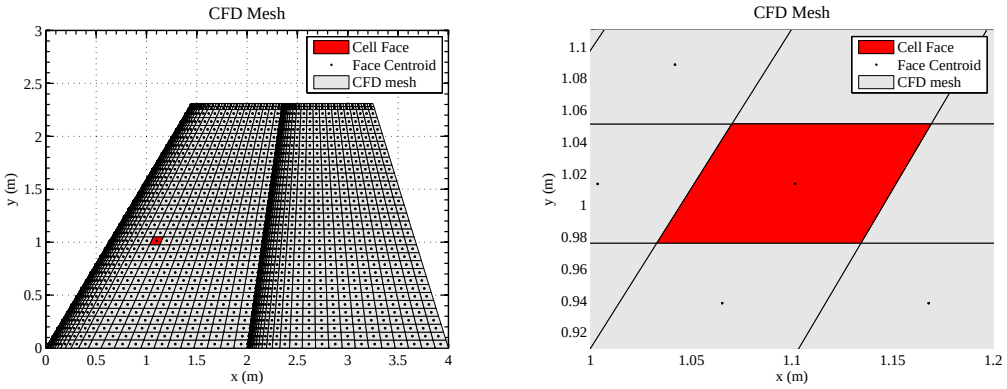

(a) CFD mesh at the surface of the wing. (b) Zoom on a face of one cell.

Figure 3.4: CFD mesh of the wing boundary

contribution of the faces of the fluid cells, $\partial\Omega_k$, that define the wing. The modal shape function, ψ_i is evaluated at the centroid of each face, $\boldsymbol{x}_k$, to express the generalized loads as given by Eq. (3.17).

$$Q_i \simeq \sum_{k=1}^{N_{cells}} \psi_i\left(\boldsymbol{x}_k\right) \int_{\partial\Omega_k} -P\left(\boldsymbol{x}\right) n_z dS \tag{3.17}$$

The quantity $\int_{\partial\Omega_k} -P\left(\boldsymbol{x}\right) n_z dS$ is the contribution of one face to the force in the $z-$direction. It is extracted from the CFD++ code by the mean of an output file after each time step.

The CFD++ code cannot calculate the Q_i's therefore verification of this calculation is infeasible. However, for a sanity check, the resultant forces and moments can be calculated in a similar manner and compared to the ones calculated by CFD++. To calculate the resultant forces in the vertical direction $\psi_i\left(\boldsymbol{x}_k\right) = 1$ is used, and $\psi_i\left(\boldsymbol{x}_k\right) = x_k - x_{ea}$ for the moment in the y–direction.

The results showed perfect agreement with the present approach. This integration, in Eq. (3.17), is consistent with the pressure discretization (second order multi–dimensional Total Variation Diminishing (TVD) scheme) that pertains to the CFD algorithm implemented in CFD++. Consequently the only approximation made in this approach comes

from the calculation of the shape function at the centroid of the fluid cell faces, $\psi_i(\boldsymbol{x}_k)$. For consistency, this value is given by the mesh deformation method.

Remark An alternative approach for calculating the generalized loads has been considered and found to be inaccurate, and it was discarded. For completeness, this method is briefly presented in this paragraph. The consistent generalized loads calculation requires that pressure is interpolated at the integration points of the FEM cells. In this case, the generalized loads are given by Eq. (3.18).

$$Q_i \simeq -\sum_{k=1}^{N_{FEMcells}} \sum_{k=1}^{N_k} A_k w_k \psi_i(\boldsymbol{x}_k) P(\boldsymbol{x}_k) n_z \tag{3.18}$$

In this work, the CFD++ solver is used as a black box and the calculation of Q given by Eq. 3.18 requires extensive postprocessing at each time step: calculation of the normals, cells areas, locations of the integration points of the FEM mesh at the wetted interface, and interpolation of pressure which is known at the CFD nodes only. It generates numerical errors and ignores the pressure discretization that pertains to the CFD solution (2^{nd} order in space). The errors in the resultant forces and moments are of the order of 3% and up to 10% respectively. Because of these reasons, this approach is not suitable and has been discarded.

3.3.2 Approximate Aerodynamic Loading Using Piston Theory

Piston theory (PT) has been used extensively in studies on hypersonic aeroelasticity [1]. Third order piston theory (PT) was used successfully in flutter prediction of a typical supersonic control surface in hypersonic flow. The PT was shown to outperform other approximate approaches when compared against CFD calculation [1]. Due to its computational efficiency PT is used to bracket the flutter Mach number before performing expensive CFD simulations. Piston theory gives a point–wise relationship between local deformation and pressure, as given in Eq. (3.19), assuming perfect gas and inviscid isentropic flow.

$$\frac{P - P_\infty}{P_\infty} = \gamma \left[\frac{v_n}{a_\infty} + \frac{\gamma + 1}{4} \left(\frac{v_n}{a_\infty} \right)^2 + \frac{\gamma + 1}{12} \left(\frac{v_n}{a_\infty} \right)^3 \right] \tag{3.19}$$

The pressure depends on the free stream conditions and v_n, the velocity of the air at the boundary normal to the mean surface of the wing, given in Eq. (3.20), where Z_s accounts for the thickness of the airfoil and w for the aeroelastic deformation.

$$v_n(x, y, z) = \begin{cases} \frac{\partial w}{\partial t} + U_\infty \left[\frac{\partial}{\partial x} (Z_s + w) + \alpha_s \right] & z > 0 \\ -\frac{\partial w}{\partial t} + U_\infty \left[\frac{\partial}{\partial x} (Z_s - w) - \alpha_s \right] & z < 0 \end{cases} \tag{3.20}$$

Note that piston theory gives a quasi–steady representation of the aerodynamic loading, additional details are given in Appendix C. The PT approximate model yields a quasi–steady representation of the aerodynamic loading and the resulting generalized loads are linear with respect to small deformations which justify the usage of the system identification (SI) considered.

3.4 Mesh Deformation Using RBF

A RBF, ϕ, is a scalar function whose value depends only on the distance from the origin, $r = \|\boldsymbol{x}\|$. The RBFN are an effective tool for multivariate interpolation of both scattered and gridded data [50], as presented in Section 2.5.4. In aeroelastic applications, the displacement, w, is the quantity being interpolated from the fluid–structure interface to the rest of the CFD mesh. Given a set of N_s sampling points, also called *driving points*, $\boldsymbol{x}_j$, at which the deformation is known: $(\boldsymbol{x}_j, w_j)_{j=1,N_s}$, the RBF interpolant of w, $\hat{w}$, is constructed in the form given by Eq. (3.21). The interpolated value at a new point, $\boldsymbol{x}$, depends only on the Euclidian distance between $\boldsymbol{x}$ and the driving points $(\boldsymbol{x}_{dj})_{j=1,N_s}$.

$$\hat{w}(\boldsymbol{x}) = \sum_{j=1}^{N_s} \alpha_j \phi \left(\|\boldsymbol{x} - \boldsymbol{x}_{dj}\| \right) + p(\boldsymbol{x}) \tag{3.21}$$

In Eq. (3.21), the polynomial $p(\boldsymbol{x})$ and the fitting coefficients α_j are determined such that the interpolant, $\hat{w}$, is equal to the structural deformation w at the sampling points, as given in Eq (3.22).

$$w_i = \hat{w}(\boldsymbol{x}_{di}) = \sum_{j=1}^{N_s} \alpha_j \phi\left(\|\boldsymbol{x}_{di} - \boldsymbol{x}_{dj}\|\right) + p(\boldsymbol{x}_{di}) \quad 1 \leq k \leq N_s \tag{3.22}$$

Introducing $\left(p_n(\boldsymbol{x})\right)_n$ as a polynomial basis, $p\left(\boldsymbol{x}\right)$ is written as $\sum_{n=0}^{P} \beta_n p_n(\boldsymbol{x})$. The coefficients β_n uniquely determine p. To ensure uniqueness of the form given in Eq. (3.21), i.e. the uniqueness of the coefficients α_j and β_n, additional conditions given in Eq. (2.55) have to be satisfied.

$$\sum_{j=1}^{N_s} \alpha_j p_n\left(\boldsymbol{x}_{dj}\right) = 0 \quad n = 0, P \tag{3.23}$$

Combining Eqs. (3.22) and (3.23), α_j and the coefficients β_n are uniquely defined by solving the linear system written in the form of Eq. (3.24), where $\boldsymbol{M_{bb}}\left(\boldsymbol{x}\right)) = [\phi\left(\|\boldsymbol{x} - \boldsymbol{x}_{dj}\|\right)]$, $\boldsymbol{Q_b}\left(\boldsymbol{x}\right) = \left[p_n(\boldsymbol{x})\right]_{j=1,N_s;\, n=0,P}$.

$$\begin{bmatrix} \boldsymbol{M_{bb}}\left(\boldsymbol{x_d}\right) & \boldsymbol{Q_b}\left(\boldsymbol{x_d}\right) \\ \boldsymbol{Q_b}\left(\boldsymbol{x_d}\right)^T & \boldsymbol{0} \end{bmatrix} \begin{Bmatrix} \boldsymbol{\alpha} \\ \boldsymbol{\beta} \end{Bmatrix} = \begin{Bmatrix} w^S\left(\boldsymbol{x_d}\right) \\ \boldsymbol{0} \end{Bmatrix} \tag{3.24}$$

The displacement at any other point is given by Eq. (3.25).

$$w^F\left(\boldsymbol{x}\right) = \begin{bmatrix} \boldsymbol{M_{bb}}\left(\boldsymbol{x}\right) & \boldsymbol{Q_b}\left(\boldsymbol{x}\right) \end{bmatrix} \begin{Bmatrix} \boldsymbol{\alpha} \\ \boldsymbol{\beta} \end{Bmatrix} \tag{3.25}$$

The computational cost of the mesh deformation is reduced when assuming small deformations and using a modal representation of the structure. Combining the RBF interpolant in Eqs. (3.24) and (3.25) with Eq. (3.4) yields Eq. (3.26).

$$w^F(\boldsymbol{x}) = \underbrace{\begin{bmatrix} \boldsymbol{M_{bb}}(\boldsymbol{x}) & \boldsymbol{Q_b}(\boldsymbol{x}) \end{bmatrix} \begin{bmatrix} \boldsymbol{M_{bb}}(\boldsymbol{x_d}) & \boldsymbol{Q_b}(\boldsymbol{x_d}) \\ \boldsymbol{Q_b}(\boldsymbol{x_d})^T & \mathbf{0} \end{bmatrix}^{-1} \begin{bmatrix} \{\psi_1(\boldsymbol{x_d})\} & \dots & \{\psi_{N_m}(\boldsymbol{x_d})\} \\ \mathbf{0} & \dots & \mathbf{0} \end{bmatrix}}_{\boldsymbol{\psi^F} = \left\lfloor \psi_1^F(\boldsymbol{x}) \dots \psi_{N_m}^F(\boldsymbol{x}) \right\rfloor} \{\boldsymbol{q}\} \tag{3.26}$$

In Eq. (3.26), each column of the matrix $\boldsymbol{\psi^F}$ corresponds to the deformation of the fluid mesh for a given structural mode shape, calculated before the start of the aeroelastic simulation. Subsequently, at each time step the deformation of the fluid mesh is calculated directly from the modal degree of freedom, $\boldsymbol{q}$, by a matrix multiplication as given by Eq. (3.27). It increases the memory requirement but reduces the computational cost of each time step since no matrix inversion is needed.

$$w^F(\boldsymbol{x}) = \left\lfloor \psi_1^F(\boldsymbol{x}) \dots \psi_{N_m}^F(\boldsymbol{x}) \right\rfloor \{\boldsymbol{q}\} \tag{3.27}$$

In the RBF approach several components are chosen to obtain the best fit possible, such as the the polynomial order, the choice of RF and the set of driver points. In aeroelastic simulations, a polynomial of order 1 is considered such that rigid body motions are captured by the polynomial component of the expansion. The radial function, Volume spline, is chosen: $\phi(\|\boldsymbol{x} - \boldsymbol{x}_{dj}\|) = \|\boldsymbol{x} - \boldsymbol{x}_{dj}\|$.

The choice of the driving points is important. The deformation of the fluid–structure interface is known at the FEM nodes. Several alternative approaches are used to deform the fluid mesh based on this information. One approach interpolates the deformation from the FEM nodes to the fluid mesh. In this case the driving points are the FEM nodes on the interface between the structure and the fluid. Due to the global form of the RBF interpolant, the deformed interface defined by the fluid mesh does not coincide perfectly with

the structural one for fluid points located between adjacent FEM nodes. The FEM mesh is usually coarse when compared to the fluid mesh, as illustrated schematically in Fig. 3.5. A simplified CFD mesh is deformed using the FEM nodes at the interface as driving points. The FEM deformed interface is represented by the thick dotted line in Fig. 3.5, and the CFD interface by the thin line with crosses in Fig. 3.5. Both interfaces do not necessarily match.

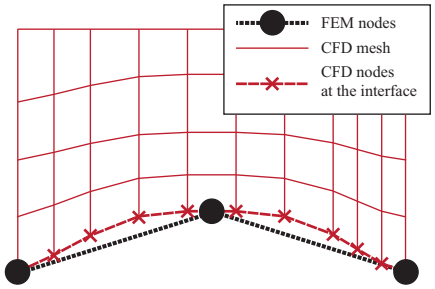

Figure 3.5: Illustration of the usage of RBF for mesh deformation

To ensure that the structure and fluid boundaries match, the set of FEM nodes is augmented with additional driving points at which the deformation is calculated based on the FEM model. If necessary, every fluid node of the interface can be used as driving points and a RBF interpolation based on these points is generated for interior points. This second approach is used in this study. The deformation of the interface at the fluid mesh is calculated using a piecewise bilinear interpolation between the FEM nodes.

To quantify the error at the fluid–structure interface due to RBF interpolation, different error metrics given in Eqs. (3.28) through (3.30) are used. The reference deformation w_{ref} is either the analytical form of the deformation, when available, or a piecewise interpolation between the FEM points; $\hat{w}$ is the deformation predicted by the RBF interpolation. The errors are normalized with respect to the maximum amplitude of the deformation of the fluid–structure interface.

$$L_2 = \sqrt{\frac{1}{N}\sum \frac{\left(\hat{w} - w_{ref}\right)^2}{\max(w_{ref}^2)}} \tag{3.28}$$

$$L_1 = \frac{1}{N}\frac{\sum \|\hat{w} - w_{ref}\|}{\max(\|w_{ref}\|)} \tag{3.29}$$

$$L_{max} = \frac{\max\left(\|\hat{w} - w_{ref}\|\right)}{\max\left(\|w_{ref}\|\right)} \tag{3.30}$$

3.5 Stability Boundary Calculation

The stability boundary is obtained by identifying the damping in the system using a system identification (SI) method described in this section. It is assumed that the aeroelastic system can be treated as a linear dynamic system, so that frequencies and damping coefficients of the aeroelastic system can be determined and its stability boundary obtained.

3.5.1 ARMA

The auto regressive moving average (ARMA) method is an effective system identification method used to extract the frequencies and corresponding damping from the transient response of an aeroelastic system. It has been used for flutter prediction of hypersonic problems in Refs. [84] and [103]. A detailed description of the ARMA method is given in Appendix B. A brief overview is presented here.

The general formulation is given by Eq. (3.31). The aeroelastic response of the structure at a given point, w, is modeled by Eq. (3.31), where w_k is the displacement of a given point of the structure and e_k is the excitation at time kT_s.

$$w_k + a_1 w_{k-1} + a_2 w_{k-2} + \ldots + a_n w_{k-n} = b_1 e_{k-1} + b_2 e_{k-2} + \ldots + b_m e_{k-m} \tag{3.31}$$

In flutter studies, $n = 2N_m$ and $m = 1$ are typical values. The choice of $m = 1$ com-

bined with $e_{k-1} = 1$ is only required to account for a non–zero static offset. Based on the aeroelastic transient response, the coefficients (a_i) are calculated. From those coefficients, the frequencies and damping of the system are calculated.

It assumes that at each time step the response of the system is a linear combination of the response at the n previous time steps and a linear combination of the input e at current and previous time steps k to $k - m$. For this reason, ARMA approach is applicable to systems which behavior is identified as linear combination of damped harmonic oscillations [84].

The ARMA method only requires the transient response at one point to estimate frequencies and damping. In order to accurately identify the modal response of the aeroelastic system, all modes need to be excited. The sampling time T_s is a parameter in this method, chosen to be $T_s \simeq \frac{\pi}{2\omega_{n,max}}$. [84]

3.5.2 Least Squares Curve Fit

The least–squares curve fit method (LSCF) is another approach that has been used to identify the frequencies and damping coefficients of an aeroelastic response. It is assumed that the transient response of the system consists of a linear combination of damped harmonic responses given by Eq. (3.32).

$$\tilde{w}(t) = a_0 + \sum_{i=1}^{N_m} e^{\zeta_i \omega_i t} \left[a_i \cos\left(\omega_{di} t\right) + b_i \sin\left(\omega_{di} t\right) \right] \tag{3.32}$$

The frequencies and damping are calculated by minimizing the squared error between the aeroelastic transient response and the expression in Eq. (3.32). The resulting minimization problem is given in Eq. (3.33).

$$\min_{\omega_i, \zeta_i, a_i, b_i} \left(\sum_{k=1,N_t} \left[w_k - \tilde{w}(t_k) \right]^2 \right) \tag{3.33}$$

In the current implementation, it is solved using two to five iterations of the FMINCON function available in MATLAB. The solution of this highly nonlinear optimization problem

is expensive and sensitive to the initial guess of the different variables. However error estimates of the approximation are available and convergence of the fit can be assessed.

3.5.3 p–Method

The p–method is a well–known approach for determining the stability of a linear aeroelastic system [101, 151]. It requires that the generalized loads to be a known function of the generalized degrees of freedom and their time derivatives, as given in Eq. (3.34).

$$\boldsymbol{Q}\left(t, \boldsymbol{q}, \dot{\boldsymbol{q}}, \ddot{\boldsymbol{q}}\right) = \mathbf{M_A}\ddot{\boldsymbol{q}} + \mathbf{C_A}\dot{\boldsymbol{q}} + \mathbf{K_A}\boldsymbol{q} \tag{3.34}$$

To determine the stability of the system, the EOM given in Eq. (3.6) are combined with Eq. (3.34). The solution is assumed in the form of $\boldsymbol{q} = \boldsymbol{q}_0 e^{pt}$, which yields the flutter equation, Eq. (3.35).

$$\left\{\left(\mathbf{M} - \mathbf{M_A}\right)p^2 - \mathbf{C_A}p + \mathbf{K} - \mathbf{K_A}\right\}\boldsymbol{q}_0 = 0 \tag{3.35}$$

Solutions of the flutter equation are obtained for values of p that satisfy the characteristic equation of the aeroelastic system given by Eq. (3.36).

$$\det\left[\left(\mathbf{M} - \mathbf{M_A}\right)p^2 - \mathbf{C_A}p + \mathbf{K} - \mathbf{K_A}\right] = 0 \tag{3.36}$$

The frequencies and damping of the aeroelastic system are given by the roots, p_i, of Eq. (3.36). The frequencies and corresponding damping coefficients are uniquely identified by the real and imaginary parts of p_i, Eq. (3.37).

$$p_i = \zeta_i\omega_i + \boldsymbol{i}\omega_{di} \tag{3.37}$$

When the aerodynamic loads are computed using unsteady CFD, the analytical form given by Eq.(3.34) is not available. However, at each time step the generalized degrees of

freedom and generalized loads are calculated and are stored as represented in Eq. (3.38).

$$\left\{ \begin{array}{c} \boldsymbol{q}_1 \\ \dot{\boldsymbol{q}}_1 \\ \vdots \\ \boldsymbol{q}_{N_t} \\ \dot{\boldsymbol{q}}_{N_t} \end{array} \right\} \quad \text{and} \quad \left\{ \begin{array}{c} \boldsymbol{Q}_1 \\ \vdots \\ \boldsymbol{Q}_{N_t} \end{array} \right\} \tag{3.38}$$

Therefore the relation between the $\boldsymbol{Q}$ and the $\boldsymbol{q}, \dot{\boldsymbol{q}}, \ddot{\boldsymbol{q}}$ can be approximated in the form given by Eq.(3.34).

At this point, note that PT is a quasi static formulation of the relation between the deformation and unsteady pressure loading as presented briefly in Section. 3.3.2 and in details in Appendix C. In addition it agrees well with CFD in previous studies. Therefore, it is assumed that $\mathbf{M_A}$ is negligible in the relation between aerodynamic loading and deformation. It yields Eq. (3.39).

$$\boldsymbol{Q}\left(t, \boldsymbol{q}, \dot{\boldsymbol{q}}, \ddot{\boldsymbol{q}}\right) \simeq \mathbf{C_A}\dot{\boldsymbol{q}} + \mathbf{K_A}\boldsymbol{q} \tag{3.39}$$

A linear least squares fit is used to estimate the aerodynamic influence matrices. The estimates of the aerodynamic stiffness and damping matrices are given by solving the least squares problem stated in Eq. (3.40).

$$\min_{\hat{K}_{Aij}, \hat{C}_{Aij}} \left(\sum_{k=1,N_t} \left\| \boldsymbol{Q_k} - \mathbf{C_A}\dot{\boldsymbol{q}}_{\boldsymbol{k}} - \mathbf{K_A}\boldsymbol{q_k} \right\|^2 \right) \tag{3.40}$$

The solution is obtained using a linear least squares approach [145] and given in Eq. (3.41).

$$\left[\hat{\mathbf{K}}_{\mathbf{A}}, \hat{\mathbf{C}}_{\mathbf{A}}\right]^T = \left(\mathbf{X}^T\mathbf{X}\right)^{-1}\mathbf{X}^T\mathbf{Q} \quad \text{where } \mathbf{X} = \begin{bmatrix} \boldsymbol{q}_1 & \cdots & \boldsymbol{q}_{N_t} \\ \dot{\boldsymbol{q}}_1 & \cdots & \dot{\boldsymbol{q}}_{N_t} \end{bmatrix}^T \quad \text{and} \quad \boldsymbol{Q} = \begin{bmatrix} \boldsymbol{Q}_1^T \\ \vdots \\ \boldsymbol{Q}_{N_t}^T \end{bmatrix} \tag{3.41}$$

This method uses the generalized loads and takes full advantage of all the information available in the computational framework. Both previous methods used only the deformation at one or several points. Note that for a perfectly linear system, the frequencies and damping coefficients are recovered.

3.6 The CFD++ Code, its Description and Application

3.6.1 Overview of the CFD++ Code

The CFD++ code is a modern and effective commercially available for solution of the compressible unsteady Reynolds-averaged Navier-Stokes (RANS) equations [152].

It uses a unified grid methodology that can handle a variety of grids including structured, unstructured, multi-block meshes and cell types, including patched and overset grid features. It treats all meshes as unstructured.

Spatial discretization of the Navier-Stokes equations is based on a second order multi–dimensional Total Variation Diminishing (TVD) scheme. For temporal discretization a point–implicit algorithm with dual time-stepping and multigrid acceleration is used. Dual time–stepping schemes are constructed by appending a pseudo time-derivative term to the Navier–Stokes equations. The pseudo time-derivative term is solved using sub–iterations for improved accuracy. The CFD code is Message Passing Interface (MPI) compatible, allowing the user to perform computations on multiple CPU clusters.

The multigrid acceleration scheme uses levels of grid coarsening to increase the speed

of the simulation. Several turbulence models are available in CFD++, ranging from 1-equation to 3-equation transport models.

The CFD++ code is capable of accounting for different gas models. The simpler one are perfect gas and ideal gas. Chemistry can be incorporated by providing the list of species and reaction rates of the chemical reactions. Therefore the CFD++ code is a suitable candidate for this study.

3.6.2 Turbulence Modeling with Spalart–Allmaras Turbulence Model

The Spalart Allmaras turbulence model (SA) is viewed as reasonable one–equation model for hypersonic flows [153, 154] and is the one used for the aeroelastic calculations presented in this work. It was also the one used in the previous work performed using the NASA Langley CFL3D computational aeroelastic code (CFL3D) [84, 149], which is used as comparison. Details of the implementation are given here to highlight the main differences between CFD++ and CFL3D.

It is implementation in CFD++ can be found in Ref. [152] and described in details in this section. The dependent variable is the eddy viscosity, ν_t, which is related directly to Reynolds stress as given by Eq. (3.42).

$$-\overline{u_i' u_j'} = \nu_t \left(\frac{\partial u_i}{\partial x_j} + \frac{\partial u_j}{\partial x_i} - \frac{2}{3} \frac{\partial u_k}{\partial x_k} \delta_{ij} \right) \tag{3.42}$$

The eddy viscosity is formulated using $\tilde{\nu}$ defined by:

$$\nu_t = \tilde{\nu} f_{v1} \quad \text{where} \quad f_{v1} = \frac{\chi^3}{\chi^3 + c_{v1}^3} \quad \text{and} \quad \chi \equiv \frac{\tilde{\nu}}{\nu} \tag{3.43}$$

The dynamic of $\tilde{\nu}$ is dictated by the transport equation given in Eq. (3.44).

$$\begin{aligned}\frac{D\tilde{\nu}}{Dt} &= \frac{\partial\tilde{\nu}}{\partial t} + (\boldsymbol{u}\cdot\nabla)\,\tilde{\nu} \\ &= c_{b1}f_{r1}\,(1-f_{t2})\,\tilde{S}\tilde{\nu} + \frac{1}{\sigma}\left[\nabla\cdot\left((\nu+\tilde{\nu})\,\nabla\tilde{\nu}\right) + c_{b2}\,(\nabla\tilde{\nu})^2\right] - \\ &\quad \left[c_{w1}f_w - \frac{c_{b1}}{\kappa^2}f_{t2}\right]\left(\frac{\tilde{\nu}}{d}\right)^2 \qquad (3.44)\end{aligned}$$

(3.45)

$$\mu_t = \rho\nu_t f_{v1} \quad \text{where} \quad f_{v1} = \frac{\chi^3}{\chi^3 + c_{v1}^3} \quad \text{and} \quad \chi = \frac{\nu_t}{\nu} \qquad (3.46)$$

where ρ is the density, $\nu = \frac{\mu}{\rho}$ is the kinematic viscosity. In addition:

$$\tilde{S} \equiv S + \frac{\nu}{\kappa^2 d^2}f_{v2} \quad f_{v2} = 1 - \frac{\chi}{1+\chi f_{v1}} \qquad (3.47)$$

$$f_w = g\left(\frac{1+c_{w3}^6}{g^6+c_{w3}^6}\right)^{\frac{1}{6}} \quad \text{where} \quad g = r\left[1+c_{w2}\left(r^5-1\right)\right] \quad \text{where} \quad r = \frac{\tilde{\nu}}{\tilde{S}\kappa^2 d^2} < 10 \qquad (3.48)$$

$$f_{t2} = c_{t3}\exp\left(-c_{t4}\chi^4\right) \qquad (3.49)$$

$$\sigma = \frac{2}{3} \quad c_{b1} = 0.1355 \quad c_{b2} = 0.6220 \quad \frac{1+c_{b2}}{\sigma} \approx 2.4 \qquad (3.50)$$

$$c_{w1} = \frac{c_{b1}}{\kappa^2} + \frac{(1+c_{b2})}{\sigma} \qquad (3.51)$$

f_{r1} is a complicated function of the Reynolds stresses and vorticity to account for rotation and curvature effects. This term is given in Eq. 3.52 but is not present in the CFL3D

implementation of the SA model.

$$f_{r1} = (1 + c_{r1}) \frac{2r^*}{1 + r^*} \left[1 - c_{r3} \tan^{-1}\left(c_{r2}\tilde{r}\right)\right] - c_{r1} \tag{3.52}$$

The constants are:

Table 3.1: Constants and BCs for the Spalart–Allmaras turbulence model

	c_{b1}	σ	c_{b2}	κ	c_{w2}	c_{w3}	c_{v1}	c_{t3}	c_{t4}	$\frac{\nu_{t\infty}}{\nu_\infty}$	$\nu_{t\ wall}$
CFL3D v.5	0.1355	2/3	0.622	0.41	0.3	2	7.1	*1.2*	*0.5*	$\simeq 0.009$	0
CFL3D v.6	0.1355	2/3	0.622	0.41	0.3	2	7.1	*1.2*	*0.5*	user input	0
CFD++	0.1355	2/3	0.622	0.41	0.3	2	7.1	*1.1*	*2*	$[3,\ 5]$	0

Comparing CFL3D and CFD++, most of the constants are equals except c_{t3} and c_{t4}. The main difference between both implementations is in the treatment of the free stream boundary. In CFL3D, the dependent variable is set to a much lower value compared to the range to be considered in CFD++. Therefore, the boundary layer is different and the pressure distribution at the surface of the wing is affected. This difference can affect the aeroelastic and aerothermoelastic predictions.

3.6.3 The Algebraic Transition Prediction Model

Transition prediction is an active area of research. Modeling the mechanism of transition is under development. In addition, predicting the exact location of transition requires information that is often assumed in a computational framework such as fluctuations in the free stream or surface properties (temperature, roughness, ...) [152]. In particular, transition prediction models [155] are sensitive to free–stream/inflow turbulence levels. If the levels of turbulence are too low, the flow remains laminar, if they are high, transition occurs further upstream. Unfortunately, these quantities are rarely known, making it difficult to predict deterministically transition.

In CFD++, several transition models exist. The simplest model is an extension of the

k–ϵ model by modifying the source terms in both the k– and ϵ– transport equations. It is based on modifying the generation term, applied to both $k-$ and $\epsilon-$ transport equations. The modification is based on a correlation using the parameter $\frac{k\otimes}{\nu S^2}$ where k is turbulence kinetic energy, $\otimes$ is mean vorticity magnitude, ν is molecular kinematic viscosity and S is mean strain magnitude. It provides a measure for the magnitude of the turbulence in the flow and serves as a trigger for generating turbulent flows.

3.6.4 Perfect Gas and Real Gas Modeling

Solving the Navier–Stokes equations for hypersonic flow is computationally expensive. However, the benefit is that the computed flow over the structure can account for high temperature effects. Two convenient models of the fluid are available: perfect (PG) and thermally imperfect or ideal (IG) gas, and provided in Table 3.2. Chemical reactions can also be incorporated to account for the dissociation of molecules at high temperatures, for this case the model is referred to as real gas (RG).

	Perfect Gas (PG)	Ideal Gas (IG)
Equation of state	$P = \rho RT$	
Internal energy	$\partial e_a = c_v \partial T$	$\partial e_a = c_v\left(T\right)\partial T$
Enthalpy	$\partial h_a = c_P \partial T$	$\partial h_a = c_P\left(T\right)\partial T$
γ	$\gamma = constant$	$\gamma\left(T\right)$

Table 3.2: Perfect and Ideal gas models

For both perfect gas (PG) and ideal gas (IG) gas models, the fluid is modeled by a single specie and there is no chemical reaction. Pressure, temperature, and density are related by the same equation of state. In the perfect gas model, the specific heats are constant. Therefore internal energy, e_a, and enthalpy, h_a, are linear functions of temperature. The specific heat ratio, $\gamma = \frac{c_p}{c_v}$ is constant and assumed to be equal to 1.4. Under these assumptions, limitations of the model manifest themselves at high speed. The compression ratio $\frac{\rho_0}{\rho_\infty}$ is artificially limited to be below 6 and stagnation temperature is unrealistically high. Thus,

this model is often deemed to be inadequate for hypersonic high altitude flight or reentry problems where high gas temperatures are accompanied by non–equilibrium flows [7].

For ideal gas, specific heats are not constant with temperature, as shown by the expression of internal energy and enthalpy in Table 3.2. Similarly γ is a function of temperature. Polynomial fitting using experimental data can estimate the internal energy and enthalpy of air as functions of temperature. In ideal gas, the compression ratio can increase up to 20 and produce a significant reduction in the stagnation temperature when compared to perfect gas prediction.

Real gas effects are incorporated by considering a multi–species gas. The Navier Stokes (NS) equations are complemented by the transport equations of each additional species. The user provides the list of species and the reaction rates of the chemical reactions that need to be accounted for. The reaction properties are a user input and allows to account for increased complexity of the fluid: one specie to multiple species, equilibrium or non–equilibrium flow.

The real gas (RG) model considered is taken from Ref. [156], and is given in Table 3.3. It contains 5 species and 8 reactions to account for the dissociation of O_2, N_2, and NO. Chemical equilibrium is assumed and there is no ionization. For each reaction, the reaction constant is given by $k = A_r T^{\eta} \exp\left(-\frac{E_a}{RT}\right)$.

Table 3.3: Reactions

Reactions	η	$A_r\ (cm^3/mol)$	$\frac{E_a}{R}\ (K)$	
$O_2 + M \rightarrow 2O + M$	-1.50	2.0×10^{21}	59500	$M = N_2,\ O_2,\ NO$
$O_2 + M \rightarrow 2O + M$	-1.50	1.0×10^{22}	59500	$M = N,\ O$
$N_2 + M \rightarrow 2N + M$	-1.60	7.0×10^{21}	113200	$M = N_2,\ O_2,\ NO$
$N_2 + M \rightarrow 2N + M$	-1.60	3.0×10^{22}	113200	$M = N,\ O$
$NO + M \rightarrow N + O + M$	0.00	5.0×10^{15}	75500	$M = N_2,\ O_2,\ NO$
$NO + M \rightarrow N + O + M$	0.00	1.1×10^{17}	75500	$M = N,\ O$
$N_2 + O \rightarrow NO + N$	-1.00	6.4×10^{17}	38400	
$NO + O \rightarrow O_2 + N$	0.00	8.4×10^{12}	19450	

3.6.5 Meshing strategy

The computational grids used in this study are generated using the ANSYS ICEM CFD meshing software. The software produces as output the grid files in the plot3D format which is compatible with the CFD++ code. However, for the three dimensional (3D) meshes, significant rounding error and discrepancies were present close to the leading and trailing edges, and wing tips. Therefore the meshes had to be pre–processed using a MATLAB script to realigned the nodes at the surface of the wing and ensure that the grid are perfectly symmetric with respect to the (x,y) plane.

Hypersonic flows require a small computational domain compared to subsonic flows. The information in air travels in the fluid at the speed of sound. Consequently, information coming from the outer boundary of the fluid domain only affects a limited portion of the flow, called the zone of influence determined by the local Mach number. Therefore, the inflow boundary of the computational domain can be close to the leading edge of the structure. The outflow boundary is located close to the structure as well. However the boundary layer should have sufficient time to return to supersonic flow before exiting the fluid domain. Finally shocks, such as leading edges shock, should be allowed to exit the computational domain without being perturbed. Therefore, characteristic–based boundary conditions are used for any boundary that is not the inflow.

As a result of these constrains, the computational domain is relatively small when compared to subsonic calculations and extends about 10 cells in front of the structure and about 2 chord length between the surface of the structure and the outflow and far field boundaries. The grids are clustered at the airfoil wall boundaries such that the dimensionless distance of the first grid point from the boundary, given by $y^+ = \frac{y\sqrt{\tau_w}}{\mu\sqrt{\rho}}$, is maintained below 1 and the turbulence equations are directly solved at the wall without assuming any wall functions. The dimension of the first cell normal to the surface of the structure is of the order of 10^{-6} to 10^{-5} m and the expansion rate is between 1.1 and 1.2. Close to the discontinuities present in the flow due to shocks or expansion fans, the aspect ratio of the cells is kept close

to 1. In the case of the low aspect ratio wing, the mesh is very fine at the vicinity of the leading and trailing edges, wing tip and mid–chord.

When considering deforming meshes, two strategies are considered: fixed outer boundary or fully moving mesh. In both cases, cell entanglement can occur. Yet it less likely when there is no constraint on the outer boundary of the fluid domain. The CFD++ code allows for moving outer boundaries. Constraining the outer boundary to be fixed may be required by the solver such as in CFL3D. In this case, the fluid domain is extended by about a chord length or two in front of the leading edge to allow for a smooth mesh deformation. In this work, different strategies are investigated in the aeroelastic stability of a two dimensional (2D) typical section. For the 3D low aspect ratio wing, an extended mesh provided also better mesh quality than a triangular mesh when using ICEM CFD.

CHAPTER 4

UNCERTAINTY PROPAGATION IN THE AEROELASTIC STABILITY OF A TYPICAL SECTION

The aeroelastic stability of a typical section in hypersonic flow is studied using the uncertainty quantification (UQ) framework. This represents the first example for propagating uncertainty in hypersonic aeroelasticity. Uncertainty is incorporated in the uncoupled natural frequencies. The performance of several response surface methods are compared.

4.1 Description of the Aeroelastic Problem

The flutter Mach number for a double wedge typical section representative of a control surface of a hypersonic vehicle is examined to illustrate the usage and performance of various UQ approaches. The typical section, shown in Fig. 4.1, is characterized by pitch (α) and plunge (h) degrees of freedom. This problem was treated deterministically in Ref. [2].

For this problem, the equations of motion given in Eq. (4.1), are obtained using Lagrange's equations assuming small deflections and no structural damping. The aerodynamic loading is obtained from 3^{rd} order PT given by Eq. (3.19).

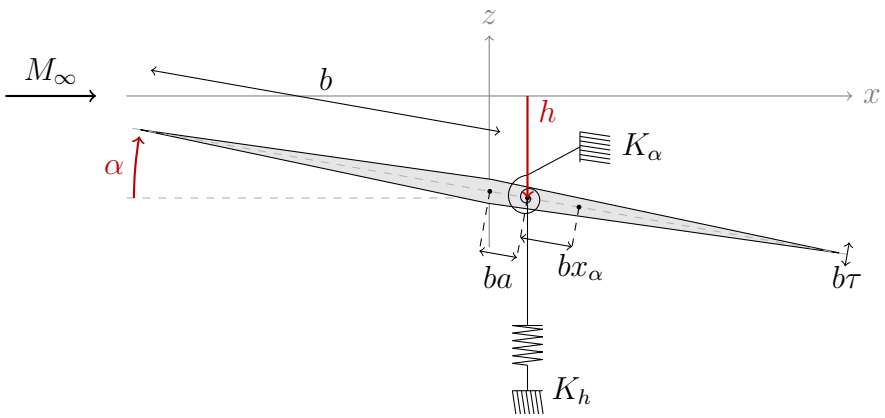

Figure 4.1: Two degree-of-freedom typical section geometry

$$\begin{bmatrix} m & S_\alpha \\ S_\alpha & I_\alpha \end{bmatrix} \begin{Bmatrix} \ddot{h} \\ \ddot{\alpha} \end{Bmatrix} + \begin{bmatrix} K_h & 0 \\ 0 & K_\alpha \end{bmatrix} \begin{Bmatrix} h \\ \alpha \end{Bmatrix} = \begin{Bmatrix} -L \\ M_{ea} \end{Bmatrix} \tag{4.1}$$

As the free stream Mach number increases, flutter ensues and the flutter Mach number M_f corresponds to zero damping in one of the two modes of the aeroelastic system. The output of interest is the flutter Mach number, M_f. In the probabilistic approach, the probability that the flutter Mach number is less than some fraction of the deterministic prediction as given by Eq. (4.2), is quantified. In this example, the value of $\beta = 85\%$ is assumed to be an acceptable limit for flutter Mach number. It corresponds to an aeroelastic stability margin of 15%.

$$p_f(\beta) = p(M_f < \beta M_{fd}) \tag{4.2}$$

The variability is introduced in the uncoupled natural frequencies, ω_α and ω_h, to account for uncertainty due to potential changes in frequencies due to aerodynamic heating. Therefore, the output of interest for this problem is a function of two uncertain inputs, denoted $\Delta\omega_h$ and $\Delta\omega_\alpha$, which correspond to the variations in natural frequencies. The aeroelastic stability is determined using a damping identification method known as the ARMA model [84]. Damping is extracted from the transient response of the system. The flutter

Mach number M_f depends also on the offset a between the elastic axis and the mid-chord.

For the results presented, it is important to note that the altitude (H = 12 km) at which the aeroelastic studies are conducted is not realistic of hypersonic flight. However more realistic altitudes of 25–30 km would yield very high Mach numbers. Therefore the altitude is artificially reduced in order to obtain more practical values. However, as pointed out in Ref. [2], incorporation of aerodynamic heating leads to a reduction of the flutter Mach number, and thus aerothermoelastic studies which account for the effects of heat transfer will produce operating altitudes and Mach numbers more representative of hypersonic vehicle operating regime; this approach is implemented in the later sections of this study.

4.2 Uncertainty Propagation Results

The system is represented by the parameters given in Table 4.1, taken from Ref. [2]. As indicated in Ref. [157], changes in frequencies are considered to be representative of the combined effects of material degradation and thermal stresses that occur in a heated structure. The bending frequency increases as the structure heats up, the torsional frequency decreases [157]. The range of variation of the bending and torsional frequencies observed for typical trajectories of a airbreathing hypersonic vehicle are $[-3\%,\ +14\%]$ and $[-30\%,\ +0\%]$ respectively [157]; and these where selected as representative values. The respective probability distribution is chosen to be uniform as summarized in Table. 4.2. In all results, the 95% confidence interval for the flutter Mach number and minimum and maximum values are obtained by conducting 50000 Monte Carlo simulations on the approximate problem represented by the response surface.

The selection of the degree of the polynomial required for the SC expansion is based on a convergence study. In the convergence study, a and H are fixed at 0.0 and 12 km respectively. The mean and the variance associated with the flutter Mach number obtained from polynomial expansion up to 10^{th} order are compared to results obtained from a 15^{th}

Table 4.1: Baseline configuration for the typical section

Parameter	Value	Units
H	[12 30]	km
a	[-0.4 0.4]	N/A
c	2.35	m
τ	3.36	%
x_α	0.2	N/A
ω_h	13.4	Hz
ω_α	37.6	Hz

Table 4.2: Uncertain parameters associated with the 2D typical section

Parameter	Range	Distribution
ω_h	[-3% +14%]	Uniform
ω_α	[-30% +0%]	Uniform

order expansion based on $(15+1)^2 = 256$ analysis evaluations. The relative errors associated with the mean and standard deviation are shown in Fig. 4.2. Furthermore, the accuracy of the various polynomial expansions is quantified by comparing the response surface predictions with the exact values obtained for a 16 by 16 cartesian uniform grid spanning the uncertain variables space. For the corresponding 256-points set, maximum and sum of squares (L_2) relative errors between the computed value and the response surface prediction is shown in Fig. 4.3. The maximum error is close to the expected accuracy of the analysis for a response surface based on a 6^{th} order expansion (i.e. 49 collocation points). The converged response surface is depicted in Fig. 4.3(a). The local error of the response surface is of the order of 10^{-5} % and its distribution is given in Fig. 4.3(b). In both figures, the black dots indicate the collocation points and the black line shows the value of $0.85M_{fd}$.

For comparison, other response surface approximations are considered: polynomial chaos expansion (PCE) and kriging surrogate (KG). The convergence of the different methods are compared in Figs 4.4(a) and 4.4(b) for the L_∞ and L_2 norms, respectively. The three

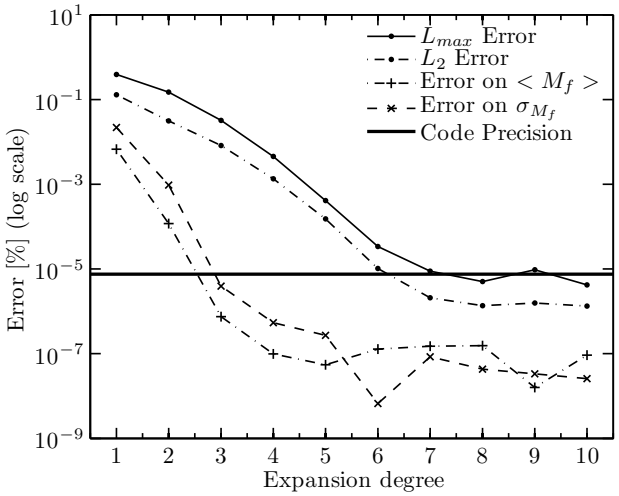

Figure 4.2: Convergence study for SC method, a = 0, H = 12 km

response surfaces are constructed using the same collocation points. Note that PCE agrees perfectly with SC, which is expected since both correspond to polynomial approximations of the function. The KG gives a good approximation to the analysis but is outperformed by SC and PCE in this case.

Detailed results are given in Table 4.3 for SC, PCE and KG using numerical quadrature points as collocation points. It shows perfect agreement between the three different response surfaces. Note that the same 50000 LHS points are used to perform the IMCS for the three approaches. If it were not the case, small differences ($\sim .1\%$) would be present in the estimation of the 95% CI and probability of failure. Such differences would be explained by the difficulty associated with the estimation of statistical quantities using random point generators, even for a very large number of random points.

The expected feasibility function (EFF) approaches are also considered to compare the performance of adaptive methods to SC, PCE and KG for this aeroelastic study. Adaptive sampling is based on either the EFF (KG-EFF) or the proposed $\widetilde{EFF}$ (KG-$\widetilde{EFF}$). The first one stops after 10–11 function evaluations but yields errors in the approximation of the CI or maximum and minimum values of the flutter Mach number. The second approach converges after 35 evaluations and compares well with the first three methods considered.

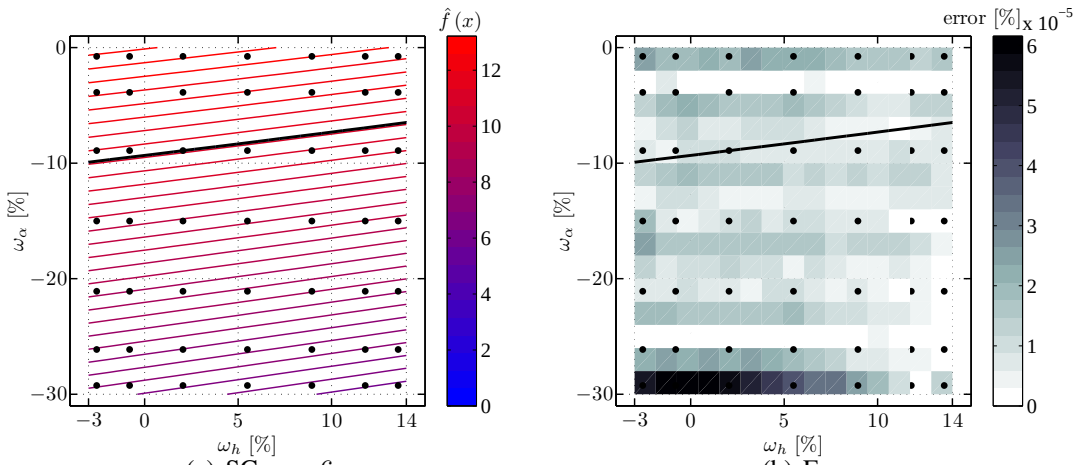

(a) SC, $p = 6$ (b) Error

Figure 4.3: SC response surface, a = 0, H = 12 km

Both response surfaces and sampling points distributions are illustrated in Figs. 4.5(a) and 4.5(b) respectively, together with their errors shown in Figs. 4.5(c) and 4.5(d). In both cases, the limit y_{lim} is accurately captured. Note that the errors are of the order of 0.1 and 10^{-4}% for the KG-EFF and KG-$\widetilde{EFF}$ response surfaces, respectively. The KG-EFF response surface is accurate only at the vicinity of the limit state. In comparison, the KG-$\widetilde{EFF}$ response surface is accurate over the entire range of the uncertain variables and the sampling points are evenly distributed as dictated by their uniform PDF.

Similar convergence is found for all the combinations of altitude and elastic axis offset considered in this study. Therefore, the 6^{th} order polynomial expansions are used for generating the results corresponding to various values for the elastic axis offset a and the altitude H. Note that certain parameters associated with the analysis had to be modified in order to obtain reliable results when propagating uncertainty: the time step is divided by 2 and the simulated time is increased by a factor of 5 compared to that used in the deterministic calculations. These modifications are necessary to allow the ARMA method to identify both frequencies and damping coefficients in the transient response, particularly when ω_h and ω_α are close to each other.

Uncertainties associated with the pitch and plunge natural frequencies are propagated

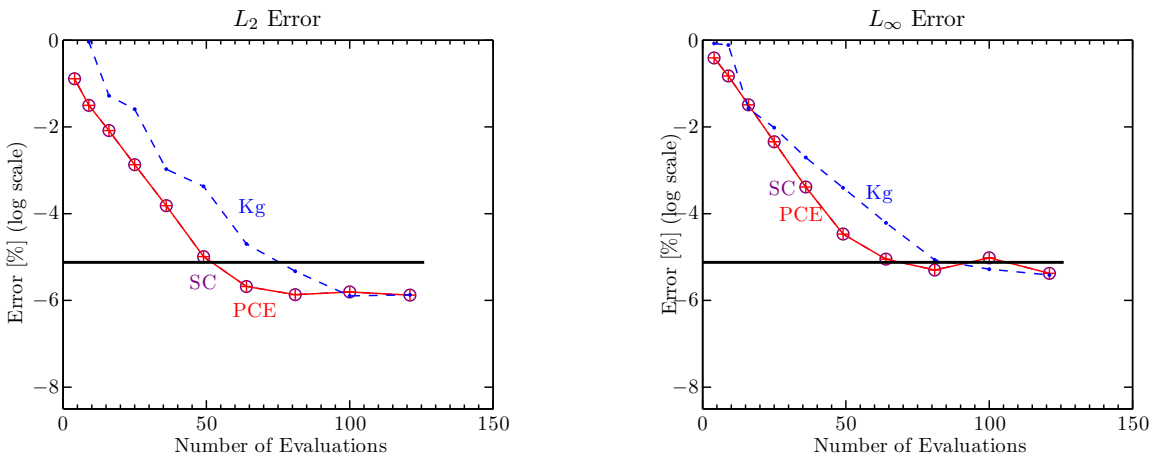

(a) Convergence of L_2 (b) Convergence of L_∞

Figure 4.4: Convergence study for different UQ methods, $a = 0$, $H = 12$ km

to the flutter Mach number using a 6^{th} order polynomial response surface generated by stochastic collocation. The results are depicted in Figs. 4.6(a) and 4.6(b) and summarized in Table. 4.4. In both figures, the deterministic flutter Mach number, represented by a thick line and diamond symbols, is compared to the mean in flutter Mach numbers due to the uncertainties. The expected value of flutter Mach number is depicted using the crosses. Furthermore, an interval likely to include the flutter Mach number with 95% confidence (95% CI) is represented by a shaded area. The dashed and dash–dot lines corresponds to the minimum and maximum values, respectively. The 15% margin in flutter Mach number is represented by the plain line with the dots.

In Fig. 4.6(a), the elastic axis offset, a, varies from -0.4 to 0.4 and the altitude is constant at 12 km. The results show that the maximum flutter Mach number is close to the deterministic value. Recall that the baseline analysis does not correspond to the mean values of the uncertain parameters but to $\Delta\omega_h = 0$ and $\Delta\omega_\alpha = 0$ which are close to the bounds of the uncertain parameters interval. The mean of $\Delta\omega_h$ and $\Delta\omega_\alpha$ correspond to a modification of ω_h and ω_α by +11.5% and -15% respectively. As a result of uncertainty modeling for the probabilistic case, the natural frequencies are closer to each other for 99.7% of the cases when compared to the deterministic analysis; ω_h increases and ω_α decreases. It yields a

Table 4.3: Flutter Mach number variability predicted by 3 different response surfaces, H = 12 km

	Method	N_s	$\langle M_f \rangle$	σ_{M_f}	$[M_{fmin}\ M_{fmax}]$	95% CI	p_f
$a = -0.4$	SC	49	18.2	2.6	[12.5 23]	[13.6 22.4]	0.623
	PCE	49	18.2	2.6	[12.5 23]	[13.6 22.4]	0.623
	KG	49	18.2	2.6	[12.5 23]	[13.6 22.4]	0.623
	KG-EFF	9	18.2	2.57	[12.5 23]	[13.8 22.4]	0.622
	KG-$\widetilde{EFF}$	35	18.2	2.6	[12.5 23]	[13.6 22.4]	0.623
$a = 0$	SC	49	9.75	1.93	[5.97 13.4]	[6.52 12.9]	0.726
	PCE	49	9.75	1.93	[5.97 13.4]	[6.52 12.9]	0.726
	KG	49	9.75	1.93	[5.97 13.4]	[6.52 12.9]	0.726
	KG-EFF	10	9.75	1.93	[5.97 13.4]	[6.51 12.9]	0.726
	KG-$\widetilde{EFF}$	34	9.75	1.93	[5.97 13.4]	[6.52 12.9]	0.726
$a = 0.4$	SC	49	6.41	1.5	[3.61 9.32]	[3.98 8.93]	0.776
	PCE	49	6.41	1.5	[3.61 9.32]	[3.98 8.93]	0.776
	KG	49	6.41	1.5	[3.61 9.32]	[3.98 8.93]	0.776
	KG-EFF	11	6.41	1.5	[3.54 9.32]	[3.94 8.93]	0.776
	KG-$\widetilde{EFF}$	33	6.41	1.5	[3.61 9.32]	[3.98 8.93]	0.776

lower flutter Mach number in most cases. The standard deviation varies from 11% to 16% of the deterministic value. The 95% CI's interval varies from -61%, to +1% of the deterministic value. Similarly, the variation of the flutter Mach number with altitude is depicted in Fig. 4.6(b), the elastic axis offset is equal to 0.1. Finally, in both cases the 15% margin lies inside the interval given by the expected value and the standard deviation as well as the 95% CI which corresponds to high probability of that the flutter Mach number is less than this limit.

The probability distributions of the flutter Mach number are given in Figs. 4.7(a) to 4.7(c) for various elastic axis offsets. The bars represent the PDF and the line represents the cumulative density function (CDF) for the flutter Mach number. The deterministic value and its probability is indicated on the CDF curve by a diamond. The 15% margin is indicated by a the left–pointing triangle. It shows that there is a significant probability that the system will flutter before the value predicted based on the baseline parameters and the margin se-

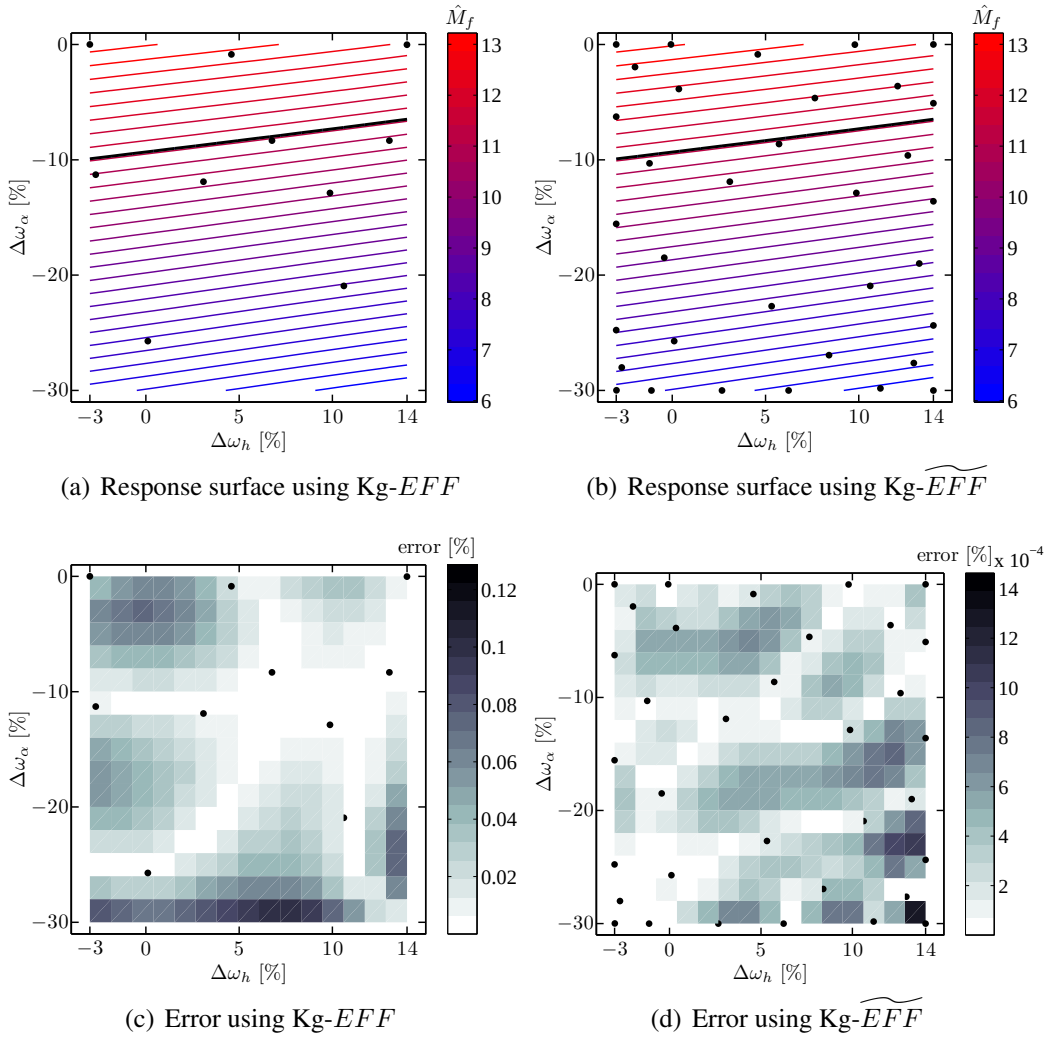

(a) Response surface using Kg-EFF

(b) Response surface using Kg-$\widetilde{EFF}$

(c) Error using Kg-EFF

(d) Error using Kg-$\widetilde{EFF}$

Figure 4.5: Response surface predicted using EFF, $a = 0$,$H = 12$ km

lected. This illustrates the significance of using non–deterministic approaches to properly quantify the uncertainty in the aeroelastic stability boundary.

Additional information is extracted from the uncertainty quantification analysis. In Fig. 4.8(a), the probability that the flutter Mach number is less than some fraction of the deterministic prediction given by Eq. (4.2) is depicted. For example, depending on the value of the elastic offset, there is a 63–78% probability that the control surface will flutter at a Mach number that is 15% less than the deterministic prediction, when assuming a PDF corresponding to Beta(1,1).

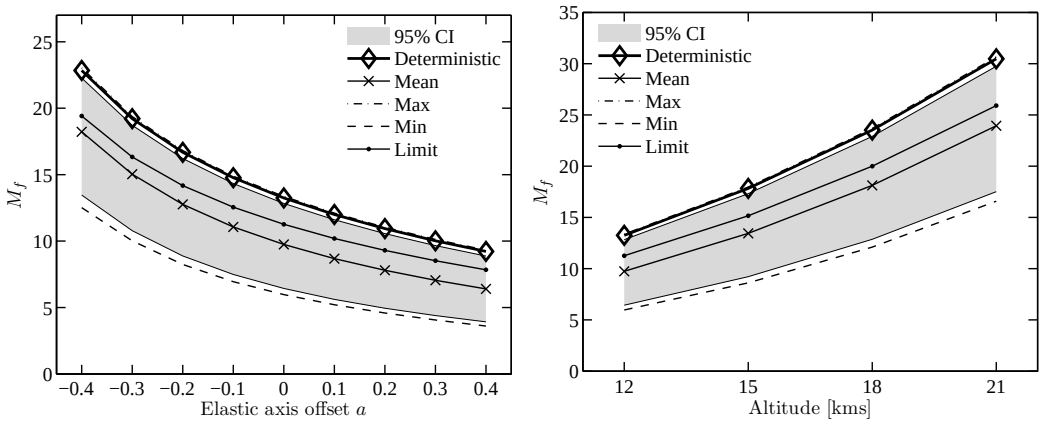

(a) H = 12 km (b) $a = 0$

Figure 4.6: Uncertainty propagation results for varying elastic axis (a) or altitude (b)

Table 4.4: Flutter Mach number variability, H = 12 km

Elastic offset	$a = -0.4$	$a = 0$	$a = 0.4$
M_f	22.84	13.25	9.22
$\langle M_f \rangle$	18.23 *(-20.17%)*	9.75 *(-26.38%)*	6.41 *(-30.46%)*
σ_{M_f}	2.60 *(11.40%)*	1.93 *(14.59%)*	1.50 *(16.26%)*
95 CI	[13.47 , 22.28]	[6.44 , 12.84]	[3.92 , 8.88]
95 CI (%)	*[-41.09 , -2.48]*	*[-51.47 , -3.15]*	*[-57.54 , -3.76]*
Range	[12.52 , 23.03]	[5.97 , 13.36]	[3.61 , 9.32]
Range (%)	*[-45.18 , 0.86]*	*[-54.92 , 0.85]*	*[-60.89 , 1.06]*

These results demonstrate that uncertain inputs can produce significant levels of variability in predicted flutter Mach numbers. By treating the problem in a probabilistic manner, more information about the flutter margin is obtained. In this particular case the deterministic analysis is inadequate since large variations in the flutter Mach number due to the assumed uncertainties are evident.

The effect of the input probability distribution shape of the random inputs on the stochastic output probability distribution is also considered. The range for the frequencies is unchanged. Both $\Delta\omega_h$ and $\Delta\omega_\alpha$ have the identical probability distributions for all cases shown in Figs. 4.8 and 4.9. The results illustrate the effect of the probability distribution in the input, as illustrated by Figs. 4.8(b) through 4.8(d) and Figs. 4.9(b) through 4.9(a). The choice

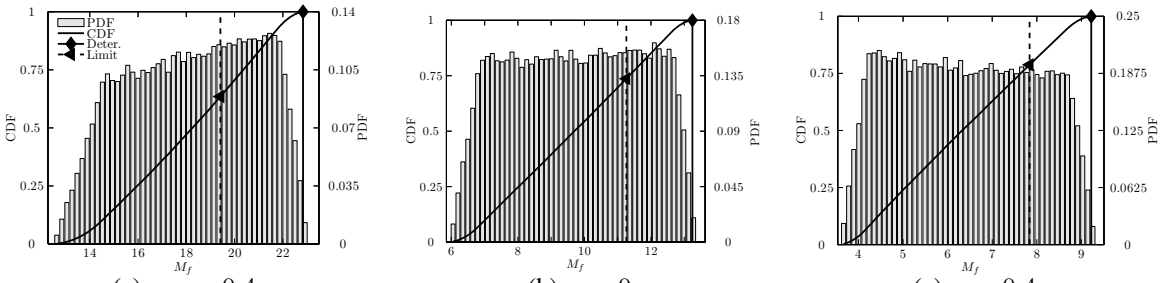

(a) $a = -0.4$ (b) $a = 0$ (c) $a = 0.4$

Figure 4.7: Flutter Mach number PDF prediction using a 6^{th} order polynomial expansion in SC, H = 12 km

of input probability distribution affects all the stochastic analysis quantities i.e. mean or expected value, standard deviation, 95% CI and probability of failure. As expected, maximum and minimum are not modified since the ranges of the uncertain inputs are the same. In all cases, the CI is reduced. This behavior is a result of the monotonic relation between the inputs and output as well as the shape of the probability distributions chosen for the inputs. All three distributions give more probability to the interior of the domain. Therefore the CI of the inputs is smaller resulting in a smaller CI for the output. In addition, the CI of the flutter Mach number moves closer to the maximum in the case of Beta(3,2) and closer to the minimum in the case of Beta(2,3). In fact, the Beta(2,3) distribution gives more probability to the lower values of the frequencies compared to Beta(3,2). Therefore there is more probability given to the lower Mach numbers. This behavior illustrates that the statistical results should be interpreted in the context of the assumptions made regarding the uncertainty of the inputs. [158]

4.3 Sobol's Sensitivities results

The sensitivity analysis presented in Section 2.3 illustrates the effect of the probability distributions. The results are shown in Table. 4.5. The variances associated with the frequency alone, D_{ω_α} and D_{ω_h} are smaller by a factor of 2 for beta distributions than that for the uni-

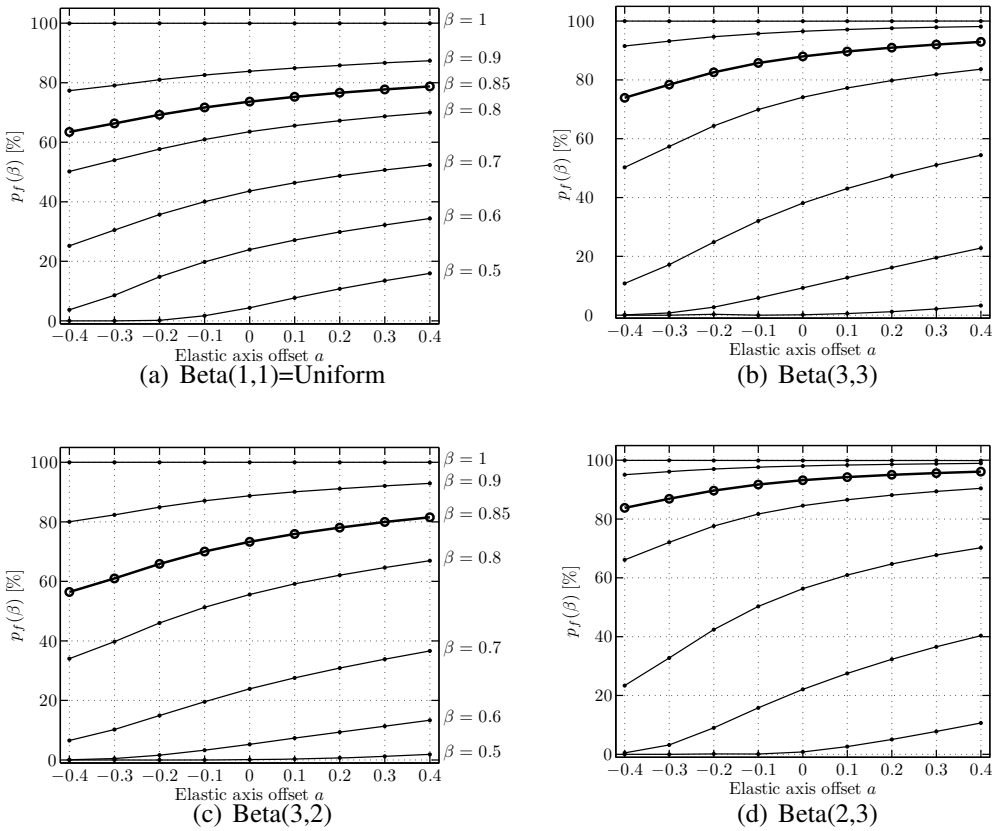

(a) Beta(1,1)=Uniform (b) Beta(3,3)

(c) Beta(3,2) (d) Beta(2,3)

Figure 4.8: $p_f\,(\beta)$ for different inputs probability distributions, H = 12 km

form distribution. This is due to the fact that non–uniform beta distributions have smaller variances than uniform PDF, and propagate through the analysis accordingly. In all cases, the stronger dependencies are observed for the pitching frequency. Two effects add up: the flutter Mach number is more sensitive to ω_α and the range of variation of ω_α is larger than that of ω_h. The effect of the interaction between the two variables is negligible. The effect of the elastic axis location is also negligible as shown in Figs. 4.10 and 4.11. The effect of altitude is also negligible, as illustrated in Fig. 4.12.

This simple problem illustrates the results that can be obtained using the UQ framework. Next a more complex problem is considered.

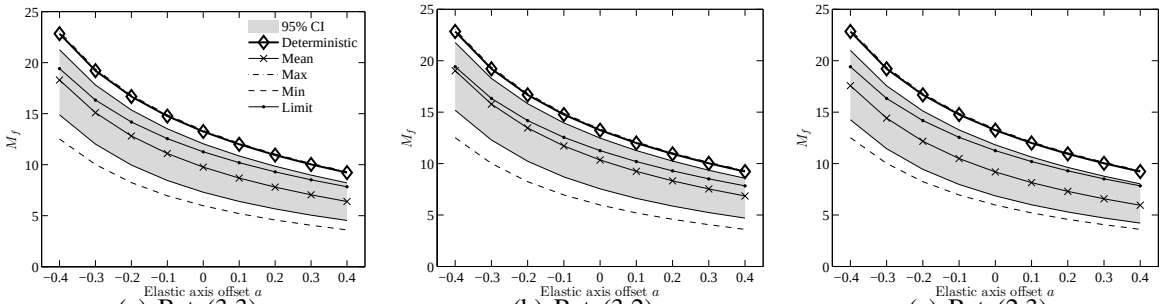

(a) Beta(3,3) (b) Beta(3,2) (c) Beta(2,3)

Figure 4.9: Uncertainty propagation results for different input probability distribution, H = 12 km

Table 4.5: Sobol Sensitivities , $a = 0$, H = 12 km

PDF	D			S [%]		
	ω_h	ω_α	$\omega_h\omega_\alpha$	ω_h	ω_α	$\omega_h\omega_\alpha$
Uniform	0.05	3.66	0.00	1.43	98.56	0.01
Beta(3,3)	0.02	1.58	0.00	1.45	98.55	0.00
Beta(3,2)	0.02	1.76	0.00	1.39	98.61	0.01
Beta(2,3)	0.03	1.77	0.00	1.50	98.49	0.00

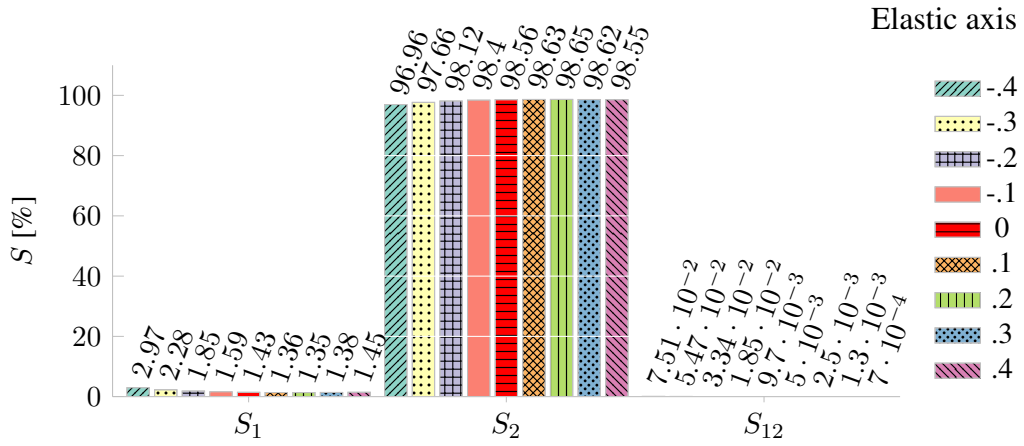

(a) Uniform

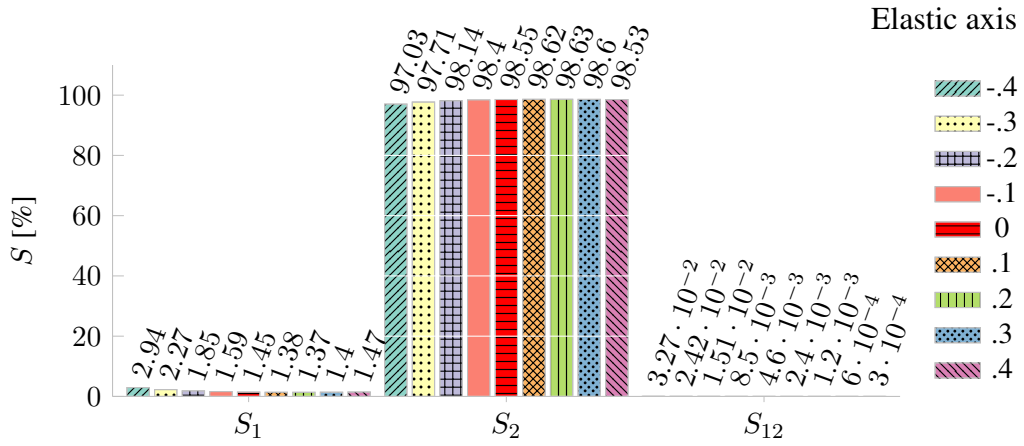

(b) Beta(3,3)

Figure 4.10: Sobol Sensitivities as function of a, symmetric PDF, H = 12 km

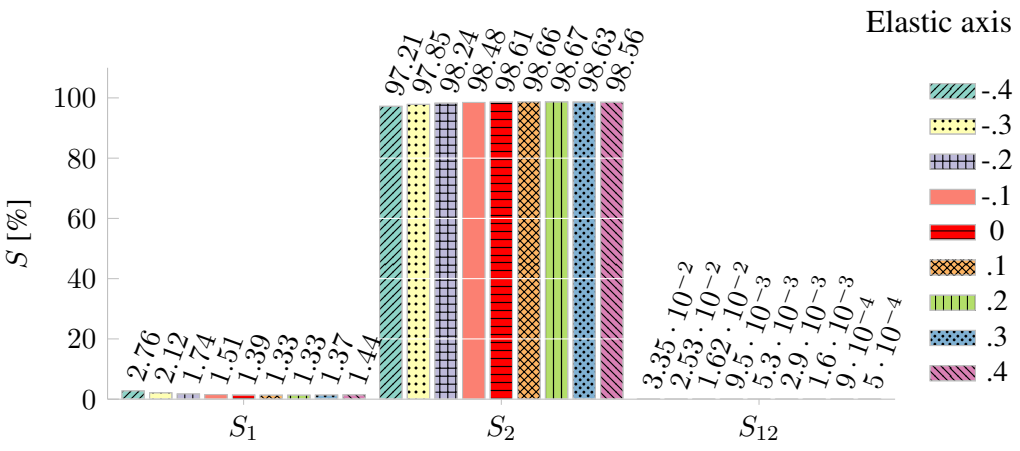

(a) Beta(3,2)

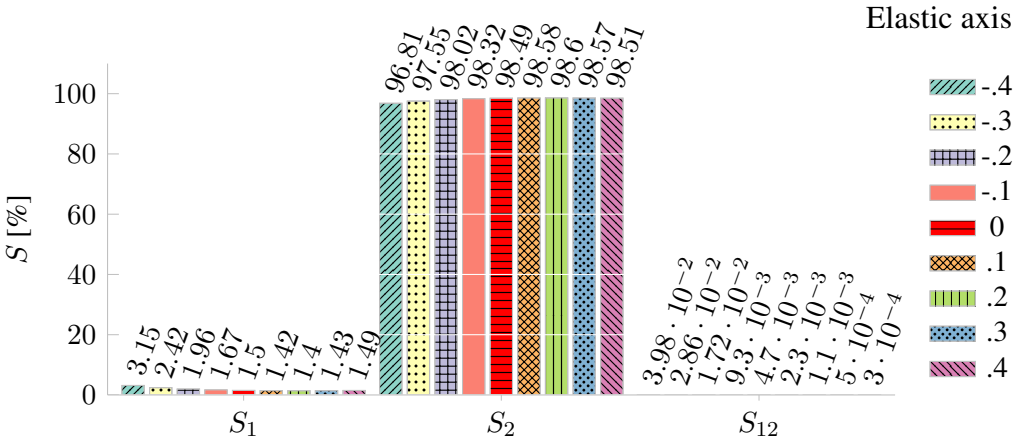

(b) Beta(2,3)

Figure 4.11: Sobol Sensitivities as function of a, non–symmetric PDF, H = 12 km

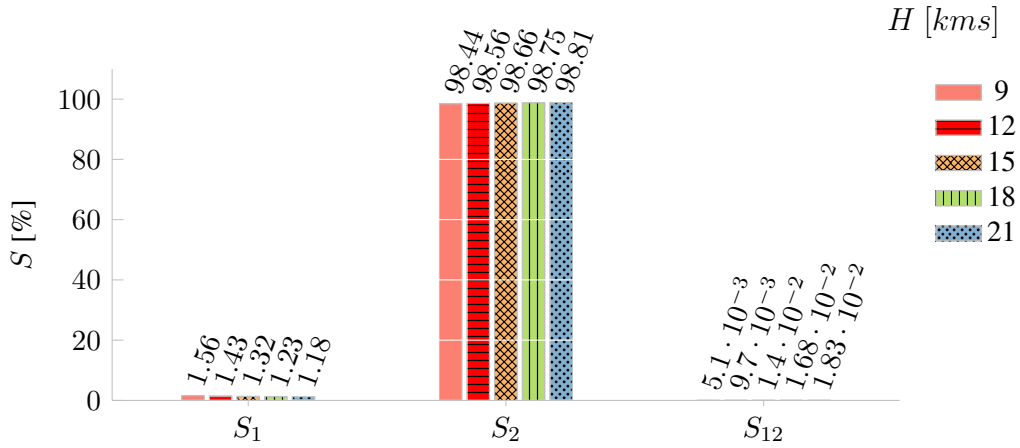

Figure 4.12: Sobol Sensitivities as function of H, uniform PDF, a = 0

CHAPTER 5

UNCERTAINTY PROPAGATION IN THE AEROTHERMOELASTIC BEHAVIOR OF A PANEL

The second problem considered in this study is the aerothermoelastic stability of a panel located on the surface of a hypersonic vehicle. Uncertainty in the heat flux prediction is quantified and propagated so as to demonstrate its effect on the aerothermoelastic stability of the panel.

5.1 Description of the Aerothermoelastic Analysis

The panel, depicted in Fig. 5.1, is located on the surface of a hypersonic vehicle. It is assumed that the panel is covered by a thermal protection system consisting of a radiation shield and thermal insulation, shown in Fig. 5.2. The radiation shield is a PM–2000 honeycomb sandwich and the thermal insulation is Internal Multiscreen Insulation (IMI). The plate structure is composed of high-temperature grade of titanium (Ti-6Al-2Sn-4Zr-2Mo). The material properties are given at $300^o K$ in Table 5.1. Specific heat and thermal conductivity are temperature–dependent. [63, 65, 159]

A detailed deterministic study was performed in Ref. [159]. The aerothermoelastic model for this problem is obtained by combining the two-dimensional, moderate deflection

Table 5.1: Properties of the thermal structure at $300^o K$

	$\rho\ [kg/m^3]$	$c\ [J/kg/K]$	$k\ [W/m/K]$	$h_i\ [mm]$
Radiation shield	359	465	0.250	7.4
Thermal insulation	73.0	729	0.0258	10.0
Plate structure	4540	463	6.89	5.0

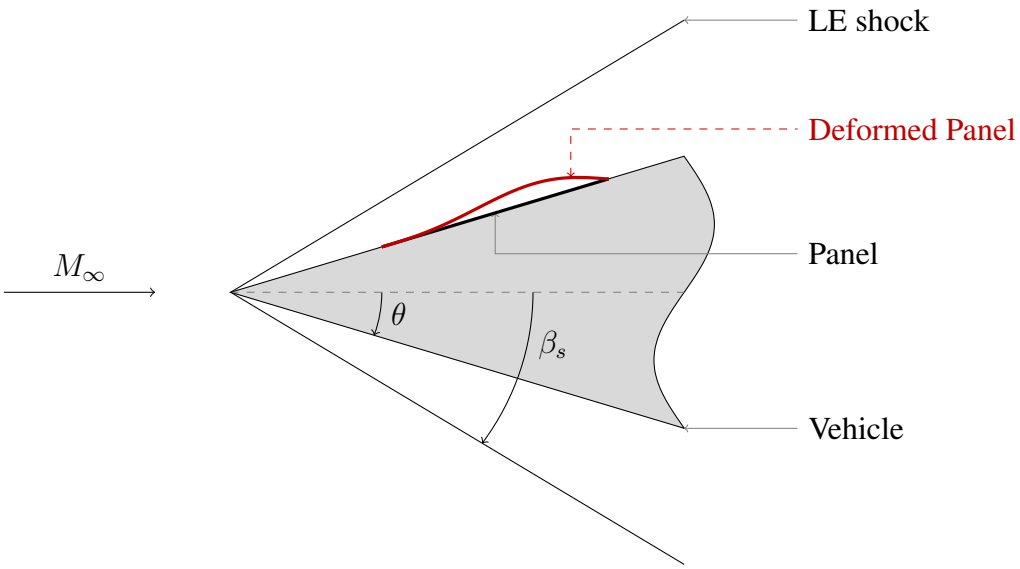

Figure 5.1: Panel located on an inclined surface of a wedge-shaped forebody

von Karman plate theory, given in Eq. (5.1), with unsteady aerodynamic loading q_a, based on 3^{rd} order piston theory. It accounts for thermal stresses as well as change in material properties due to effect of temperature. The effects of thermal loading due to arbitrary, in–plane and through–thickness temperature distributions are included in N_x and M_T, respectively. The TPS contributes to the mass but not to the stiffness.

$$D\frac{\partial^4 w}{\partial x^4} - N_x\frac{\partial^2 w}{\partial x^2} + \rho_p\frac{\partial^2 w}{\partial t^2} + q_a + \frac{\partial^2 M_T}{\partial x^2} = 0 \tag{5.1}$$

The panel is simply supported at its ends. The nonlinear equations of motion are solved using a Galerkin approach to discretize the spatial dependance. The panel response in the time domain is obtained from a fourth order Runge–Kutta scheme. The out of plane dis-

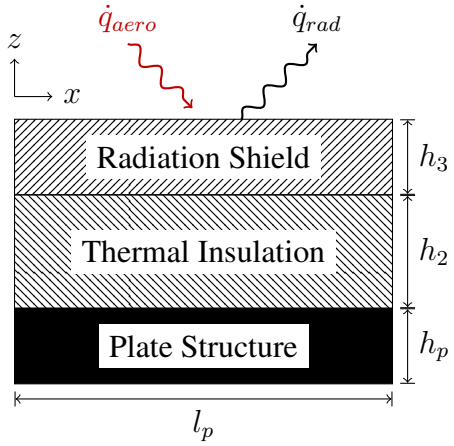

Figure 5.2: Two-dimensional model of the thermal structure

placement $w(x,t)$, Eq. (5.2), is expressed as a combination of sine modes and a third order polynomial function uniquely defined to satisfy non–homogeneous boundary conditions due to thermal loads.

$$w(x,t) = \sum_{n=1}^{6} A_n(t) \sin(n\pi \frac{x}{l_p}) + C_1(t) + C_2(t)x + C_3(t)x^2 + C_4(t)x^3 \tag{5.2}$$

The heat transfer problem is treated using Eckert's reference enthalpy model for evaluating the aerodynamic heat flux [121]. The temperature distribution in the structure is computed from a finite difference solution of the heat transfer problem given by Eq. (5.3).

$$\rho c_m \frac{\partial T}{\partial t} = k_x \frac{\partial^2 T}{\partial x^2} + k_z \frac{\partial^2 T}{\partial z^2} \tag{5.3}$$

In the structural analysis of the heated structure, the temperature distribution along the length of the panel is fitted using a second order polynomial function. It allows one to integrate the equation of motion required for this Galerkin approach. The temperature distribution, and the heat flux distribution at the surface of the panel, are assumed to be continuous and smooth. This analysis cannot account for the presence of transition from laminar to turbulent at the surface of the panel.

The vehicle is in straight and level flight, at a constant altitude and Mach number. Since the edges of the panel are fixed at its end points, thermal stresses develop as the panel is heated, leading to buckling and eventual aerothermoelastic instability. The through–the–thickness temperature gradients bend the panel upwards before it flutters. The instant when the panel starts to flutter determines the flight time, T_f, that characterizes the stability boundary of the system and it represents the time to failure. This flight time corresponds to the instant when the out of plane panel displacement at the mid-chord point reaches -10% of the panel thickness. This metric is chosen as a value useful for identifying the onset of flutter from the transient response of the panel. This metric for the onset of flutter is accurate to within ± 1 second of flight time, based on the results generated.

Since aerodynamic loading, elastic deformation, inertial loads and heat transfer are tightly coupled [159], heat flux prediction is a key component of the analysis. The use of Eckert's reference enthalpy model implies several assumptions about the modeling of the heating problem which introduce sources of uncertainty and affect the stability of the system. Therefore, uncertainty in the heat flux prediction has to be quantified. A scaling factor α_q for the heat flux is introduced and treated as the first random variable, ξ_1. The location of the transition from laminar to turbulent flow, x_t, is treated as the second random variable, ξ_2. First the deterministic results are presented, followed by the probabilistic results.

5.2 Deterministic Results

The input parameters are provided in Table 5.2 for the baseline configuration. The altitude is 30 km (98,500 feet) and the free stream Mach number varies between 8 and 12. The forebody inclination is 5 degrees, the panel is assumed to be 1.5 meters long and is located at a distance of 1.0 meter from the leading edge of the vehicle. The flow over the panel is assumed to be fully turbulent since transition is assumed to start at the leading edge of the

vehicle and to end before the leading edge of the panel.

Table 5.2: Baseline configuration for the panel

Parameter	Value	unit
H	30	km
M_∞	8-12	N/A
θ	5	deg
l_p	1.5	m
h_p	5	mm
T_0	300	K
x_e	1.0	m
x_{ti}	1.0	m

The transient response of the panel at mid–chord is given for 5 different Mach numbers. First, the full response is given for Mach 9 in Fig. 5.3. The panel is initially flat, buckles upward and eventually starts to flutter which determines the flight time, T_f, indicated by a vertical line.

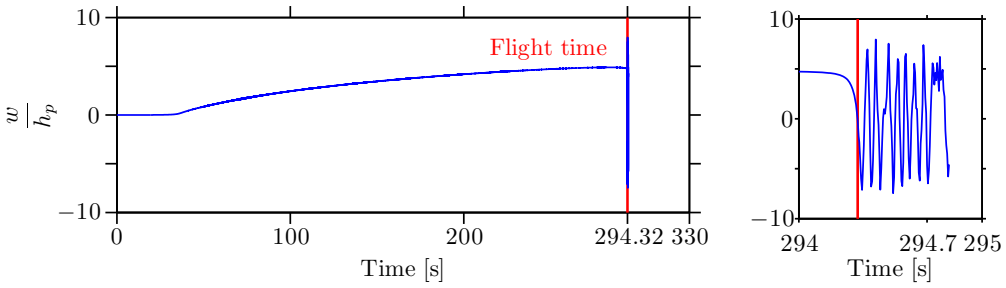

Figure 5.3: Transient response of the panel for turbulent flow, $M_\infty = 9$

A closer view of the response of the panel is given for Mach 8 to 12 in Figs. 5.4(a) to 5.4(d). At lower Mach number, the flutter onset is gradual. Therefore the flight time can only be determined to a certain degree as explained in the previous section.

In the deterministic analysis, it is assumed that the panel is exposed to fully developed turbulent flows. For fully laminar flows, the aerodynamic heat flux on the panel is approximately one fifth of the heat flux due to turbulent flows. It results in longer flight times. In

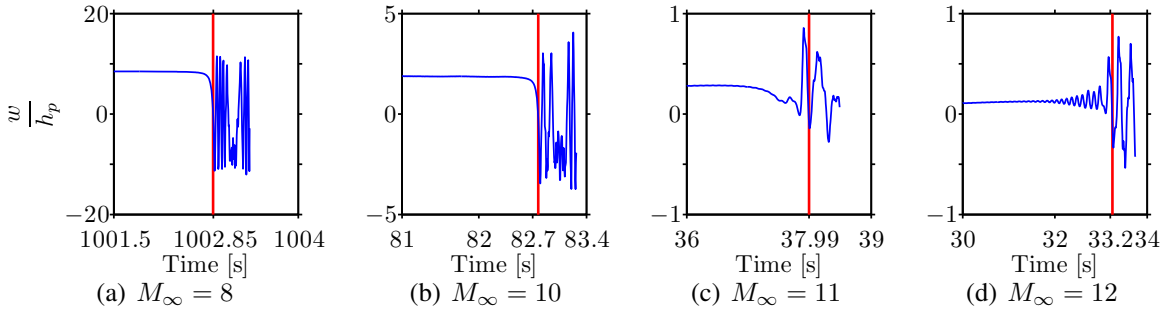

(a) $M_\infty = 8$ (b) $M_\infty = 10$ (c) $M_\infty = 11$ (d) $M_\infty = 12$

Figure 5.4: Transient response of the panel for turbulent flow

Table 5.3, the flight times are given for both turbulent and laminar cases. Turbulent flow allows one to fly for twice as long before flutter occurs. Therefore, turbulent flow appears to represent a conservative assumption. The UQ results presented next reveal that it is not the case.

Table 5.3: Deterministic flight times

M_∞		8	9	10	11	12
T_f [s]	Laminar	> 1500	672.0	133.2	62.3	55.5
	Turbulent	1002.8	294.3	82.8	38	33.2
$\frac{T_f^{lam} - T_f^{tur}}{T_f^{tur}}$ [%]		–	128.3	61.0	63.9	67.0

5.3 Uncertainty Propagation Results

Appropriate modeling of turbulence and gas properties is a key factor for accurate prediction of the aerodynamic heat flux on the structure. In Ref. [159], two sources of uncertainty have been identified. The first is associated with uncertainty in turbulence modeling, and the second pertains to uncertainty in the transition from laminar to turbulent flow. Both influence the heat flux, and thus have a direct impact on the aerothermoelastic stability of the panel.

Turbulence Modeling The uncertainty due to turbulence modeling was quantified by comparing Eckert's reference enthalpy model [121] with CFD results based on two turbulence models. This comparison is depicted in Fig. 5.5. The CFD results were generated with the CFL3D code [160] for a flight Mach number of 8.0, and a surface temperature on the panel of 900 K. For the panel deflections shown in Figs. 5.5(a) and 5.5(c), the predicted heat flux distributions along the panel computed using the various models are illustrated in Figs. 5.5(b) and 5.5(d). It is evident that the results depend on the model used to compute the convective heat flux. Four different predictions are compared: two based on CFD computations with different turbulence models, namely Menter and Wilcox available in CFL3D [160], and two based on Eckert's reference enthalpy and reference temperature models [159, 161]. The models considered in Fig. 5.5 result in similar spatial distribution shapes for the heat flux and differ only in magnitude of the heat flux.

Based on these results, uncertainty due to turbulence modeling is characterized by the variation in heat flux predictions based on the differences between Eckert's reference models, and the CFD results based on different turbulence models, is accounted for by using a scaling factor α_q that modifies the Eckert's reference enthalpy heat flux Q_{aero} to yield $\alpha_q Q_{aero}$. The range for α_q is chosen to be $0.95 < \alpha_q < 1.25$ in order to encompass the difference between Eckert's reference enthalpy and both the CFD results shown in Figs. 5.5(b) and 5.5(d). A value of $\alpha_q = 1$ corresponds to the baseline value employed in Ref. [161]. The probability distribution for α_q is assumed to be uniform, i.e. Beta(1,1).

Transition Location Prediction In addition to the uncertainty associated with the turbulence model, the uncertainty associated with the location of the onset of transition is also modeled. In Ref. [159], the location at which the flow transitions from laminar to turbulent was arbitrarily selected to correspond to the distance between the leading edge of the vehicle and the leading edge of the panel. Transition modeling in hypersonic flow is a complex issue. The location of the transition region depends on numerous parameters such as

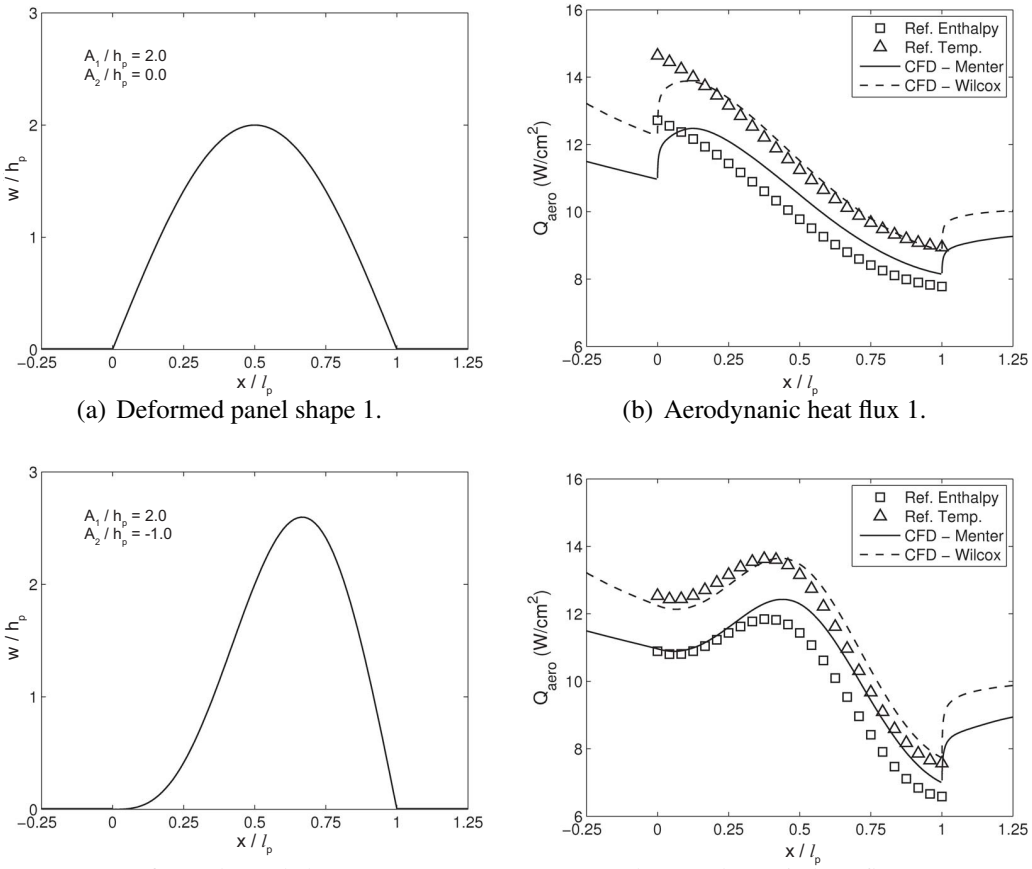

(a) Deformed panel shape 1.

(b) Aerodynanic heat flux 1.

(c) Deformed panel shape 2.

(d) Aerodynamic heat flux 2.

Figure 5.5: Comparison of aerodynamic heating predictions over two deformed panel shapes, $T_{wall} = 900K$, $M = 8$

flight conditions, wall temperature, surface roughness or disturbances levels present in the flow [7].

Uncertainty in transition is quantified by using CFD++ a commercially available CFD solver. The CFD++ code contains several turbulence models. A turbulence model recommended for external hypersonic aerodynamic predictions is the $k - \epsilon$ model. To model the transition location, an algebraic transition (AT) model is used in conjunction with the $k - \epsilon$ model [152]. It triggers transition based on detection of local flow curvature by augmenting local shear stress.

For each of the additional turbulence equations, boundary conditions are needed. The

dependent variable associated with each freestream boundary condition is computed given two freestream turbulence characteristic parameters: the turbulent kinetic energy intensity, T_u, and the turbulent to laminar viscosity ratio, μ_T/μ_L. The quantity T_u varies from 0.1 to 1% and μ_T/μ_L varies from 2 to 5 for external flows according to 'CFD++ Best Practices' [152]. The combination of both parameters characterizes the level of turbulence in the freestream flow. However, these parameters are rarely known [152] and therefore should be treated as uncertain parameters. To estimate their impact on the heat flux prediction that depends on laminar to turbulent transition region location on the vehicle, four simulations were conducted for different cases that correspond to the extreme values of both parameters. For level flight at Mach 8 and a constant wall temperature of 900 K, the location of the turbulence transition region is determined from the heat flux distributions shown in Fig. 5.6. The sharp vertical increases in heat flux indicate transition from laminar to turbulent flow. Turbulence transition location for different values of kinetic energy intensity varies from close to the leading edge of the vehicle, which corresponds to $x/l_p = -0.67$, up to the leading edge of the panel ($x/l_p = 0$).

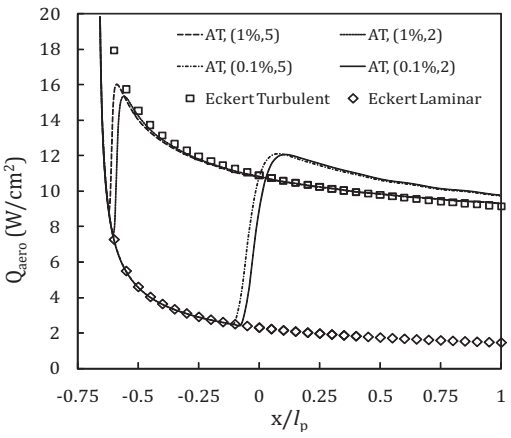

Figure 5.6: Heat flux prediction using CFD++ $k-\epsilon$ augmented with algebraic transition model (AT), $T_{wall} = 900K$, $M = 8$

Furthermore, there is uncertainty associated with the location of the transition due to variability in the turbulence level of the freestream flows. In order to quantify the effects of

uncertainty associated with the turbulence onset location, x_{ti}, the distance of the onset location from the leading edge of the panel is varied from 0.2 meter to 1 meter corresponding to $-0.67 \leq x_{ti}/l_p \leq -0.1$. The distance of 1 meter corresponds to an onset of turbulent flow at the leading edge of the vehicle, which represents the baseline value assumed in Ref. [159]. The turbulence onset location is assumed to be uniformly distributed between 0.2 and 1m.

Table 5.4: Uncertain Parameters

Parameter	Baseline value	Range	Distribution
α_q	1	[0.95 1.25]	Uniform
$x_{ti}[m]$	1	[0.2 1]	Uniform

Both uncertainties associated with the turbulence model and the transition location, summarized in Table 5.4, are propagated through the analysis and their impact on the flight time is determined. Recall that flight time is used as a metric for onset of instability. A 6^{th} order polynomial response surface is constructed based on 49 analysis runs; i.e. 7 collocation points for the two random variables. Uncertainty propagation results for different Mach numbers are shown Figs. 5.7(a) and. 5.7(b). In both figures, the lines correspond to the deterministic values. The thick bars correspond to the expected values +/- the standard deviation and the error bars correspond to the 95% CI. The downward and upward pointing triangles correspond to the maximum and minimum values respectively. In Fig. 5.7(b), the same results as depicted in Fig. 5.7(a) are given in terms of variation of flight time, ΔT_f, and are normalized with respect to the deterministic value, T_{fd}.

At Mach 8 the mean value of the flight time is 922 sec, compared to the deterministic value of 1003 sec. The standard deviation and range are 45.1 sec (4.5%) and 820–1032 sec ([-18%, +3%]) respectively, where percentages are in terms of the deterministic value. The results indicate that the expected flight time is less than the deterministic value which is close to the maximum flight time at each specified Mach number. This trend is to be

expected considering the choice of the uncertain variables and their respective ranges. The range of the coefficient α_q leads to increased heat flux amplitude in 83% of the cases. When transition is located closer to the leading-edge of the panel, the heat flux on the panel is also increased. These effects reduce the flight time.

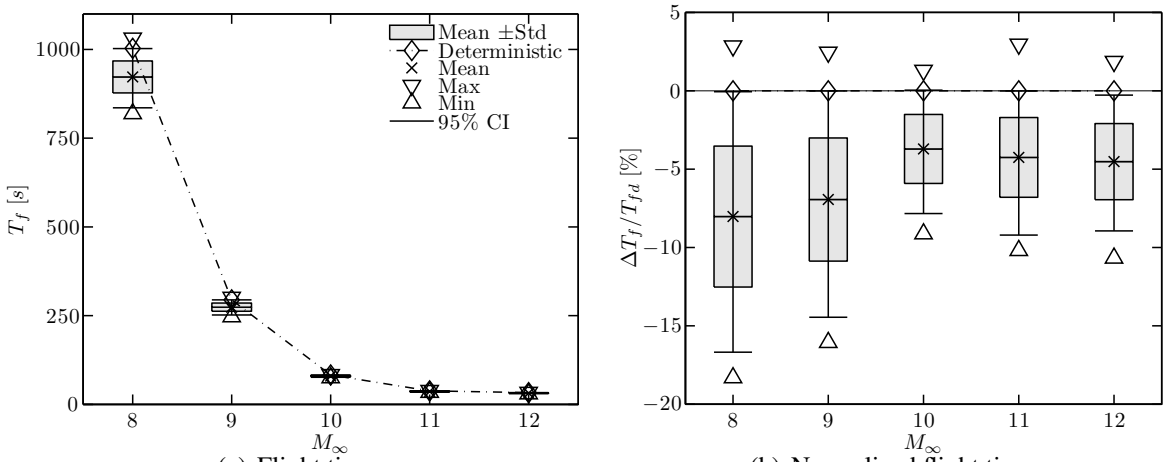

(a) Flight time (b) Normalized flight time

Figure 5.7: Flight time as a function of flight Mach number using SC

The PCE and KG response surfaces are generated using the information of the collocation points used in the SC approach. The uncertainty propagation results are given in Figs. 5.8(a) and 5.8(b) for PCE and KG respectively. The results obtained with SC and PCE agree well, indicating a converged response surface. The kriging response surface predicts the same 95% CI but over predicts the maximum value of T_f for M_∞=11 and 12. This behavior is due to the fact that kriging does not perform well when extrapolating outside the range covered by the collocation points.

Additional details are gleaned from the probability distribution shown in Fig. 5.9. The bars represent the PDF and the curved line corresponds to the CDF. The deterministic value is identified by the vertical line and the diamond symbol. The output probability distribution indicates a significant probability that the flight time will be much less than its deterministic value at Mach 8. These results illustrate the importance of incorporating uncertainty in a more complicated aerothermoelastic problem.

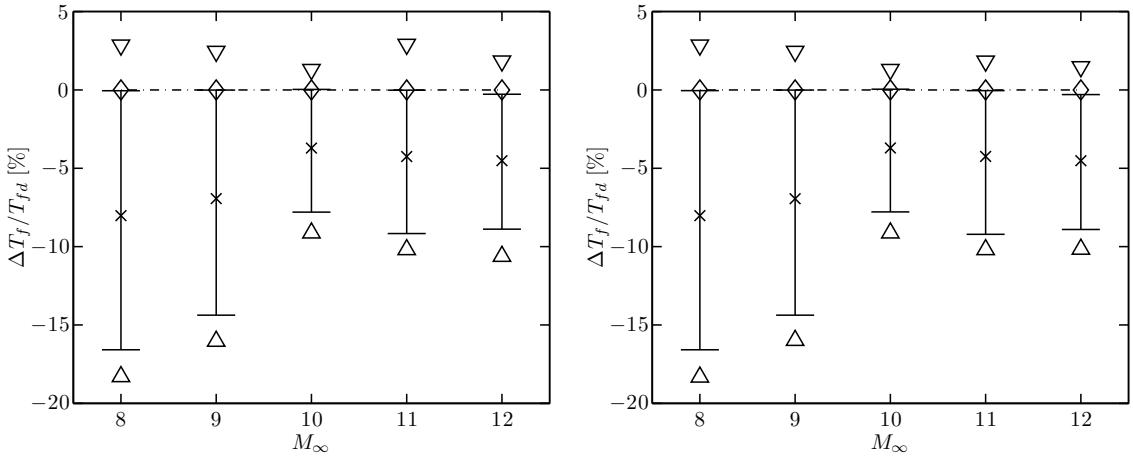

(a) PCE (b) KG

Figure 5.8: Normalized flight time as a function of flight Mach number using PCE and KG

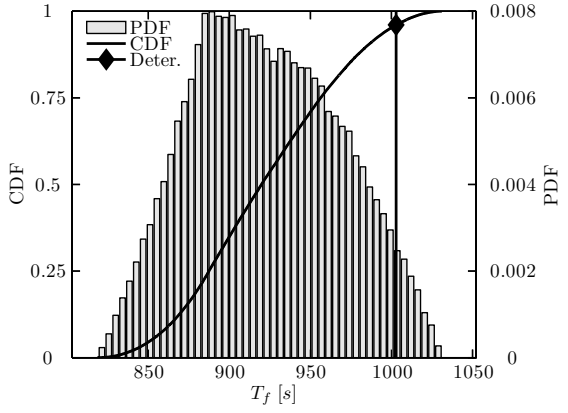

Figure 5.9: PDF for the flight time at Mach 8, H = 30 km

The same uncertainty is also propagated at different Mach numbers, and a concise summary of the probabilistic results is presented in Table 5.5. The probability distributions for the additional Mach numbers are given in Fig. 5.10. The ranges for α_q and the transition location determined from Mach 8 results are used in these computations. The trends observed for Mach 9 and 10 depicted in Figs. 5.10(a) and. 5.10(b) are similar. However, discrepancies are observed for Mach number 11 and 12, as shown in Figs. 5.10(c) and 5.10(d), respectively. The shapes of the PDF curves are not smooth despite lack for any physical reasons that would justify strong nonlinear relation between the uncertain inputs and output. Approximately ± 1 second errors occur in the estimations of flight time as described in Section 5.1. For lower Mach numbers, this error is insignificant compared to the magnitude of the deterministic value and the stochastic variability of the output. However, for higher Mach numbers, this error grows and becomes significant compared to the estimated flight times and significatively affects the response surface fit. These results illustrate difficulties in performing and interpreting UQ results when the stochastic variability is close to the error present in the deterministic analysis. [158]

Table 5.5: Flight Time variability

Mach Number	M_∞ = 8	M_∞ = 9	M_∞ = 10
T_f (sec)	1002.8	294.3	82.8
$\langle T_f \rangle$ (sec)	922.4 *(-8.0%)*	273.9 *(-6.9%)*	79.7 *(-3.71%)*
σ_{T_f} (sec)	45.1 *(4.5%)*	11.6 *(3.9%)*	1.8 *(2.2%)*
95% CI (sec)	[842.5 1009.2]	[253.5 296.0]	[76.6 83.1]
95% CI (%)	$[-16.0 \ +0.6]$	$[-13.9 \ +0.57]$	$[-7.5 \ +0.4]$
Range (sec)	[819.3 1031.5]	[247.1 301.6]	[75.2 83.9]
Range (%)	$[-18.3 \ +2.9]$	$[-16.0 \ +2.5]$	$[-9.1 \ +1.3]$

The effect of the assumed probability distribution is illustrated next. Two non–symmetric probability distribution are considered next: Beta(2,3) and Beta(3,2). The results are given for the three flight Mach numbers $M_\infty = 8$, 9 ,10. The range of flight time is unchanged, however its distribution is skewed towards the higher values in the case of propagating the

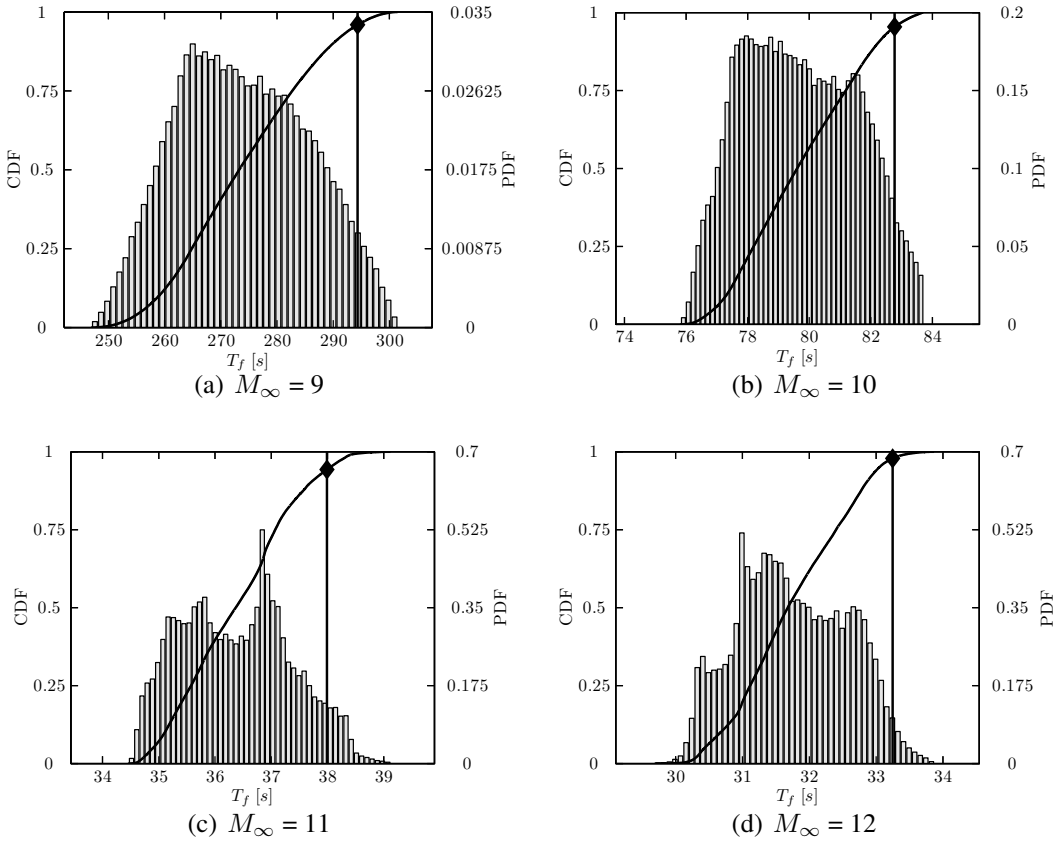

(a) $M_\infty = 9$ (b) $M_\infty = 10$

(c) $M_\infty = 11$ (d) $M_\infty = 12$

Figure 5.10: PDF of the Flight time for 9 to 12 flight Mach number

Beta(2,3) distribution and towards the lower ones for Beta(3,2).

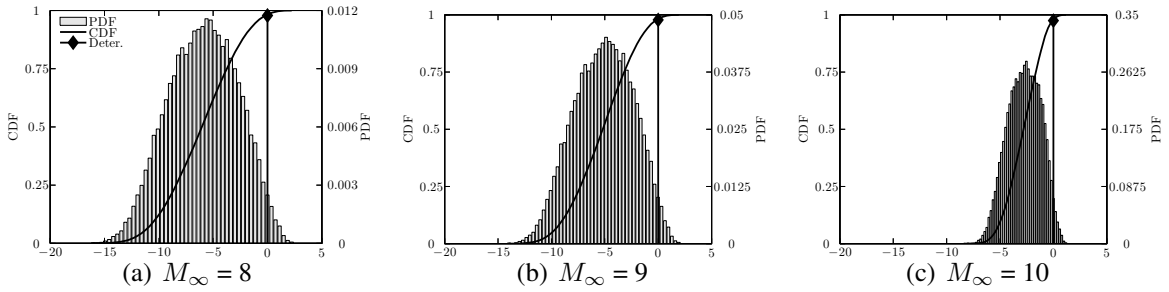

(a) M_∞ = 8 (b) M_∞ = 9 (c) M_∞ = 10

Figure 5.11: PDF of T_f assuming Beta(2,3) for the uncertain inputs

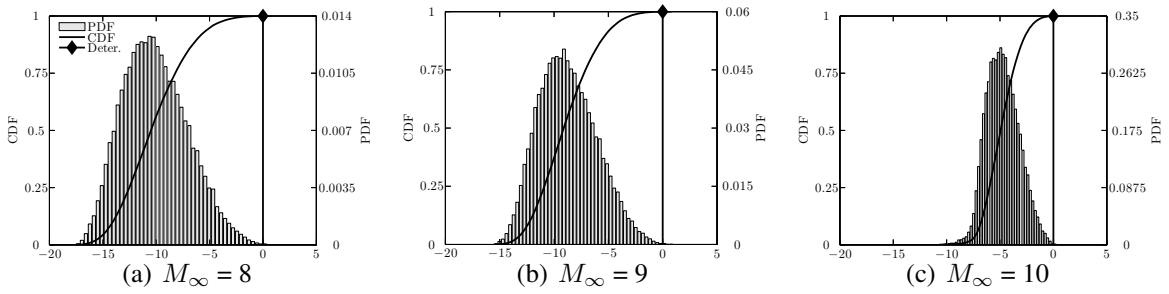

(a) M_∞ = 8 (b) M_∞ = 9 (c) M_∞ = 10

Figure 5.12: PDF of T_f assuming Beta(3,2) for the uncertain inputs

5.4 Sobol's Sensitivities

To extract the importance of each variables, Sobol's sensitivities are calculated in the case of uniform probability distribution. The results are given in Table 5.6 and depicted in Fig. 5.13. The variability of flight time is higher at lower Mach number as shown by the higher D's at $M_\infty = 8$. In all cases, the uncertainty associated with the magnitude of the heat flux is responsible for 80% to 85% of the variability in flight time; transition location contributes to 15% to 20%. The effect of the interaction between both variables is negligible.

Table 5.6: Sobol Sensitivities for the panel

M_∞	D			S [%]		
	α_q	x_t	$\alpha_q x_t$	α_q	x_t	$\alpha_q x_t$
8	1587.43	443.40	1.01	78.13	21.82	0.05
9	106.01	27.75	0.05	79.22	20.74	0.04
10	2.96	0.36	0.00	89.00	10.96	0.04
11	0.77	0.16	0.01	81.79	16.69	1.52
12	0.55	0.10	0.00	84.10	15.44	0.46

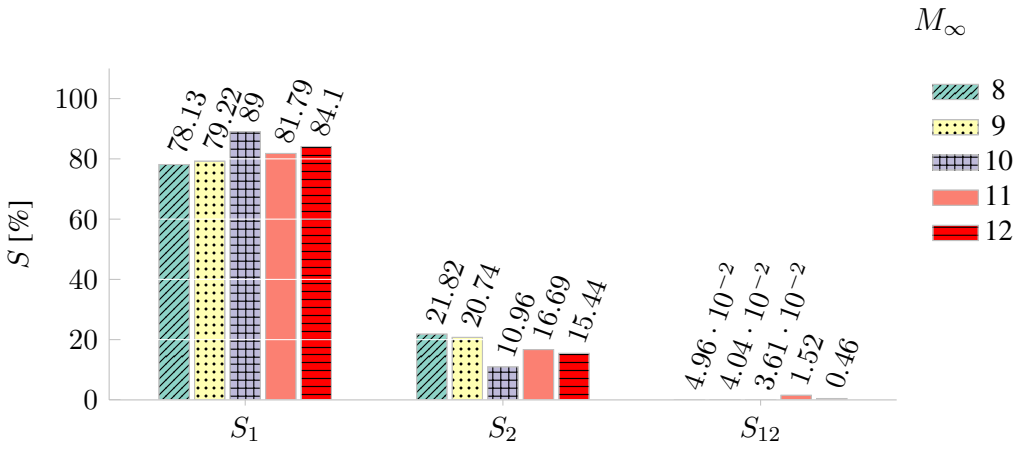

Figure 5.13: Sobol Sensitivities as function of M_∞

CHAPTER 6

UNCERTAINTY PROPAGATION IN INTEGRATED AIRFRAME–PROPULSION SYSTEM ANALYSIS

Air–breathing hypersonic vehicles are based on airframe integrated Scramjet engine. The elongated forebody that serves as the inlet of the engine is subject to harsh aerothermodynamic loading which causes it to deform. Unpredicted deformations may produce unstart, combustor chocking or structural failure due to increased loads. In this chapter, the impact of aerothermoelastic deformations on the prediction of the engine performance is quantified using a UQ approach. Aerothermoelastic deformations are calculated for various flight conditions and used as bounds in the UQ analysis. First the analysis is presented. Next the aerothermoelastic analysis results are given, and finally the results of the UQ approach are presented.

6.1 Integrated Airframe–Propulsion System Analysis with MASIV

The aerothermoelastic analysis and engine analysis of a generic hypersonic vehicle is illustrated by the flow chart in Fig. 6.1. The prediction of aerothermoelastic propulsive effects

on the engine requires four different analysis capabilities: a propulsion model with deforming geometry, a structural model with temperature–dependent material properties, an aerodynamic analysis capable of predicting heat transfer of external hypersonic flow and a heat transfer analysis.

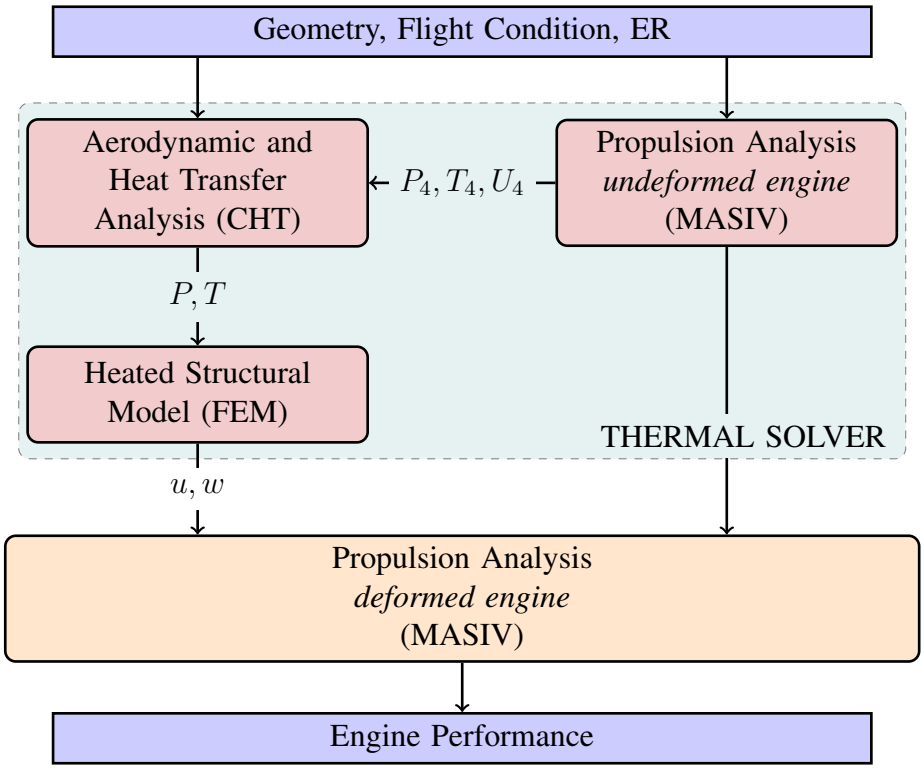

Figure 6.1: Aerothermoelastic–Propulsion Framework

The vehicle is assumed to be in straight and level flight. A flight condition is determined by the altitude, H, the Mach number M_∞, the angle of attack of the vehicle, α, which determines the free stream conditions; and the equivalence ratio, ER. The external aerodynamics and heat transfer equations are solved simultaneously. This analysis is referred to as conjugate heat transfer (CHT). A conjugate heat transfer analysis is performed at a given flight condition, free stream and combustor conditions to predict the aerodynamic load and temperature distribution in the load carrying structure as function of time. Pressure and temperature are transferred to a structural FEM from which thermal elastic deformation of the vehicle airframe is obtained. The aerothermoelastic analysis is used to

estimate the amplitude of maximum static deformations. Due to these assumptions, the deformation are treated as uncertainties. An uncertainty propagation analysis is performed to evaluate the sensitivity of engine performance to the deformed configuration. Details of each component in the analysis are given in the following subsections.

6.1.1 Geometry

The geometry of the vehicle considered in this study is inspired by the X–43 depicted in Fig. 6.2. The (x, y, z) axes are attached to the body and corresponds to the longitudinal, spanwise, and vertical directions, respectively.

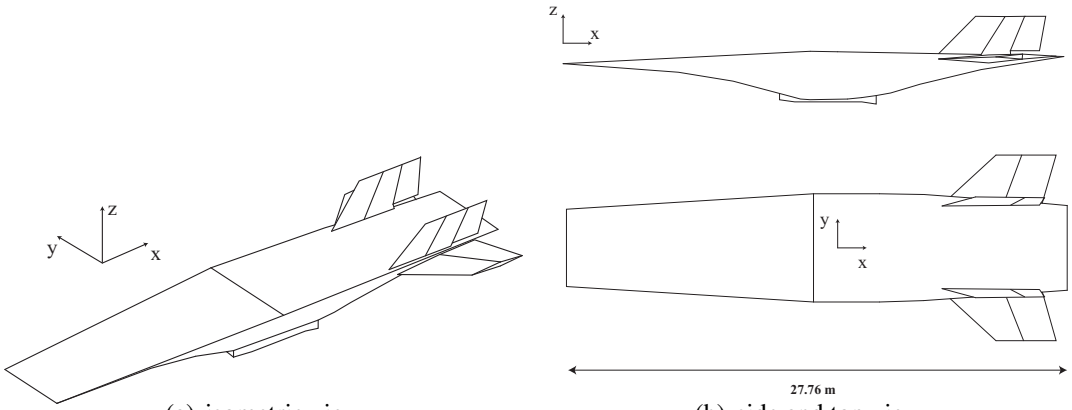

(a) isometric view (b) side and top view

Figure 6.2: Current vehicle geometry

This generic geometry is representative of an airframe–integrated air–breathing Scramjet propulsion system. The inlet is a slender wedge which compresses the free stream before it enters the isolator and the combustor. The isolator prevents inlet unstart caused by the increase of pressure in the combustor. The combustor is the part of the engine where the fuel is injected and burns. The nozzle ensures expansion of the flow from the combustor conditions to the free stream conditions and generates thrust. The performance of the engine is estimated using a reduced–order model, MASIV, described next.

6.1.2 Propulsion System Analysis with MASIV

The Michigan/Air Force scramjet in vehicle code (MASIV) code is an approximate, control–oriented model of the propulsion system of air–breathing SCRAMjet engines [162, 163]. The geometry of the mean flowpath is depicted in Fig. 6.3. Each section corresponds to a component of the engine. Along the axial direction, the propulsion system is divided into three components: the inlet and isolator, the combustor, and the nozzle. The points indicated in Fig. 6.3 define the geometry of the mean flowpath.

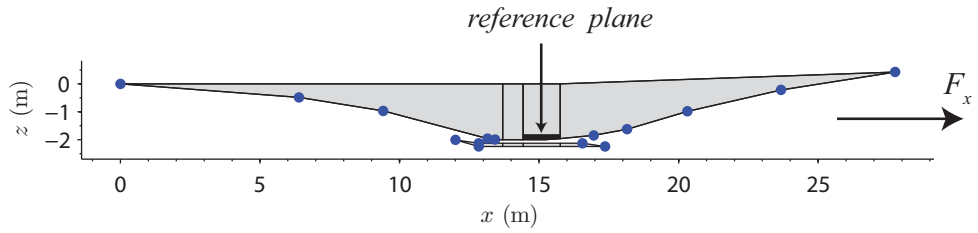

Figure 6.3: Engine flow path

This study focuses on the performance of the engine. The resultant of the pressure forces in the $x-$direction on the engine flowpath, F_x, is representative of the engine performance with trust as the quantity of interest in this study. The number of points defining the compression ramp represents the number of compression shocks which compress the free stream before it enters the cowl. There are three compression shocks in the inlet ramp as illustrated in Fig. 6.3. The steady flow solution is calculated using the shock/expansion approach. Expansion fans are discretized into a finite number of 'expansion shocks'. Marching downstream, shock–shock and shock–discrete expansion fans interactions are solved by the solution of the local Riemann problem for perfect gas. Given a flight condition (altitude, H, Mach number, M_∞, and angle of attack, α), the mean flow properties at the entrance of the engine in the isolator are predicted: density, static pressure, temperature and velocity. Mean flow properties at the entrance of the engine are computed and fed to the engine model. Enthalpy tables of a calorifically imperfect gas are used to account for high temperature effect at the entrance of the engine. In a calorically imperfect gas IG

model, the specific heat c_p and c_v of the fluid vary with temperature due to the excitation of vibrational energy of the molecules of gas [164]. Consequently, $\gamma = \frac{c_p}{c_v}$ is also a function of temperature. A more accurate prediction of the combustor inflow properties is achieved with this correction. The same model as for the inlet is also used for the nozzle.

The equivalence ratio, $ER = \left(\frac{\dot{m}_f}{\dot{m}_{O_2,4}}\right) / \left(\frac{\dot{m}_f}{\dot{m}_{O_2,4}}\right)_{st}$, corresponds to the ratio of the flow mass rate of fuel over the oxygen flow mass rate divided by the same ratio at stoichiometric condition. An ER of 1 corresponds to stoichiometric mixture of fuel and oxygen. An ER smaller than one means that there is more oxidizer than necessary. The ER controls the amount of fuel that is injected in the combustor.

The engine model is described in Ref. [165]. The combustor model is a one dimensional (1D) model that solves for conservation of mass, momentum, and energy using equation of state and additional algebraic equations marching axially through the combustion duct. An algebraic spreading model allows transverse jet mixing which is required to model engines which are mixing–limited. The steady Laminar Flamelet Model (SLFM) is an approximate combustion model which considers finite–rate chemistry. The chemistry model is expect to be valid for an equivalence ratio, ER, between 0.1 and 2. The MASIV code was recently used in a control study of a rigid hypersonic vehicle [135]. The effect of angle of attack and inflow rate on the forces acting on a full vehicle (lift, drag, net thrust and pitching moment) were evaluated and used in a trim analysis.

The mass flow of the fuel is assumed to be independent of the deformation and corresponds to the mass flow at the prescribed equivalence ratio for the undeformed engine. An alternative approach assumes that the amount of fuel depends on the oxidizer mass flow at the entrance of the engine to keep the ER constant at all time. In this case, the fuel mass flow is affected by the deformation. The effect of the deformation on engine performance is then amplified. If the capture area decreases due to deformation, the air mass flow rate decreases in the combustor, the engine generates less thrust. If the equivalence ratio is kept constant when the vehicle deforms, less fuel is injected and thrust decreases accordingly.

The plane corresponding to the top wall of the combustor is the plane of reference for the deformation of the vehicle, indicated in back in Fig. 6.3. The points, indicated with circles in Fig. 6.3, allow the analysis of a deformed engine. These points are used to transfer the deformation from the aerothermostructural model to the engine analysis.

6.1.3 Structural Model

The structure of an air–breathing hypersonic vehicle is subjected to significant non-uniform aerodynamic heating and pressure loading. In the development of hypersonic vehicles, structural components and design have played a important role [6, 63, 64, 69, 72, 109, 138, 166, 167]. The structure experiences high temperature gradients and intense pressure and heat loading which can cause local buckling or flutter. These challenges require innovative solutions: new high temperature materials, thermal protection system (TPS), and possibly coated leading edges with active cooling. The maximum operating temperature of titanium-based alloys varies between 800 to 1300 K [63, 69]. Those materials were studied for potential application in the National Space Plane (NASP) program. In Ref. [168], materials for structural components are titanium–aluminides and titanium matrix composites. The structural model is developed to estimate the longitudinal aerothermoelastic deformation of the airframe and cowl and identify the principal contributors to aerothermoelastic deflections. The problem of local buckling of the leading edges is ignored. Similarly issues related with aerothermoelasticity of the wings and control surfaces are not considered.

The MSC.NASTRAN structural model of the vehicle is illustrated in Fig. 6.4. It contains 540 nodes, 3240 degrees of freedom , with 208 CQUAD4 shell elements which represent the skin of the vehicle and the primary load carrying structure. The interior of the vehicle is filled with 534 CHEXA solid elements to prevent breathing modes–type deformation of the structure. A single element fills in the space between the upper and lower surface of the airframe.

There is no reinforcer inside the airframe. The skin is the load carrying structure repre-

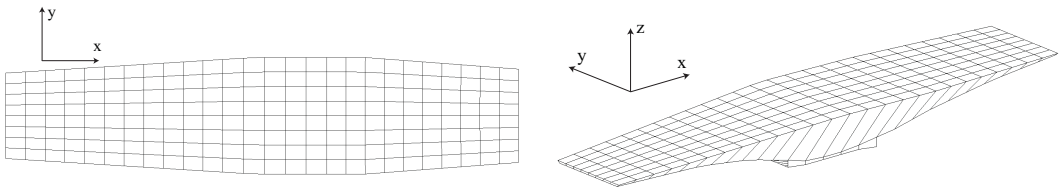

(a) top view (b) isometric

Figure 6.4: Structural Mesh

sented by corrugated panels made of high temperature titanium alloy illustrated in Fig. 6.5 and described in Ref. [169] as a potential load carrying structure for hypersonic vehicles. The model of the corrugated panel is used to determine the longitudinal Young modulus of the skin of the vehicle. The material properties assigned to the solid elements correspond to an orthotropic material with high stiffness in the (y, z) plane and low stiffness in the x–direction. This approach prevents unrealistic breathing modes and longitudinal deformations of the vehicle depend only on the skin properties. The vehicle behaves similarly to a sandwich beam where the cross sections remain planar. Material properties are functions of temperature.

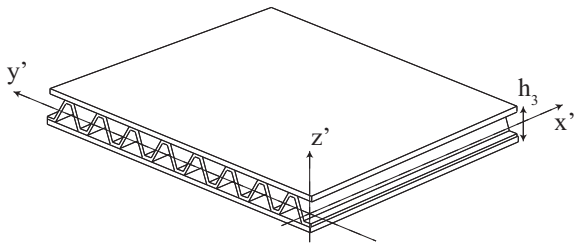

Figure 6.5: Truss–core sandwich panel

The rigid body degrees of freedom are suppressed using the inertia relief option in MSC.Nastran. It allows one to compute the deformation of the structure with respect to a given point in its reference frame. The forces which result from a rigid body acceleration of the degrees of freedom at a prescribed node in the specified directions, referred to as "SUPORT", are calculated. Accelerations are applied to the structure in the "SUPORT" directions to balance the artificially applied loads. Free flight deformation is computed.

The computed solution is relative to any rigid body motion that is occurring. It was verified that deformation are independent of the choice of the support point where all degrees of freedom are constrained. The point at the center of the top wall of the combustor, in Fig. 6.3, is chosen as the reference point.

The nodal temperature and pressure are computed using a conjugate heat transfer analysis. There is no feedback mechanism to account for deformation in the aeroheating and heat transfer analysis.

6.1.4 Conjugate Heat Transfer Analysis

The solution of a structure heated by a fluid flow at one of its boundaries is called conjugate heat transfer (CHT) problem. In this study, it is used to estimate the temperature distribution inside the undeformed load carrying structure of the vehicle as function of time and flight condition. Temperature distribution in the structure is calculated using CFD++, a commercial finite volume code capable of solving heat transfer problems in solid and conjugate heat transfer problems [152]. Using CFD++, the Navier–Stokes equations and the heat equation are solved simultaneously for the fluid and structural domains, respectively. Heat flux is conserved through the fluid–TPS and TPS–structure interfaces. The gas model corresponds to calorifically imperfect gas: specific heat, c_p, is function of temperature, γ is not a constant. Turbulence is modeled using Goldberg turbulence model which is a single equation model for the undamped eddy viscosity, R_t, recommended for external turbulent hypersonics flows [152].

To protect the load carrying structure from intense aerodynamic heating, a TPS barrier is placed between the airflow and the structure as depicted in Fig. 6.6. The TPS is composed of an upper layer of radiation shield made of PM2000 Honeycomb and a lower internal multiscreen insulation (IMI) barrier which is a simplified layout used in Refs. [159] and [64]. This TPS system is shown to be a light and efficient in Refs. [70, 71]. The IMI is also used in Ref. [167] as the main heat barrier for a long range hypersonic vehicle. The

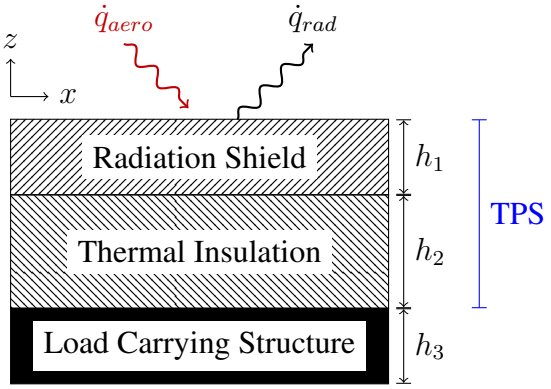

Figure 6.6: TPS layout of the structure of the vehicle

thicknesses of the TPS layers are uniform. An optimization analysis is often required in order to design the TPS distribution, such as performed in Ref. [167]. However, it was not performed in the present study.

The mesh for the fluid domain is depicted in Fig. 6.7. The thin skin structural layout is represented in Fig. 6.7(b). The leading edge of the vehicle experiences high aerodynamic heating. It is a critical component of the vehicle. However the emphasis of this study is on the body deformation. For this reason the leading edge is treated as an adiabatic wall in the CHT analysis. This assumption is also used for the cowl boundary. The combustor is the only part of the engine that is not represented. The MASIV model is used to estimate the flow conditions at the exit of the combustor. The entrance of the combustor is modeled by an outflow–only boundary condition. There is no back–pressure boundary condition in the analysis because the engine is operating in Scram mode similarly to the assumption of MASIV analysis.

Pressure and temperature are linearly interpolated from the entrance of the combustor to the exit of the combustor and then transferred to the structural model. This approximation alleviates the high thermal and pressure loading that occurs in the combustor, a region that has the highest temperature and pressure on the vehicle. Further refinement of both aerodynamic and structural models is required to capture the aerothermoelastic effects that

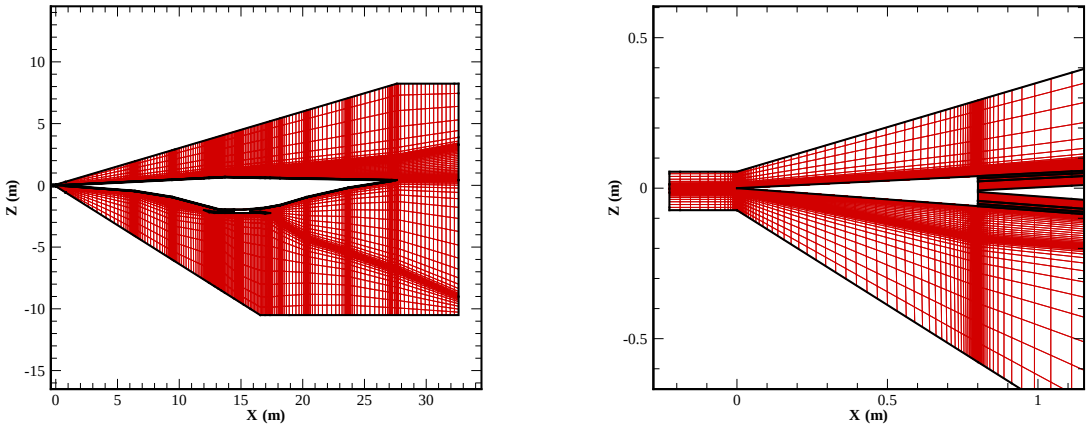

(a) Full mesh (b) Leading edge view

Figure 6.7: CHT mesh

occur in the combustor. However, modeling these effects is outside the scope of the present study.

Transient temperature distributions in the structure are computed for a level flight trajectory characterized by a constant altitude, Mach number and angle of attack, α_f. Pressure loading is calculated based on the angle of attack, α which maybe different of α_f, in the case of manoeuver for instance.

6.1.5 The Uncertain Variables

The deformation of the engine geometry in MASIV is given by Eq. 6.1, where $\bar{w}_{FEM,1}$ and $\bar{w}_{FEM,2}$ refer to the interpolated displacements from the FEM model for the vehicle and the cowl respectively, at the (x, z) coordinates of the points which define the geometry of the flowpath shown in Fig. 6.3.

$$w_i^{MASIV}(x,z) = \xi_i \bar{w}_i^{FEM}(x,z;t,\alpha_f) \quad i = 1,\ 2 \tag{6.1}$$

The deformed shapes of the body of the vehicle, $\bar{w}_{FEM1}$ and the cowl, $\bar{w}_{FEM2}$ deter-

mined by a flight history characterized by α_f and a flight time t, are treated as maximum possible deformations of the vehicle. The amplitudes of the deformations of the vehicle and the cowl, ξ_1 and ξ_2 respectively, are treated as variables in an uncertainty propagation analysis for engine performance. The axial displacement, u, is treated the same way.

The efficient uncertainty analysis accounts for approximations in the calculation of the displacement. Transferring the deformation as random variables is effective for mitigating the effect of approximations and facilitates the introduction of deformation at an early stage in the design.

6.2 Baseline Configuration

The vehicle is assumed to be 27.8 meters long, this length has been chosen based on the work done on NASP and Hyper–X programs as well as previous concepts [6,138,170,171]. In Ref. [163], the performance of two different flowpath geometries of the system inlet–combustor–nozzle are compared. The first configuration is optimized for a single flight condition being $M_\infty = 8$, $H = 26014.5\ m$ and $\alpha = 0^o$. The second configuration is designed to be less sensitive to changes in free stream Mach number and angle of attack [163]. Both geometries yield three compression shocks in the inlet ramp and two compression turns in the cowl. The more robust geometry contains an additional turn at the shoulder of the inlet which defines the entrance of the internal inlet. This geometry is that used in this study, as described in Fig. 6.3.

The flight condition used in this study corresponds to Mach 8 at an altitude of 26 km (85 000 ft) with 0^o angle of attack which corresponds to the average design conditions of the inlet [162]. The free stream condition is given in Table. 6.1. Using the MASIV code, the average flow condition at the exit of the combustor, given in Table. 6.2, are obtained. These conditions at the exit of the combustor are used in the CHT analysis as boundary conditions.

Table 6.1: Free stream conditions

Parameter		Value	Unit
Angle of attack	α	rad	0
Altitude	H	m	26000
Mach number	M_∞	-	8
Static pressure	p_∞	Pa	2183.8
Temperature	T_∞	K	222.5588
Stagnation temperature	$T_{0,\infty}$	K	3071.3
Density	ρ_∞	$kg.m^{-3}$	0.0342
Reynolds number	$Re_{,\infty}$	m^{-1}	5.6245×10^6
Dynamic pressure	q_∞	Pa	98000 (2000 psf)

Table 6.2: Combustor conditions

Parameter		Value	Unit
Mach number	M_4	1.95	-
Static pressure	p_4	3.5742 10^5	Pa
Temperature	T_4	2039.0	K
Stagnation temperature	$T_{0,4}$	3584.7	K
Density	ρ_4	0.47	$kg.m^{-3}$

6.2.1 Conjugate Heat Transfer Results

The thermal properties and thicknesses of the TPS layers are given in Table. 6.3.

Table 6.3: TPS material properties

		PM 2000	IMI	Structure
Thickness	$h_i\ (m)$	0.0074	.01	0.03
Density	$\rho_M\ (kg/m^{-3})$	7196.567	72.864	4306
Emissivity	ϵ	0.75	–	–
Thermal Conductivity	$k\ (W/m/K)$	18.25	0.0582	21.9
Specific Heat	$c\ (J/kg/K)$	770	107	540

The CHT results are depicted in Figs. 6.8(a), 6.8(b), 6.8(c), and 6.8(d) which shows respectively temperature, pressure, Mach and γ contours around the vehicle. At the upper surface, the flow experiences a compressive shock at the leading edge followed by an expansion after the second edge downstream as observed in Figs. 6.8(a), 6.8(b), and 6.8(c). At the lower surface, the free stream experiences three compression shocks due to the lower surface of the inlet before it reaches the leading edge of the cowl and enters the internal inlet and isolator where a series of shock occurs. At the nozzle, the flow expands creating propulsive force for the vehicle. In the internal inlet and expansion fan as well as boundary layers, the static temperature of the fluid is much higher and γ is reduced to 1.3 as indicated in Fig. 6.8(d). The reduction of γ illustrates the importance of high temperature modeling for these regions.

The temperature at the lower surface of the skin as function of time is shown in Fig. 6.9. During flight, the load carrying structure heats up through the TPS. The aerodynamic heating rate is higher at the lower surface of the vehicle. Consequently the temperature rise is significant at the lower surface. Note that most of the vehicle remains at a temperature lower than 800 K for the first hour of flight. The central part of the engine: internal inlet, isolator, and internal nozzle experience the highest temperatures and may require additional thermal protection system or active cooling. The exact structural layout or cooling

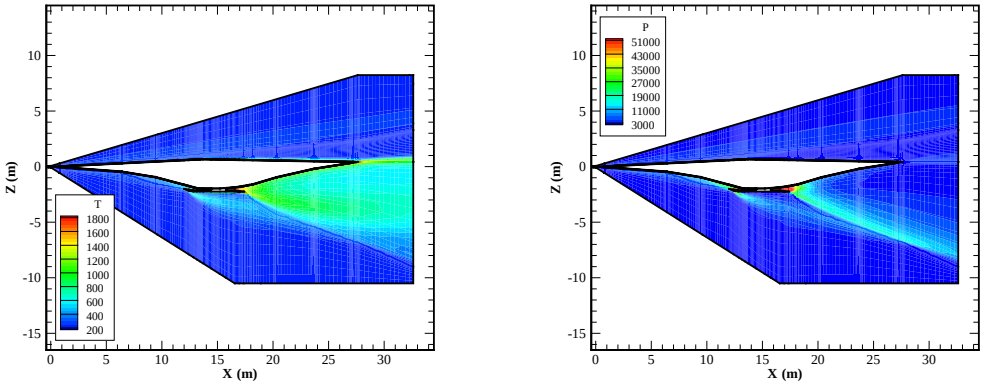

(a) Temperature (K)

(b) Pressure (Pa)

(c) Mach

(d) γ

Figure 6.8: CHT results

technology for those components is currently not well defined.

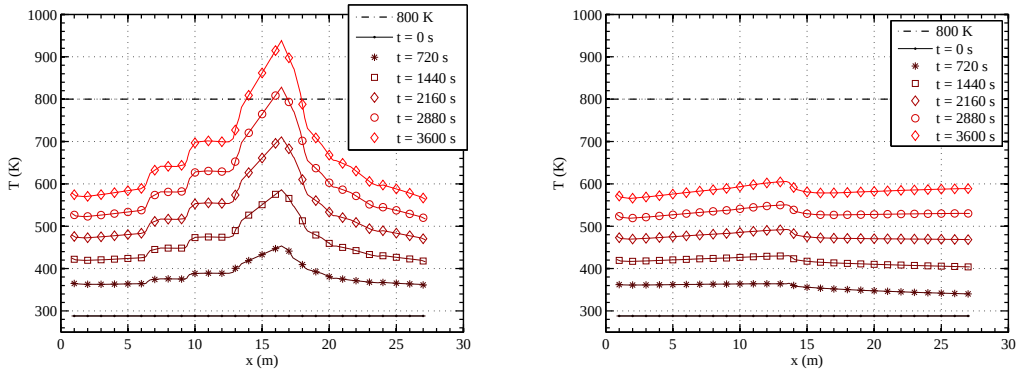

(a) Upper skin (b) Lower skin

Figure 6.9: Temperature in the skin as a function of time, $\alpha_f = 0^o$, $ER = 1.0$

The temperature distribution across the thickness of the vehicle is depicted in Fig. 6.10 and corresponds to four different locations of the vehicle skin. These stations corresponds to the location of the first compression turn in the inlet ramp, Fig. 6.10(c), and the last compression turn in the nozzle, Fig. 6.10(d), and their equivalent on the upper surface of the vehicle, Figs 6.10(a) and 6.10(b) respectively. The temperature in the thin structure is considered uniform across the thickness compared to the variation in the longitudinal direction.

Temperature is linearly interpolated from the CHT results to the structural model as illustrated in Fig. 6.11(a) where the squares and lines represent information pertaining to the FEM model and the CHT model, respectively, for both upper and lower surface of the vehicle body. The two dimensional (2D) CHT model is used to compute the 2D loads on the three dimensional FEM model. The nodal pressures applied at each node are calculated based on their longitudinal coordinate, x, such that the total pressure applied along the center line of the vehicle is conserved. In Fig. 6.11(b), the nodal pressure is represented with square–shaped symbols. In order to conserve pressure loading, the pressure at the nodes may be different than the linearly interpolated value. As a first approximation, the pressure on the side of the vehicle is interpolated from the upper surface to the lower surface. The

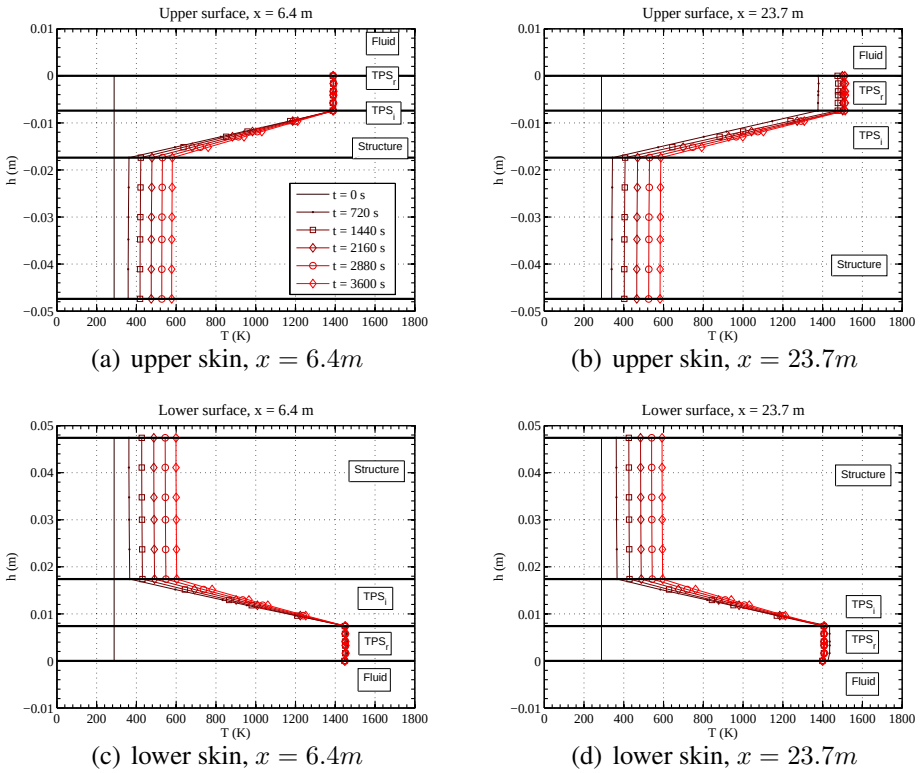

(a) upper skin, $x = 6.4m$

(b) upper skin, $x = 23.7m$

(c) lower skin, $x = 6.4m$

(d) lower skin, $x = 23.7m$

Figure 6.10: Temperature across skin thickness, $h = 0$ corresponds to TPS / freestream interface

leading edges and trailing edges of the vehicle are assumed to be rigid and are not represented in the FEM model. However, the resultant aerodynamic forces and moments on the leading edges and trailing edges computed in the CHT model are applied as distributed forces at the respective leading edge and trailing edge of the vehicle FEM to conserve total force from the CHT model to the FEM model.

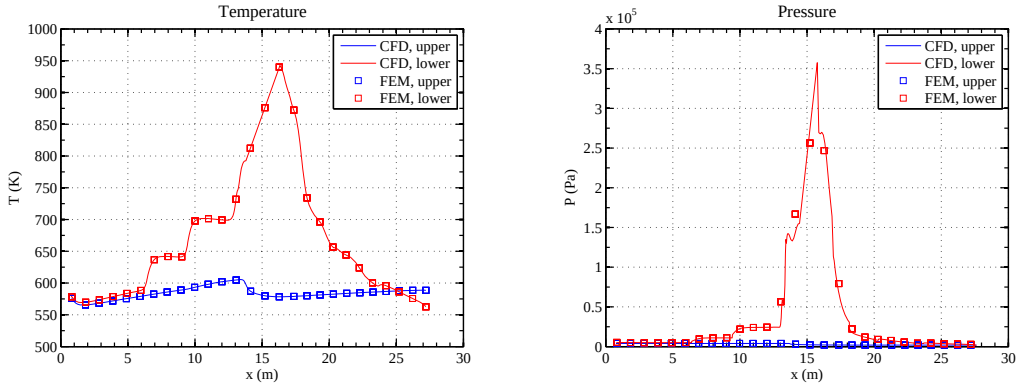

(a) Temperature (b) Pressure

Figure 6.11: CHT and structural coupling, $\alpha_f = 0^o$, $t = 1h$, $ER = 1.0$

6.2.2 Aerothermoelastic Deformations

The skin of the vehicle is represented by an equivalent panel with homogenized properties [169] given in Table 6.4. By comparing the specific modulus i.e. the ratio $\frac{E}{\rho_M}$, the corrugated panel is identified as a lighter structure for comparable stiffness requirements. The thickness of top and bottom sheets is 1.5 mm. The corrugated sheet, in Fig. 6.5, obtained from superplastical forming and diffusion binding process, is 0.75 mm. The total thickness of the panel, h_3, is 0.03 m. The leading edges are assumed to be perfectly rigid. The upper surface of the internal inlet, isolator, combustor and internal nozzle are assumed to be made of titanium alloys. The high stiffness associated with this structural component of the airframe where the engine is mounted coincides with the highest thermal and pressure loads.

Table 6.4: Panel Properties

Titanium alloy	ρ_M	4306 $kg.m^{-3}$
	E	112×10^9 Pa
	α_T	7.74×10^{-6} K^{-1}
	ν	0.3
	$\frac{E}{\rho_M}$	2.6×10^7
Titanium alloy panel	D_x	6.2×10^4 Nm
	h_3	0.03 m
	ρ_M	737.2 kg/m^3
	$\bar{E} = \frac{12D_{x'}(1-\nu^2)}{h^3}$	32×10^9 Pa
	$\frac{E}{\rho_M}$	4.3×10^7
Interior material properties	ρ_M	180 $kg.m^{-3}$
	E_x	10000 Pa
	E_y,E_z	26×10^9 Pa
	α_T	7.74×10^{-6} K^{-1}
	ν	0

The total mass of the vehicle given by the FEM model is 43 tons. For comparison purposes, the SR–71 is 32.74 meters long and its empty weight and maximum takeoff weight are 30 and 78 tons respectively. The natural modes shape of the vehicle are shown in Fig. 6.12. The first two and fourth elastic modes correspond to the first longitudinal bending modes having a natural frequency of 12.3, 19.2 and 26.7 Hz respectively. The third mode at 25.9 Hz is a lateral bending mode. The fifth mode with natural frequency of 28.2 Hz is the first torsional mode.

The young modulus of the titanium alloy varies linearly with temperature from 100% to 70% at 288 and 810 K respectively. The coefficient of thermal expansion varies from to 7.74×10^{-6} $K^{-1}$to 9.54×10^{-6} K^{-1} at 288 and 810 K respectively. These values are representative of a high temperature titanium alloy such as Ti–6Al–2Sn–4Zr–2Mo [66]. The initial temperature for the thermal expansion of the structure is set to 288 K which is the sea level temperature in a standard atmosphere model.

The temperature contours on the lower surface of the FEM model of the vehicle are

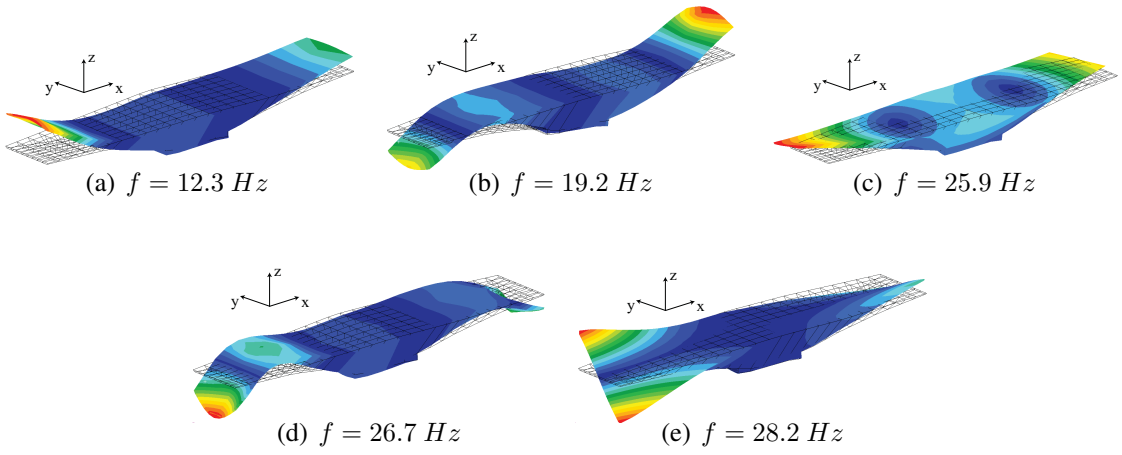

(a) $f = 12.3\ Hz$ (b) $f = 19.2\ Hz$ (c) $f = 25.9\ Hz$

(d) $f = 26.7\ Hz$ (e) $f = 28.2\ Hz$

Figure 6.12: First 5 natural mode shapes

shown in Fig. 6.13 and corresponds to the temperature shown in Fig. 6.11(a). The highest temperature, $950\ K$, corresponds to the exit of the combustor. The lowest temperature at the upper surface is less than 600 K.

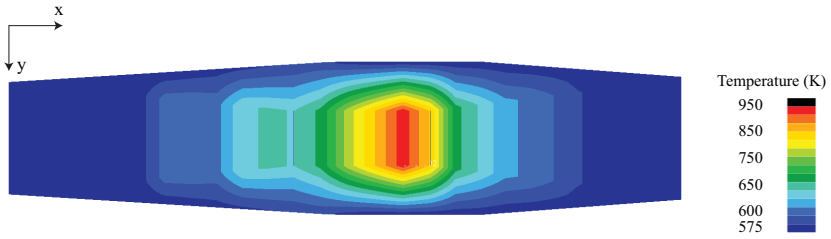

Figure 6.13: Temperature contours at the lower surface of the vehicle at $\alpha_f = 0^o$, $t = 1h$, $ER = 1.0$

Similarly, pressure contours on the lower surface of the FEM are shown in Fig. 6.14 and correspond to the pressure shown in Fig. 6.11(b). As expected, temperature and pressure are dependent only on the $x-$coordinate on the lower surface. The variation along the span-wise direction is due to the interpolation from the elements of the lateral skin comprising the sides of the vehicle.

The vehicle is in a straight and level flight at constant altitude and Mach number. The angle of attack is constant and assumed to be $\alpha_f = 0^o$. The temperature increases in the

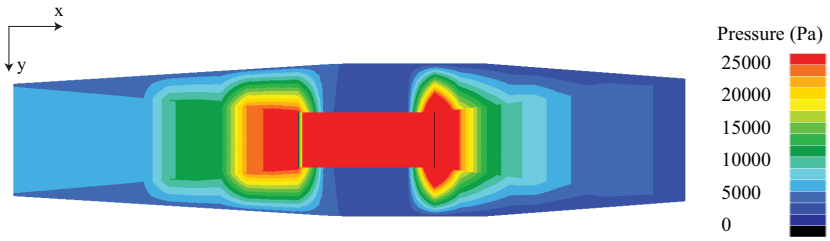

Figure 6.14: Pressure contours at $\alpha_f = 0^o$, $t = 1h$, $ER = 1.0$

structure as function of time. As the structure heats up, material degradation and thermal stresses decrease the natural frequencies, shown in Fig. 6.15. The different bars in the figure correspond to different thermal loads. The variation in modal frequencies is of the order of 10% after an hour of flight at 0^o angle of attack. For a uniform temperature of 800 K, the variation in frequencies is of the order of -16% which corresponds primarily to material degradation.

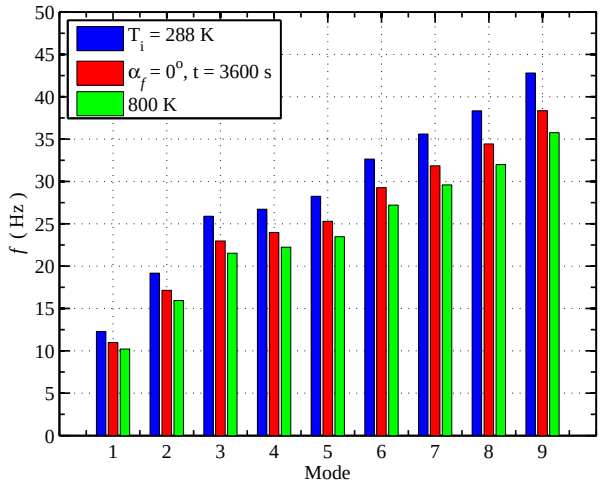

Figure 6.15: Natural frequencies of the heated airframe

The static deformations are computed at different times. The aerothermoelastic deformation of the vehicle along its plane of symmetry, $(y = 0)$, is shown in Fig. 6.16. The leading edge and trailing edge of the body deflects upward due to increasing temperature difference between the upper and lower surface at the inlet and nozzle respectively. After

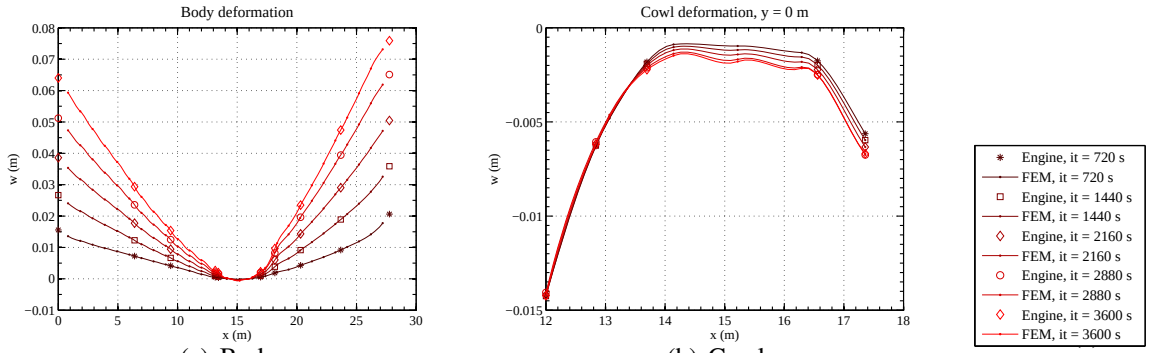

(a) Body (b) Cowl

Figure 6.16: FEM deformation as function of time along the centerline of the vehicle

one hour of flight, the amplitude of the deflections is approximately 8 cm which corresponds to 0.6% of the length of the inlet from the leading of the vehicle to the leading edge of the cowl. The deflections varies significantly with time: the aeroelastic deformation may be limited initially, but as the vehicle flies and heats up, material degradation and thermal stresses play a significant role in deforming the vehicle. At the center line , the cowl deflects downwards due to high pressure loading at its upper surface. It is important to note that the cowl is modeled using a single shell element through the thickness. For this reason the temperature gradients which may occur between the upper and lower surface of the cowl are not accounted for. The temperature is assumed to be uniform across the thickness of the cowl. In an actual vehicle, similar to the inlet, the temperature at the upper surface of the cowl is higher than the temperature at the bottom of the cowl. However some active cooling design may alleviate part of the temperature difference through the thickness. In the model, the cowl structure has been assumed to be sufficiently flexible to account for potential deformations as a result of high pressure and thermal loading. Deflections of the order of 1.5 to 2 cm are obtained. It corresponds to approximately 0.9 % of the width of the engine. At the edge of the engine, the cowl is attached to the vehicle and its deformation follows the shape of the vehicle. The leading edge of the cowl deflects upwards. The amplitude of the deflection is of the order of -0.4 times the deflection at the center line

at 0^o angle of attack. It dictates the range of the uncertain variable, ξ_2, in the uncertainty propagation analysis.

In Fig 6.17(a), the vehicle deformations are computed for different angles of attack from -1 ^{o} to 5 ^{o} at times $t = 720\ s$ and $t = 3600\ s$. The temperature distribution in the structure is due to the flight time elapsed, while the pressure loading corresponds to the attitude of the vehicle at a particular time. In Fig 6.17(a), deformations are due to a flight time of $t = 720\ s$ and $t = 3600\ s$ at $\alpha_f = 0^o$ angle of attack followed by a change of angle of attack which creates a different pressure loading on the heated vehicle. The results shows that the variation of the deformation with change in angle of attack is less than that with change in flight time. It confirms the fact that changes in temperature distribution have a greater effect on the deformation of the airframe than the changes in pressure loading. In Fig. 6.17(b), results are shown for only $t = 3600\ s$, for sake of clarity. The deformation of the cowl does not depend significantly of the flight history. Its deformation depends primarily on aerodynamic loading since the cowl is not subject to temperature gradients across its thickness in this model.

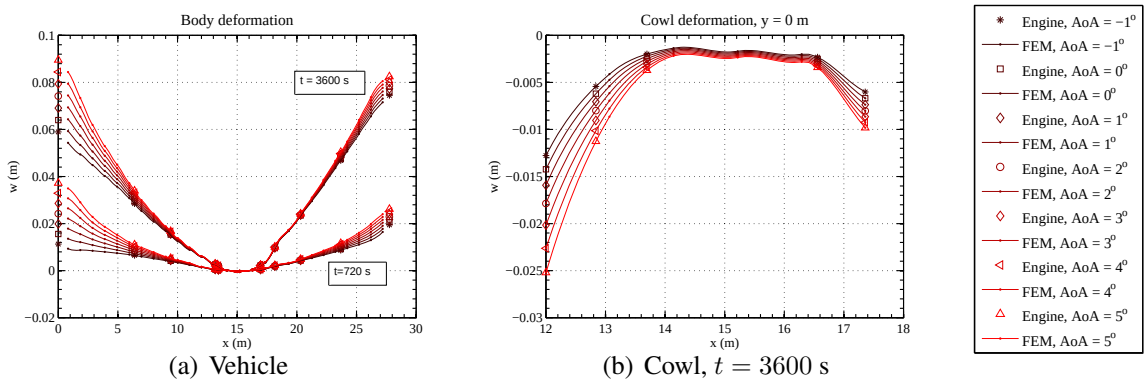

(a) Vehicle (b) Cowl, $t = 3600$ s

Figure 6.17: FEM deformation as function of angle of attack, $\alpha_f = 0^o$

In Table 6.5, the displacements at two different flight times and two different angles of attack are given. The axial deformations of the cowl leading edge are relatively small. The difference between the vertical displacements between the two trajectories is 16% at

$t = 720$ s and 25% at $t = 3600$ s. Flight history increases the deformation of the vehicle.

Table 6.5: Displacements at the leading edges of the cowl and of the vehicle, $y = 0$

Flight history		$u\ (m)$	$w\ (m)$
$t = 720s$			
$\alpha_f = 0^o$	Vehicle	-0.0073	0.0156
	Cowl	-0.0039	-0.0142
$\alpha_f = 1^o$	Vehicle	-0.0073	0.0181
	Cowl	-0.0039	-0.0142
$t = 3600s$			
$\alpha_f = 0^o$	Vehicle	0.0114	0.0640
	Cowl	-0.0038	-0.0142
$\alpha_f = 1^o$	Vehicle	0.010	0.0803
	Cowl	-0.0044	-0.0142

Once the aerothermoelastic deflections have been studied, the uncertainty propagation analysis is performed for the two uncertain variables corresponding to the amplitude of the deformations.

6.3 Uncertainty Propagation Results

The uncertainties associated with thermal deflections of the vehicle and cowl were propagated through the analysis and their impact on the axial force, F_x are quantified. The 2D MASIV code predicts a force per unit length which is multiplied by the width of the cowl, 2.1 m, to give a force F_x in N. In Table 6.6, the amplitude, ξ_1, of the deformation of the vehicle is assumed to vary between 0 and 1 and it corresponds to the deformation observed during the first hour of the flight. The amplitude of the deformation of the cowl, ξ_2, varies between -0.4 and 1 to cover the range of variation encountered during the first hour of flight and encompass the deformation shape which varies significantly from the centerline to the sides of the cowl where it is bonded to the vehicle.

A convergence study is performed to determine the degree of the polynomial for the response surface which yields to an accurate approximate the analysis. A 5th order poly-

Table 6.6: Displacement bounds and PDF for uncertainty propagation

	Variable	Lower Bound	Upper Bound	PDF
Vehicle deformation	ξ_1	0	1	uniform
Cowl deformation	ξ_2	-0.4	1	uniform

nomial response surface was constructed based on $(5+1)^2 = 36$ analysis runs; i.e. 6 collocation points for the 2 random variables. Using this information, 50000 IMCS were performed on the polynomial response surface generated by extended stochastic collocation (SCE). The SCE approach is chosen so that to prevent extrapolation and thus captures the boundaries of the uncertain parameters in the design space accurately, which is important since the minimum and maximum values of F_x are located at the boundary of the uncertain design space. The accuracy of the polynomial response surface is evaluated by comparing its prediction with the analysis at 77 uniformly–distributed reference points that are different from the collocation points. For this case, the maximum error is less than 0.8% of the deterministic value for all equivalence ratios and angles of attack for the 81 test points. Therefore the polynomial response surface is considered to be a good approximation of the MASIV analysis. Mean and standard deviation predicted by IMCS and numerical quadrature were within 0.7%. The response surfaces are shown in Figs 6.18(a) to 6.18(d). The relation between both uncertain variables and the force F_x is highly dependent on the angle of attack and Mach number. A low angle of attack, ξ_1 and ξ_2 affect significantly the engine performance. At higher angle of attack, xi_2 prevails, i.e. the deformation of the cowl prevails. The importance of each variable is quantified in a later section using the Sobol's sensitivities.

The results of the uncertainty propagation study are shown in Fig. 6.19(a). The black line corresponds to the predicted axial force as a function of angle attack for two different equivalence ratios, $ER = 0.5$ and $ER = 1.0$. Examining the deformed configuration ($\xi_1 = 1$ and $\xi_2 = 1$) indicates that the performance of the engine is affected by the deformation.

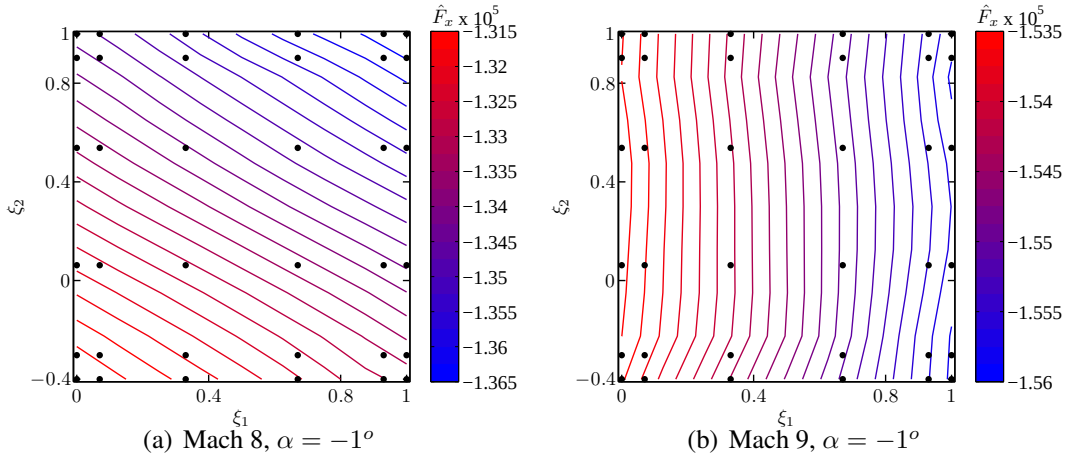

(a) Mach 8, $\alpha = -1^o$ (b) Mach 9, $\alpha = -1^o$

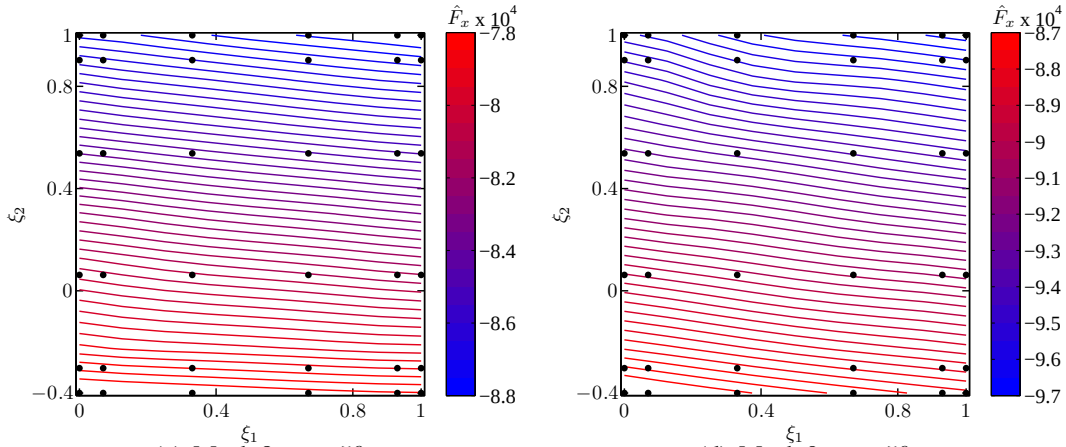

(c) Mach 8, $\alpha = 5^o$ (d) Mach 9, $\alpha = 5^o$

Figure 6.18: Response surfaces and collocation points for $\alpha_f = 0^o$, $ER = 0.5$

The vehicle deforming upwards and the cowl deforming downwards increase the magnitude of the axial force. This is due to the additional compression that occurs in the deformed inlet as well as an increased mass flow rate in the engine. In Fig. 6.19(a), the grey areas represent the full range of the axial force given the uncertainty in the deformation of the geometry. The change of performance is relatively small in magnitude and varies with the angle of attack from 4% to 28% of the value predicted for the undeformed configuration at $ER = 0.5$. The mean values are indicated with the dotted line. Error bars indicate the value of the mean plus or minus the standard deviation. The same deformation shapes obtained for Mach 8 are used to perform the same analysis of the engine performance at Mach number of 9. The increase in Mach number indicates whether the same level of deformations have a different effect on engine performance at another flight condition. The results are shown in Fig. 6.19(b). This level of deformations have a comparable impact on the engine performance at Mach 9. This information is useful in a design process when estimating the level of acceptable deformation.

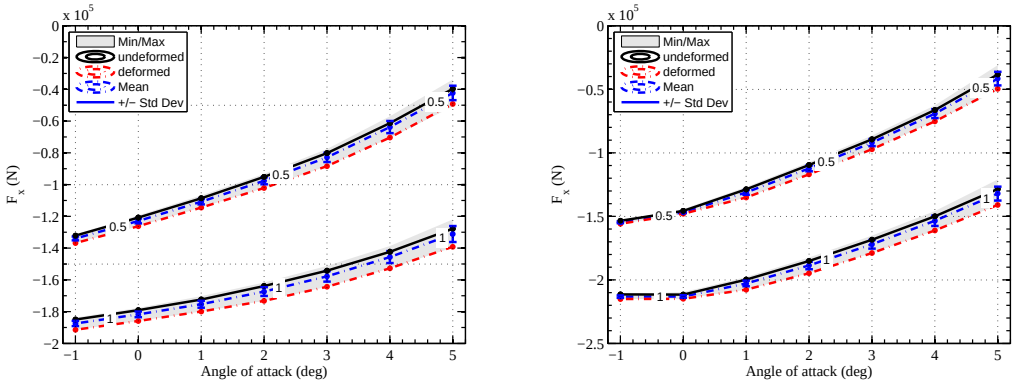

(a) Mach 8 (b) Mach 9

Figure 6.19: Uncertainty propagation results for $\alpha_f = 0^o$

In Fig. 6.20, the results of the uncertainty propagation analysis are normalized with respect to the value for the undeformed configuration and compared for two different trajectories. The first trajectory corresponds to a level flight for one hour at $\alpha_f = 0^o$ angle of attack at Mach 8, and an altitude of 26 km. The second one corresponds to a flight angle

of attack of $\alpha_f = 1^o$. The vertical deformation at the leading of the vehicle is 25% higher in the second case because of the additional increase of temperature due to the variation in this specific flight condition. The difference between both cases is relatively minor. The cowl deformations are almost equal in both cases, therefore it appears that the cowl is the principal contributor to the effect on propulsion performance.

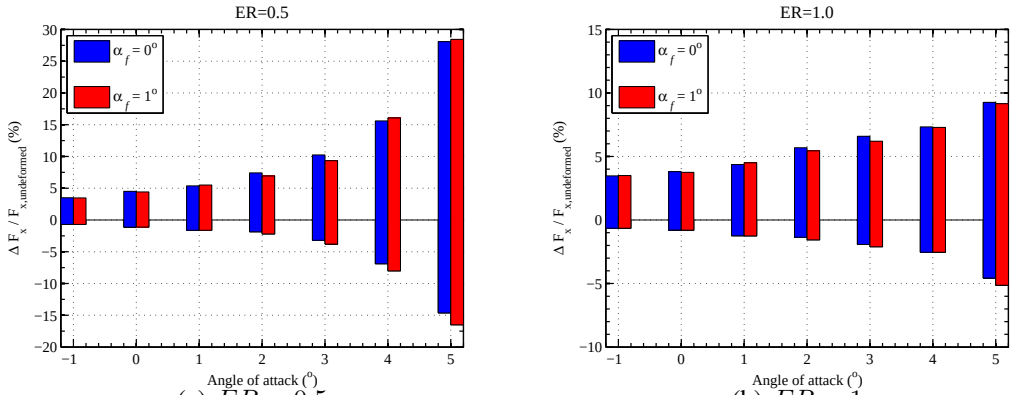

(a) $ER = 0.5$ (b) $ER = 1$

Figure 6.20: Comparison of uncertainty propagation results for two different trajectories, $M_\infty = 8$

The output probability distribution extracted from IMCS results are shown in Figs. 6.21, which indicates that there is a significant probability that the magnitude of the axial force increases due to the deformation. In each figure, the horizontal axis shows the range of the axial force. The PDF of the output, as represented by the bars, indicates the regions with higher probability. The CDF, depicted with the curve, gives the probability that the output is smaller than the given value of the output $f(\xi)$: for instance, the probability that $\|F_x\|$ is less than the deterministic value is indicated by the symbols in each figure.

The probability of failure, p_f is defined as the probability that the magnitude of the axial force is less than the deterministic value. Its value is calculated based on the IMCS results the CDF. It varies from a few percent to 34% at 5^o angle of attack as illustrated in Fig. 6.22. These results clearly demonstrate the additional information which is obtained by incorporating uncertainty in propulsion analysis problems [172].

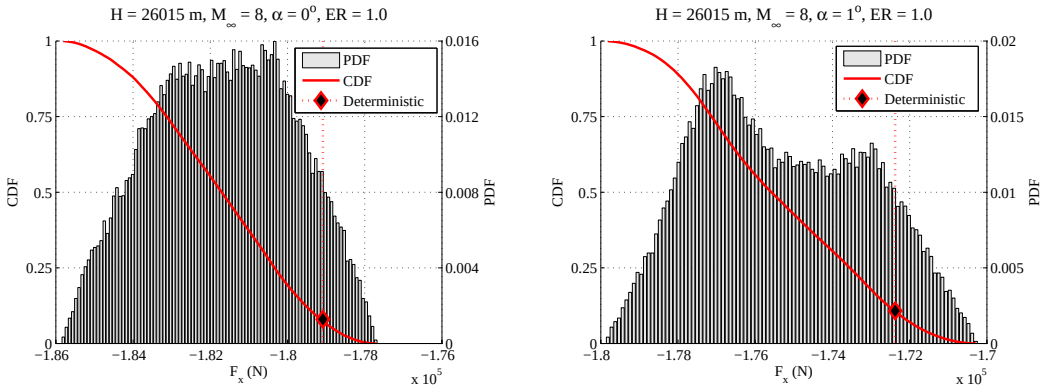

(a) F_x, $\alpha = 0$ (b) F_x, $\alpha = 1$

Figure 6.21: Uncertainty propagation results for Mach 8, $\alpha_f = 0^o$, $t = 1h$, $ER = 1$

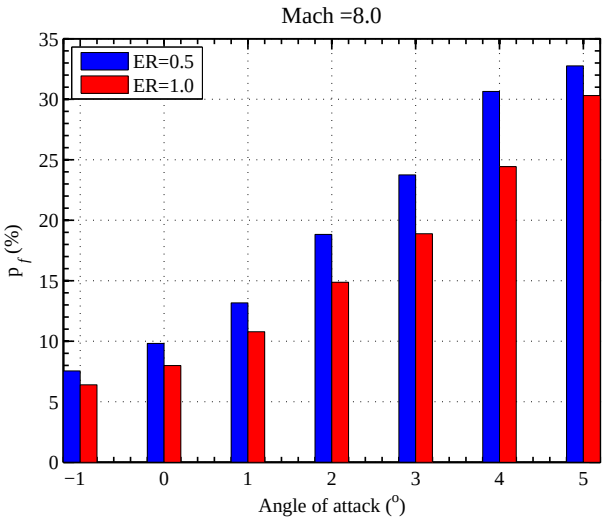

Figure 6.22: Probability of failure

To show the effect of keeping a constant equivalence ratio, ER, in the undeformed configuration, a similar study is performed without prescribing constant fuel flow mass rate. Results shown in Figs. 6.23(a) and 6.23(b) indicate that there is a significant increase in the effect of deformation on the change in axial force for both Mach 8 and Mach 9. The variation range increases to up to 50% at an angle of attack of $\alpha = 5^o$ and $ER = 0.5$. In addition more fuel is injected in the combustor as illustrated in Fig 6.23(c). The range of the vehicle may decrease. In Fig. 6.23(d), the change in maximum pressure is depicted. The effect of deformation increases maximum pressure in the combustor which may affect significantly the chemistry of the combustion process. It is important to note that the reaction rates are interpolated from a database based on the local temperature. Currently the database is limited and its extension to a wider range of temperature is planned for the future.

6.4 Sobol's Sensitivities

The sensitivity analysis is used to identify the contribution of each variable in the uncertainty of the engine performance. The results are shown in Table. 6.7. The variances associated with the deformation of the airframe and the cowl alone, D_1 and D_2 respectively are the main contributors. The interaction between the two deformations is negligible. The normalized Sobol's sensitivities are depicted in Figs. 6.24 and 6.25 for Mach 8 and 9 respectively. At Mach 8, regardless of the angle of attack, the main contributor is the deformation of the cowl. However at Mach 9 and small angles of attack, the main contributor is the deformation of the airframe, as previously shown in Fig. 6.18. At these flight conditions, the compression shocks due to the inlet enters in the engine behind the cowl, making deformation of the cowl less important. At higher angle of attack, the shocks move closer to the leading edge of the cowl. The shock structure is therefore more sensitive to its geometry, causing it to become the main contributor to the uncertainty in F_x.

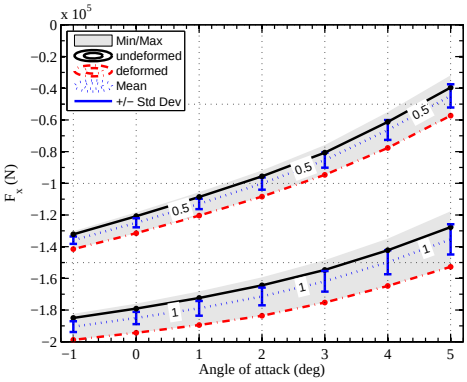

(a) F_x, Mach 8

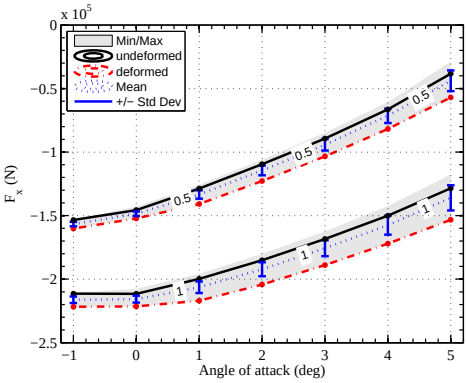

(b) F_x, Mach 9

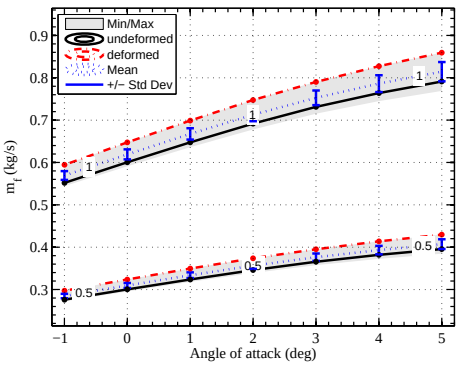

(c) Mach 8, Fuel flow mass rate, $\dot{m}_f$

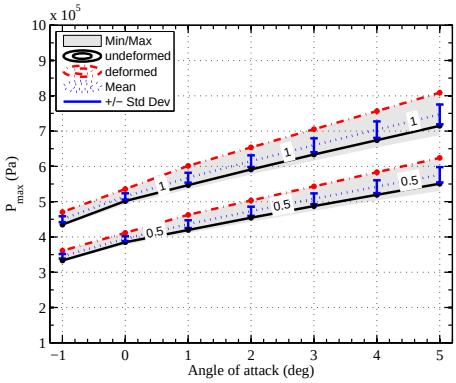

(d) Mach 8, Maximum Pressure in the combustor

Figure 6.23: Uncertainty propagation results for $\alpha_f = 1^o$, constant ER

Table 6.7: Sobol's Sensitivities as function of α,

	α [^{o}]	$D \times 10^5$, $ER = 0.5$			$D \times 10^5$, $ER = 1$		
		ξ_1	ξ_2	$\xi_1\xi_2$	ξ_1	ξ_2	$\xi_1\xi_2$
	-1	3.35	10.96	0.00	7.24	18.70	0.01
	0	3.55	19.87	0.00	6.60	25.84	0.00
	1	2.47	26.13	0.06	5.40	41.62	0.10
M_∞ = 8	2	1.60	47.17	0.07	4.92	71.77	0.07
	3	0.62	82.98	0.04	3.41	106.36	0.00
	4	0.36	146.11	0.10	0.68	142.64	0.07
	5	1.55	204.56	0.01	0.02	254.57	0.17
	-1	4.66	0.01	0.00	8.67	0.23	0.00
	0	3.84	0.95	0.04	7.33	2.67	0.05
	1	3.70	30.22	0.00	6.69	41.63	0.00
M_∞ = 9	2	3.06	50.85	0.01	6.31	79.94	0.00
	3	1.26	73.67	0.03	3.74	113.58	0.03
	4	0.12	123.84	0.01	0.87	163.14	0.06
	5	1.60	287.43	0.08	0.09	298.46	0.31

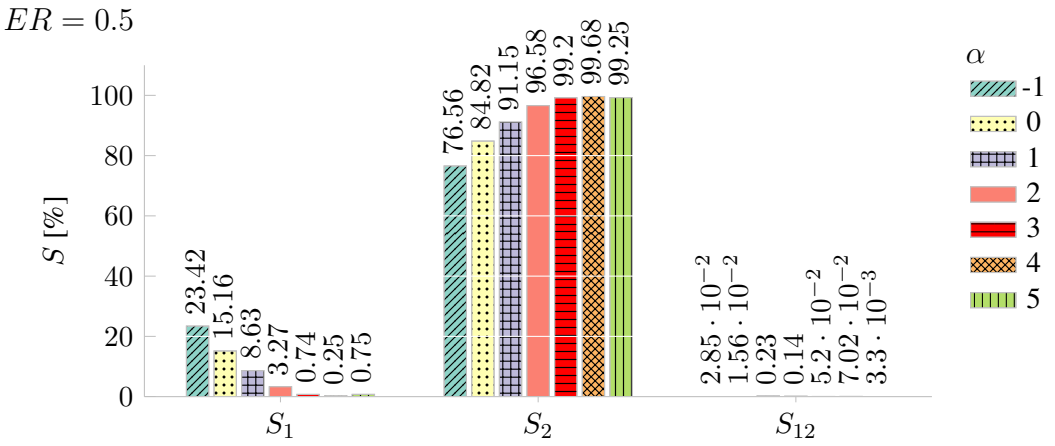

(a) $ER = .5$

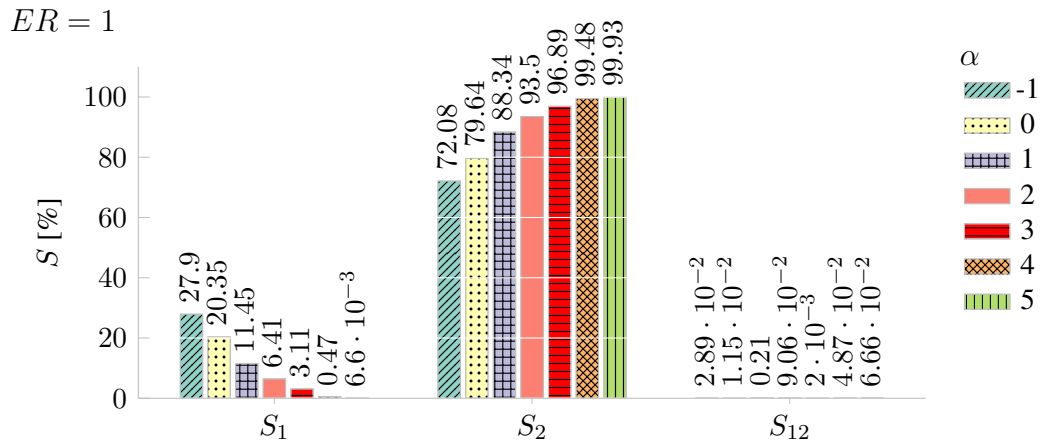

(b) $ER = 1$

Figure 6.24: Sobol's Sensitivities as function of α, M_∞ = 8

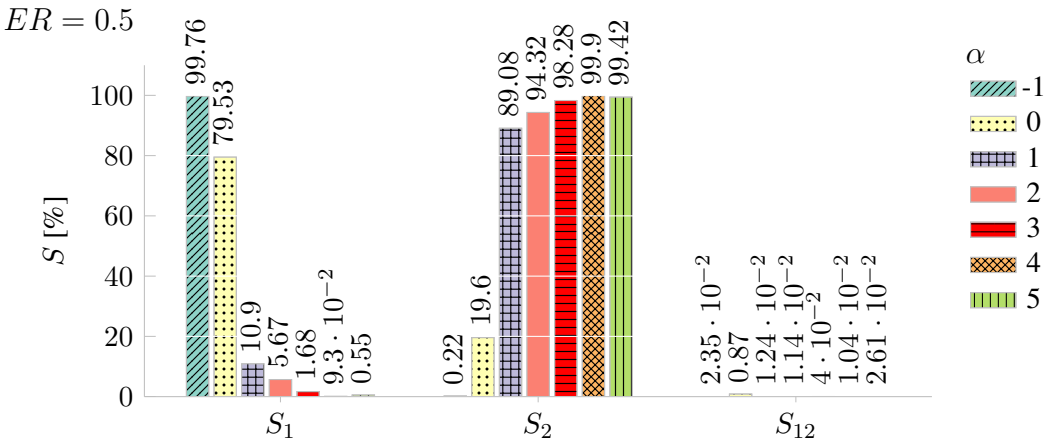

(a) $ER = .5$

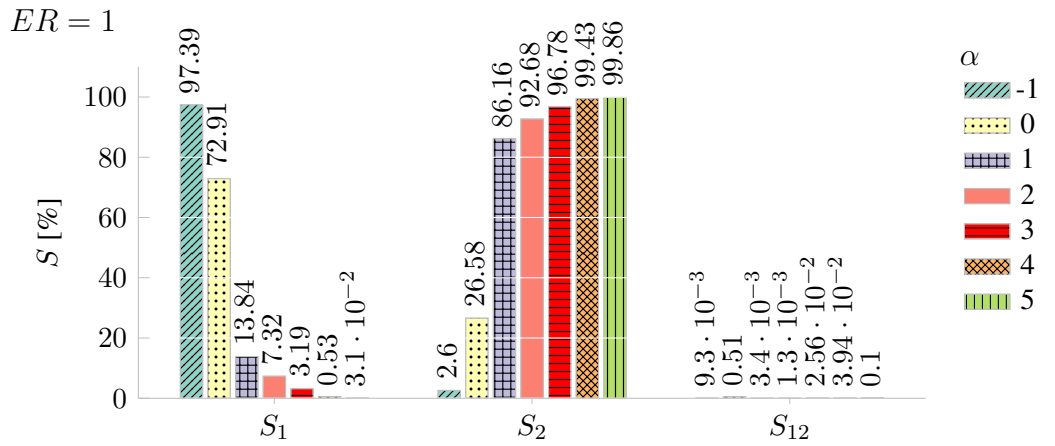

(b) $ER = 1$

Figure 6.25: Sobol's Sensitivities as function of α, M_∞ = 9

CHAPTER 7

AEROELASTIC RESULTS

In this chapter, preliminary results are presented to illustrate the RBF mesh deformation and then test the new system identification method. Next, the aeroelastic simulations are performed for a double–wedge section and a low aspect ratio wing and compared with results obtained in Ref. [84].

7.1 Mesh Deformation

A simple example is used to illustrate the effect of the radial function (RF) choice on the shape of the fluid–structure interface. A simple two dimensional mesh composed of uniformly distributed nodes is considered. The deformed mesh is obtained for several RFs, presented in Table 2.3, and illustrated in Fig. 7.1(a) and Fig. 7.1(b) for volume spline and gaussian RF respectively. The mesh covers the unit square. The lower boundary is a moving boundary. The upper and side boundaries are fixed. Five driving points are distributed on the outer boundary to control the mesh deformation and are represented by the diamonds. The deformation at the moving boundary is prescribed at the drivers points, equal to $w = 0.2 \sin(2\pi x)$. Note that the deformed boundary defined by the fluid mesh, represented by empty circles, depends on the RF used and does not necessarily coincide with the deformed boundary defined by the FEM nodes, represented with the full circles. For instance, volume spline tends to interpolate linearly between driving points whereas gaussian RF smoothes the interpolation.

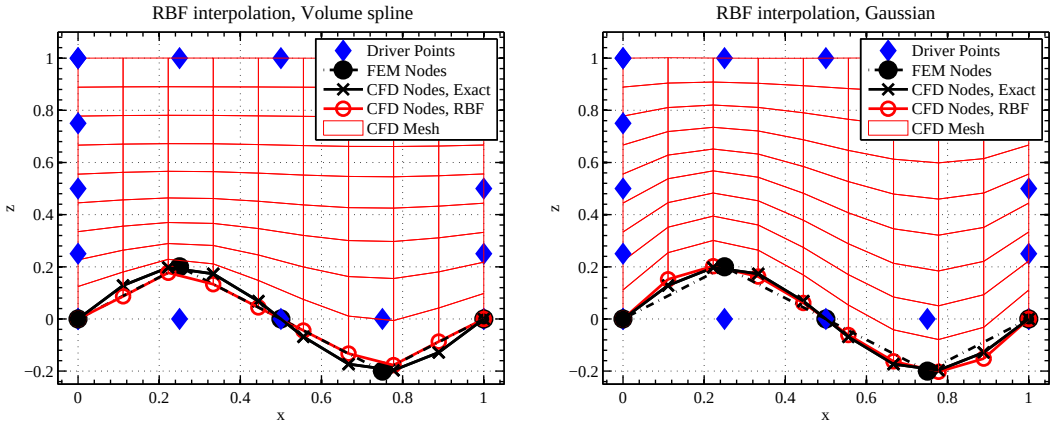

(a) Volume Spline (b) Gaussian

Figure 7.1: Illustration of a mesh deformation using two different radial functions for $w = 0.2\sin(2\pi x)$

Quantitatively, the difference between the RBF prediction and the exact value of the deformation at the interface is computed and given in Fig. 7.2(a) for the error metric presented in Section 3.4, Eqs. (3.28)–(3.30). The RF are given in details in Table 2.3. Depending on the RF considered, the error at the moving interface varies from less than 5% to 25% of the maximum deformation. Duchon's thin plate spline, Hardy's multiquadratics, Wendland's C^2 and Gaussian RF have the better accuracy. However, in a practical case, the analytical expression of the deformed surface at the interface is not available. Therefore, the prediction of the RBF is also compared to a piecewise linear interpolation between the driving points. The results are shown in Fig. 7.2(b). The volume spline, Euclid's hat, and Wendland's C^0 RF's give a very good approximation of a piecewise linear interpolation with a maximum error of less than 2% of the maximum deformation.

This example illustrates the effect of the choice of the RF. The driving points are sparsely distributed on the boundary, therefore the range of error is artificially large. As mentioned in Section 3.4, the mesh deformation in the aeroelastic studies is based on volume spline.

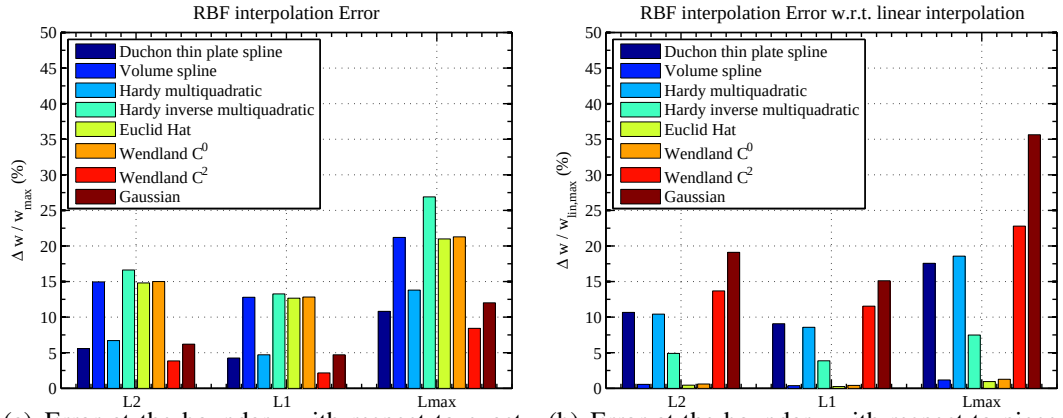

(a) Error at the boundary with respect to exact value

(b) Error at the boundary with respect to piecewise linear interpolation

Figure 7.2: Error quantification at the moving boundary using different radial functions for a deformation of $w = 0.2 \sin(2\pi x)$ at the $z = 0$ boundary

7.2 System Identification

The stability of a low aspect ratio wing combined with piston theory is used to verify the SI methods considered in this study before integrating them into more realistic studies using CFD based loads.

The p–method described in Section 3.5.3 has not be used before. Therefore it is necessary to verify this new approach with a simple model before implementing its usage for a more complicated aeroelastic model. The three dimensional low aspect ratio wing is considered. The aerodynamic loading is represented by the classical 3^{rd} order piston theory. The Mach number at which the wing flutters at a given altitude of 12 km (40000 ft) is predicted using the three different system identification methods: ARMA, LSCF and the p–method. Furthermore, the linearization of piston theory allows an exact calculation of the aerodynamic influence matrices, $\mathrm{K_A}$ and $\mathrm{C_A}$. It provides an additional approach for evaluating the frequencies and damping of the system, referred to as *Linearized* in the rest of this document.

Frequencies and damping coefficients as function of the Mach number are shown in Figs. 7.3(a) and 7.3(b) respectively. The symbols correspond to the Mach number at which

a transient simulation is performed. Each symbols and color correspond to a different mode. The different types of lines correspond to different SI methods. Therefore to each mode correspond 1 color, 1 symbol and 4 different line types. In this case, the lines cannot be differentiated from each other since the predictions of each method perfectly match with the others.

The fitting error associated with each method is small, close to machine precision, and the small difference in the prediction of the flutter Mach number is summarized in Table. 7.1. In the case of the p–method, the generalized loads are the quantities being fitted. The error is relatively small and does not affect flutter boundary predictions when compared with the exact approach. All SI methods agree.

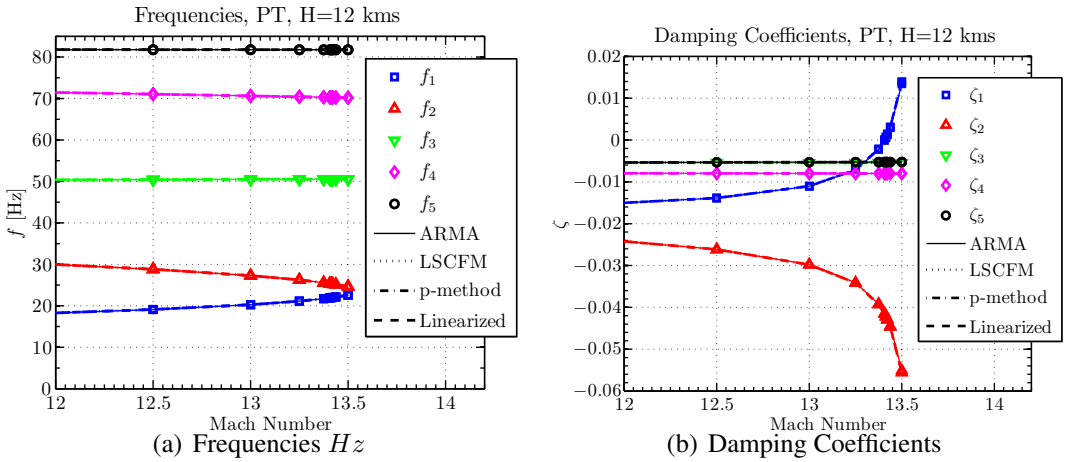

(a) Frequencies Hz (b) Damping Coefficients

Figure 7.3: Flutter analysis for the low aspect ratio wing using 3^{rd} order Piston Theory at an altitude of 12 km (40000 ft)

	ARMA	LSQCF	p–method	Linearized
Fitting Error, L_2 (%)	10^{-11}	10^{-11}	10^{-5}	N/A
Flutter Mach Number	13.4075	13.4075	13.4054	13.4054

Table 7.1: Flutter Mach number predicted using different system identification methods with 3^{rd} order Piston theory aerodynamics

7.3 Two Dimensional Typical Section

7.3.1 Overview

The flutter Mach number associated with a double wedge typical section is examined first. The typical section, shown in Fig. 7.4, and presented in Section 4.1, is characterized by pitch (α) and plunge (h) degrees of freedom. The mode shapes correspond to rigid body motions.

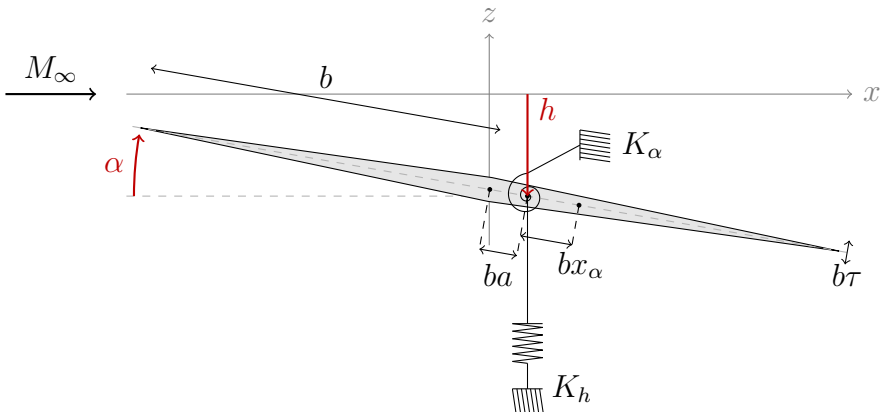

Figure 7.4: Two degree–of–freedom typical wing section geometry of a supersonic vehicle

The stability of the two–dimensional typical section is investigated using CFD. The Navier-Stokes equations are solved with a Spalart-Allmaras turbulence model. Goldberg turbulence model, which is an acceptable turbulence model for hypersonic flow [154], is also considered for comparison. The boundary condition at the wall corresponds to an adiabatic wall (AD).

7.3.2 Meshing Strategies

The guidelines for meshing for hypersonic flows are given in Section 3.6.5 and illustrated in this section for the case of the typical section. Different fluid domains shown in Figs. 7.5(a), 7.5(b), and 7.5(c) have been considered based on a previous similar study

in Ref. [84]. In hypersonic flow the domain of dependency of the pressure on the airfoil is limited. Therefore, it is reasonable to consider only a limited region around the airfoil. In all the domains, the leading edge shock is contained inside the mesh for all the flight conditions considered. The boundary layer returns to supersonic speeds before it exits the fluid mesh. The spacing close to the airfoil has to ensure that the required condition for accurate capture of turbulent flows, $y^+ < 1$, is satisfied. Grid symmetry is preserved by importing the lower half of the grid in CFD++ and replicating it in the upper half.

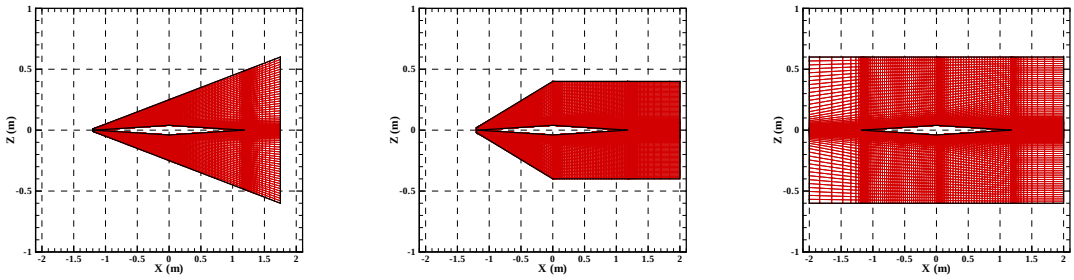

(a) Grid 1 (b) Grid 2 (c) Grid 3

Figure 7.5: Possible grids for the typical section

Grid 1 and Grid 2, illustrated in Fig. 7.5(a) and Fig. 7.5(b) respectively, fit the shock structure at the leading edge, whereas Grid 3 in Fig. 7.5(c) represents a larger fluid domain to accommodate for fixed outer boundaries when deforming the mesh.

This example involves only rigid body displacements and thus does not require a FE model. Two different strategies are considered to deform the mesh: (1) a moving mesh with fixed outer boundaries and (2) a fully moving mesh. The first mesh deformation strategy enforces fixed outer boundaries, which may be a requirement due to the imposition of boundary conditions in the CFD solver. The driving points are uniformly spaced on the airfoil surface and around the outer boundary of the fluid domain, as shown in Fig. 7.6(a) in the case of 96 points, 17 on each boundary. The deformed mesh is depicted in Fig. 7.6(b) for a large deformation corresponding to a pitch angle of $\alpha = 10^o$. This deformation is not representative of the small deformation that occur in the calculation of the transient

response of the aeroelastic system. However, it illustrates the smoothness of the RBF mesh deformation scheme.

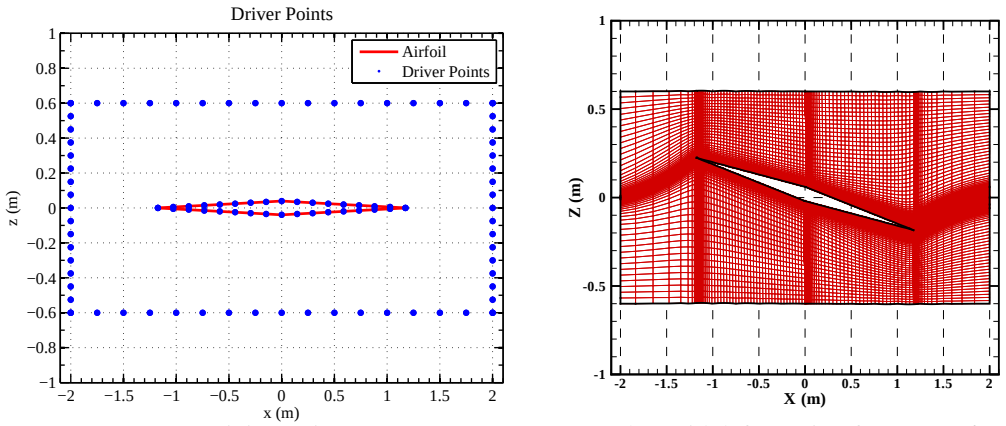

(a) Driving points (b) Grid deformation for $\alpha = 10^o$

Figure 7.6: Grid deformation using 96 points and fixed outer boundaries

Note that wiggles appear at the top and bottom boundaries and at the airfoil surface. It is necessary to quantify the error introduced by the RBF mesh deformation. Since the airfoil undergoes rigid body motions, the analytical form of the deformation is known and is compared to that given by the RBF for different RF. For each mode, the airfoil is deformed and both deformations are compared. The results are presented in Figs 7.7(a) and 7.7(b) for two different sets of driving points.

In both cases, the driving points are located at the boundaries of the CFD mesh as depicted in Fig. 7.6(a). In Fig. 7.7(a), 96 points are used to drive the mesh. The maximum error varies from 1% of the maximum deflection up to 3.4% depending on the RF chosen. Volume spline, Euclid's hat and Wendland's C^2 RF give the best approximation. It shows that these RFs approximate a linear interpolation more accurately. In Fig. 7.7(b), 426 driving points are considered. The error is decreased by more than an order of magnitude to less than 0.05% for most of the RF's. It shows that in the case of constrained outer boundary, the number of driving points need to be carefully chosen to preserve the shape of the moving airfoil.

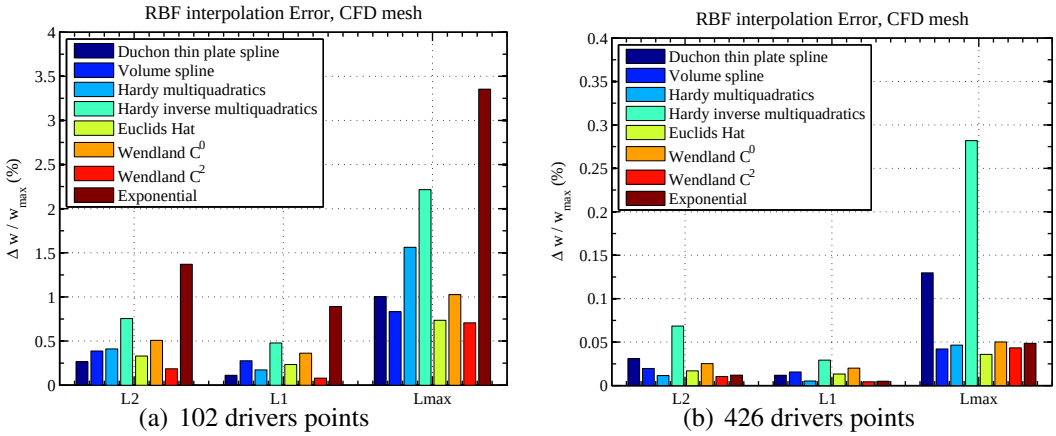

(a) 102 drivers points (b) 426 drivers points

Figure 7.7: Effect of the choice of the radial basis function (Grid 3)

A fully moving mesh approach is considered next. For the 2D section, the degrees of freedom are the rigid body motions. Thus, the number of driving points is not important as long as there are enough points to capture each rigid body motion, pitch and plunge. In theory, 3 non-collinear driving points are sufficient to create an accurate RBF interpolant. In practice, a set of 10 points is considered to ensure better conditioning of the RBF system, given by Eq. (2.56). The driving points are the leading and trailing edges, both midchord points on the top and bottom surface of the airfoil and 6 additional points far from the airfoil. The deformations associated with both rigid body motions of the airfoil, plunge and pitch, are computed exactly, as depicted in Figs 7.8(a) and 7.8(b), respectively. As mentioned in Section 3.4, a first order polynomial in the RBF interpolation ensures that it is the case. Based on this preliminary results on mesh deformation, Volume spline is chosen as the RF and the mesh is a fully moving mesh.

Grid refinement studies are performed first to examine the effect of grid resolution on the CFD simulation results at $M_\infty = 12$, $H = 12$ km. Four different grids with varying levels of refinement are generated. Convergence of the resultant forces and moments is examined for increasing number of cells. A grid with 45k cells predicts the aerodynamic forces with less than 1% error when compared to a grid with 100k cells. Therefore this grid

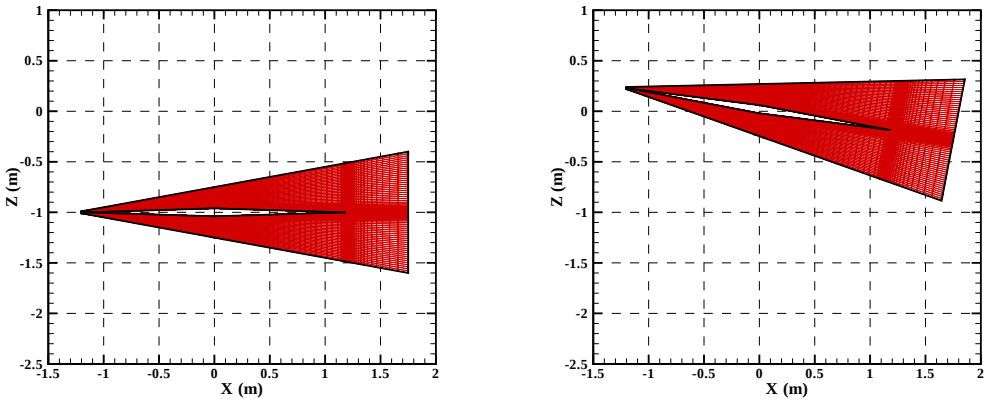

(a) Grid deformation for $h = 1$

(b) Grid deformation for $\alpha = 10^o$

Figure 7.8: Grid deformation using 66 points and moving outer boundaries (Grid 1)

is used for all subsequent simulations in this thesis.

7.3.3 Aeroelastic Calculations

The parameters related to the time–stepping and the computational cost for an aeroelastic transient simulation are given in Table 7.2. The main contributor to the computational cost associated with the aeroelastic simulations is the CFD calculation. Each aeroelastic simulation requires 2500 initial iterations to converge the steady state solution of the N–S equations. For each time step, several subiterations of the CFD solver are required to march the fluid in time as explained previously. At each time step, the new node locations are written in the mesh file and the CFD code is restarted. It generates significant amount of additional processing time which would not be present in a fully integrated aeroelastic solver.

Verification of the SI methods The aeroelastic simulations are performed at constant altitude of 12 km and different Mach numbers. For each Mach number, the frequencies and damping are computed using each SI method presented in Section 3.5. The results corresponding to Euler aerodynamics are presented first in Fig. 7.9. Frequencies and damping

Number of time step	1000
Time step	0.125 ms
Number of subiterations per time step	30
Number of cells	45k
Number of processors	2
Processor	Intel(R) Xeon(R)CPU X5650, 2.67GHz
Computational time	10 hrs

Table 7.2: Parameters and computational cost of 2D calculations using Navier–Stokes aerodynamics

coefficients as functions of the Mach number are shown in Figs. 7.9(a) and 7.9(b) respectively. The symbols correspond to the Mach numbers at which a transient simulation is performed. Each mode is identified by a unique color and symbol. The different types of lines correspond to different SI methods. The thicker line corresponds to the results obtained using 3^{rd} order PT combined with ARMA. The symbols correspond to the Mach numbers at which the aeroelastic simulations are computed using Euler aerodynamics. The three SI methods predict identical frequencies and damping coefficients, and therefore there is no distinction between the lines. The predicted flutter Mach number is 12.1 which is in good agreement with that obtained using PT. This agreement is expected as PT is a good approximate model for thin bodies oscillating in hypersonic flows.

Next, viscosity is introduced. The results obtained are presented in Fig. 7.10 for the case of Grid 3 with moving outer boundaries and 10 driving points. The crosses refer to the results computed using NASA Langley CFL3D computational aeroelastic code (CFL3D) in Ref. [84]. The symbols correspond to the Mach numbers considered. The different lines correspond to the different SI methods which are almost identical before flutter occurs at Mach $M_\infty \simeq 11.3$. The damping coefficients are more sensitive to the SI method. The flutter Mach number predicted by each method corresponding to the different grids, and moving mesh strategies are given in Table. 7.3. Adding more driving points ensures that the motion of the airfoil is captured more accurately and the flutter prediction converges

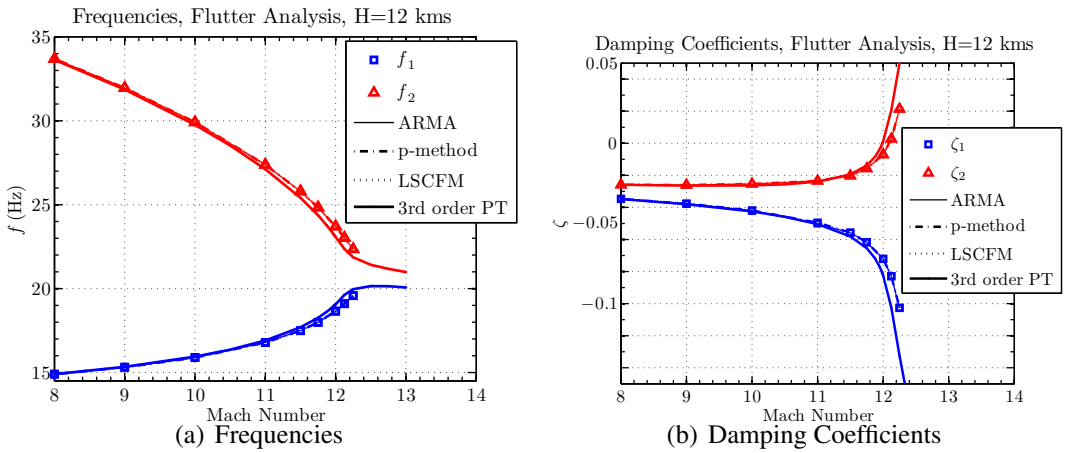

(a) Frequencies (b) Damping Coefficients

Figure 7.9: Aeroelastic stability analysis using Euler aerodynamics for the typical section, H = 12 km

toward the fully moving mesh approach. The three SI methods agree with each other. The flutter Mach number is predicted within less than 1% error depending on the grid or the mesh deformation strategy. Compared to the results obtained with CFL3D, the flutter onset occurs at a lower Mach number. The difference is approximately 6%.

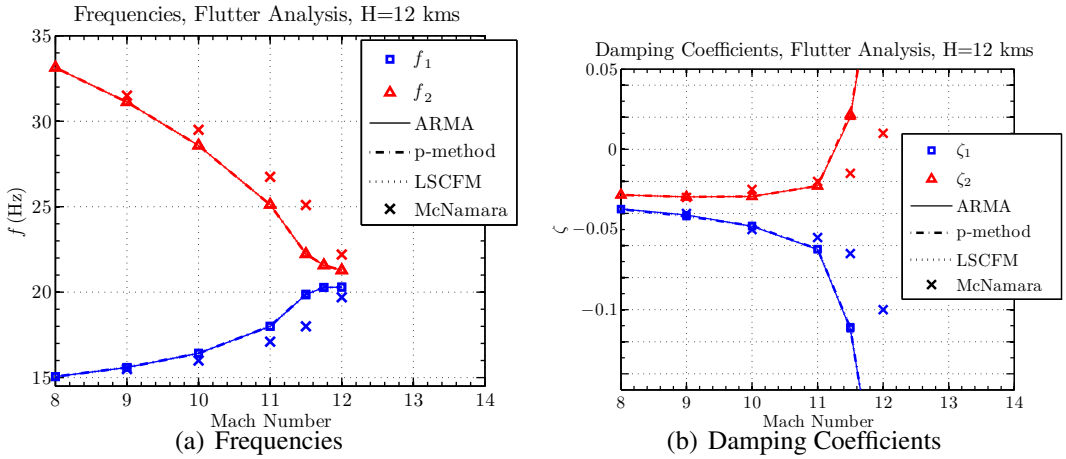

(a) Frequencies (b) Damping Coefficients

Figure 7.10: Aeroelastic stability analysis using N–S aerodynamics for the typical section, H = 12 km

This preliminary study illustrates the use of RBF in a typical aeroelastic calculation and verifies the usage of the SI methods. Compared to the results obtained with CFL3D, the

		Number of driving points	ARMA	LSQCF	p–method
All moving	Grid 1	66	11.32	11.32	11.32
	Grid 2	66	11.32	11.32	11.32
	Grid 3	**10**	**11.27**	**11.26**	**11.26**
	Grid 3	96	11.34	11.34	11.32
	Grid 3	420	11.25	11.25	11.25
	Grid 3, fine	12	11.31	11.31	11.32
Fixed outer boundary	Grid 3	96	11.32	11.32	11.32
	Grid 3	420	12.27	11.27	11.27
	CFL3D		11.9		N/A

Table 7.3: Flutter Mach number for the typical section using Navier–Stokes aerodynamics

flutter onset occurs at a lower Mach number, by approximately 6%. Note that in all cases presented, the three SI methods predict the same flutter Mach number.

Effect of Turbulence and Gas modeling The effect of turbulence on flutter boundary prediction is investigated. Euler and laminar flow are compared to turbulent flow for low and high values of free stream turbulence. The one equation Goldberg turbulence model is also considered. Considering various turbulence models provides additional material for explaining the difference between CFL3D calculations and the present framework. In both CFL3D and CFD++, the Spalart Allmaras turbulence model (SA) is available and is used for the flutter calculations [153]. In CFL3D v.5, the additional turbulence equation does not require any user input and the intensity of the free stream turbulence is set by the ratio $\left(\frac{\mu_T}{\mu_L}\right)_\infty = 0.009$ as boundary and initial condition of the turbulence equation. However, in CFD++, this parameter is a user input.

The results are given in Table. 7.4; note that adding turbulence decreases the flutter boundary by up to 7%. An abrupt change is observed when comparing the results for laminar flow, which is close to Euler, to those for turbulent flow. The flutter Mach number predicted for the SA model with $\left(\frac{\mu_T}{\mu_L}\right)_\infty = 1$ is close to that for $\left(\frac{\mu_T}{\mu_L}\right)_\infty = 10$. However the case of Goldberg turbulence model and $\left(\frac{\mu_T}{\mu_L}\right)_\infty = 1$ compares well with laminar flow. This

comparison illustrates the variability associated with turbulence modeling and its effect on flutter boundary.

In Table. 7.4, the results are also presented for IG and RG. At this flight condition, the effect of gas modeling is negligible for the flight condition considered.

Model		Turbulence Model	$\left(\frac{\mu_T}{\mu_L}\right)_\infty$	ARMA	LSCFM	p–method
PG	EU	–	–	12.09	12.09	12.09
	NS	Laminar	–	11.82	11.83	11.83
		SA	0.009	11.63	11.63	11.63
		SA	3	11.47	11.50	11.43
		SA	10	11.27	11.26	11.26
		Goldberg	1	11.83	11.83	11.83
			10	11.15	11.15	11.15
IG	NS	SA	3	11.53	11.52	11.52
RG	NS	SA	3	11.50	11.46	11.50

Table 7.4: Flutter Mach number for the typical section using different turbulence and gas models, $H = 12$ km

The decrease of flutter boundary with increasing turbulence can be attributed to the boundary layer that is thicker for the more turbulent cases. The larger effective thickness increases the pressure and decreases the onset of flutter. To illustrate the effect of the assumptions associated with turbulence modeling, steady pressure coefficients for different models are shown in Fig. 7.11 for $M_\infty = 12$. Euler calculations are compared with laminar flow, SA and Goldberg turbulence models for different values of $\left(\frac{\mu_T}{\mu_L}\right)_\infty$. In the case of viscous flow, a pressure peak occurs at the leading edge. Laminar flow, SA with very small $\left(\frac{\mu_T}{\mu_L}\right)_\infty$ and Goldberg model with $\left(\frac{\mu_T}{\mu_L}\right)_\infty = 1$ produce the same magnitude of pressure distribution over the airfoil. With increased turbulence level, SA with $\left(\frac{\mu_T}{\mu_L}\right)_\infty = 1$ and Goldberg model with $\left(\frac{\mu_T}{\mu_L}\right)_\infty = 10$, pressure is increased which implies increased thickness of the boundary layer and the associated effective shape. The case labeled '*S–A (mod.)*' refers to the Spalart–Allmaras model, the coefficients associated with this model are modified from their default values in CFD++ to match CFL3D's implementation. In

addition the same boundary condition as in CFL3D for the turbulence equation is used: $\left(\frac{\mu_T}{\mu_L}\right)_\infty = 0.009$. The results indicate that for this particular case the difference did affect the pressure distribution significantly. A numerical onset of transition occurs in the middle of the first half of the airfoil. The Mach number contours reveal a thicker boundary layer associated with the default settings, depicted in Fig. 7.12(a) as opposed to that predicted using CFL3D parameters shown in Fig. 7.13(a). Similarly the turbulence equation variable is depicted for both cases in Figs. 7.12(b) and 7.13(b) respectively and shows an increased boundary layer thickness when using the recommended settings in CFD++.

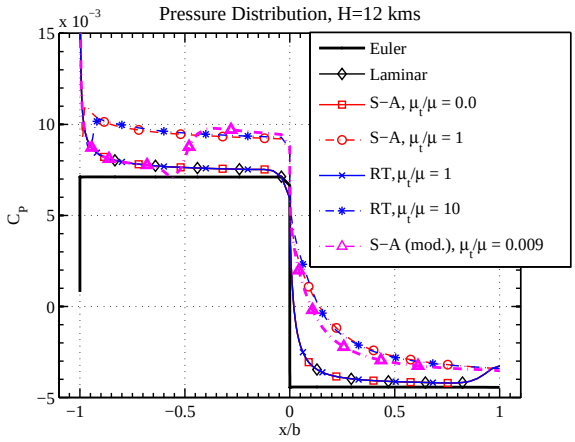

Figure 7.11: Steady pressure coefficient for different models for turbulence. $M_\infty = 12$

Stability Boundaries Additional results at different altitudes are presented in Figs. 7.14. The trends observed previously are confirmed at both higher and lower altitudes. In Fig. 7.14(a), the effect of turbulence is considered. Both lines corresponding to PT and laminar flow coincide and predict the higher flutter boundary at all altitudes. Turbulence is a modeled by the SA model and the cases of $\left(\frac{\mu_T}{\mu_L}\right)_\infty = 0.009$ (low T.) and $\left(\frac{\mu_T}{\mu_L}\right)_\infty = 10$ (high T.). The lowest flutter onset is predicted for highest turbulence case. The low turbulence case is close to the high turbulence case at low altitude. For H=21km, the flutter onset for low turbulence is close to that for laminar flow.

In Fig. 7.14(b), the effect of gas modeling is considered. Turbulence is modeled by

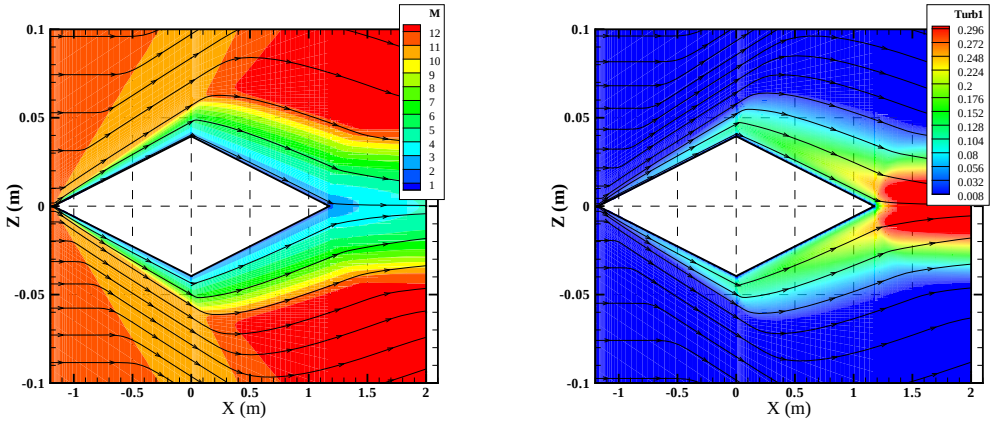

(a) Mach number (b) Turbulence variable in S–A model

Figure 7.12: Steady state solution computed using CFD++ default parameters and $\frac{\mu_T}{\mu} = 1.0$

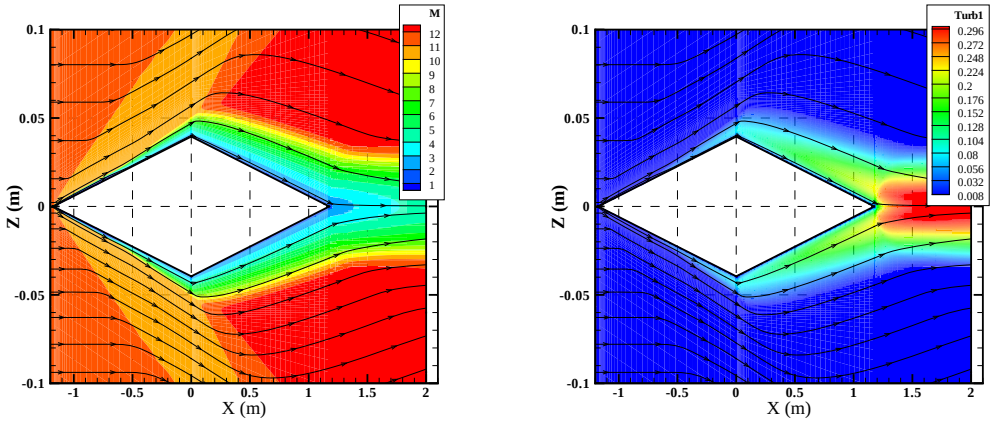

(a) Mach number (b) Turbulence variable in S–A model

Figure 7.13: Steady state solution computed using CFD++ modified parameters and $\frac{\mu_T}{\mu} = 0.009$

the SA model assuming $\left(\frac{\mu_T}{\mu_L}\right)_\infty = 3$. The three results corresponding to PG, IG, and RG models coincide.

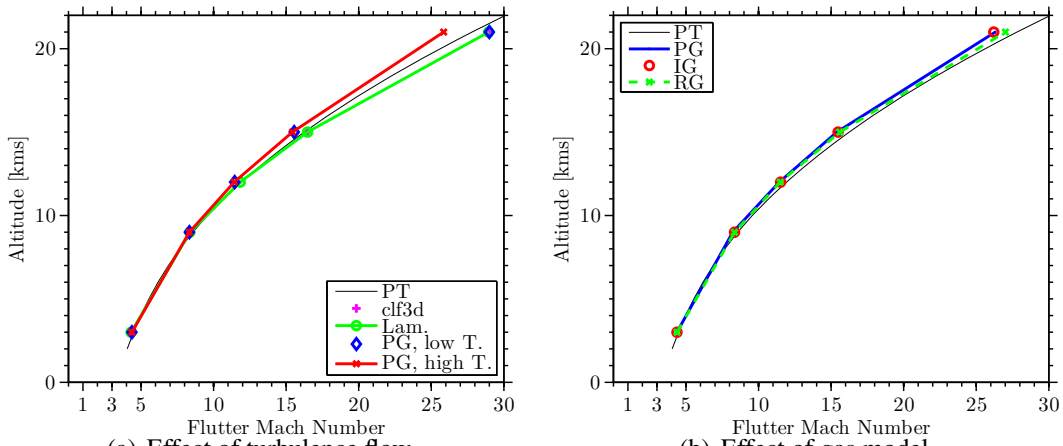

(a) Effect of turbulence flow (b) Effect of gas model

Figure 7.14: Aeroelastic stability analysis for the typical section for different turbulent flow, H = 12 km

7.4 Three Dimensional Low Aspect Ratio Wing

7.4.1 Overview

The three-dimensional low-aspect-ratio wing is shown in Fig. 7.15. The wing is based on the Lockheed F–104 Starfighter wing. Its geometry is similar to the fins control surfaces of a prospective long–duration, airbreathing hypersonic vehicles such as the X–43 or NASP. The structural model is extracted from a finite element model (FEM) created in MSC.NASTRAN and previously studied in Refs. [2] and [84]. For aeroelastic stability prediction, the FEM is reduced to the first five natural modes [84] which are depicted in Fig. 7.16. The natural modes are normalized by to their generalized mass.

The structure of the wing is represented by five natural modes depicted in Fig. 7.16. The 1327 FEM nodes are uniformly distributed on the surface of the wing as illustrated in Fig. 7.17.

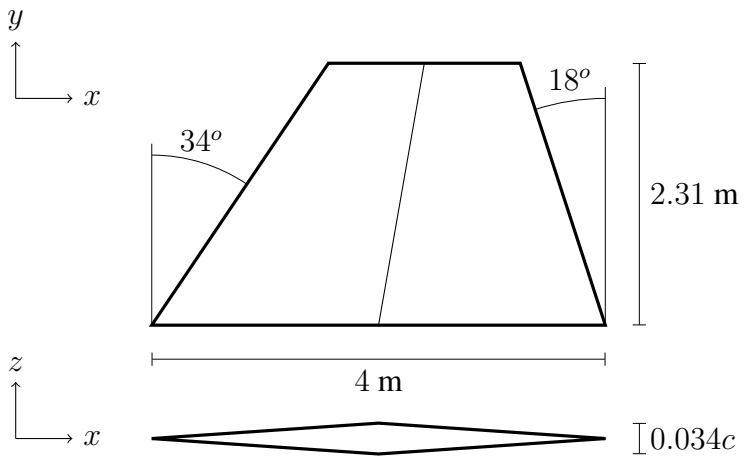

Figure 7.15: 3D low aspect ratio wing

7.4.2 Meshing Strategies

Similarly to the 2D case, different fluid domains have been considered and are depicted in Figs. 7.18(a), 7.18(b), and 7.18(c). The first two meshes, Grid 1 and 2, can be used in a fully moving mesh strategy. In this case, the driving points are only located on the wing surface and correspond to the FEM nodes. The third mesh, Grid 3, is considered to enforce a non-moving outer boundary. However, discrepancies occurred when exporting the mesh files from ICEM CFD, such as rounding errors in writing the mesh in a plot3d format which result in misalignment of the nodes at the surface of the wing. Therefore, the third mesh, Grid 3, had the best mesh quality at the surface of the wing and is used for all the cases.

The driving points are located on the wing and on the outer boundary of the mesh as illustrated in Fig. 7.19. In this example, the set of the FEM nodes is complemented with 386 points uniformly distributed on the outer boundaries of the fluid domain.

In the 3D case, the analytical form of the mode shape is not available since they are obtained using a FEM calculation. Inaccuracies are likely to appear when using the RBF mesh deformation based on the FEM points. To assess this issue, the deformed wing configuration using RBF is compared with that obtained with a piecewise linear interpolation between the FEM nodes for the second mode shape, ϕ_2. In Table. 7.5, two cases are com-

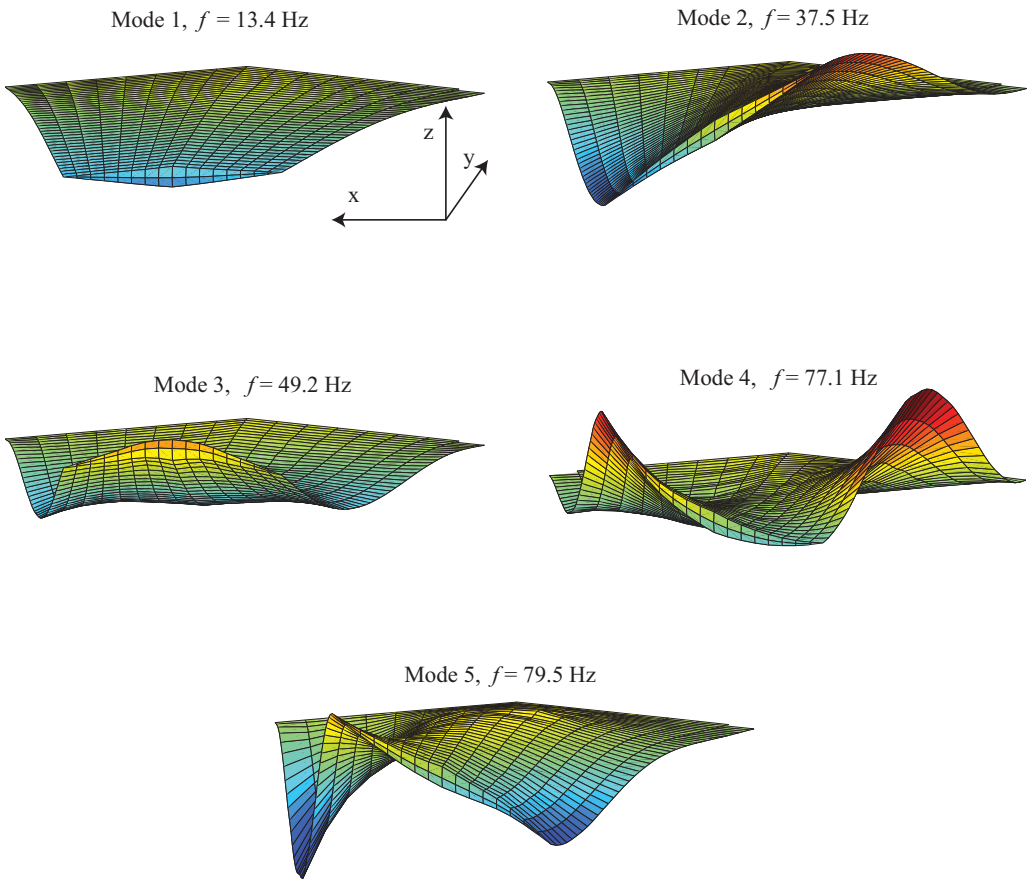

Figure 7.16: Structural model

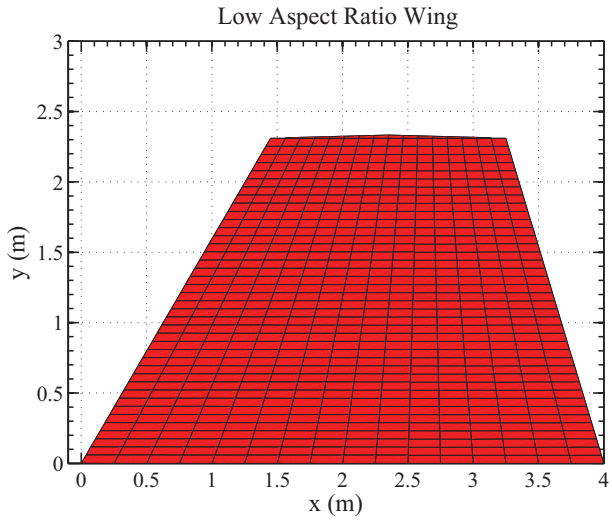

Figure 7.17: Finite element mesh of the low aspect ratio wing

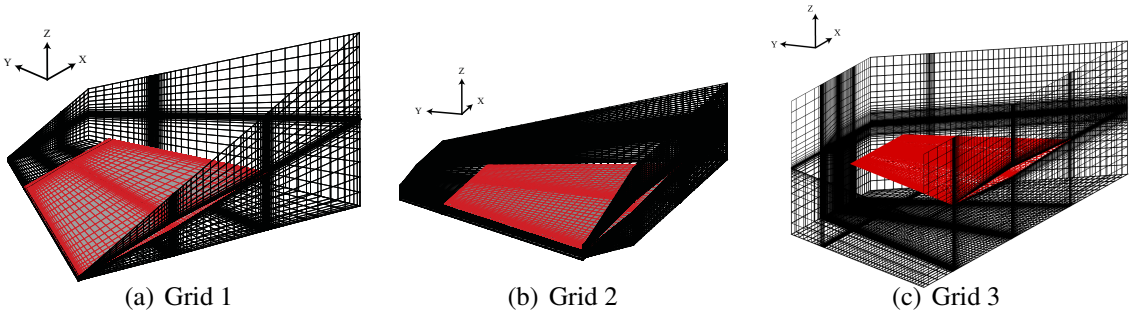

(a) Grid 1 (b) Grid 2 (c) Grid 3

Figure 7.18: CFD mesh for the low aspect ratio wing

pared for mesh 3: (1) the driving points are the FEM nodes and (2) the driving points are the CFD nodes at the wing interface.

For the first case when the FEM nodes at the surface of the wing are the driving points, the maximum difference between the deformation obtained with RBF and that based on piecewise linear interpolation is of 0.9% and 1.4% for a moving and fixed outer boundary, respectively. Adding driving points to prescribe a static outer boundary significantly affects the shape of the deformed wing.

For the second case, the fluid mesh points at the surface of the wing are the driving points. As expected, the difference between the RBF and the reference shape is completely

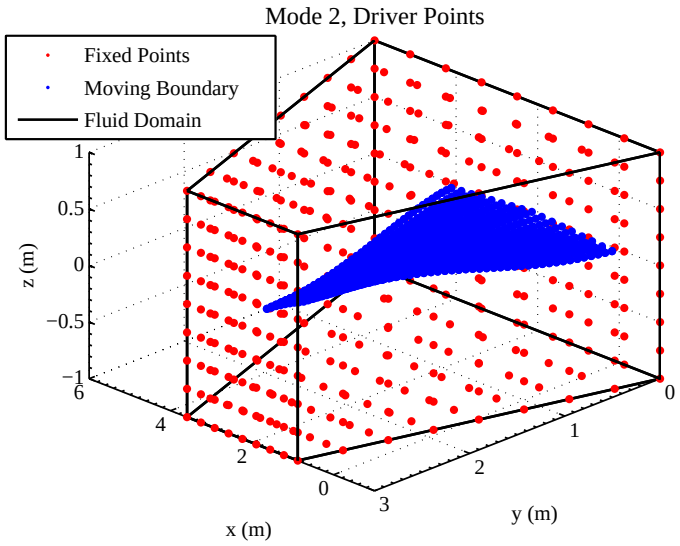

Figure 7.19: Driver Points for fixed outer boundary

eliminated. Similarly for the centroid, there is good agreement between RBF and piecewise linear interpolation. This example demonstrates some of the issues associated with RBF mesh deformation.

For the results presented in this report, the CFD nodes are chosen as the driving points. Volume spline is the RF of choice and the mesh is fully moving.

		Fixed outer boundaries			Moving outer boundaries		
		L_2 (%)	L_1 (%)	L_∞ (%)	L_2 (%)	L_1 (%)	L_∞ (%)
FEM based	Fluid Mesh	0.214	0.09	1.4	0.114	0.053	0.887
	Face centroid	0.21	0.10	1.26	0.109	0.060	0.768
CFD based	Fluid Mesh	0.001	0.001	0.018	0.001	0.001	0.018
	Face centroid	0.039	0.024	0.215	0.039	0.024	0.215

Table 7.5: Error due to the RBF interpolation

Grid refinement studies are performed to examine the effect of grid resolution on the CFD simulation results at $M_\infty = 12$, $H = 12$ km. Four different grids with varying levels of refinement are used. Convergence of the resultant forces and moments is observed for increasing number of cells. A grid with 1 million cells predict the aerodynamic resultants

with less than 1% error when compared to a grid with 2 millions cells. A grid with 1 million cells is used for all subsequent simulations in this thesis.

7.4.3 Aeroelastic Results

The aeroelastic simulations are performed at constant altitude of 12 km and different Mach numbers. The computational cost and the parameters associated with the time stepping of the aeroelastic simulations are presented in Table. 7.6. The time step is set to $\Delta t = 1.25 \times 10^{-4}$ s which corresponds approximately to 100 and 500 time steps per period for the highest and lowest natural frequencies, respectively. Depending on the complexity of the gas model (turbulence, chemistry) the computational time varies from 80 hours for laminar flow to 190 hrs when chemistry and a turbulence model are included. The main contributor to the computational cost associated with the aeroelastic simulations is the CFD calculation. Each aeroelastic simulation requires 2500 initial iteration for the steady state solution of the NS equations to converge. For each time step, several subiterations of the CFD solver are required to march the fluid in time as explained previously. At each time step, the new node locations are written in the mesh file and the CFD code is restarted. It generates significant amount of additional processing time which could be eliminated in a fully integrated aeroelastic solver.

Number of time step	1000
Time step	0.125 ms
Number of subiterations per time step	50
Number of cells	1M
Number of processors	6
Processor	Opteron 240–254
Computational time	80–190 hrs

Table 7.6: Simulations parameters for 3D calculations

Verification of the SI methods The aeroelastic simulations are performed at constant altitude of 12 km and different Mach numbers. For each Mach number, the frequencies and damping are computed using each SI method presented in Section 3.5. The results corresponding to Euler aerodynamics are presented first in Fig. 7.20. Frequencies and damping coefficients as functions of the Mach number are shown in Figs. 7.20(a) and 7.20(b) respectively. The symbols correspond to the Mach numbers at which a transient simulation is performed. Each mode is indicated with a unique color and symbol. The different types of lines correspond to different SI methods. The three SI agree perfectly. In the case of Euler aerodynamics, there is a good agreement with CFL3D and the present results. The predicted flutter Mach number is 13.7.

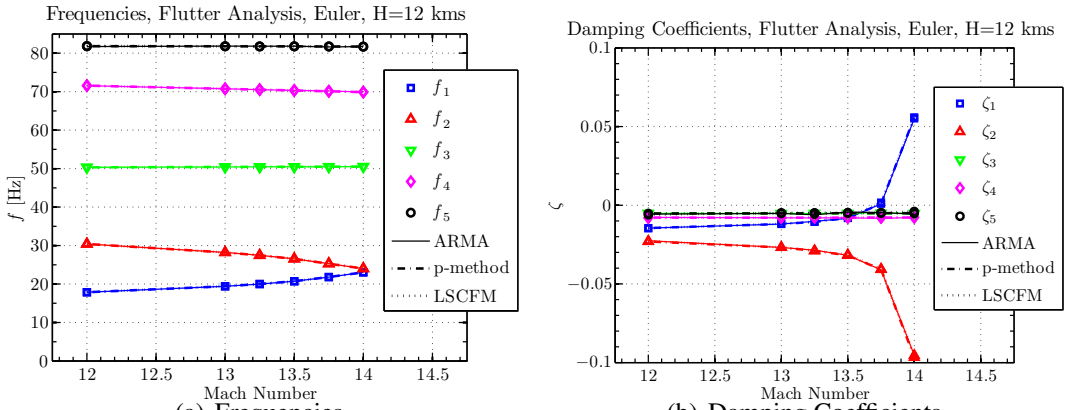

(a) Frequencies (b) Damping Coefficients

Figure 7.20: Aeroelastic stability analysis using Euler aerodynamics for the low aspect ratio wing, H = 12 km

The results corresponding to Navier–Stokes aerodynamics with laminar flow assumptions are presented in Fig. 7.21. Frequencies and damping coefficients as functions of the Mach number are shown in Figs. 7.21(a) and 7.21(b) respectively. The ARMA method does not compare well with the other two approaches. However, the other two methods compare very well.

When considering turbulent flows, the ARMA method did not provide good results. However the p–method is reliable and is the method of choice for generating the results.

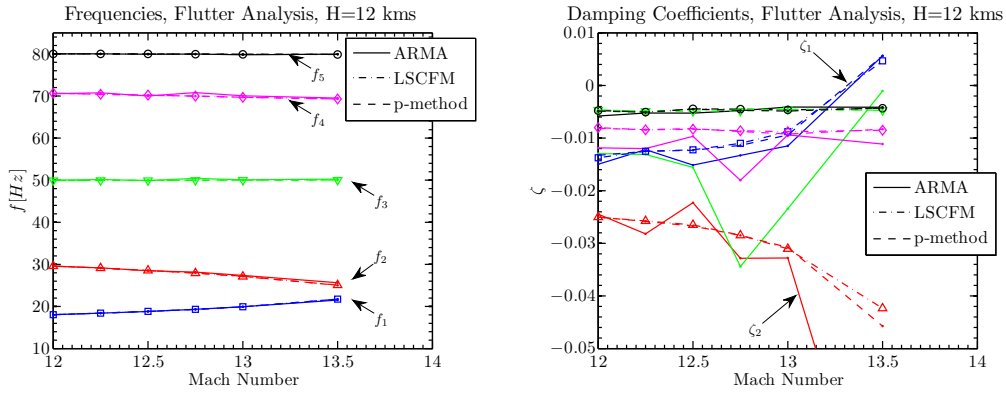

(a) Frequencies (b) Damping Coefficients

Figure 7.21: Aeroelastic stability analysis using laminar flows for the low aspect ratio wing, H = 12 km

Effect of Turbulence and Gas modeling The results of the flutter analysis are shown in Figs. 7.22 and 7.23. The effect of turbulence on flutter boundary prediction is summarized in Table. 7.7. Euler and laminar flow are compared to turbulent flow for low and high values of free stream turbulence. It illustrates the dependency on turbulence modeling. Adding turbulence decreases the flutter boundary by up to 7%. An abrupt change is observed when comparing the results for laminar flow, which is close to Euler, to the results from turbulent flow. The flutter Mach number predicted in the case of SA model with $\left(\frac{\mu_T}{\mu_L}\right)_\infty = 0.009$ is close to that with $\left(\frac{\mu_T}{\mu_L}\right)_\infty = 3$. The decrease of flutter boundary with increasing turbulence may be due to the thicker boundary layer for the more turbulent cases, which in turn can produce a higher static pressure on the airfoil due to the thicker effective shape and it explains the decrease in onset of flutter. The effect of gas modeling is negligible for the flight condition considered.

In Fig. 7.22, flutter analysis for various turbulence modeling assumptions is summarized. Figure 7.22(a) depicts the frequencies of the aeroelastic system as function of flutter Mach number. The different types of lines correspond to different turbulence assumptions. In Fig. 7.22(b), only the damping coefficients corresponding for the first two modes are shown. The frequencies of the aeroelastic system are not sensitive to the model considered.

Gas Model	Gas Model	Turbulence	$\left(\frac{\mu_T}{\mu_L}\right)_\infty$	ARMA	LSCF	p–method
PG	EU	–	–	13.73	13.71	13.72
	NS	Laminar	–	13.16	13.33	13.22
		SA	0.009	*12.33*	*12.85*	12.76
		SA	3	12.74	12.75	12.78
IG	NS	SA	3	*12.75*	*12.78*	13.0
RG	NS	SA	3	*12.62*	*13.02*	12.87
CFL3D [84]	EU	–	–	13.7		-
	NS	SA mod.	0.009	13.65		-
3^{rd} order PT				13.4		

Table 7.7: Flutter Mach number for the low aspect ratio wing using different turbulence and gas models, $H = 12$ km

The flutter Mach number predicted using CFL3D and Navier–Stokes is smaller than the one obtained with Euler. Adding turbulence increases the effective shape due to the presence of the boundary layer and eventually results in an increased local pressure on the wing and a decrease in flutter Mach number.

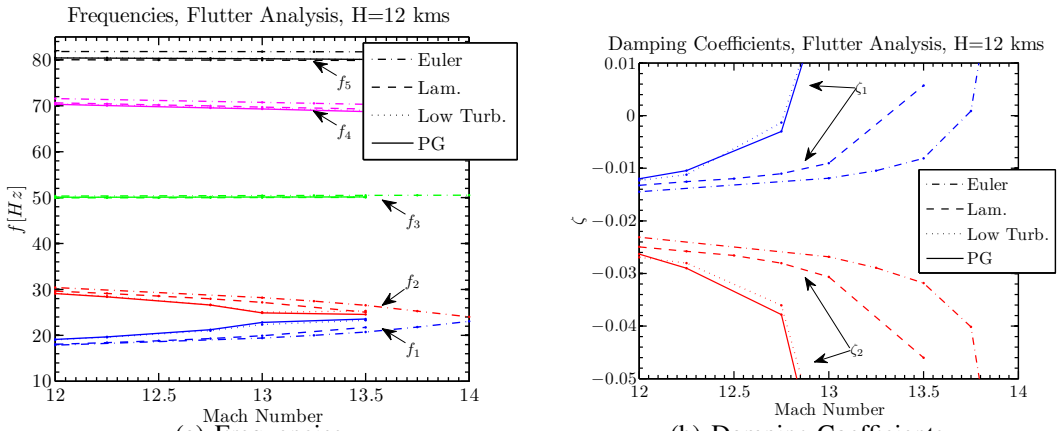

(a) Frequencies (b) Damping Coefficients

Figure 7.22: Aeroelastic stability analysis for the low aspect ratio wing for different turbulent flow , H = 12

The results of the flutter analysis are shown in Fig. 7.23 for different gas models. Figure 7.23(a) depicts the frequencies of the aeroelastic system as function of flutter Mach

number. The different lines correspond to different turbulence assumptions. In Fig. 7.23(b), the damping coefficients are affected by the gas model. Going from perfect gas to real gas affects the flutter boundary by about 3%. The difference between IG and RG is 1%.

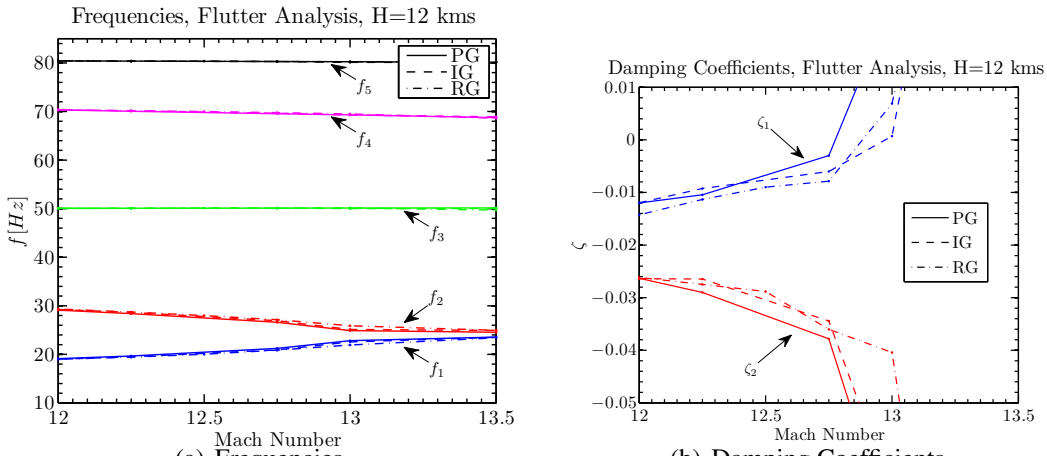

(a) Frequencies (b) Damping Coefficients

Figure 7.23: Aeroelastic stability analysis for the low aspect ratio wing for different gas model , H = 12 km

Stability Boundaries The flutter boundaries are calculated at the altitudes of 15 and 21 km and are presented in Figs. 7.24(a) and 7.24(b). In Fig. 7.24(a), the effect of turbulence is considered. Laminar flow (Lam.) is compared to turbulent flows (Turb.). Note that the flutter boundaries are very close to each other and also close to that obtained with piston theory. The results labeled (Mod. Turb.) corresponds to a modified SA turbulence model. The CFD++ code is used with the SA turbulence model, similar to the turbulent case, however the coefficients of the SA model are modified to match the CFL3D code implementation. There is a small change in flutter boundary. It seems that the CFL3D code predicts a flow that is less turbulent than that with CFD++ which is the reason for the difference in the flutter boundary calculations.

In Fig. 7.24(b), the effect of gas modeling is investigated. Perfect gas model (PG) is compared to real gas (RG). The flutter boundaries are very close to each other and close to that with piston theory. There is a small change in flutter boundary due to real gas effects.

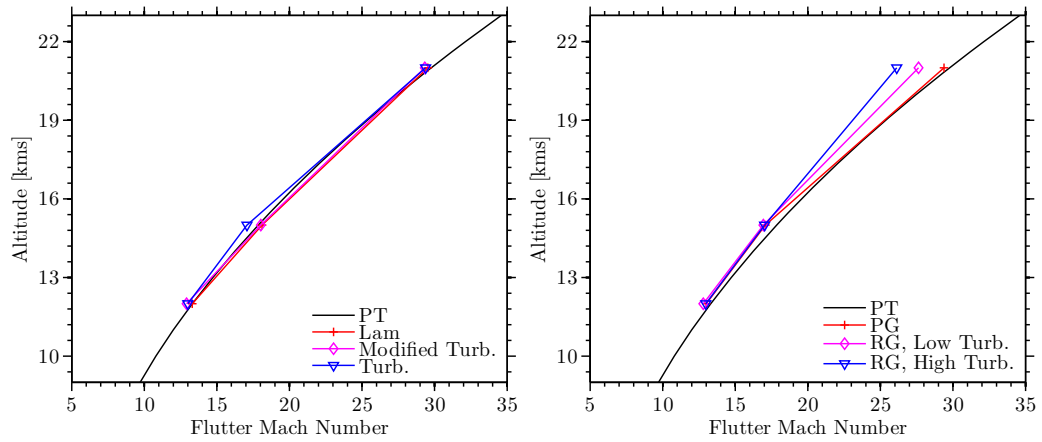

(a) Effect of turbulence (b) Effect of gas model

Figure 7.24: Flutter boundaries for the low aspect ratio wing for different gas model and turbulence model, H = 12 km

The change is significant at high Mach number where real gas effects are important. As in the case of PG, adding turbulence decreases the flutter boundary.

To conclude, turbulence is the main contributor to the variability in flutter Mach number and affect the stability boundary by 7%. Real gas effects affect the flutter boundary by 3%. [173]

Remark Note that the altitudes, 12–21 km, at which the aeroelastic studies are conducted are not representative of hypersonic flight. More realistic altitudes of 20–30 km produce very high Mach numbers, and therefore the altitude is artificially reduced in order to reduce these to practical values. However, as mentioned earlier, incorporation of aerodynamic heating leads to a reduction of the flutter Mach number, and thus aerothermoelastic studies can be conducted at more reasonable altitudes. In the following section, the aerothermoelastic problem is considered.

CHAPTER 8

AEROTHERMOELASTIC RESULTS

The aerothermoelastic stability of a wing in turbulent and laminar flows is studied using both a deterministic and probabilistic approach. The effect of transition is incorporated. The reliability associated with the assumption that turbulent flow is the worst case scenario is quantified.

8.1 Structural Model Used

The geometry of the three–dimensional low–aspect–ratio wing is presented in Section 7.4 and shown in Fig. 7.15. A thermal protection system (TPS) prevents over–heating of the aluminium structure of the wing from aerodynamic heating. The TPS layers are described in Ref. [85]. The radiation shield is composed of a 0.45 mm René 41 metal. The thermal insulation layer is made of 3.8 mm flexible Min–K layer. The René 41 heat shield can withstand temperatures up to approximately 1500^o K and is assumed to have an emissivity of 0.85.

The aeroelastic stability of the wing is considered in Section 7.4. For the aerothermoelastic study, the structure is reinforced at the leading edges to prevent early local buckling. Reinforcements were added in the wing. Leading and trailing edges were stiffened [85], resulting in higher natural frequencies given in Table 8.1.

	Original Wing	Modified Wing	Diff.
Wing Mass [kg]	350.05	377.73	8%
f_1 [Hz]	13.41	14.28	7%
f_2 [Hz]	37.51	40.94	9%
f_3 [Hz]	49.18	60.06	22%
f_4 [Hz]	77.14	81.86	6%
f_5 [Hz]	79.48	97.25	22%

Table 8.1: Mass and natural frequencies of the wing

8.2 Aerothermoelastic Results

The vehicle is in straight and level flight, at a constant altitude, H, and Mach number, M_∞. The flight conditions are summarized in Table. 8.2. To investigate the effect of turbulence on the aerothermoelastic behavior of the wing, both laminar and turbulent heat flux are considered. In addition, transition is artificially incorporated by arbitrarily choosing the location of transition point, $\frac{x_t}{c}$, on the wing and combining the laminar heat flux with that corresponding to turbulent flow. For a given trajectory, the influence of the transition location, $\frac{x_t}{c}$, is investigated by arbitrarily varying its location from the leading edge to the trailing edge of the wing.

Flutter boundaries based on CFD are in good agreement with those based on PT. Therefore, in order to limit the computational cost, PT was used for computing the results in this section.

Table 8.2: Flight conditions considered

Parameter	Value	unit
H	30	km
M_∞	8–10	N/A
$\frac{x_t}{c}$	0–100	%

The framework presented in Section 3.1 is used to study the aeroelastic stability of the heated structure on a straight and level trajectory. The important dependencies to consider

are listed below:

1. H, M_∞, x_t : A trajectory is characterized by altitude, Mach number, and also flow regime (laminar, turbulent, or transition location x_t).

2. $f_i\,(t, H, M_\infty, x_t)$: The natural frequencies and modes shapes of the heated structure are function of time along a given trajectory.

3. $M_{fm}\,(t, H, M_\infty, x_t)$: To each instant of time along a trajectory corresponds a heated structure and its flutter margin.

The aerodynamic heat flux results are presented in Figs. 8.1 and 8.2 for a level flight at Mach 8 and 10, respectively. In each set of figures, the distribution of heat flux coefficient, adiabatic wall temperature and equilibrium radiation temperature are given by the color shading for three cases: fully turbulent flow, transition flow with $\frac{x_t}{c} = 25\%$, and fully laminar flow. The line crossing the wing from its root to its tip, at constant $\frac{x_t}{c}$, indicates the transition location. From the leading edge of the wing to transition, the flow is laminar. Downstream the transition point, the flow is turbulent.

The results show a high heat flux coefficient at the leading edge of the wing for all cases. The enhanced heating in the front half of the wing produces higher radiation equilibrium temperature T_R on the surface of the wing. Note that the heat flux in laminar flow is an order of magnitude smaller than its value for fully turbulent flows. Thus, incorporating transition on the surface of the wing generates heat flux gradients producing temperature gradients on the wing.

The thermal analysis results for a vehicle in level flight at Mach 8 and an altitude of 30 km are shown in Fig. 8.3. The different times, $t = 15$, 30 and 50 mins along the trajectory. are considered. Temperature distributions on the wing are given for three heat fluxes corresponding to laminar, turbulent, and transition flow. After a flight time of 15 mins of flight, the temperatures in the load carrying structure are close to the initial temperature of $288^o K$. As the wing heats up, the temperature rises. For laminar and turbulent flow,

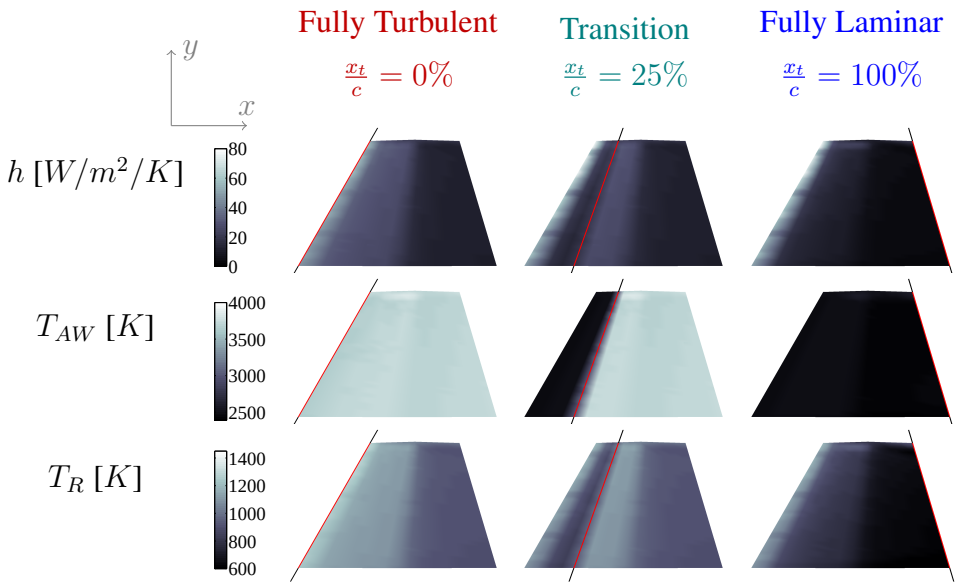

Figure 8.1: Aerodynamic heating results for $M_\infty = 8$ and $H = 30$ km

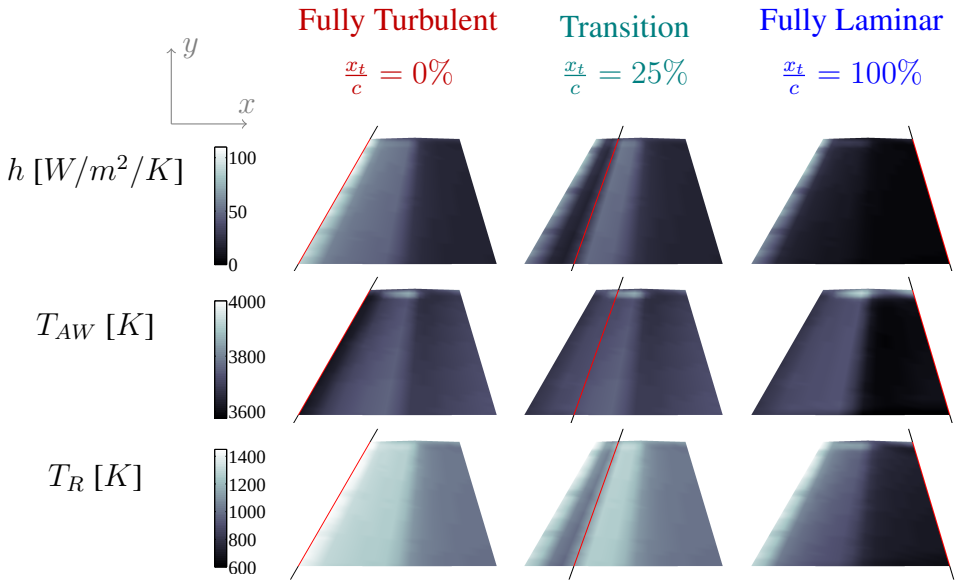

Figure 8.2: Aerodynamic heating results for $M_\infty = 10$ and $H = 30$ km

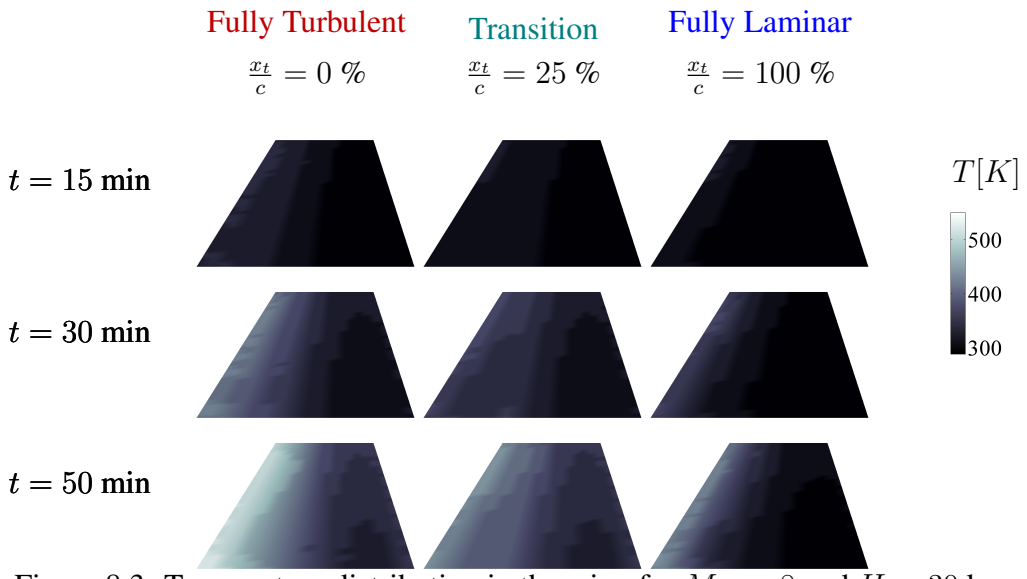

Figure 8.3: Temperature distribution in the wing for $M_\infty = 8$ and $H = 30$ km

the temperature decreases smoothly from the leading edge to the trailing edge of the wing. The maximum temperature occurs in turbulent flow and reaches $513^o K$ after 50 min. As expected, the wing in laminar flow has the lowest temperature increase. For a wing experiencing transition on its surface, the temperature decreases up to the transition location where a small increase occurs. From the transition location to the trailing edge, the temperature decreases smoothly. The transition on the surface of the wing affects the magnitude of the temperature in the wing as well as its distribution.

In Fig. 8.4, the results from a modal analysis for a vehicle in level flight, at a M =8 and an altitude of 30 km, are shown for 3 different times, $t = 15$, 30 and 50 mins along the trajectory. At each time, the frequencies of the heated structure are provided as a function of the flow conditions: from fully turbulent for $\frac{x_t}{c} = 0$ to fully laminar for $\frac{x_t}{c} = 100\%$. The thin lines corresponds to the natural frequencies of the cold structure, and are given for reference. Note, that the natural frequencies decrease faster for the case of turbulent flow, $x_t = 0$, than for laminar flow, $x_t = c$. The lower frequencies for the case of turbulent flow are to be expected due to the higher heat flux. For flow with transition in the first half of the wing, the heated frequencies are much lower for $t = 30$ mins and $t = 50$ mins. However, the behavior of a wing with transition on its surface does not lie between that for

either fully turbulent or fully laminar flow. Nonlinearities due to thermal stresses occur and significantly affect the structural integrity of the wing.

It is important to relate these frequencies to their corresponding mode shapes. For each instant in time, the first 8 mode shapes are depicted for 3 flow conditions: turbulent (Turb.), transition located at $\frac{x_t}{c} = 25\%$ (Trans.), and laminar (Lam.). All the modes shapes are normalized such that the magnitude of the maximum displacement is 1. The dark color corresponds to a value of -1, and white to a value of +1. At $t = 15$ mins, the modes shapes corresponding to the three heating conditions are similar to that of the cold structure. However at $t = 30$ mins and $t = 50$ mins new modes shapes appear and are highlighted by an enclosing rectangle. These mode shapes are not present in the unheated structure nor at the beginning of the trajectory. With increased temperature and the resulting thermal stresses changes manifest themselves in the first 8 modes. The new modes display local buckling due to thermal stresses.

The heat transfer results are given for a vehicle in level flight at Mach 10 and an altitude of 30 km, for 3 different times, t =15, 30 and 50 mins along the trajectory are given in Fig. 8.5. The temperature distribution of the wing is given for three heat fluxes: laminar, turbulent and transition flow. The maximum temperature is encountered for turbulent flow and it reaches 632^oK after 50 mins. The wing under laminar flow has the lowest temperature increase as expected. The trends observed are similar to those observed for $M_\infty = 8$.

Results for a vehicle in level flight at $M_\infty = 10$ and $H = 30$ km are shown in Fig. 8.6. The trends observed are similar to the case of $M_\infty = 8$. Note that the changes in frequencies and mode shapes are more important than that for the lower Mach number due to the increased heat flux at the surface of the structure. At t=30 and 50 mins, the frequencies for transition flow can be lower than that for turbulent flow or higher than that for laminar flow. The nonlinear behavior is a result of thermal buckling induced by thermal stresses.

In Fig. 8.7, the flutter margins for a vehicle in level flight at M=8 and an altitude of 30

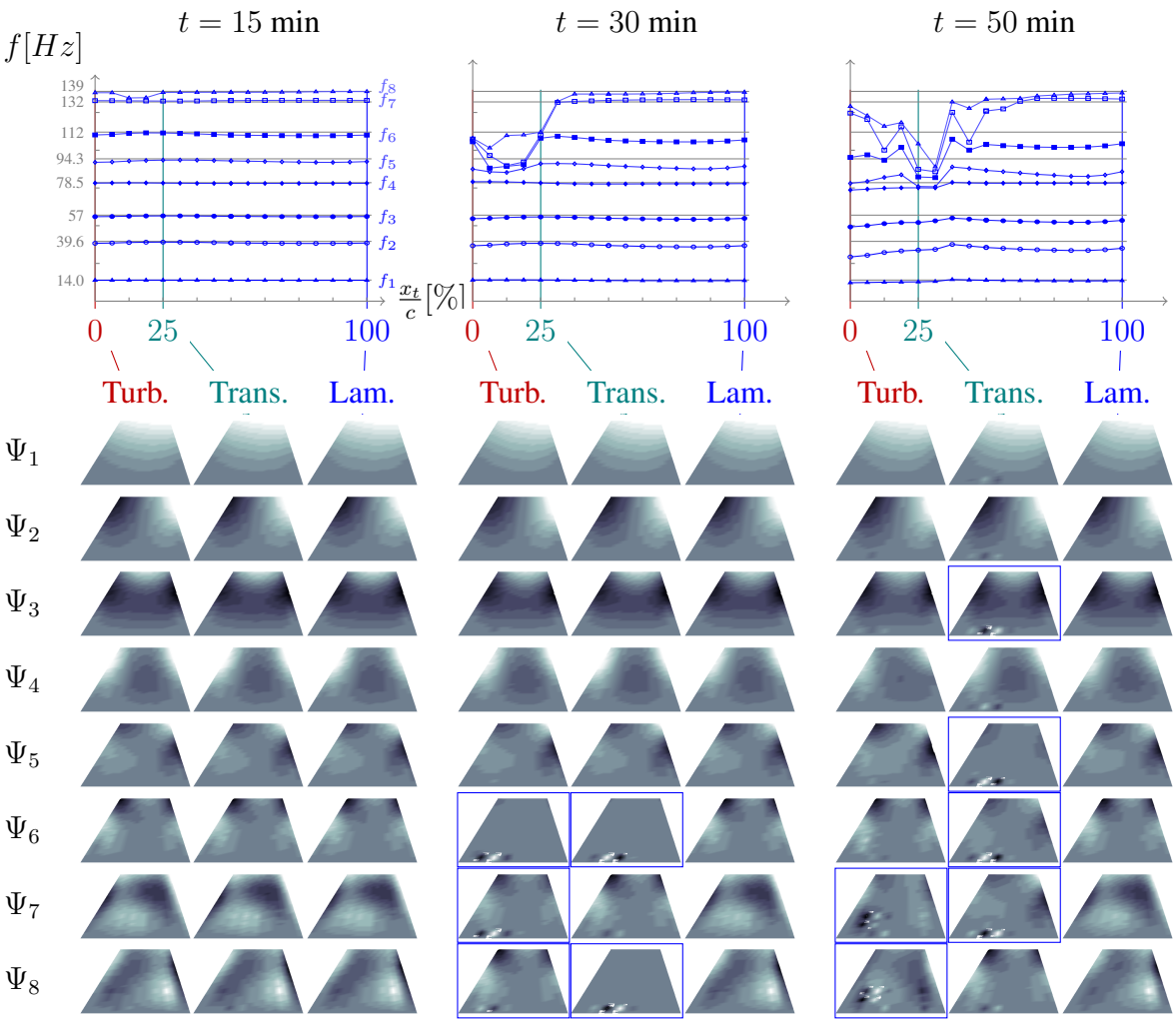

Figure 8.4: Modal analysis of the heated structure for $M_\infty = 8$ and $H = 30$ km

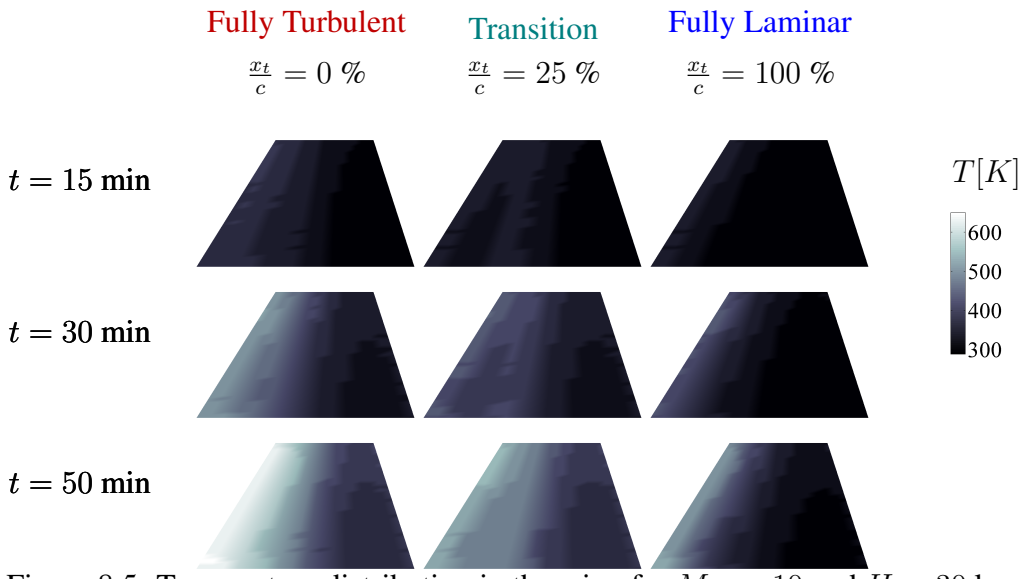

Figure 8.5: Temperature distribution in the wing for $M_\infty = 10$ and $H = 30$ km

km are provided at 3 different times, t=15, 30 and 50 min. At each time the flutter margins are given in terms of the flutter margin Mach number M_{fm} as function of altitude, H, and for 3 flow conditions: turbulent ($\frac{x_t}{c} = 0$), transition located at $\frac{x_t}{c} = 25\%$ (Trans.), and laminar ($\frac{x_t}{c} = 1$). The shaded region corresponds to the range of flutter margins as the transition location is moved from the leading edge of the wing to its trailing edge. The thin line corresponds to the flutter margin of the cold structure and is provided for reference. The same flutter margins are provided in the lower portion of the figure as a function of the transition location x_t for 4 different altitudes of H = 9, 12, 15 and 21 km. Note that the flutter margin for the structure under turbulent heating always corresponds to the lowest one. However, the margin for laminar case is not necessarily the highest one. Depending the transition location, the flutter margin of the heated wing can vary significantly. This highlights the importance of the thermal stresses that influence the aeroelastic stability of the heated structure.

In Fig. 8.8, the variations of aeroelastic stability margin for an altitude of 12 km are given as function of time for the 3 different flow conditions highlighted previously. The behavior of the flutter margins corresponding to 9, 15 and 21 km is similar. The dashed lines corresponds to cases without thermal stresses. When only material degradation is

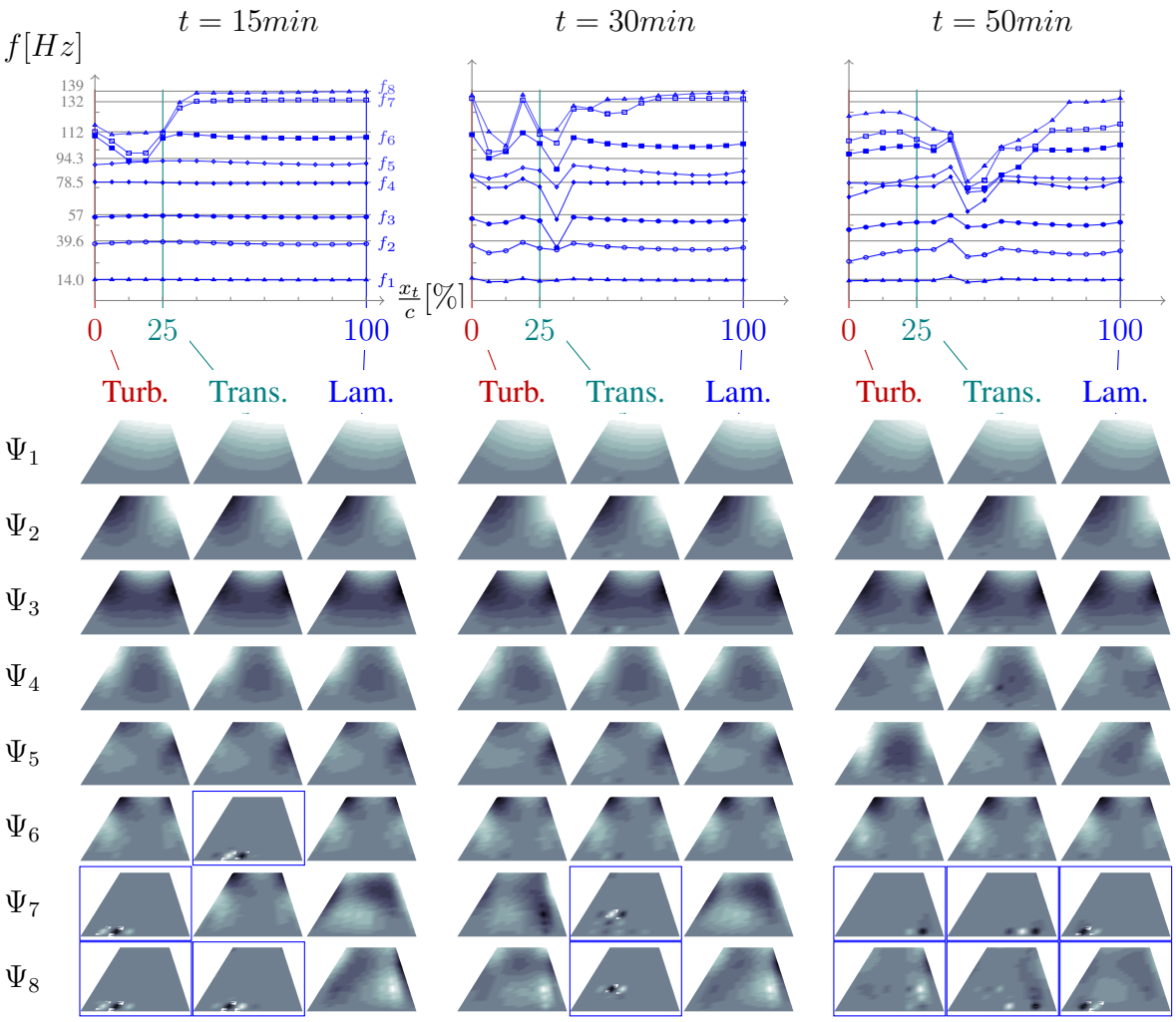

Figure 8.6: Modal analysis of the heated structure for $M_\infty = 10$ and $H = 30$ km

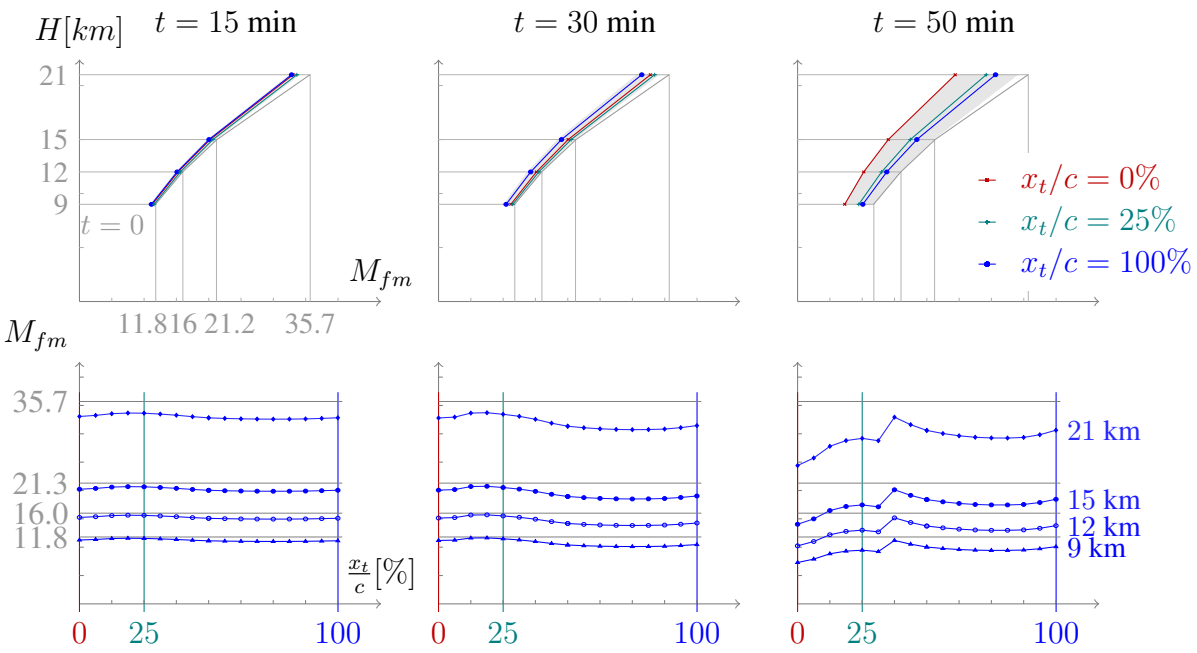

Figure 8.7: Flutter margin of the heated structure for $M_\infty = 8$ and $H = 30$ km

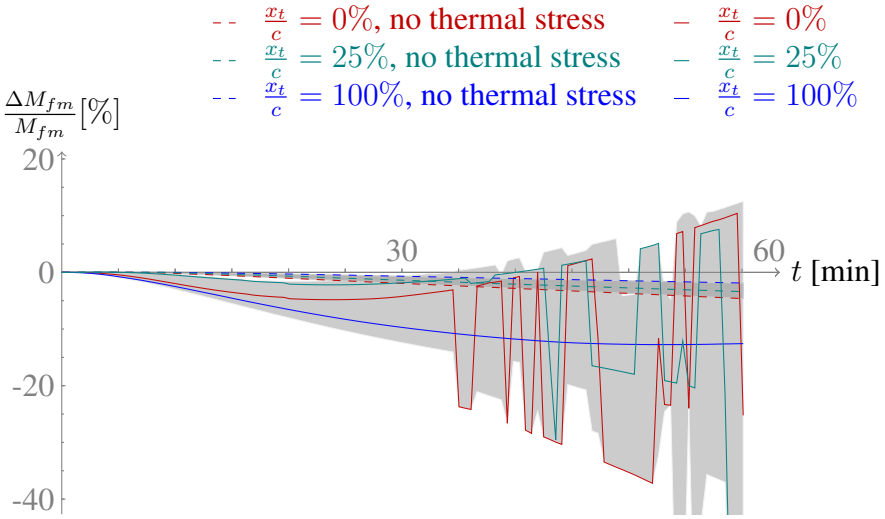

Figure 8.8: Variation of aeroelastic stability margin of the heated structure for $M_\infty = 8$ and $H = 30$ km

considered, the flutter margins are decreased by less than 5% after an hour of flight. The wing under turbulent flow has the lowest margin, that under laminar flow has the highest margin. The wing which experiences transition at its surface has an intermediate flutter margin. When thermal stresses are accounted for, the behavior of the heated wing is not as intuitive anymore. Note, that discontinuities start to occur after 35 minutes of flight time for the wing under turbulent flow and after 34 minutes under transition flow. Before these flight times, the flutter margins are, from the lowest to the highest, for the wing under laminar, turbulent and transition flow. This order is counter intuitive and is caused by increasing thermal stresses. Turbulent flows generate high heat flux and high temperature in the wing, however transition at the surface of the wing causes higher temperature gradients.

In Fig. 8.9, the flutter margins for a vehicle in level flight at $M_\infty = 10$ and $H = 30$ km at 3 different times, t =15, 30 and 50 min, are shown. Note that the flutter margin for the structure under turbulent heating does not correspond to the lowest one nor is the margin for laminar flow the highest.

In Fig. 8.10, the variations of flutter margins for an altitude of 12 km are given as function of time for the 3 different flow conditions mentioned previously. Two cases are considered: with and without thermal stresses. Removing thermal stresses allows one to identify only the effect of thermal degradation. Without thermal stresses, after an hour of flight, the flutter margins are decreased by less than 10% due to thermal degradation. The wing under turbulent flow has the lowest flutter margin while the one under laminar flow has the highest. The wing under transition flow has a flutter margin that is between that for laminar and turbulent, as for the case of $M_\infty = 8$. Thermal degradation affects the wing in a smooth way. With thermal stress, the behavior of the wing is highly nonlinear. The stability margin drops significantly after 20 mins of flight for the wing under turbulent flow, after 25 mins for transition flow, and 53 mins in the case of laminar flow. During the first 20 mins, the flutter margins are, from the lowest to the highest, for the wing under laminar, turbulent and transition flow. Again, this order is counter intuitive and due to thermal stresses.

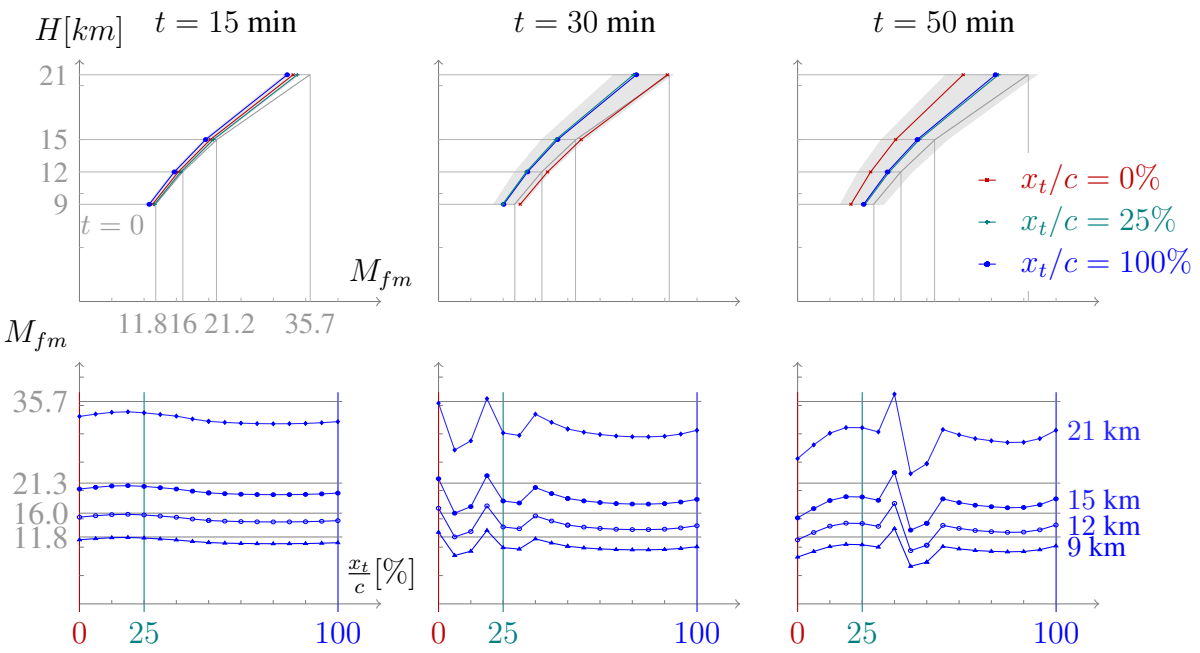

Figure 8.9: Flutter margin of the heated structure for $M_\infty = 10$ and $H = 30$ km

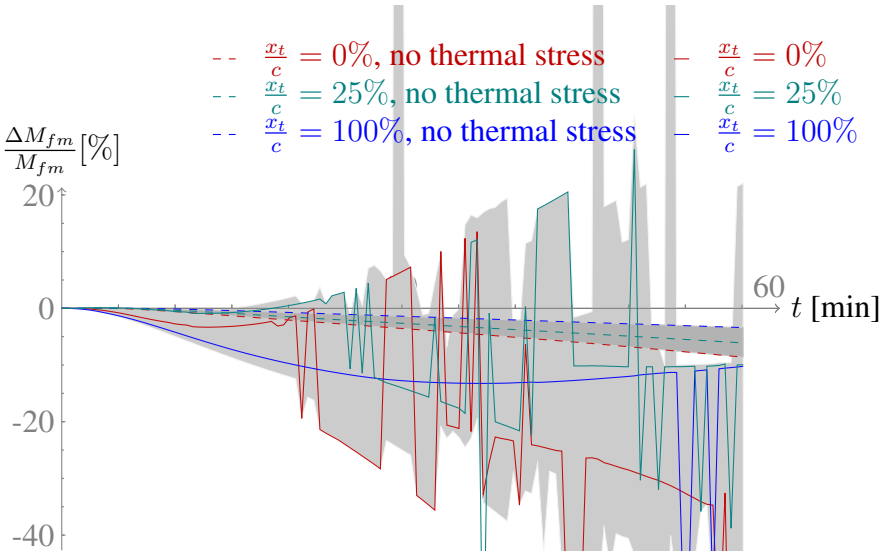

Figure 8.10: Variation of aeroelastic stability margin of the heated structure for $M_\infty = 10$ and $H = 30$ km

The aerothermoelastic results are summarized in Table 8.3. The time T_f denotes the flight time. It corresponds to the instance of time when the first discontinuity in the aeroelastic margins occurs. The maximum drop in aeroelastic stability margin, $\Delta M_{fm} = M_{fm}(t) - M_{fc}$, before T_f is given as well. The variation in stability margin is normalized with respect to the flutter Mach number of the cold structure, M_{fc}. The wing under turbulent flows is the first to buckle, reflected by its significant loss in aeroelastic stability margin. However, in the early part of the flight, the wing under laminar flows has the highest decrease in flutter margin.

Table 8.3: Aerothermoelastic behavior

Trajectory		with thermal stresses		no thermal stresses	
		$\max(\Delta M_{fm})$ [%]	T_f [min]	$\max(\Delta M_{fm})$ [%]	T_f [min]
$M_\infty = 8$	Laminar	-12.7	> 60	-1.9	–
	$\frac{x_t}{c} = 25$ %	-2.2	35	-3.4	–
	Turbulent	-4.8	34	-4.6	–
$M_\infty = 10$	Laminar	-13.2	54	-3.4	–
	$\frac{x_t}{c} = 25\%$	-0.9	22	-6.1	–
	Turbulent	-3.3	18	-8.6	–

Further details are given in Fig. 8.11. The time to buckling is given as function of transition location and M_∞ for $H = 30$ km. At Mach 7 and 8, the wing buckles only for transition located before $x_t = 25\%$ and 40% respectively. At Mach 10, the buckling time is the lowest for transition located in the first half of the wing, and does not vary much, close to 55 mins for transition located in the second half of the wing. When $x_t = 75\%$, the wing does not buckle in the first hour of flight which explains the gap in the curve.

These results highlight the importance of nonlinearities due to transitional flow and thermal stresses in the aerothermoelastic behavior of the structure [174]. It is not sufficient to consider only turbulent or laminar flow conditions, since transition on the surface of the wing can significantly alter its structural behavior.

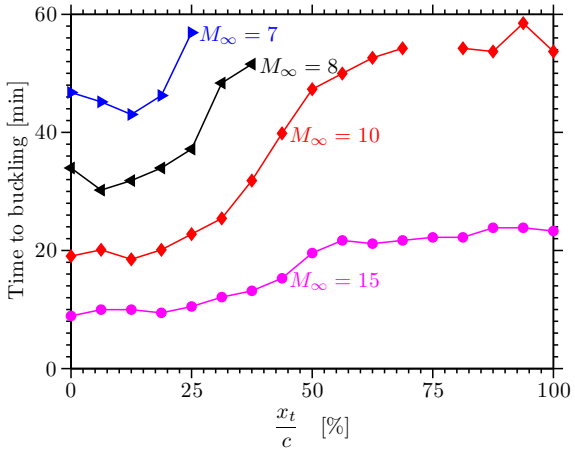

Figure 8.11: Time to buckling as function of transition location and flight Mach number, $H = 30$ km

Flutter Boundaries The results presented in this section correspond to flutter margins of the heated wing which are different from flutter boundaries. In Ref. [157], such a flutter margin is referred to as a *virtual* flutter boundary. The exact flutter boundaries are determined by fixing a flight duration, ΔT, and by finding the flight Mach number M_∞ at which the flutter margin M_{fm} is M_∞ after ΔT. This approach required a sequential iteration on M_∞ until convergence to a flutter margin is achieved. Eventually the Mach number defines the flutter boundary after ΔT.

To illustrate this process, a flight condition characterized by $H = 20$ kms, with $\Delta T = 30$ min is considered. The initial flight Mach number $M_\infty = 10$ yields a flutter margin of $M_{fm} = 33.5$ after 30 min of level flight. The Mach number is updated to $M_\infty = \frac{10+33.5}{2} = 21.7$. At this flight condition, the wing buckles before it flutters and the flutter margin does not converge. Similarly, at $H = 30$ kms, the initial $M_\infty = 10$ yields a flutter margin of $M_{fm} = 59.0$. The Mach number is updated to $M_\infty = \frac{10+59.0}{2} = 34.5$. At this flight condition, the wing buckles before it flutters and the flutter margin does not converge either. The implication of this behavior is that the iterative procedure for updating the flutter margin leads to local buckling which is the main cause of failure.

8.3 Uncertainty Propagation Results

In this section, the UQ is used to examine the hypothesis that fully turbulent flow is a conservative assumption. Therefore, the transition location is considered as an uncertain variable. The output of interest is the flutter margin as a function of time.

The probability of failure, defined by Eq. (8.1), is the probability that the flutter Mach number is less than that predicted under the *hypothetical* conservative assumption of fully turbulent flow.

$$p_f(t) = p\left(M_{fm}(t, x_t) < M_{fm}(t, x_t = 0)\right) = \int_{M_{fm}(t,x_t)<M_{fm}(t,0)} p_{x_t}(x_t)\, dx_t \qquad (8.1)$$

If fully turbulent flows correspond to the worst case scenario, the probability of failure is 0. The p_f represents the degree of error associated with the assumption that turbulent flow is a lower bound for the behavior of the heated wing.

The transition location is the uncertain variable, however, its probability distribution is unknown. Intuitively, transition is more likely to occur closer to the leading edge. Three different probability distributions are examined: uniform, $Beta(1,3)$ and $Beta(2,3)$.

In the case of uniform PDF, the SC approach with a 9^{th}–order polynomial function is used to obtained converged response surface for $t < T_f$. For $t > T_f$, the relation between flutter margin and transition location, $M_{fm} = f(x_t)$, is highly non–linear, reflecting buckling. Therefore polynomial response surfaces such as SC or PCE failed to converge. In addition, Kriging and spline interpolations were considered but failed to converge as well. Therefore, UQ results are generated for $t < T_f$.

The prediction of the response surface is compared to the exact value at 17 uniformly distributed points to quantify the error of the response surface. Various response surfaces are illustrated in Fig. 8.12. The PCE and RBF approach do not perform as well as SC. Kriging (KG) is very oscillatory and does not provide a good fit in this case.

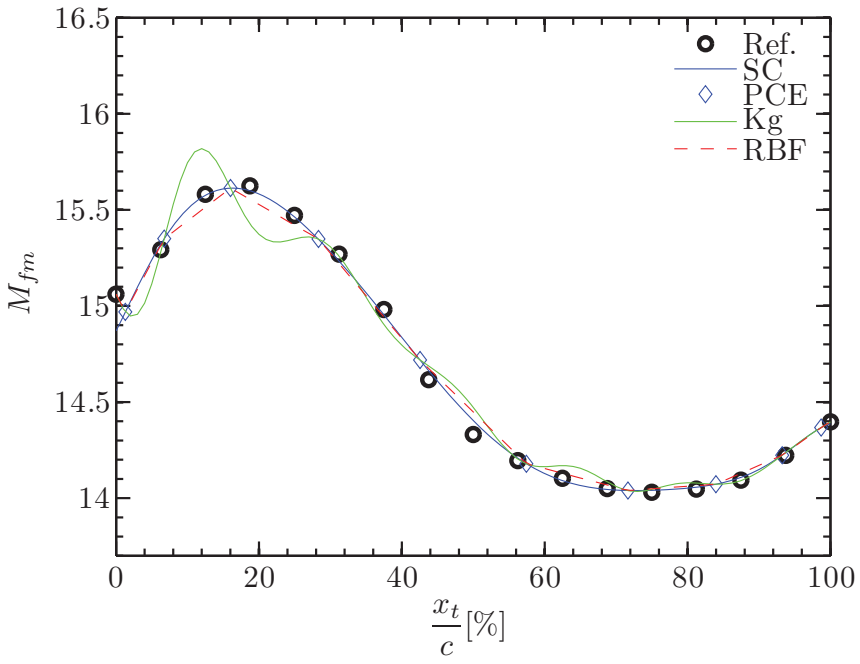

Figure 8.12: Flutter margin response surfaces for uniform PDF, $M_\infty = 8$, $H = 12$ km, $t = 27$ mins

In the cases using Beta(2,3) and Beta(1,3), the SC indicates oscillations close the trailing edge at $x_t = c$. The response surfaces are given in Fig. 8.13(a) for the case of Beta(1,3). Figure 8.13(b) is a closer view at $x_t = c$. The RBF interpolation gives a better approximation than the other approaches. Note that the SC and PCE approaches predict lower values of flutter Mach numbers at $x_t = c$ and therefore are not suitable for the UQ approaches. The bad performance of these polynomial based approaches is explained by the fact that the relationship between x_t and M_{fm} is highly non-linear and cannot be approximated by global polynomials. In addition, the polynomial response surfaces are constructed based on a limited number of points and require extrapolation at the edges of the uncertain parameters design space which adversely affect accuracy. The RBF based response surface using volume spline is reliable and is used for the results presented in this section. For the cases presented next, the mean error of the response surface was less than 0.3% of the deterministic value.

The results of the uncertainty propagation results are given in Figs. 8.14(a), 8.14(b),

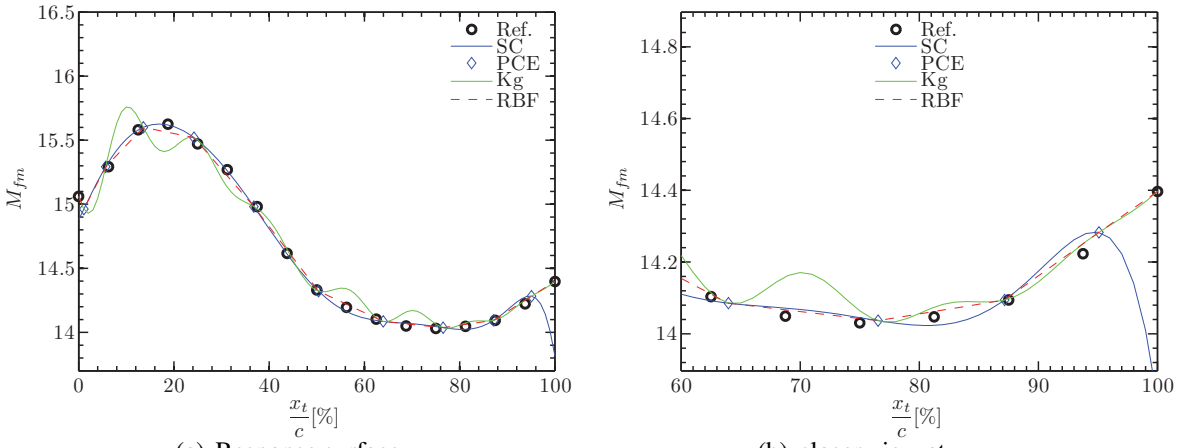

(a) Response surface (b) closer view at $x_t = c$

Figure 8.13: Flutter Mach number response surfaces for Beta(1,3) PDF, $M_\infty = 8$, $H = 12$ km, $t = 27$ mins

and 8.14(c), respectively, for $M_\infty = 8$ and $H = 30$ kms, and a flutter margin at $H = 12$ kms. In each figure, the assumed probability of the transition location is depicted. The Beta(1,3) distribution gives more probability to the leading edge of the wing; the Beta(2,3) emphasizes the front half of the wing.

The PDF of the variation of flutter margin is given for 6 time instants and these are superimposed on the deterministic results presented in the previous section. The red shading of the PDF corresponds to the cases when the flutter margin is less than that predicted for fully turbulent, quantifying the probability of failure, p_f.

The probability of failure, p_f, gives the probability that the stability margin is less than that for turbulent flows. This information is given in Table 8.4 and illustrated in Fig. 8.15 for the 3 probability distributions of x_t. The probability of failure is the lowest for Beta(1,3) and the highest for Uniform PDF. It emphasizes the fact that transition located close to the leading edge of the wing yields a higher flutter Mach number than that for turbulent flows. Therefore the Beta(2,3) and Beta(1,3) yield less emphasis to the values of transition location that corresponds to a lower flutter Mach number.

Additional results for $M_\infty = 6$, 7 and 10 are presented in Figs. 8.16(a) to 8.16(c), re-

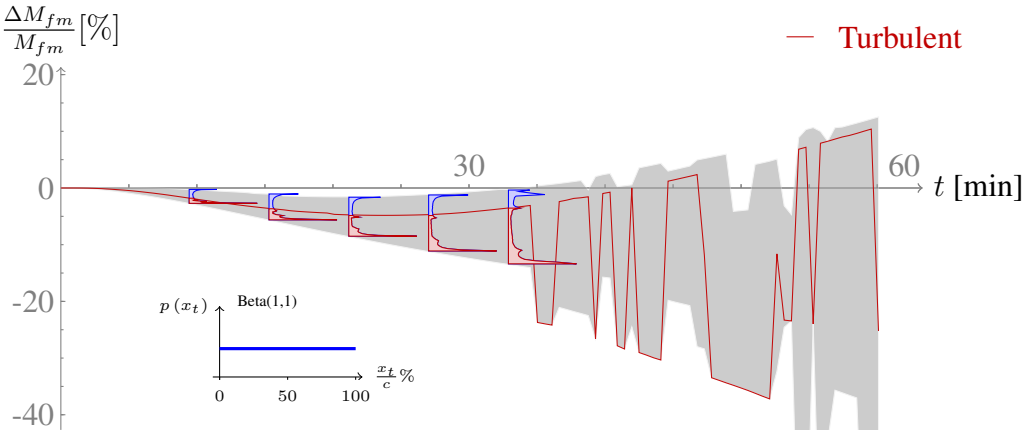

(a) Uniform

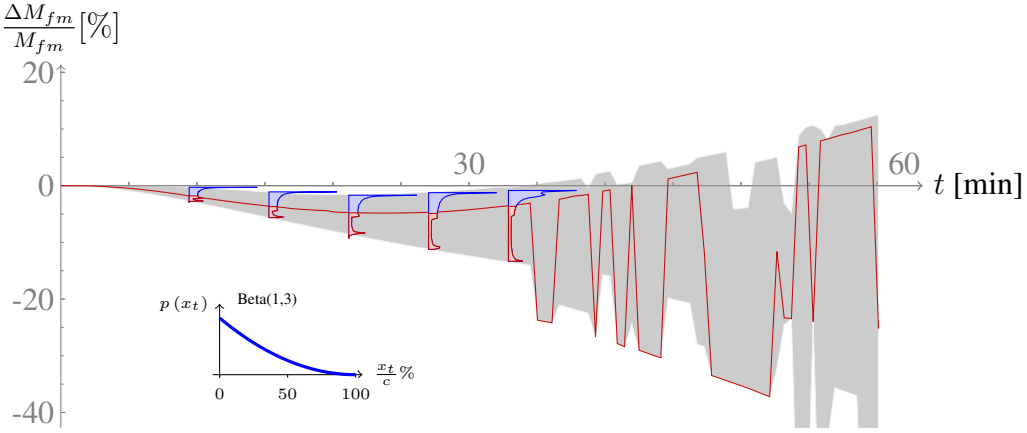

(b) Beta(1,3)

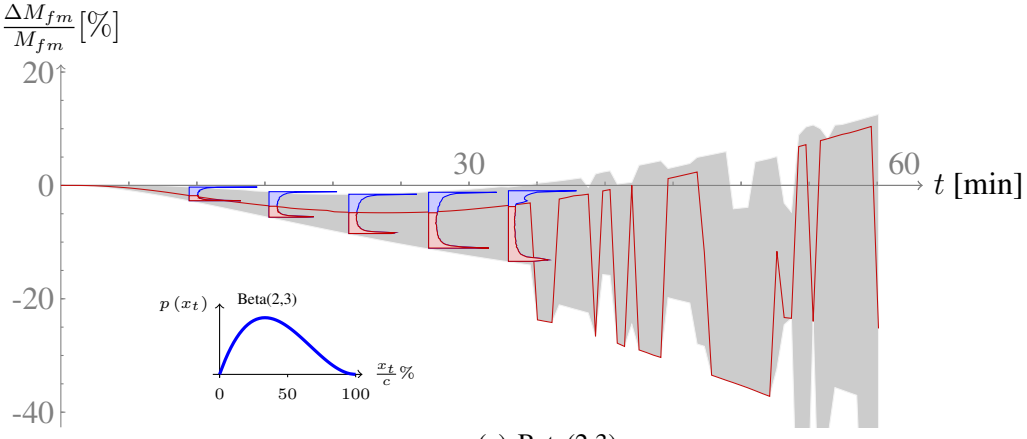

(c) Beta(2,3)

Figure 8.14: Uncertainty propagation results for the flutter margin, $H = 12$ km

Table 8.4: Probability of failure p_f [%], $M_\infty = 8$

Time [min]	3.57	9.43	15.30	21.17	27.03	32.90
Uniform	65.30	60.76	63.03	65.72	68.59	70.08
Beta(2,3)	47.03	40.56	44.02	49.54	56.73	63.17
Beta(1,3)	32.53	27.67	28.60	30.36	34.44	36.50

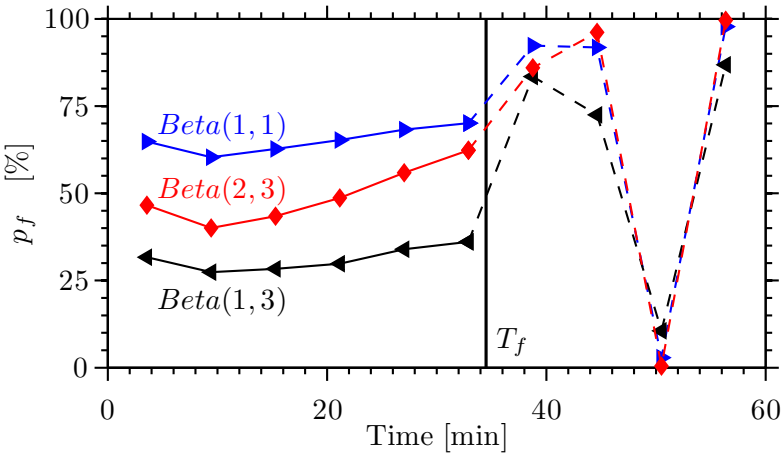

Figure 8.15: Probability of failure p_f [%] as function of time for $M_\infty = 8$ and various probability distributions.

spectively. The transition location is assumed to be distributed according to the $Beta(1,3)$ distribution. The PDF of the variation of flutter Mach number is shown for the time instants before buckling occurs.

The probability of failure is given in Fig. 8.17. Depending on the Mach number, the chances that the stability margin is less than the one predicted using fully turbulent flows varies between 25 and 50%. This illustrates that the turbulent case is not the worst case possible.

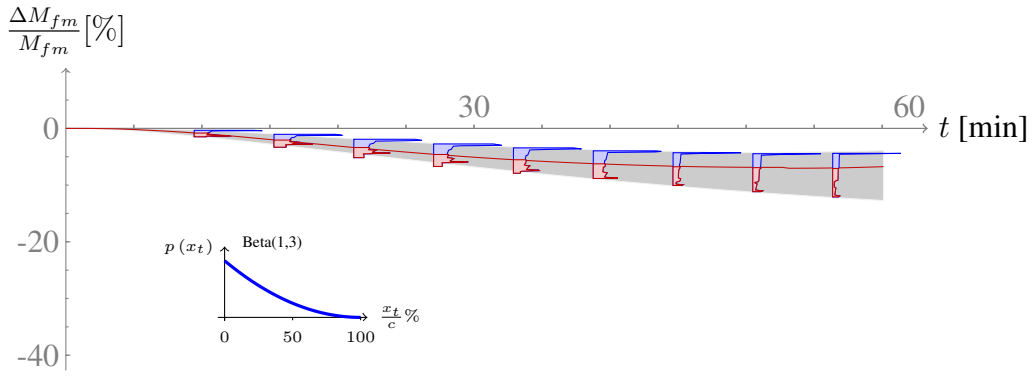

(a) $M_\infty = 6$

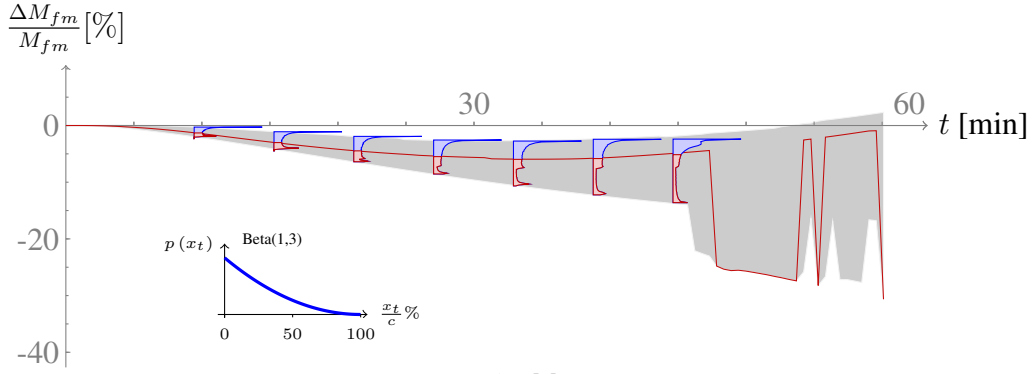

(b) $M_\infty = 7$

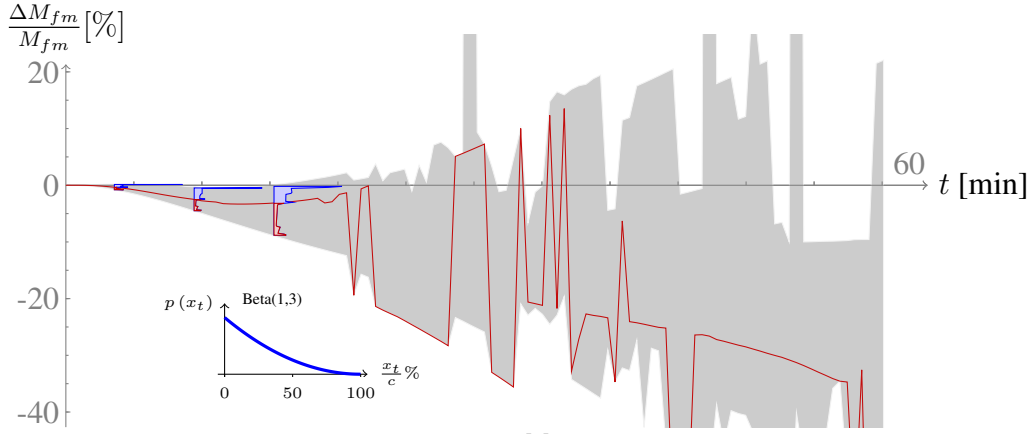

(c) $M_\infty = 10$

Figure 8.16: Uncertainty propagation results for the flutter margin for various flight Mach numbers, $H = 12$ km

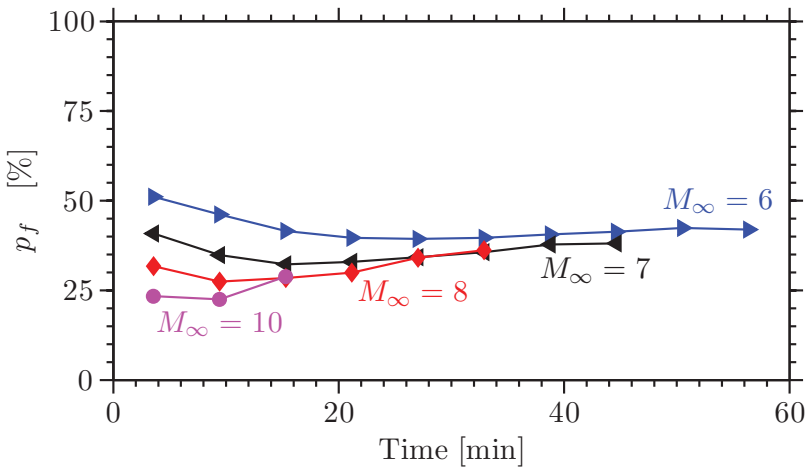

Figure 8.17: Probability of failure p_f [%] as function of time, for $p_{x_t} = p_{xBeta(1,3)}$

CHAPTER 9

CONCLUSIONS AND RECOMMENDATIONS FOR FUTURE RESEARCH

A systematic study of the effect of various uncertainties present in air–breathing hypersonic aerothermoelastic vehicles was carried out. The primary goal was to explore the use of uncertainty propagation in the context of hypersonic vehicle aeroelasticity and aerothermoelasticity. The novel contributions consist of identifying and quantifying uncertainties, using probability distributions, in principal variables of the problem and using stochastic collocation to propagate it. The variability in turbulence and real gas modeling is also considered. The results demonstrate the importance of (1) including uncertainty in the aerodynamic quantities (heat flux, transition), (2) turbulence modeling, and (3) the high sensitivity of hypersonic vehicles to thermal effects. Several uncertainty propagation approaches based on the response surface approach were investigated. A loosely–coupled aerothermoelastic framework using CFD, suitable to consider several gas and turbulence models, was developed.

9.1 Conclusions

The conclusions presented here should be considered within the assumptions made in these studies. Stochastic collocation is an efficient approach for propagating uncertainty in aeroelastic and aerothermoelastic analyses. It provides a framework which can account for a

wide range of cases. The results demonstrate that deterministic quantification of aeroelastic and aerothermoelastic stability boundaries may be inadequate for hypersonic vehicle analysis and hence, non–deterministic approaches are required.The principal conclusions of this study are:

1. Stochastic collocation is an efficient approach to propagate uncertainties when the number of variables is limited to less than 5. It provides a computationally efficient method for computing output statistics such as: the expected value, standard deviation, probability distribution and the probability of failure. However, it does not perform well in presence of discontinuities and strong nonlinearities.

2. The effect of thermal loading on the aeroelastic stability of a typical section is estimated using the uncertainty propagation framework. The predicted flutter Mach number can decrease by up to 60% from its value without thermal effect. The deterministic flutter Mach number is close to the maximum flutter Mach number for each particular flight condition and elastic offset.

3. The probability distributions of the random inputs have a significant effect on the probabilistic results of the flutter Mach number, and thus the probability of failure.

4. For the aerothermoelastic stability of a panel, the uncertainties inherent in turbulence modeling and transition prediction introduce additional sources of error. The uncertainties associated with transition location and the heat flux prediction influence the onset of instability. A 20% variation in the heat flux amplitude combined with the uncertainty in transition location yields up to a 18% decrease in flight time. Note that the transition is considered only in front of the leading edge of the panel and not on the panel itself.

5. The complexity of high fidelity aerothermoelastic analyses requires expensive computations which are not suitable for analyzing integrated airframe–propulsion effects.

However, estimating aerothermoelastic deflections at an early stage and propagating them through the propulsion analysis can alleviate the computational cost of the fully coupled analysis. Thus, it provides a first step towards an improved understanding for the effect of flexibility and thermal deformations on airframe–integrated scramjet engine system.

6. For the complete vehicle, the aerothermoelastic deformations are small. The cowl is identified as an important contributor to uncertainty and sensitivity of the integrated propulsion system analysis. Accurate modeling of the thermal gradient through the main components of the structure is required. The structural model has to account for thermal gradients through the thickness of the vehicle airframe and cowl.

7. A framework for hypersonic aerothermoelastic calculation using CFD is presented. The RBF approach is a robust and efficient mesh deformation scheme. However, the exact geometrical shape is not preserved throughout the deformation unless a sufficient number of driving points is used.

8. A robust system identification method for determining the flutter speed has been developed. It compares well with ARMA and LSCF in the case of the typical section. For the low aspect ratio wing, the ARMA approach did not perform well and the new SI was the method of choice.

9. This is the first study to explore real gas effects on aeroelastic stability in a systematic manner. This work shows that real gas effects modify the aeroelastic stability boundary by 3% to 6% at the flight conditions considered.

10. Turbulence modeling introduces a degree of uncertainty in the calculation of aeroelastic stability margins by introducing a degree of uncertainty. A thicker boundary layer results in an increase in aerodynamic loading, consequently viscosity reduces the flutter margin.

11. The behavior of the wing in high speed flight is strongly dependent on the thermal stresses. Thermal buckling causes significant loss in aeroelastic stability margins. Turbulent flow results in a shorter flight time when compared to that for laminar flow.

12. Transition was found to be a key parameter for the aerothermoelastic behavior of the wing. It significantly affects the thermal problem and the aerothermoelastic behavior of the wing. Transition at the surface of the wing creates temperature gradients in the load carrying structure which modify thermal stresses and structural properties. Investigating the limiting cases of turbulent or laminar flow is not sufficient when transition is likely to occur on the structure.

9.2 Future Work

This dissertation has considered efficient and accurate computational approaches for uncertainty propagation in various aerothermoelastic analyses. This work highlights important factors and assumption that are usually either discarded (transition) or considered as conservative (turbulent flows) in hypersonic vehicle analysis. Therefore, it exposes several aspects of hypersonic flight that require further investigations.

A natural extension of this work is to consider the stability of a 3D panel with both high fidelity and approximate fluid models coupled to a FEM–based structural model.

Transition is an important factor in determining thermal stresses. Predicting transition is a current area of research. Accurate determination of transition location is difficult. It is sensitive to several parameters whose exact value is unknown in a deterministic sense (free stream turbulence levels, surface roughness,etc). Therefore, use of a simple approximate model or a surrogate model fitted from a database obtained from experiments or high fidelity simulation such as direct numerical simulation (DNS) may be useful. The surrogate model is used in a more comprehensive model where both prediction and associated

uncertainty are propagated. This approach is suitable for aerothermoelastic studies where transition is included, as represented by the stability of a heated three dimensional panel in hypersonic flows with transition on its surface. The surrogate used to predict transition can be trained using either experimental data or high fidelity computations for various shapes of the panel and surface temperatures to capture the relation between transition location, the surface geometry, and temperature. Wall temperature and surface roughness can also be included.

The present work emphasizes the important role of thermal stresses in the structural model. The structure of a hypersonic vehicle is subjected to nonlinear behavior due to the extreme heat loads and changes over cycles of flights due to nonlinear effects (high thermal stresses, plasticity, fatigue) [15, 175]. Characterizing uncertainties due to defects, degraded material properties or non–homogeneous material properties is important. The structural components of the inlet, engine, or control surfaces are expected to be the most sensitive to defects and misalignments. Thermal degradation and non–homogeneous distribution of material properties are also important. Uncertainty propagation techniques can be used to estimate the sensitivity of representative components of hypersonic vehicles to changes in initial and boundary conditions as well as in material properties. The ability to identify and quantify the uncertainty in these parameters is difficult.

In aeroelastic applications, the aerodynamic influence matrices can be obtained from various aerodynamic theories. Using CFD is computationally expensive. In this thesis, a system identification was implemented. It relied on estimating the aerodynamic influence matrices. These aerodynamic influence matrices can be used with a kriging interpolation for efficient flutter Mach number determination or control of the flexible aircraft. Creating a surrogate or a curve fit of the aerodynamic influence matrices would reduce the cost of determining flutter boundaries. It has been done in the past but without propagating the error associated with the fit [48, 176].

Finally, as a natural extension of the airframe–integrated scramjet engine analysis, in-

cluding trim and considering the tight aerothermoelastic coupling including the propulsion system can shed light on the interactions between the control strategy and the aerothermoelastic deformations over the range of typical trajectories.

APPENDIX A

NUMERICAL INTEGRATION

In a computational framework, analytical integrations of quantity $f(x)$ are replaced by weighted sums as given in Eq. (A.1). The weight function $p_x(x)$ which can be a probability distribution for instance. The w_i's are positive scalars, called weights, which depend on the domain of integration Ω_x, and $p_x(x)$. The $(x_i)_{i=1,N_I}$ are called integration points.

$$\int_{\Omega_x} p_x(x) f(x) dx = \sum_{i=1}^{N_I} w_i f(x_i) \tag{A.1}$$

The number of points determines the accuracy of the scheme. Conventionally these schemes are developed based on the assumptions that polynomials are integrated exactly to a certain order. Gaussian quadrature is the most accurate scheme and integrates exactly polynomials up to order $2P-1$ using $N_I = P$ points. An efficient algorithm to compute the numerical integration points and corresponding weights for any order is presented in Ref. [144].

Multidimensional integration is an extension of the one dimensional case by considering the cartesian product of the integration scheme in each dimension. In the case of N_v variables, it yields to $(N_I)^{N_v}$ integration points. Therefore the computational cost of multidimensional integration rises exponentially with the number of variables.

Alternatively, several methods have been considered as a computationally cheaper alternative to gaussian quadrature, illustrated in Fig. A.1(a). Three additional examples are given in Fig. A.1. Clenshaw–Curtis quadrature, illustrated in Fig. A.1(b), provides nested

quadrature schemes making convergence studies less expensive [177]. In theory it provides a first order convergence rate, however it has been shown in practice that it may be as efficient as Gauss quadrature [177]. Newton Cotes quadrature is illustrated in Fig. A.1(c). It uses equally spaced quadrature points which can be an interesting feature. However convergence properties are not guaranteed [177]. Newton Cotes can be used piecewise by splitting the interval in several subintervals and using a low order scheme in each interval, proving freedom for adaptability. Finally, in order to mitigate the curse of dimensionality, sparse grid methods have been developed using Smolyaks algorithm [178–180] as illustrated in Fig. A.1(d). These schemes are especially efficient when the interaction between the variables $x_1, \ldots, x_{Nv}$ is weak.

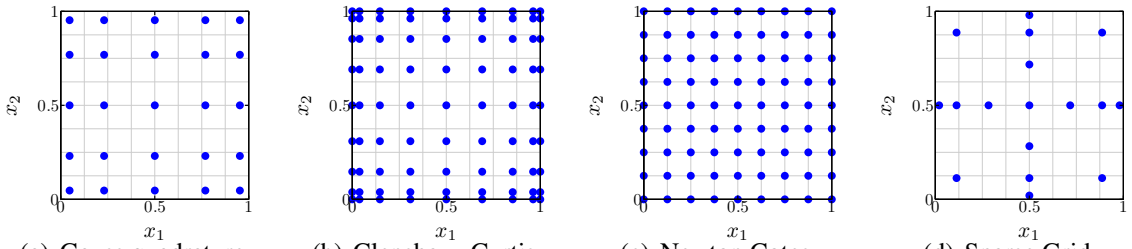

(a) Gauss quadrature (b) Clenshaw–Curtis (c) Newton Cotes (d) Sparse Grid

Figure A.1: Example of numerical integration points for $N_v = 2$

In this work, gaussian quadrature is utilized, motivated by its strong convergence, adaptability to account for various probability distributions, and the Lagrange–based interpolation SC framework which requires a cartesian grid.

APPENDIX B

AUTO REGRESSIVE MOVING AVERAGE

Autoregressive Moving-Average (ARMA) method is an efficient system identification method to compute the frequencies and corresponding damping coefficient from the transient response of the aeroelastic system. It has been used for flutter prediction of hypersonic systems in Refs. [103] and [84]. Based on a set of transient responses at different Mach number, the flutter boundary is interpolated.

The aeroelastic response, w of the structure at a given point due to an excitation is modeled by Eq. (B.1), where w_k is the displacement of a given point of the structure and e_k is the excitation at time kT_s. It assumes that at each time step the response of the system is a linear combination of the response at the n previous time steps and a linear combination of the input e at current and previous time steps k to $k-m$. For this reason, ARMA approach is applicable to systems which behavior can be identified as linear combination of damped harmonic oscillations [84].

$$w_k + a_1 w_{k-1} + a_2 w_{k-2} + \ldots + a_n w_{k-n} = b_1 e_{k-1} + b_2 e_{k-2} + \ldots + b_m e_{k-m} \qquad \text{(B.1)}$$

This approach assumes that the response (w_k) and excitation (e_k) are obtained either by measurement or numerical results at constant time step.In Eq. (B.1), a_i and b_i coefficients and orders, n and m are unknown. In flutter studies, $n = 2N_m$ and $m = 1$ are typical values. The choice of $m = 1$ is only required to account for a non–zero static offset.

In order to identify accurately the modal response of the aeroelastic system, all modes need to be excited. In experiments, the excitation due to turbulence can be considered as uncorrelated to the deformation w. Therefore the excitation can be considered as a white noise. However it needs to be sufficiently high in order to accurately identify frequencies and damping. In a numerical approach, in order to make sure that all the modes are excited, the initial conditions are set such that all components of the velocity, $\dot{q}$, are non-zero.

Based on the aeroelastic transient response, the coefficients (a_i) are calculated using a least–square method. In a state space form, the dynamic of the system can be written as given in Eq. (B.2).

$$\{\boldsymbol{X_p}\}_{k+1} = [\boldsymbol{A_p}]\,\{\boldsymbol{X_p}\}_k \quad w_k = \lfloor \boldsymbol{C_p} \rfloor\,\{\boldsymbol{X_p}\}_k \tag{B.2}$$

where

$$[A_p] = \begin{bmatrix} -a_1 & 1 & 0 & \dots & 0 \\ -a_2 & 0 & 1 & \dots & 0 \\ \vdots & \vdots & \vdots & \ddots & \vdots \\ -a_{2N_m-1} & 0 & 0 & \dots & 1 \\ -a_{2N_m} & 0 & 0 & \dots & 0 \end{bmatrix} \tag{B.3}$$

$$\boldsymbol{C_p} = \lfloor\ 1 \quad 0 \quad 0 \quad \dots \quad 0\ \rfloor \tag{B.4}$$

The state vector is defined as in Eq. (B.5).

$$\{\boldsymbol{X_p}\}_k = \begin{Bmatrix} w_k \\ h_1(k) \\ \vdots \\ h_{2N_m-1}(k) \end{Bmatrix} \tag{B.5}$$

with

$$w_k = -a_1 w_{k-1} + h_1(k-1) \tag{B.6}$$

$$h_1(k) = -a_2 w_{k-1} + h_2(k-1) \tag{B.7}$$

$$\vdots$$

$$h_{2N_m-1}(k) = -a_{2N_m} w_{k-1} \tag{B.8}$$

The frequencies and damping of the response are determined by the eigenvalues Λ_i of the transition matrix $[A_p]$ which are complex conjugate, Eq. (B.9).

$$\Lambda_i = r_i \pm \boldsymbol{i} s_i \quad 1 \leq i \leq N_m \tag{B.9}$$

The frequencies and corresponding damping are given by Eqs. (B.10) and (B.11), where $T_s = \frac{\pi}{2\omega_{n,max}}$ is the sampling time step used to calculate the AR coefficients, a_i.

$$\omega_{di} = \frac{1}{T_s} \tan^{-1}\left(\left|\frac{s_i}{r_i}\right|\right) \tag{B.10}$$

$$\omega_i \zeta_i = \frac{1}{2T_s} \ln\left(s_i^2 + r_i^2\right) \tag{B.11}$$

In the sampling time, $(\omega_n)_{max}$ is the maximum natural frequency in rad/s. The sampling time step corresponds to 4 points per period for the higher frequency mode.

The stability of the system is determined by the characteristic polynomial given in Eq. (B.12).

$$G(z) = a_0 z^{2N_m} + \sum_{i=1}^{2N_m} a_i z^{2N_m - i}, \quad a_0 = 1 \tag{B.12}$$

For $N_m = 2$, Jury's criteria provides with a metric F_Z which decreases linearly with increasing dynamic pressure, defined in Eq. (B.13) [84, 104].

$$F_Z = \frac{F^-(2N_m - 1)}{F^-(2N_m - 3)^2} = \frac{F^-(3)}{F^-(1)^2} \tag{B.13}$$

where

$$F^-(j) = \det\left(X_j - Y_j\right) \tag{B.14}$$

and

$$X_j = \begin{bmatrix} a_0 & \dots & a_{j-1} \\ 0 & \ddots & \vdots \\ 0 & 0 & a_0 \end{bmatrix}, \quad Y_j = \begin{bmatrix} a_{2N_m} & \dots & a_{2N_m+1-j} \\ \vdots & \ddots & 0 \\ a_{2N_m} & 0 & 0 \end{bmatrix} \tag{B.15}$$

When F_Z is positive, the system is stable and unstable when it becomes negative. The flight condition at which $F_Z = 0$ determines the flutter boundary. This method has been tested and appears to be efficient to perform system identification of the aeroelastic response [84]. For a number of mode greater than 2, the proposed parameter to predict flutter boundary is F_N defined in Eq. (B.16) [84, 181]. The metric F_Z shows good prediction of the stability boundary in the case of a two-degrees of freedom system but F_N looses its strength for more than two modes.

$$F_N = \frac{F^-(2N_m - 1)}{F^-(2N_m - 2)^2} \tag{B.16}$$

The ARMA method only requires the transient response at one point to estimate frequencies and damping.

APPENDIX C

LINEARIZATION OF PISTON THEORY

Third order piston theory (PT) was used in flutter prediction of a typical supersonic control surface in hypersonic flow and it outperformed other approximate approaches [2] when compared with CFD. This appendix shows that the third order expansion of PT is required only to capture the effect of thickness and not the effect of the aeroelastic deformations. A new approach to piston theory is presented in this appendix. Pressure is linearized with respect to the generalized degrees of freedom only. This approach that produces a linearized theory compares well with third order PT. It is shown that, in the case of aeroelastic stability studies, pressure and the generalized forces are a linear function of the generalized degrees of freedom and their time derivatives.

First, classical piston theory and its expansions are presented. Next, the linearization of PT is described. Finally results are given for the typical section and the low aspect ratio wing.

C.1 Piston Theory

Piston theory was developed by Lighthill [82], and became a popular approximation for aeroelastic analyses at high Mach numbers as the result of the work of Ashley and Zartarian [83].

In piston theory, the pressure at a given location on a moving surface is function of the

deformation and velocity of the surface at the point only. Thus PT provides a point–wise relationship between deformation and pressure, Eq. (C.1).

$$\frac{P(\boldsymbol{x},t)}{P_\infty} = \left[1 + \frac{\gamma-1}{2}\frac{v_n}{a_\infty}\right]^{\frac{2\gamma}{\gamma-1}} \tag{C.1}$$

The normal velocity of the structure, v_n, given by Eq. (C.2), is function of the cross sectional shape, or thickness distribution, Z_s, the angle of attack α_s, and the structural deformation w. The quantity $\frac{\partial Z_s}{\partial x}$ is the thickness ratio $\pm\tau$.

$$\frac{v_n}{a_\infty}(\boldsymbol{x}, w, \dot{w}) = \frac{1}{a_\infty}\frac{\partial w}{\partial t} + M_\infty\left[\frac{\partial}{\partial x}(Z_s + w) + \alpha_s\right] \tag{C.2}$$

In a modal representation of the structure, the deformation is given by Eq. (C.3), and v_n can be written as Eq. (C.4). For brevity, M_n is defined as $M_n = \frac{v_n}{a_\infty}$, in this Appendix.

$$w = \sum_{i=1}^{N_m} \psi_i q_i \tag{C.3}$$

$$M_n = \frac{v_n}{a_\infty}(\boldsymbol{x}; q, \dot{q}) = \sum_{i=1}^{N_m}\left[\frac{1}{a_\infty}\psi_i\dot{q}_i + M_\infty\frac{\partial\psi_i}{\partial x}q_i\right] + M_\infty\left(\frac{\partial Z_s}{\partial x} + \alpha_s\right) \tag{C.4}$$

C.2 Classical Piston Theory Expansions

Classical expansions of piston theory assume small M_n and the non-linear relation between pressure and v_n can be simplified using a Taylor expansion. The different orders of the expansion yield polynomial relations between P and v_n with different degrees of accuracy. The classical first to third order piston theory are given by Eq. (C.5) where the order refers to the highest order of M_n that is retained in the expansion.

$$\frac{P(x,t) - P_\infty}{P_\infty} \approx \gamma\left[M_n + \frac{\gamma+1}{4}M_n^2 + \frac{\gamma+1}{12}M_n^3\right] \tag{C.5}$$

This approaches assumes small static angle of attack, small airfoil thickness, and small deformation. These limitations are given by Eqs. (C.6) and (C.7) in terms of the undeformed airfoil and the deformation, respectively.

$$M_\infty \alpha_s \ll 1 \quad \text{and} \quad M_\infty \tau \ll 1 \tag{C.6}$$

$$\frac{\dot{w}}{a_\infty} \ll 1 \quad \text{and} \quad M_\infty \frac{\partial w}{\partial x} \ll 1 \tag{C.7}$$

Assuming simple harmonic oscillations with a frequency ω_i, the velocity of the structural deformation, $\dot{w}$, is of the order of magnitude of $\omega_i \bar{w}$, where ω_i is a natural frequency and $\bar{w}$ is the amplitude of the structural deformation. In addition, it can be assumed that $\frac{\partial w}{\partial x}$ is of the same order of magnitude as $\frac{\bar{w}}{c}$. Therefore, Eq. (C.7) is replaced by Eq. (C.8).

$$\omega_i \bar{w} \ll a_\infty \quad \text{and} \quad \frac{\bar{w}}{c} \ll \frac{1}{M_\infty} \tag{C.8}$$

C.3 Linearized Piston Theory

In aeroelasticity, a relation between unsteady pressure (or the loads) and the generalized degrees of freedom is important. Expanding, piston theory with respect to the generalized degrees of freedom *only* is presented in this section. Note that M_n is an affine function of the generalized degrees of freedom as given in Eq. (C.4). It combines a linear function of the degrees of freedom and a constant term that accounts for α_s and the thickness of the wing. Combining Eqs. (C.1) and (C.4), pressure is given by:

$$\frac{P(\boldsymbol{x},t)}{P_\infty} = \left[\underbrace{1 + \frac{\gamma-1}{2} M_\infty \left(\frac{\partial Z_s}{\partial x} + \alpha_s \right)}_{\text{static term}} + \underbrace{\frac{\gamma-1}{2} \sum_{i=1}^{N_m} \left(\frac{1}{a_\infty} \psi_i \dot{q}_i + M_\infty \frac{\partial \psi_i}{\partial x} q_i \right)}_{\text{deformation related term}} \right]^{\frac{2\gamma}{\gamma-1}} \tag{C.9}$$

Equation (C.9) is rewritten as:

$$\frac{P(\boldsymbol{x},t)}{P_\infty} = \left[1 + \frac{\gamma-1}{2} M_\infty \left(\frac{\partial Z_s}{\partial x} + \alpha_s \right) \right]^{\frac{2\gamma}{\gamma-1}} \left[1 + \frac{\gamma-1}{2} \frac{\sum_{i=1}^{N_m} \left(\frac{1}{a_\infty} \psi_i \dot{q}_i + M_\infty \frac{\partial \psi_i}{\partial x} q_i \right)}{1 + \frac{\gamma-1}{2} M_\infty \left(\frac{\partial Z_s}{\partial x} + \alpha_s \right)} \right]^{\frac{2\gamma}{\gamma-1}} \tag{C.10}$$

Equation (C.10) can be rewritten as:

$$\frac{P(\boldsymbol{x},t)}{P_\infty} = \eta \left[1 + \frac{\gamma-1}{2} \tilde{M}_n \right]^{\frac{2\gamma}{\gamma-1}} \tag{C.11}$$

where

$$\eta = \left[1 + \frac{\gamma-1}{2} M_\infty \left(\frac{dZ_s}{dx} + \alpha_s \right) \right]^{\frac{2\gamma}{\gamma-1}} \tag{C.12}$$

$$\tilde{M}_n = \frac{a_\infty}{\tilde{a}} \sum_{i=1}^{N_m} \psi_i \frac{\dot{q}_i}{a_\infty} + M_\infty \frac{d\psi_i}{dx} q_i \tag{C.13}$$

$$\tilde{a} = a_\infty \left[1 + \frac{\gamma-1}{2} M_\infty \left(\frac{dZ_s}{dx} + \alpha_s \right) \right] \tag{C.14}$$

The expression of pressure in Eq. (C.11) is similar to piston theory, Eq. (C.1). The differences are 1) a correction term η and 2) a modified $\tilde{M}_n$, defined by Eqs. (C.12) and (C.13), respectively. The factor η accounts for the nonlinearities present in the undeformed steady state and corresponds to the ratio between the free stream pressure and the local steady pressure acting on the undeformed geometry. The $\tilde{M}_n$ term has a form similar to M_n used in

conventional piston theory but only accounts for the structural deformation. It corresponds to a form of local piston theory with corrected steady pressure ηP_∞ and speed of sound $\tilde{a}$. The expression in Eq. (C.11) distinguishes between the contribution of static effects (angle of attack and shape) and deformations, q and $\dot{q}$.

Pressure, given by Eq. (C.11), is expanded with respect to small deformations $\mathbf{q}$ and $\dot{\mathbf{q}}$ which corresponds to small $\tilde{M}_n$. It yields Eq. (C.15).

$$\frac{P}{P_\infty} = \eta \left[1 + \gamma \tilde{M}_n + \gamma \frac{\gamma+1}{4} \tilde{M}_n^2 + \gamma \frac{\gamma+1}{12} \tilde{M}_n^3 \right] \tag{C.15}$$

The expression of pressure is very similar to the classical 1^{st} to 3^{rd} order piston theory, and is referred to a linearized piston theory in this document. The only assumption is small deformations as determined by the relations given by Eq. (C.16). There is no assumptions on α_s and $\left|\frac{\partial Z_s}{\partial x}\right| = \tau$.

$$\omega_i \bar{w} \ll a_\infty \quad \text{and} \quad \frac{\bar{w}}{c} \ll \frac{\tilde{a}/a_\infty}{M_\infty} \tag{C.16}$$

It is relevant to note that the various expansions of piston theory allow analytical integration of the pressure loads when using a Rayleigh–Ritz approache. When the integration of the loads is performed numerically using Gaussian quadrature, there is no analytical nor computational benefit in expanding Eq. (C.1). However, the expansions provide a way to quantify the degree of non–linearity in the relation between pressure and deformation.

C.4 Aerodynamic influence matrices

Keeping only the linear part of the linearized piston theory in Eq. (C.15), the aerodynamic influence matrices are derived by identifying the contribution of $\boldsymbol{q}$ and $\dot{\boldsymbol{q}}$ in the expression of the generalized loads given by Eq. (C.17).

$$\boldsymbol{Q} = -\int_{\partial\Omega} \psi_i P\left(\boldsymbol{q}, \dot{\boldsymbol{q}}\right) n_z dS = \mathbf{K_A q} + \mathbf{C_A \dot{q}} \tag{C.17}$$

The aerodynamic stiffness and damping matrices, $\mathbf{K_A}$ and $\mathbf{C_A}$, are given by Eqs. (C.18) and (C.19) respectively.

$$\mathrm{K}_{\mathrm{A}ij} = -\int_{\partial\Omega} \psi_i \gamma M_\infty P_\infty \left[1 + \frac{\gamma - 1}{2} M_\infty \left(\frac{dZ_s}{dx} + \alpha_s\right)\right]^{\frac{2\gamma}{\gamma-1}-1} \frac{d\psi_j}{dx} n_z dS \tag{C.18}$$

$$\mathrm{C}_{\mathrm{A}ij} = -\int_{\partial\Omega} \psi_i P_\infty \frac{\gamma}{a_\infty} \left[1 + \frac{\gamma - 1}{2} M_\infty \left(\frac{dZ_s}{dx} + \alpha_s\right)\right]^{\frac{2\gamma}{\gamma-1}-1} \psi_j n_z dS \tag{C.19}$$

C.5 Results and Conclusion

The flutter boundary of the low aspect ration wing is computed for different altitudes. Flutter boundaries are given in terms of flutter Mach number and dynamic pressure, and compared to Ref. [157] results for 3^{rd} order piston theory as presented in Figs. C.1(a) and C.1(b), respectively. In addition, the same results are given for the two dimensional airfoil in Figs. C.2(a) and C.2(b). Different forms of piston theory are used: classical first order (1 PT), second order (2 PT), third order (3 PT) piston theory as well as linearized PT (Lin. PT). Full order PT (Full PT) corresponds to the formula without any linearization given in Eq. (C.1).

Note that 3^{rd} order PT agrees with the results obtained in Ref. [157] which verifies the aeroelastic calculations. Similarly, 1^{st} and 2^{nd} order piston theory do not give good predictions of the flutter boundary as shown in previous studies, since they do not account for thickness effects. The stability boundary obtained with the linearized piston theory and full order piston theory agree with each other perfectly. These results show that it is not

necessary to use high order terms for the deformation of the wing in piston theory as long as the steady state (thickness and angle of attack) is captured accurately. The requirements of using 3^{rd} order piston theory are only due to the thickness ($\tau = 3\%$) of the wing, especially at high Mach number for which $M_\infty \tau$ is large.

In conclusion, for aeroelastic stability studies, the generalized forces are linear functions of the structural degrees of freedom and their time derivative when considering piston theory. However the steady part which accounts for thickness effect and static angle of attack is not small and needs to be captured appropriately by either considering third order piston theory or the alternative linearization presented here.

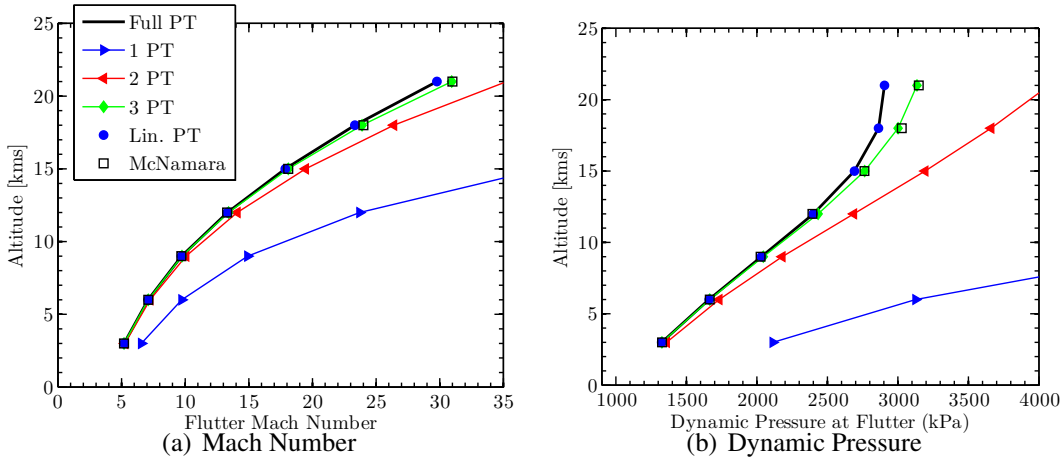

Figure C.1: Flutter boundary using different order of piston theory for the low aspect ratio wing

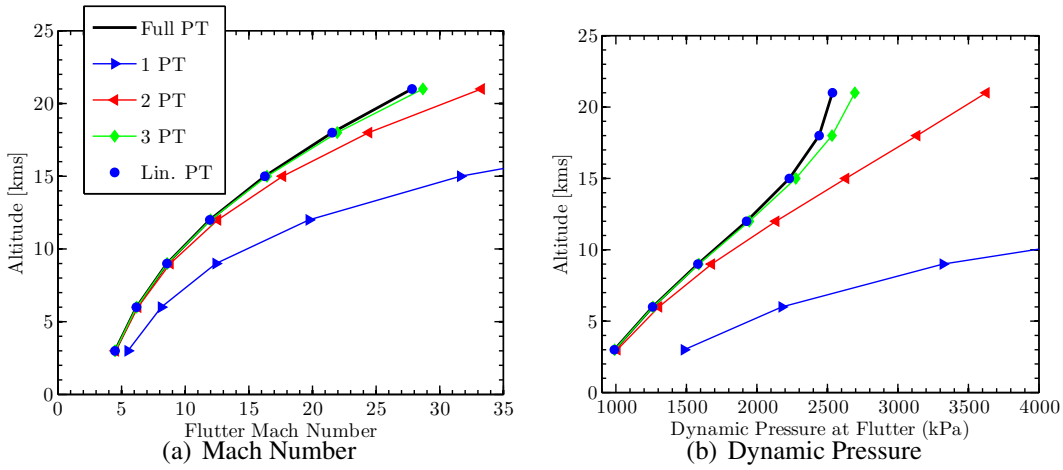

Figure C.2: Flutter Boundary using different order of piston theory for the typical section

BIBLIOGRAPHY

[1] McNamara, J. J. and Friedmann, P. P., "Aeroelastic and Aerothermoelastic Analysis in Hypersonic Flow: Past, Present, and Future," *AIAA Journal*, Vol. 49, No. 6, June 2011, pp. 1089–1122.

[2] McNamara, J. J., Friedmann, P. P., Powell, K., Thuruthimattam, B., and Bartels, R., "Aeroelastic and Aerothermoelastic Behavior in Hypersonic Flow," *AIAA Journal*, Vol. 46, No. 10, Oct. 2008, pp. 2591–2610.

[3] Fidan, B., Mirmirani, M., and Ioannou, P. A., "Flight Dynamics and Control of Air-Breathing Hypersonic Vehicles: Review and New Directions," *Proceedings of the 12th AIAA International Space Planes and Hypersonic Systems and Technologies*, Norfolk, Virginia, December 15–19 2003, AIAA Paper No. 2003-7081.

[4] Hallion, R. P., "The History of Hypersonics: or, Back to the Future - Again and Again," *Proceedings of the 43rd Aerospace Sciences Meeting and Exhibit*, Reno,Nevada, January 10–13 2005, AIAA Paper No. 2005-329.

[5] Dolvin, D. J., "Hypersonic International Flight Research and Experimentation (HIFiRE), Fundamental Sciences and Technology Development Strategy," *Proceedings of the 15th AIAA International Space Planes and Hypersonic System and Technologies Conference*, Dayton, Ohio, April 28 – May 1 2008, AIAA Paper 2008–2581.

[6] Rodriguez, A. A., Dickeson, J. J., Cifdaloz, O., Kelkar, A., Vogel, J. M., and Soloway, D., "Modeling and Control of Scramjet-Powered Hypersonic Vehicles: Challenges, Trends, and Tradeoffs," *Proceedings of AIAA Guidance, Navigation and Control Conference and Exhibit*, Honolulu, Hawaii, August 18–21 2008, AIAA Paper No. 2008-6793.

[7] Bertin, J. J., *Hypersonic Aerothermodynamics*, AIAA Education Series, 1994.

[8] Anderson, J. D., *Modern Compressible Flow with Historical Perspective*, Third Edition Mc Graw Hill Editions, 2004.

[9] Fry, R., "A century of ramjet propulsion technology evolution," *Journal of propulsion and power*, Vol. 20, No. 1, 2004, pp. 27–58.

[10] Jenkins, D. R., "Hypersonic Before the Shuttle: A concise History of the X-15 Research Plane. Monographs In Aerospace History 18," *National Aeronautics and Space Administration, Washington, DC*, 2000.

[11] Merlin, P., "Design and Development of the Blackbird: Challenges and Lessons Learned," *Proceedings of the 47th Aerospace Sciences Meeting Including The New Horizons Forum and Aerospace Exposition*, Orlando, Florida, January 5–8 2009, AIAA Paper No. 2009-1522.

[12] Heppenheimer, T. A., "Facing the heat barrier: a history of hypersonics," Report NASA SP-2007-4232, NASA history series, 2007.

[13] Augenstein, B. W., Harris, E. D., Aroesty, J., Blumenthal, I., Brooks, N., Frelinger, D. R., Garber, T. B., Gottemoeller, R. E., Hiland, J. R., Liu, S.-k., Pace, S., Rosen, J., Rowell, L., and Stucker, J., *The National Aerospace Plane (NASP): Development Issues for the Follow–on Vehicle*, RAND Corporation, 1993.

[14] Merlin, P. W., "Mach 3+: NASA/USAF YF-12 flight research, 1969-1979," Report NASA SP 2001-4525, NASA history series, Monographs in aerospace history, no. 25, 2002.

[15] Eason, T. G. and Spottswood, S., "A Structures Perspective on the Challenges Associated with Analyzing a Reusable Hypersonic Platform," *Proceedgins of the 54th AIAA/ASME/ASCE/AHS/ASC Structures, Structural Dynamics, and Materials*, April 8–11 2013, AIAA Paper 2013–1747.

[16] Dugundji, J. and Calligeros, J. M., "Similarity Laws for Aerothermoelastic Testing," *Journal of Aerospace Sciences*, Vol. 29, No. 8, Aug. 1962, pp. 935–950.

[17] Haldar, A. and Mahadevan, S., *Probability, Reliability and Statistical Methods in Engineering Design*, Jon Wiley and Sons, Inc., 2000.

[18] Eldred, M. S. and Burkardt, J., "Comparison of Non-Intrusive Polynomials Chaos and Stochastic Collocation Methods for Uncertainty Quantification," *Proceedings of the 47th AIAA Aerospace Sciences Meeting Including The New Horizons Forum and Aerospace Exposition*, Orlando, Florida, January 5–8 2009, AIAA Paper No. 2009-976.

[19] Pettit, C., "Uncertainty Quantification in Aeroelasticity: Recent Results and Research Challenges," *Journal of Aircraft*, Vol. 41, No. 5, September-October 2008, pp. 1217–1229.

[20] Hosder, S., Grossman, B., Haftka, R. T., Mason, W. H., and Watson, L. T., "Quantitative relative comparison of CFD simulation uncertainties for a transonic diffuser problem," *Computers & fluids*, Vol. 35, No. 10, 2006, pp. 1444–1458.

[21] Smarslok, B., Culler, A., and Mahadevan, S., "Error Quantification and Confidence Assessment of Aerothermal Model Predictions for Hypersonic Aircraft," *Proceedings of the 53rd AIAA/ASME/ASCE/AHS/ASC Structures, Structural Dynamics, and Materials*, April 23–26 2012, AIAA Paper 2012-1817.

[22] Riley, M. E., Grandhi, R. V., and Kolonay, R., "Quantification of Modeling Uncertainty in Aeroelastic Analyses," *Journal of Aircraft*, Vol. 48, No. 3, 2011, pp. 866–873.

[23] Kennedy, M. C. and O'Hagan, A., "Bayesian calibration of computer models," *Journal of the Royal Statistical Society: Series B (Statistical Methodology)*, Vol. 63, No. 3, 2001, pp. 425–464.

[24] McFarland, J., Mahadevan, S., Romero, V., and Swiler, L., "Calibration and uncertainty analysis for computer simulations with multivariate output," *AIAA Journal*, Vol. 46, No. 5, 2008, pp. 1253–1265.

[25] Ghanem, R. G. and Spanos, P. D., *Stochastic Finite Elements, a Spectral Approach, Revised Edition*, Dover, 1991.

[26] Mathelin, L., Hussaini, M. Y., and Zang, T. A., "Stochastic Approaches to Uncertainty Quantification in CFD Simulations," *Numerical Algorithms Journal*, Vol. 38, No. 1, March 2005, pp. 209–236.

[27] Walters, R. W., "Towards Stochastic Fluid Mechanics via Polynomial Chaos," *Proceedings of the 41st Aerospace Sciences Meeting and Exhibit*, Reno, Nevada, January 6–9 2003, AIAA Paper No. 2003-413.

[28] Witteveen, J., Loeven, A., and Bijl, H., "An adaptive stochastic finite elements approach based on Newton–Cotes quadrature in simplex elements," *Computers & Fluids*, Vol. 38, No. 6, 2009, pp. 1270–1288.

[29] Eldred, M. S., Webster, C. G., and Constantine, P. G., "Design Under Uncertainty Employing Stochastic Expansion Methods," *Proceedings of the 12th AIAA/ISSMO Multidisciplinary Analysis and Optimization Conference*, Orlando, Florida, September 10–12 2008, AIAA Paper No. 2008-6001.

[30] Murugan, S., Harursampath, D., and Ganguli, R., "Material Uncertainty Propagation in Helicopter Nonlinear Aeroelastic Response and Vibration Analysis," *AIAA Journal*, Vol. 46, No. 9, Sept. 2008, pp. 2332–2344.

[31] Styuart, A. V., Livne, E., Demasi, L., and Mor, M., "Flutter Failure Risk Assessment for Damage-Tolerant Composite Aircraft Structures," *AIAA Journal*, Vol. 49, No. 3, March 2011, pp. 655–669.

[32] Lindsley, N. J., Beran, P. S., and Pettit, C. L., "Integration of Model Reduction and Probabilistic Techniques with Deterministic Multi-physics Models," *Proceedings of the 44th AIAA Aerospace Sciences Meeting and Exhibit*, Reno, Nevada, January 9–12 2006, AIAA Paper No. 2006-192.

[33] Lindsley, N. J., Beran, P. S., and Pettit, C. L., "Effects of Uncertainty on Nonlinear Plate Response in Supersonic Flow," *Proceedings of the 9th AIAA/ISSMO Symposium on Multidisciplinay Analysis and Optimization*, Atlanta, Georgia, September 4–6 2002, AIAA Paper No. 2002-5600.

[34] Epureanu, B., Tang, L., and Paidoussis, M. P., "Exploiting chaotic dynamics for detecting parametric variations in aeroelastic systems," *AIAA Journal*, Vol. 42, No. 4, 2004, pp. 728–735.

[35] Kurdi, M., Lindsley, N., and Beran, P., "Uncertainty Quantification of the Goland Wing's Flutter Boundary," *Proceedings of the AIAA Atmospheric Flight Mechanics Conference and Exhibit*, Hilton Head, South Carolina, August 20-23 2007, AIAA Paper No. 2007-6309.

[36] Leijonhufvud, M. C. and Karlsson, A., "Industrial Application of Robust Aeroelastic Analysis," *Journal of Aircraft*, Vol. 48, No. 4, 2011, pp. 1176–1183.

[37] Pitt, D., Haudrich, D., Thomas, M., and Griffin, K., "Probabilistic Aeroelastic Analysis and Its Implications on Flutter Margin Requirements," *Proceedings of the AIAA/ASME/ASCE/AHS/ASC Structures, Structural Dynamics, and Materials*, April 2008, AIAA Paper 2008-2198.

[38] Siva, C., Murugan, M., and Ganguli, R., "Uncertainty Quantification in Helicopter Performance Using Monte Carlo Simulations," *Journal of Aircraft*, Vol. 48, No. 5, 2011, pp. 1503–1511.

[39] Wright, M. J., Bose, D., and Chen, Y.-K., "Probabilistic modeling of aerothermal and thermal protection material response uncertainties," *AIAA Journal*, Vol. 45, No. 2, 2007, pp. 399–410.

[40] Schütte, G. and Staudacher, S., "Probabilistic Aspects of Scramjet Design," *Journal of Propulsion and Power*, Vol. 25, No. 2, March–April 2009, pp. 281–288.

[41] Wang, Q., Duraisamy, K., Alonso, J. J., and Iaccarino, G., "Risk assessment of scramjet unstart using adjoint-based sampling methods," *AIAA Journal*, Vol. 50, No. 3, 2012, pp. 581–592.

[42] Adams, B. M., Hart, W. E., Eldred, M. S., Dunlavy, D. M., Hough, P. D., Giunta, A. A., Griffin, J. D., Martinez-Canales, M. L., Watson, J.-P., Kolda, T. G., et al., *DAKOTA, a Multilevel Parellel Object-oriented Framework for Design Optimization, Parameter Estimation, Uncertainty Quantification, and Sensitivity Analysis: Version 4.0 Users's Manual*, United States. Department of Energy, 2006.

[43] Hosder, S., Walters, R. W., and Balch, M., "Efficient Sampling for Non-Intrusive Polynomial Chaos Applications with Multiple Uncertain Variables," *Proceedings of the 48th AIAA/ASME/ASCE/AHS/ASC Structures, Structural Dynamics, and Materials Conference*, Honolulu, Hawaii, April 23–26 2007, AIAA Paper No. 2007-1939.

[44] Beran, P. S. and Pettit, C. L., "A Direct Method for Quantifying Limit Cycle Oscillations Response Characteristics in the Presence of Uncertainties," *Proceedings of the 45th AIAA/ASME/ASCE/AHS/ASC Structures, Structural Dynamics, and Materials Conference*, Palm Springs, CA, April 19–22 2004, AIAA Paper No. 2004-1695.

[45] Choi, S.-K., Grandhi, R. V., and Canfield, R. A., "Structural Reliability under Non–Gaussian Stochasitc Behavior," *Computers and Structures*, Vol. 82, March 2004, pp. 1113–1121.

[46] Eldred, M., "Recent Advances in Non-Intrusive Polynomial Chaos and Stochastic Collocation Methods for Uncertainty Analysis and Design," *Proceeddings of the 50th AIAA/ASME/ASCE/AHS/ASC Structures, Structural Dynamics, and Materials, Palm Springs, CA*, May 4–7 2009, AIAA Paper 2009-2274.

[47] Hosder, S., Walters, R. W., and Balch, M., "Efficient Uncertainty Quantification Applied to the Aeroelastic Analysis of a Transonic Wing," *Proceedings of the 46th AIAA Aerospace Sciences Meeting and Exhibit*, Reno, Nevada, January 7–10 2008, AIAA Paper No. 2008-729.

[48] Danowsky, B. P., Chrstos, J. R., Klyde, D. H., Farhat, C., and Brenner, M., "Evaluation of Aeroelastic Uncertainty Analysis Methods," *Journal of Aircraft*, Vol. 47, No. 4, July 2010, pp. 1266–1273.

[49] Chantrasmi, T., Doostan, A., and Iaccarino, G., "Padé–Legendre approximants for uncertainty analysis with discontinuous response surfaces," *Journal of Computational Physics*, Vol. 228, No. 19, 2009, pp. 7159–7180.

[50] Buhmann, M. D., *Radial Basis Functions: Theory And Implementations*, Cambridge: Cambridge University Press, 2003.

[51] Jekabsons, G., *Adaptive Regression Splines toolbox for Matlab,ver. 1.3*, Institute of Applied Computer Systems, Riga Technical University, December 2009, Reference manual.

[52] Friedman, J. H., "Multivariate Adaptive Regression Splines," *The Annals of Statistics*, Vol. 19, No. 1, March 1991, pp. 1–67.

[53] Galbally, D., Fidkowski, K., Willcox, K., and Ghattas, O., "Non-linear model reduction for uncertainty quantification in large-scale inverse problems," *International journal for numerical methods in engineering*, Vol. 81, No. 12, 2010, pp. 1581–1608.

[54] Klimke, A., *Sparse Grid Interpolation Toolbox User's Guide, v5.1*, Institute für Angewandte Analysis und Numerische Simulation (IANS), Universität Stuttgart, 2008, ISSN 1611-4176.

[55] Bunjgartz, H.-J. and Dirnstorfer, S., "Multivariate Quadrature on Sparse Grids," *Computing, Archives for Scientific Computing*, Vol. 71, No. 1, August 23 2003, pp. 84–114.

[56] Nobile, F., Tempone, R., and Webster, C. G., "An anisotropic sparse grid stochastic collocation method for partial differential equations with random input data," *SIAM Journal on Numerical Analysis*, Vol. 46, No. 5, 2008, pp. 2411–2442.

[57] Sacks, J., Welch, W. J., Mitchell, T. J., and Wynn, H. P., "Design and Analysis of Computer Experiments," *Statistical Science*, Vol. 4, No. 4, 1989, pp. 409–435.

[58] Bichon, B. J., Mahadevan, S., and Eldred, M. S., "Reliability-based design optimization using efficient global reliability Analysis," *Proceedings of the 50th AIAA/ASME/ASCE/AHS/ASC Structures, Structural Dynamics, and Materials Conference*, Palm Springs, CA, May 4–7 2009, AIAA Paper No. 2009-2261.

[59] Viana, F. A. C., Pecheny, V., and Haftka, R. T., "Using Cross Validation to Design Conservative Surrogates," *AIAA Journal*, Vol. 48, No. 10, Oct. 2010, pp. 2286–2298.

[60] Duraisamy, K. and Chandrashekar, P., "Goal-oriented uncertainty propagation using stochastic adjoints," *Computers & Fluids*, Vol. 66, No. 0, 2012, pp. 10 – 20.

[61] Palacios, F., Duraisamy, K., Alonso, J. J., and Zuazua, E., "Robust grid adaptation for efficient uncertainty quantification," *AIAA Journal*, Vol. 50, No. 7, 2012, pp. 1538–1546.

[62] Wie, D. M. V., Drewery, D. G., King, D. E., and Hudson, C. M., "The Hypersonic Environment: Required Operating Conditions and Design Challenges," *Journal of Materials Science*, Vol. 39, March 2004, pp. 5915–5924.

[63] Shih, P., Prunty, J., and Mueller, R., "Thermostructural concepts for hypervelocity vehicles," *Journal of Aircraft*, Vol. 28, 1991, pp. 337–345.

[64] Hunt, J. L., Laruelle, G., and Wagner, A., "Systems challenges for hypersonic vehicles," *Proceedings of the Future Aerospace Technology in the Service of the Alliance, AGARD Conference*, Vol. 3, Palaiseau, France, April 1997.

[65] Handbook-MIL-HDBK, "5J-Metallic Materials and Elements for Aerospace Vehicle Structures," *Department of Defense Handbook*, Vol. 31, 2003.

[66] Handbook-MIL-HDBK, "5H-Metallic Materials and Elements for Aerospace Vehicle Structures," *Department of Defense Handbook*, , No. MIL-HDBK-5J, 2003.

[67] Ellis, D., Pagel, L., and Schaeffer, D., "Design and Fabrication of a Radiative Actively Cooled Honeycomb Sandwich Structural Panel for a Hypersonic Aircraft." Tech. rep., DTIC Document, NASA contractor Report 2957, 1978.

[68] Koch, L. C. and Pagel, L. L., "High Heat Flux Activity Cooled Honeycomb Sandwich Structural Panel for a Hypersonic Aircraft." Tech. rep., DTIC Document, NASA COntractor Report 2959, 1978.

[69] Tenney, D. R., Lisagor, W. B., and Dixon, S. C., "Materials and Structures for Hypersonic Vehicles," *Journal of Aircraft*, Vol. 26, No. 11, Nov. 1989, pp. 953–970.

[70] Myers, D. E., Martin, C. J., and Blosser, M. L., "Parametric Weight Comparison of Current and Proposed Thermal Protection System (TPS) Concepts," *Proceedings of the 33rd Thermophysics Conference*, Norfolk, VA, June 28 – July 1 1999, AIAA Paper No. 99–3459.

[71] Myers, D. E., Martin, C. J., and Blosser, M. L., "Parametric Weight Comparison of Advanced Metallic, Ceramic Tile, and Ceramic Blanket Thermal Protection Systems," Report NASA TM 2000–210289, National Aeronautics and Space Administration, June 2000.

[72] Ko, W. and Gong, L., *Thermostructural Analysis of Unconventional Wing Structures of a Hyper-X Hypersonic Flight Research Vehicle for the Mach 7 Mission*, National Aeronautics and Space Administration, Dryden Flight Research Center, NASA TP 2001–210398, 2001.

[73] Collier, C., "Stiffness, thermal expansion, and thermal bending formulation of stiffened, fiber-reinforced composite panels," *Proceedings of the 34th AIAA/ASME/ASCE/AHS/ASC Structures, Structural Dynamics, and Materials Conference, and AIAA/ASME Adaptive Structures Forum, La Jolla, CA*, April 19–22 1993, AIAA Paper 1993–1569.

[74] Collier, C., "Thermoelastic formulation of stiffened, unsymmetric composite panels for finite element analysis of high speed aircraft," *Proceedings of the 35th AIAA/ASME/ASCE/AHS/ASC Structures, Structural Dynamics, and Materials conference*, April 18–20 1994, AIAA Paper 1994–1579.

[75] Blosser, M. L., "Development of metallic thermal protection systems for the reusable launch vehicle," *Proceedings of the Space Technology and Applications International Forum Conference*, Vol. 387, January 26–30 1997, p. 1125, NASA TM–110296.

[76] Blevins, R. D., Bofilios, D., Holehouse, I., Hwa, V. W., Tratt, M. D., Laganelli, A. L., Pozefsky, P., and Pierucci, M., "Thermo-vibro-acoustic loads and fatigue of hypersonic flight vehicle structure," Tech. rep., DTIC Document, 2009.

[77] Zuchowski, B., "Air Vehicle Integration and Technology Research (AVIATR) Task Order 0015: Predictive Capability for Hypersonic Structural Response and Life Prediction Phase 1-Identification of Knowledge Gaps," Tech. rep., DTIC Document, 2010.

[78] Tzong, G., Jacobs, R., and Liguore, S., "Air Vehicle Integration and Technology Research (AVIATR) Task Order 0015: Predictive Capability for Hypersonic Structural Response and Life Prediction: Phase 1-Identification of Knowledge Gaps, Volume 1: Nonproprietary Version," Tech. rep., DTIC Document, 2010.

[79] Liguore, S. L., Pitt, D. M., Thomas, M. J., and Gurtowski, N., "Air Vehicle Integration and Technology Research (AVIATR). Delivery Order 0013 Nonlinear, Low-OrderReduced-Order Modeling Applications and Demonstration," Tech. rep., DTIC Document, 2011.

[80] Doggett, R. V., Ricketts, R. H., Noll, T. E., and Malone, J. B., "NASP Aeroservothermoelasticity Studies," Tech. rep., NASA TM 104058, April 1991.

[81] Ricketts, R. H., Noll, T. E., Whitlow Jr, W., and Huttsell, L. J., "An overview of aeroelasticity studies for the national aero-space plane," *Proceedings of the 34th AIAA/ASME/ASCE/AHS/ASC Structures, Structural Dynamics, and Materials Conference*, La Jolla, California, April 19–22 1993, AIAA Paper 93–1313.

[82] Lighthill, M. J., "Oscillating Airfoils at High Mach Number," *Journal of Aeronautical Sciences*, Vol. 20, No. 6, June 1953, pp. 402–406.

[83] Ashley, H. and Zartarian, G., "Piston theory-a new aerodynamic tool for the aeroelastician," *Journal of the Aeronautical Sciences*, Vol. 23, No. 12, 1956, pp. 1109–1118.

[84] McNamara, J. J. and Friedmann, P. P., "Flutter Boundary Identification for Time-Domain Computational Aeroelasticity," *AIAA Journal*, Vol. 45, No. 7, July 2007, pp. 1546–1555.

[85] McNamara, J. J., Friedmann, P. P., Powell, K. G., Thuruthimattam, B. J., and Barrels, R. E., "Aeroelastic and aerothermoelastic behavior in hypersonic flow," *AIAA Journal*, Vol. 46, No. 10, 2008, pp. 2591–2610.

[86] Farhat, C. and Lesoinne, M., "Two efficient staggered algorithms for the serial and parallel solution of three-dimensional nonlinear transient aeroelastic problems," *Computer Methods in Applied Mechanics and Engineering*, Vol. 182, No. 3-4, 2000, pp. 499–515.

[87] Farhat, C., Lesoinne, M., and Le Tallec, P., "Load and motion transfer algorithms for fluid/structure interaction problems with non-matching discrete interfaces: momentum and energy conservation, optimal discretization and application to aeroelasticity," *Computer methods in applied mechanics and engineering*, Vol. 157, No. 1-2, 1998, pp. 95–114.

[88] Bendiksen, O. O., "A new approach to computational aeroelasticity," *Proceedings of the 32nd AIAA/ASME/ASCE/AHS/ASC Structures, Structural Dynamics, and Materials Conference, Baltimore, MD*, April 8–10 1991, AIAA Paper 1991-939.

[89] Bendiksen, O. O., "Modern developments in computational aeroelasticity," *Proceedings of the Institution of Mechanical Engineers, Part G: Journal of Aerospace Engineering*, Vol. 218, No. 3, 2004, pp. 157–177.

[90] Bendiksen, O. O. and Seber, G., "Fluid-structure interactions with both structural and fluid nonlinearities," *Journal of Sound and Vibration*, Vol. 315, No. 3, 2008, pp. 664–684.

[91] Farhat, C., van der Zee, K. G., and Geuzaine, P., "Provably second-order time-accurate loosely-coupled solution algorithms for transient nonlinear computational aeroelasticity," *Computer Methods in Applied Mechanics and Engineering*, Vol. 195, No. 17-18, 2006, pp. 1973 – 2001.

[92] Rendall, T. and Allen, C., "Unified fluid-structure interpolation and mesh motion using radial basis functions," *International Journal for Numerical Methods in Engineering*, Vol. 74, No. 10, 2008, pp. 1519–1559.

[93] van Zuijlen, A., de Boer, A., and Bijl, H., "Higher-order time integration through smooth mesh deformation for 3D fluid-structure interaction simulations," *Journal of Computational Physics*, Vol. 224, No. 1, 2007, pp. 414 – 430.

[94] Morris, A., Allen, C., and Rendall, T., "CFD-based optimization of aerofoils using radial basis functions for domain element parameterization and mesh deformation," *International journal for numerical methods in fluids*, Vol. 58, No. 8, 2008, pp. 827–860.

[95] Van Zuijlen, A., De Boer, A., and Bijl, H., "Higher-order time integration through smooth mesh deformation for 3D fluid-structure interaction simulations," *Journal of Computational Physics*, Vol. 224, No. 1, 2007, pp. 414–430.

[96] Rendall, T. and Allen, C., "Efficient mesh motion using radial basis functions with data reduction algorithms," *Journal of Computational Physics*, Vol. 228, No. 17, 2009, pp. 6231–6249.

[97] Jakobsson, S. and Amoignon, O., "Mesh deformation using radial basis functions for gradient-based aerodynamic shape optimization," *Computers and Fluids*, Vol. 36, No. 6, 2007, pp. 1119 – 1136.

[98] de Boer, A., van Zuijlen, A., and Bijl, H., "Review of coupling methods for non-matching meshes," *Computer Methods in Applied Mechanics and Engineering*, Vol. 196, No. 8, 2007, pp. 1515 – 1525.

[99] de Boer, A., van Zuijlen, A., and Bijl, H., "Comparison of conservative and consistent approaches for the coupling of non-matching meshes," *Computer Methods in Applied Mechanics and Engineering*, Vol. 197, No. 49-50, 2008, pp. 4284–4297.

[100] Ahrem, R., Beckert, A., and Wendland, H., "A new multivariate interpolation method for large-scale spatial coupling problems in aeroelasticity," *Proceedings of the International Forum on Aeroelasticity and Structural Dynamics (IFASD), Germany*, Vol. 4, 2001.

[101] Hassig, H. J., "An approximate true damping solution of the flutter equation by determinant iteration," *Journal of Aircraft*, Vol. 8, No. 11, Nov. 1971, pp. 885–889.

[102] Cunningham, H. J., Batina, J. T., and Bennett, R. M., "Modern wing flutter analysis by computational fluid dynamics methods," *Journal of Aircraft*, Vol. 25, No. 10, 1988, pp. 962–968.

[103] Pak, C. G. and Friedmann, P. P., "New time-domain technique for flutter boundary identification," *Proceedings of the AIAA Dynamics Specialists Conference*, AIAA, Dallas, TX, April 16–17 1992, AIAA Paper 1992-2102.

[104] Torii, H. and Matsuzaki, Y., "Flutter Margin Evaluation for Discrete-Time Systems," *Journal of Aircraft*, Vol. 38, No. 1, 2001, pp. 42–47.

[105] Cowan, T. J., Arena, A. S., and Gupta, K. K., "Accelerating computational fluid dynamics based aeroelastic predictions using system identification," *Journal of Aircraft*, Vol. 38, No. 1, 2001, pp. 81–87.

[106] Raveh, D. E., Levy, Y., and Karpel, M., "Efficient aeroelastic analysis using computational unsteady aerodynamics," *Journal of Aircraft*, Vol. 38, No. 3, 2001, pp. 547–556.

[107] Raveh, D., "Identification of computational-fluid-dynamics based unsteady aerodynamic models for aeroelastic analysis," *Journal of aircraft*, Vol. 41, No. 3, 2004, pp. 620–632.

[108] Garrick, I., E., "A Survey of Aerothermoelasticity," *Journal of Aerospace Engineering*, Vol. 1, No. 22, 1963, pp. 140–147.

[109] Bisplinghoff, R. L., "Some Structural and Aeroelastic Considerations of High-Speed Flight," *Journal of Aeronautical Sciences*, Vol. 23, No. 4, April 1956, pp. 289–330.

[110] Lawrence, R. E. and Wykes, J. H., "Aerothermoelasticity-Its impact on stability and control of wingedaerospace vehicles." *Journal of Aircraft*, Vol. 2, No. 6, 1965, pp. 517–526.

[111] Budiansky, B. and Mayers, J., "Influence of Aerodynamics Heating on the Effective Torsional Stiffness of Thin Wings," *Journal of the Aeronautical Sciences*, Vol. 23, No. 12, December 1956, pp. 1081–1194.

[112] Mansfield, E. H., "Leading–Edge Buckling due to Aerodynamic Heating," R.A.E. Report Structures 250 No. 3197, Royal Aircraft Establishment, Aeronautical Research Council, Reports and Memoranda, May 1959.

[113] Watts, J. D., "Flight experience with shock impingement and interference heating on the X-15-2 research airplane," *NASA TM X-1669*, 1968.

[114] Mei, C., Abdel-Motagaly, K., and Chen, R., "Review of Nonlinear Panel Flutter at Supersonic and Hypersonic Speeds," *Applied Mechanics Reviews*, Vol. 52, 1999, pp. 321.

[115] Dowell, E. H., "Nonlinear oscillations of a fluttering plate," *AIAA Journal*, Vol. 4, No. 7, 1966, pp. 1267–1275.

[116] Xue, D. Y. and Mei, C., "Finite element nonlinear panel flutter with arbitrary temperatures in supersonic flow," *AIAA Journal*, Vol. 31, No. 1, 1993, pp. 154–162.

[117] Friedmann, P. and Hanin, M., "Supersonic non linear flutter of orthotropic or isotropic panels with"arbitrary" flow direction," *Israel Journal of Technology*, Vol. 6, 1968, pp. 46–57.

[118] Bein, T., Friedmann, P., Zhong, X., and Nydick, I., "Hypersonic flutter of a curved shallow panel with aerodynamic heating," *Proceedings of the 34th AIAA/ASME/ASCE/AHS/ASC Structures, Structural Dynamics, and Materials Conference, La Jolla, CA*, April 19–22 1993, AIAA Paper 1993–1318.

[119] Nydick, I., Friedmann, P., and Zhong, X., "Hypersonic panel flutter studies on curved panels," *Proceedings of the 36th AIAA/ASME/ASCE/AHS/ASC Structures, Structural Dynamics, and Materials*, American Institute of Aeronautics and Astronautics, April 10–13 1995, AIAA Paper 1995-1485.

[120] Librescu, L., Lin, W., Nemeth, M. P., and Starnes Jr., J. H., "Vibration of geometrically imperfect panels subjected to thermal and mechanical loads," *Journal of Spacecraft and Rockets*, Vol. 33, No. 2, March 1996, pp. 285–291.

[121] Eckert, E. R. G., "Engineering Relations for Heat Transfer and Friction in High-Velocity Laminar and Turbulent Boundary Layer Over Surfaces With Constant Pressure and Temperature," *Transactions of the ASME*, Vol. 78, No. 6, June 1956, pp. 1273–1283.

[122] Culler, A. J. and McNamara, J. J., "Studies on Fluid-Thermal-Structural Coupling for Aerothermoelasticity in Hypersonic Flow," *AIAA Journal*, Vol. 48, No. 8, Aug. 2010, pp. 1721–1738.

[123] Culler, A. J. and McNamara, J. J., "Impact of Fluid-Thermal-Structural Coupling on Response Prediction of Hypersonic Skin Panels," *AIAA Journal*, Vol. 49, No. 11, Nov. 2011, pp. 2393–2406.

[124] Culler, A. J., McNamara, J. J., and Deshmukh, R., "Response of Skin Panels to Combined Self and Boundary Layer Induced Fluctuating Pressure," *Proceedings of the 54th AIAA/ASME/ASCE/AHS/ASC Structures, Structural Dynamics, and Materials*, April 8–11 2013, AIAA Paper 3013–1744.

[125] Crowell, A. R. and McNamara, J. J., "Model Reduction of Computational Aerothermodynamics for Hypersonic Aerothermoelasticity," *AIAA Journal*, Vol. 50, No. 1, 2012, pp. 74–84.

[126] Olejniczak, J., Candler, G. V., Wright, M. J., Hornung, H. G., and Leyva, I., "High Enthalpy Double-Wedge Experiments," *Proceedings of the 19th AIAA, Advanced Measurement and Ground Testing Technology Conference*, New Orleans, LA, June 17–20 1996, AIAA Paper No. 96-2238.

[127] Smith, V., Laster, M., and Boudreau, A., "Test and evaluation challenges for hypersonic air-breathing propulsion systems," *Proceeding of the Joint Test and Evaluation, AIAA Meeting Paper Archive,London, UK*, 31 May - 02 June 1994, AIAA Paper No. 94-2675-CP.

[128] Cox, C., Lewis, C., Pap, R., Golver, C., Priddy, K., Edwards, J., and McCarty, D., "Prediction of Unstart Phenomena in Hypersonic Aircraft," *Proceedings of the 6th*

AIAA International Aerospace Planes and Hypersonics Technologies Conference, Chattanooga, TN, April 3–7 1995, AIAA Paper No. 95-6018.

[129] Falkiewicz, N. J., Cesnik, C. E. S., Crowell, A. R., and Mcnamara, J. J., "Reduced-Order Aerothermoelastic Framework for Hypersonic Vehicle Control Simulation," *AIAA Journal*, Vol. 49, No. 8, 2011, pp. 1625–1646.

[130] Skujins, T. and Cesnik, C., "Toward an Unsteady Aerodynamic ROM for Multiple Mach Regimes," *Proceedings of the 53rd AIAA/ASME/ASCE/AHS/ASC Structures, Structural Dynamics, and Materials, Honolulu, Hawaii*, April 23–26 2012, AIAA Paper 2012-1708.

[131] Heiser, W. H. and Pratt, D. T., *Hypersonic airbreathing propulsion*, AIAA, 1994.

[132] Smart, M. K., "Experimental Testing of a Hypersonic Inlet with Rectangular-to-Elliptical Shape Transition," *Journal of Propulsion and Power*, Vol. 17, No. 2, March–April 2001, pp. 276–283.

[133] Schulte, D., Henckels, A., and Neubacher, R., "Manipulation of SchockBoundary–Layer Interactions in Hypersonic Inlets," *Journal of Propulsion and Power*, Vol. 17, No. 3, May–June 2001, pp. 585–590.

[134] Dalle, D., Torrez, S. M., and Driscoll, J. F., "Rapid Analysis of Scramjet and Linear Plug Nozzles," *Journal of Propulsion and Power*, Vol. 28, No. 3, May 2012, pp. 545–555.

[135] Dalle, D. J., Frendreis, S., Driscoll, J. F., and Cesnik, C. E. S., "Hypersonic Vehicle Flight Dynamics with Coupled Aerodynamic and Reduced-Order Propulsive Models," *Proceedings of the AIAA Atmospheric Flight Mechanics Conference*, Toronto, Ontario, August 2–5 2010, AIAA-2010-7930.

[136] Torrez, S. M., Dalle, D. J., and Driscoll, J. F., "New Method for Computing Performance of Choked Reacting Flows and Ram-to-Scram Transition," *AIAA Journal of Propulsion and Power*, 2013, pp. 1–13.

[137] Raney, D. L. and McMinn, J. D., "Impact of Aeroelastic–Propulsive Interactions on Flight Dynamics of a Hypersonic Vehicle," *Journal of Aircraft*, Vol. 32, No. 2, March–April 1995, pp. 355–362.

[138] Bolender, M. A. and Doman, D. D., "Nonlinear Longitudinal Dynamical Model of an Air-Breathing Hypersonic Vehicle," *Journal of Spacecraft and Rockets*, Vol. 44, No. 2, March–April 2007, pp. 374–387.

[139] Witteveen, J. A., Duraisamy, K., and Iaccarino, G., "Uncertainty Quantification and Error Estimation in Scramjet Simulation," *17th AIAA International Space Planes and Hypersonic Systems and Technologies Conference*, April 11–14 2011, AIAA Paper 2011–2283.

[140] Hascoët, L. and Pascual, V., "The Tapenade Automatic Differentiation tool: principles, model, and specification," Rapport de recherche RR-7957, INRIA, May 2012.

[141] Sobol, I., "Global sensitivity indices for nonlinear mathematical models and their Monte Carlo estimates," *Mathematics and computers in simulation*, Vol. 55, No. 1-3, 2001, pp. 271–280.

[142] Tang, G., Iaccarino, G., and Eldred, M., "Global Sensitivity Analysis for Stochastic Collocation," *AIAA/ASME/ASCE/AHS/ASC Structures, Structural Dynamics, and Materials Conference*, April 2010, AIAA Paper 2010–2922.

[143] McKay, M., Beckman, R., and Conover, W., "A comparison of three methods for selecting values of input variables in the analysis of output from a computer code," *Technometrics*, Vol. 42, No. 1, 2000, pp. 55–61.

[144] Golub, G. H. and Welsch, J. H., "Calculation of Gauss quadrature rules," *Mathematics of Computation*, Vol. 23, 1969, pp. 221–230.

[145] Crassidis, J. L. and Junkins, J. L., *Optimal Estimation of Dynamic Systems*, Chapman & Hall/CRC Applied Mathematics and Nonlinear Science Series, 2004.

[146] Lophaven, S. N., Nielsen, H. B., and Søndergaard, J., *A Matlab Kriging Toolbox, Version 2.0*, Informatics and Mathematical Modeling, DTU, 2002, Technical Report IMM-TR-2002-12.

[147] Bichon, B., Eldred, M., Swiler, L., Mahadevan, S., and McFarland, J., "Efficient global reliability analysis for nonlinear implicit performance functions," *AIAA Journal*, Vol. 46, No. 10, 2008, pp. 2459–2468.

[148] Jones, D. R., "Direct Global Optimization Algorithm," *Encyclopedia of optimization*, Springer, 2001, pp. 431–440.

[149] Bartels, R., Rumsey, C., and Biedron, R., "CFL3D Version 6.4, General usage and aeroelastic analysis," Tech. rep., NASA TM–2006–214301, 2006.

[150] Higham, N. J., "The Scaling and Squaring Method for the Matrix Exponential," *SIAM Journal on Matrix Analysis and Applications*, Vol. 26, No. 4, 2005, pp. 1179–1193.

[151] Rodden, W. P., *Chapter 7, Theoretical and Computational Aeroelasticiy*, Crest Publishing, 2011.

[152] *CFD++ User Manual - Version 10.1*, Metacomp Technologies, Inc., Agoura Hills, CA, 2010.

[153] Spalart, P. R. and Allmaras, S. R., "A One-Equatlon Turbulence Model for Aerodynamic Flows," *Proceedings of the 30th Aerospace Sciences Meeting and Exhibit, Reno, NV*, Jan. 1992, AIAA Paper 92-0439.

[154] Roy, C. J. and Blottner, F. G., "Review and assessment of turbulence models for hypersonic flows," *Progress in Aerospace Sciences*, Vol. 42, No. 7-8, 2006, pp. 469–530.

[155] Narasimha, R., "The laminar-turbulent transition zone in the boundary layer," *Progress in Aerospace Sciences*, Vol. 22, No. 1, 1985, pp. 29–80.

[156] Park, C., *Nonequilibrium hypersonic aerothermodynamics*, Wiley-Interscience New York etc., 1990.

[157] McNamara, J. J., *Aeroelastic and Aerothermoelastic Behavior of Two and Three Dimensional Lifting Surfaces in Hypersonic Flow*, Ph.D. thesis, The University of Michigan, Ann Arbor, Michigan, 2005.

[158] Lamorte, N., Glaz, B., Friedmann, P. P., Culler, A. J., Crowell, A. R., and McNamara, J. J., "Uncertainty Propagation in Hypersonic Aerothermoelastic Analysis," *Proceeding of the 51st AIAA/ASME/ASCE/AHS/ASC Structures, Structural Dynamics, and Materials Conference*, Orlando, Florida, April 12–15 2010, AIAA Paper 2010-2964.

[159] Culler, A. and McNamara, J. J., "Studies on Fluid-Thermal-Structural Coupling for Aerothermoelasticity in Hypersonic Flow," *AIAA Journal*, Vol. 48, No. 8, 2010, pp. 1721.

[160] Krist, S., Biedron, R., and Rumsey, C., *CFL3D user's manual (version 5.0)*, NASA/TM-1998-208444, September 1998.

[161] Crowell, A., McNamara, J., and Miller, B., "Hypersonic Aerothermoelastic Response Prediction of Skin Panels Using Computational Fluid Dynamic Surrogates," *Journal of Aeroelasticity and Structural Dynamics*, Vol. 2, No. 2, 2011, pp. 3 – 30.

[162] Dalle, D., Fotia, M., and Driscoll, J., "Reduced-Order Modeling of Two-Dimensional Supersonic Flows with Applications to Scramjet Inlets," *Journal of Propulsion and Power*, Vol. 26, No. 3, 2010, pp. 545–555.

[163] Torrez, S. M., Driscoll, J. F., Dalle, D. J., and Fotia, M. L., "Preliminary Design Methodology for Hypersonic Engine Flowpaths," *Proceedings of the 16th AIAA/DLR/DGLR International Space Planes and Hypersonic Systems and Technologies Conference*, Bremen, Germany, October 19-22 2009, AIAA Paper No. 2009–7289.

[164] Anderson, J. D., *Hypersonic and High Temperature Gas Dynamics*, Mc Graw Hill Editions, 1989.

[165] Torrez, S. M., Driscoll, J. F., Dalle, D. J., and Micka, D. J., "Scramjet Engine Model MASIV: Role of Mixing, Chemistry and Wave Interaction," *Proceedings of the 45th AIAA/ASME/SAE/ASEE Joint Propulsion Conference and Exhibit*, Denver, Colorado, August 2-5 2009, AIAA Paper No. 2009-4939.

[166] Hunt, J. L. and Eiswirth, E. A., "NASAś Dual-Fuel Airbreathing Hypersonic Vehicle Study," *Proceedings of the 7th International Space Planes and Hypersonics Systems and Techonology Conference*, Norfolk, VA, November 18–22 1996, AIAA 1997-10900.

[167] Weirich, T. L., Fogarty, W., Dry, K., Iqbal, A., and Moses, P. L., "Dual-fuel Vehicle Airframe and Engine Structural Integration," *Proceedings of the 7th International Space Planes and Hypersonic Systems and Technologies Conference*, Norfolk, VA, 1996.

[168] Orton, G. F., Scuder, L. F., and Artus, J., "Airbreathing hypersonic aircraft and transatmospheric vehicles," *Future aeronautical and space systems*, 1997, pp. 297–371.

[169] Ko, W. L. and Jackson, R. H., "Combined Compressive and Shear Buckling Analysis of Hypersonic Aircraft Structural Sandwich Panels," Tech. rep., may 1991.

[170] Bolender, M. and Doman, D., "Modeling unsteady heating effects on the structural dynamics of a hypersonic vehicle," *Proceedings of AIAA Atmospheric Flight Mechanics Conference and Exhibit*, Keystone, Colorado, August 21–24 2006.

[171] Raney, D. L., McMinn, J. D., and Pototzky, A. S., "Impact of aeroelastic-propulsive interactions on flight dynamics of a hypersonic vehicle," *Journal of Aircraft*, Vol. 32, No. 2, March 1995, pp. 355–362.

[172] Lamorte, N., Friedmann, P., Dalle, D., Torrez, S., and Driscoll, J., "Uncertainty Propagation in Integrated Airframe Propulsion System Analysis for Hypersonic Vehicles," *Proceedings of the 17th International Space Planes and Hypersonic Systems and Technologies Conferences*, April 11–14 2011, AIAA Paper 2011-2394.

[173] Lamorte, N. and Friedmann, P. P., "Hypersonic Aeroelastic Stability Boundary Computations Using Radial Basis Functions for Mesh Deformation," *Proceedings of the 18th AIAA/3AF International Space Planes and Hypersonic Systems and Technologies Conference*, Tours, France, September 24–28 2012, AIAA Paper 2012-5943.

[174] Lamorte, N. and Friedmann, P. P., "Aerothermoelastic and Aeroelastic Studies of Hypersonic Vehicles using CFD," *Proceedings of the 54th AIAA/ASME/ASCE/AHS/ASC Structures, Structural Dynamics, and Materials*, April 8–11 2013, AIAA Paper 2013-1591.

[175] Sobotka, J. C., Oral, A., and Culler, A. J., "Towards a Coupled Loads-Response-Life Prediction Framework for Hypersonic Structures in Combined Extreme Environments," *Proceedings of the 54th AIAA/ASME/ASCE/AHS/ASC Structures, Structural Dynamics, and Materials*, April 2013, AIAA Paper 2013–1519.

[176] Cowan, T. J., Arena, A. S., and Gupta, K. K., "Acceleration CFD-based aeroelastic predictions using system identification," *Journal of aircraft*, Vol. 38, No. 1, January–February 2001, pp. 81–87.

[177] Trefethen, L. N., "Is Gauss quadrature better than Clenshaw-Curtis?" *SIAM review*, Vol. 50, No. 1, 2008, pp. 67–87.

[178] Klimke, A., "Sparse grid interpolation toolbox–users guide," *IANS report*, Vol. 1, 2006.

[179] Agarwal, N. and Aluru, N. R., "Weighted Smolyak algorithm for solution of stochastic differential equations on non-uniform probability measures," *International Journal for Numerical Methods in Engineering*, Vol. 85, No. 11, 2011, pp. 1365–1389.

[180] Barthelmann, V., Novak, E., and Ritter, K., "High dimensional polynomial interpolation on sparse grids," *Advances in Computational Mathematics*, Vol. 12, No. 4, 2000, pp. 273–288.

[181] Bae, J.-S., Inman, D., Kim, J.-Y., Lee, I., and Matsuzaki, Y., "Extension of Flutter Prediction Parameter for Multimode Flutter Systems," *Journal of Aircraft*, Vol. 42, No. 1, Jan. 2005, pp. 285–288.